Design of Biomimetic Pigment-Polymer Antenna Complexes based on Chlorophyll-Functionalised Polymer Brushes

Munirah Alfarhan

A thesis submitted in partial fulfilment of the requirements for the degree of

Doctor of Philosophy

The University of Sheffield

Department of Mathematical and Physical Sciences

November -2024

Declaration

The research described in this thesis was conducted at the University of Sheffield between October 2020 and November 2024 under the supervision of Professor Graham J. Leggett. It is the author's work and has not been submitted in whole or in part for any other degree at this or any other institution.

Signed: …………………

Munirah Alfarhan

November 2024

Department of mathematical and physical sciences

Dainton Building,

University of Sheffield,

Brook Hill, Sheffield,

UK. S3 7HF

Acknowledgment

Firstly, I would like to thank my supervisor, Professor Graham J. Leggett, for giving me this great opportunity to be a part of his research group. It would not have been possible for me to complete this thesis without his patience, kindness, support, and advice. Secondly, I would also like to extend my gratitude to all the members of Graham's group. Dr. Deborah Hammond deserves special recognition for her kind support with the X-ray photoelectron spectroscopy (XPS) technique. Also, I would like to thank Dr. Jodie West for providing the ellipsometry analysis, and modeling of polymer brush layers before and after dye functionalization, and for her help with spectroscopy ellipsometry (SE) data modeling for this study. Additionally, I would like to express my gratitude to Dr. Kamalika Das for her collaboration on the synthesis of HGN gold nanoparticles and for providing me with TEM images of gold nanoparticles. I extend my heartfelt gratitude to all former and current members of the Prof. Leggett group. Thank you to all my wonderful friends and the people I met along my journey. A special thank you to my dear friends Dr. Evelin, Aysha, Camery, Devy and Owen. We've worked together so closely that it feels like we are a family. The time we spent together, both professionally and personally, has been invaluable to me, and I will always cherish these moments. I am grateful to express my appreciation to the University of Sheffield and all members of the Chemistry Department.

I am deeply grateful to King Faisal University in Saudi Arabia and the Saudi embassy for their funding of my PhD.

My father, Abdullah my biggest influence, deserves special thanks. He has consistently been a pillar of strength and a source of inspiration. He has consistently been a reliable source of strength, providing persistent support and direction and a continual source of inspiration and motivation for me. His ability, compassion, and consistent dedication have significantly impacted my character, for which I am eternally grateful for his indispensable presence in my life.

I would like to thank my mother, Sarah, for believing in me. You helped me finish this journey even though you're gone.

I would like to express my gratitude to my husband, Hamad. There are no words to express how much I appreciate you. Thank you so much for your constant love and support.

Acknowledgement

I owe sincere thankfulness to my children, Saleh, Sarah, and Raghad, for their unwavering support; I could not have done this without them.

I wish to express my sincere gratitude to my sisters (Wedyan, Aysha, Norah, and Ahlam) and brothers (Abdulaziz, Hamad, and Fahad) for their unconditional support and affection during this period, as well as for their constant belief in me.

I wish to express my sincere gratitude to my best friend Norah, who has consistently supported me through both triumphs and tribulations. Your support was imperative for the completion of this work.

Finally, I would like to express my gratitude. I would like to express my sincere gratitude to my dear neighbors; Anaam, Razan, and Randah, who have been kind and supportive throughout this time and for the wonderful times we have shared with them.

Abbreviation

11-MUL	11-mercapto-1-undecanol
12-MDA	12-mercaptododecanoic acid
ATRP	Atom transfer radical polymerisation
AFM	Atomic force microscopy
AA	Ascorbic acid
Au NPs	Gold nanoparticles
AgNPs	Silver nanoparticles
APTES	3–aminopropyltriethoxysilane
ATR	The attenuated total reflection
ARGET	Activator regenerated by electron transfer
ARGET-ATRP	Activator regenerated by electron transfer-atom transfer radical
BIBB	2-bromoisobutyryl bromide
BE	binding energy
BIBUDT	Bromoisobutyrylundecanethiolate
BIBB-APTES	2-bromoisobutyryl bromide (3-aminopropyltriethoxysilane)
CVD	Chemical vapor deposition
Chl a	Chlorophyll a
Chl b	Chlorophyll b
CA	Contact angle
CTAB	Cetyltrimethylammonium bromide
CHA	Concentric hemispherical analyser
Cr	Chromium
DTBU	bis[2-(2bromoisobutyryloxy)undecyl]disulfide
DMA	(2-dimethylamino) ethyl methacrylate)
DCM	Dichloromethane
DMF	Dimethylformamide
DQ	Degree of quaternization
EBL	Electron-beam lithography
ESCA	Electron Spectroscopy for Chemical Analysis
EM	Electromagnetic
FWHM	Full width at half maximum
HOMO	Highest occupied molecular orbital
HMTETA	1,1,4,7,10,10-hexamethyltriethylenetetramine
HGN	Hollow gold nanoprism
IPA	Isopropyl alcohol
KE	Kinetic energy
LHC	Light-harvesting complexes
LUMO	Lowest unoccupied molecular orbitals
LSPs	Localized surface plasmons

LSPR	Localized surface plasmon resonance
LCST	Lower critical solution temperature
LH1	Light-harvesting complexes 1
LH2	Light-harvesting complexes 2
MS	Mass spectrometry
NMR	Nuclear magnetic resonance
NPs	Nanoparticles
OLEDs	Organic light-emitting diodes
QDs	Quantum dots
PCysMA	Poly (cysteine methacrylate)
PSPR	Propagating surface plasmon resonance
PSS	Polystyrene sodium sulphonate
PZT	Piezoelectric lead zirconate titanate
PNIPAM	poly(N-isopropylacrylamide)
POEGMA	Poly oligoethylene glycol methacrylate
PMAOEPC	poly2-methacryloyloxyethyl phosphoryl
PDMA	Poly(2-dimethylamino) ethyl methacrylate)
q-PDMA	Quaternised poly(2-dimethylamino) ethylmethacrylate)
PAAM	Poly (acryl amide)
PMETAC	Poly [2- (methacryloyloxy) ethyl] trimethylammonium chloride
PCE	Power conversion efficiency
PSD	Position-sensitive photodiode
QCM	Quartz crystal microbalance
RMS	Root mean square
RMSE	Root mean square error
RI	Refractive index
RC	Reaction centre
R-X	Alkyl halide
RAFT	Reversible addition-fragmentation Chain transfer
SPRs	Surface plasmon resonances
SAMs	Self-assembled monolayers
SE	Spectroscopic ellipsometer
SPPs	Surface plasmon polaritons
SI-ATRP	Surface-initiated atom transfer radical polymerisation
TEM	Transmission electron microscopy
TST	Trisodium citrate
THF	Tetrahydrofurane
UV/vis	Ultraviolet/Visible
UHV	Ultra-high vaccum
VASE	Variable angle spectroscopic ellipsometry
WPLEDs	White polymer light-emitting diodes
XPS	X-ray photoelectron spectroscopy
ZnChla	Zinc phyrochlorophyllide a

Table of Contents

List of Figures

List of Tables

Abstract

In the last twenty years, much effort has been directed into finding methods to ensure the efficient transmission of energy across long distances in molecular photonic materials. Exciton diffusion lengths in molecular systems are typically of the order of 10 nm, thus constraining the design of various devices. The photosynthetic light-harvesting complexes (LHCs) found in plants and bacteria have been the subject of considerable interest due to their potential role for efficient exciton transfer in molecular systems. Peptide units in these pigment-protein complexes organise chlorophyll and carotenoid molecules into specific and unique arrangements. However, the high cost of large-scale manufacturing and the natural susceptibility of the protein to damage during processing makes light-harvesting complexes unsuitable for utilisation as photonic materials. A recent study demonstrated that surface-grafted poly (amino acid methacrylate) brushes can be used to design biomimetic pigment-polymer complexes, enabling strong coupling of excitons to confine optical modes with an efficiency exceeding that found for pigment-protein complexes in photosynthesis.

This thesis explores the possibility of designing synthetic photonic materials inspired by natural light-harvesting complexes to facilitate the efficient transport of excitons across extended distances. In particular, the utilisation of poly (2-dimethylamino ethyl methacrylate) (PDMA) scaffolds formed by atom transfer radical polymerisation (ATRP) to support chlorophyll a (Chl *a*) molecules is examined. The hypothesis that tertiary amine pendant groups on the PDMA could coordinate with the metal ion at the core of the Chl *a* tetrapyrrole ring was examined. Chl *a* was isolated from spinach and incubated with PDMA grown to a thickness of ~30 nm from BIBB-APTES initiator surfaces. The binding of chlorophyll to PDMA scaffolds was investigated using X-ray photoelectron spectroscopy (XPS) and UV-visible spectroscopy (UV-vis). Binding curves were measured for the attachment of Chl *a* to PDMA scaffolds. Chl *a* concentrations in PDMA scaffolds were found to be as high as ~2M, ca. 3 times the concentration found in biological light-harvesting complexes. By partially quaternising the PDMA brush, it is possible to control the density of chlorophyll, which provides potential for future utilisation in biologically inspired energy transfer systems.

The findings provide strong evidence in support of the hypothesis that Chl *a* forms a bond with PDMA brushes by coordinating the tertiary amines in the pendant groups with the Chl *a* metal centre. It was hypothesised that by incorporating strong plasmon-exciton coupling, it would be possible to achieve long-range energy transfer in these films. Through the plasmon mode, coherent energy exchange can in principle occur between spatially separated pigments in the strong coupling regime. Gold surfaces were functionalised by the adsorption of thiols with bromine initiators at their tail ends. PDMA was grown from the initiator functionalised planar gold surfaces and characterised using XPS, atomic force microscopy (AFM), and spectroscopic ellipsometry (SE) techniques. When grown under the same conditions as used to grow PDMA brushes from BIBB-APTES, including a temperature of 90 °C, PDMA layers grown on gold were found to be very thin, attributed to the poor stability of the thiol initiator layer at elevated temperatures. However, on reduction of the temperature to 50 ºC, stable polymer layers were formed, albeit with slightly reduced thickness because of slower kinetics at the lower temperature. For fully dense brush layers, chlorophyll binding was found to be sterically inhibited. This, mixed self-assembled monolayers consisting of DTBU and MUL were formed to reduce the grafting density. Using this approach, it was found that larger concentrations of chlorophyll could be achieved in the brush layer. XPS data indicated that the best results were obtained for an initiator mole fraction in the thiol film, χBr (Au), of 0.24, which facilitated a fourfold increase in the amount of bound Chl *a*.

The incorporation of plasmonic materials into PDMA brushes was investigated as an alternative approach to creating pigment-polymer antennas on gold surfaces. However, the incorporation of gold nanoparticles of different sizes did not yield strong plasmon-exciton coupling. This was mainly due to the difference in energy between the localised surface plasmon resonance (LSPR) of the nanoparticles and excitons in Chl *a*. Further exploration involving hollow gold nanoparticles (HGN) and silver nanoparticles (AgNPs) also did not achieve the desired coupling.

Chapter 1: Introduction

1 General Introduction

1.1 Brief history of plasmonic

Plasmonic materials have garnered significant attention in recent years. A surface plasmon is the collective excitation of conduction electrons at the interface between a metal and a dielectric material.[1] The plasmons of noble metal nanoparticles have frequencies corresponding to the visible region of the electromagnetic spectrum, and they absorb light strongly, giving rise to strong colours and unique optical properties. Plasmonics has emerged as one of the most important areas within the new field of nanophotonics, with potential applications in multiple disciplines. For example, plasmonic metal nanostructures are attracting attention for applications ranging from the enhancement of photovoltaic performance [2-4] to biosensing,[5-7] because of their unique optical properties that facilitate improved absorption and scattering.[8]

Plasmons usually appear at the surfaces of noble metals, including silver (Ag), gold (Au) and copper (Cu), which possess high negative real parts and small positive imaginary components in their dielectric constants.[8, 9] Plasmonic nanostructures also have exceptional optical properties that are distinct from those of bulk metals. Gold nanoparticles (Au NPs) have gained significant attention in the area of plasmonics as a result of (i) their diverse optical properties; (ii) the notable physical and chemical stability, alongside its biocompatibility of gold; and (iii) the ease that the Au NPs' surfaces are able to be functionalised through the use of organic and biological molecules. Further, Au NPs have a high level of sensitivity to the surrounding dielectric environment, enhanced electromagnetic field, and the large absorption coefficients.[10]

Plasmonic metal nanoparticles possess a rich history, originating in the 4th century A.D. with the Lycurgus cup, (see Figure 1-1) which exhibits varying colours according to the light's angle of incidence.[10-13] Localised surface plasmons exhibit the extraordinary characteristics of this cup and, in reflected light, this exhibits a green colour whereas in transmitted light, it displays a red colour. The origin of the unique optical characteristics of colloidal gold, though has remained unclear for many decades. In 1902, Wood made the initial observation of plasmonic behaviour, noting a significant reduction in the intensity of light reflected by metallic gratings, a phenomenon termed "Wood's anomaly".[14] This anomaly arises from the excitation of surface plasmons, leading to a decrease in the energy of the reflected light.[9, 11] Garnett detailed in 1904 that the phenomenon of light scattering by particles is beneficial in the process of demonstrating the different colours that can be seen in the glass containing minute metallic particles.[15] Later Fano linked these surface waves in 1941, maintained by the grating.[9] While in 1968, Otto noted a decrease in the reflectance of incident light in attenuated total reflection (ATR). [16] This creates an evanescent wave through internal total reflection within a prism, which is linked with the surface plasmon.[17] The following year, Kretschmann and Raether observed the excitation of surface plasmons after making alterations to the setup of the ATR method. Ultimately, Ritchie *et al*.[18] employed surface plasmons as a substitute for surface waves to elucidate the phenomenon and confirm Fano's theory.[9, 11] Indeed, in recent decades, surface plasmons have been widely utilised in various applications, including cancer therapy, drug delivery, medical diagnostics and cellular imaging.[10]

Figure 1-1: The Lycurgus Cup, 4th century A.D., appears red (on the right) when viewed in transmitted light, whereas green (on the left) when viewed in reflected light.[10]

There are two types of surfaces plasmon modes: propagating surface plasmons (PSPs) and localised surface plasmons (LSPs). Surface plasmon resonance in both forms occurs at resonance conditions through the interaction of electromagnetic waves with conduction electrons in metals. If the incident light frequency matches the plasmon frequency, resonant coupling occurs, resulting in surface plasmon resonance.[9, 11, 12] Figure 1-2 clearly illustrates each category of plasmon resonance.

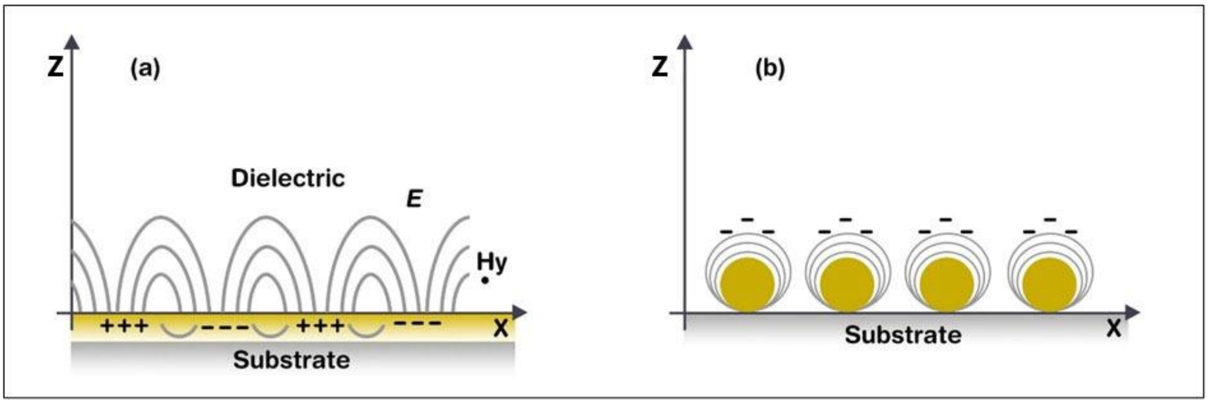

Figure 1-2: Surface plasmon types: (a) propagating surface plasmons (PSPs), which are collective electron oscillations that traverse the interface between a metallic surface and a dielectric medium and (b) localised surface plasmons (LSPs), which are localised surface plasmons confined around the surfaces of nanoparticles.

1.2 Fundamental principles of plasmonics

Surface plasmon resonance (SPR) is a phenomenon that arises from the resonant coupling of incident electromagnetic waves to plasma oscillations, which are the collective oscillations of conduction electrons around their mean positions at the interface between a metal surface and a dielectric material. SPR is observed when the frequency of electronic oscillations at the metal interface corresponds to the frequency of the incident photons. The resonance situation facilitates the coupling of photons to free electrons in the metal, resulting in a novel form of electromagnetic excitation, which is termed an evanescent wave. The transient field of this electromagnetic wave is acutely responsive to variations in the refractive index of the dielectric medium, providing surface plasmon resonance with an effective tool for sensing and characterisation purposes.[13, 19, 20] The Drude theory describes electron dynamics within metals based on the assumption that electrons are free and independent. In this case, the motion of the cloud as a whole consists of the motions of individual electrons, thus resulting in electrons acting in phase with each other. In the nanoparticles, the electron density is less uniform than in larger particles, leading to the accumulation of charges at their edges. Surface charges are formed as the electron cloud is displaced by the electric field. In particular, with surface charges positive when the electron cloud is lacking and negative when it is concentrated,[21] (see Figure 1-3). Application of an oscillating electric field (for example, coupling to electromagnetic radiation) leads to the creation of an oscillating dipole. As a result of metals' plasma-like free-electron response, their dielectric constants are negative at frequencies below the plasma frequency. Metal nanoparticles display colours in scattering, which are ascribed to the resonant interaction between the incident electromagnetic field and the charge oscillation on the nanoparticle's surface. These are referred to as localised plasmons, and the resonance frequency is contingent upon the nanoparticle's size, shape, material, and the surrounding medium.[1]

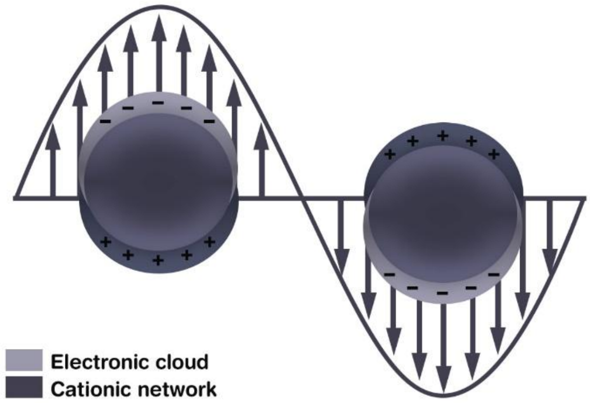

Figure1-3: Schematic illustration of spherical gold nanoparticles oscillating in the conduction band and interacting with resonant light waves, (the motion of the electronic cloud around a particle).

As a nanoparticle (NP) is smaller than the wavelength of light, it is reasonable to assert that all electrons trapped within the nanoparticle experience the same electric field simultaneously, whatever their position within the particle. This theory is referred to as the quasi-static approximation, with the electrons within the nanoparticle moving under the influence of the electric field. The oscillation of electrons within the nanoparticle leads to the creation of plasmon polaritons, which are linked to excitations of the electromagnetic field and the collective electron oscillations. This differs from the free plasmons that are able to exist in bulk metallic materials. As a result, Shopper introduced the term plasmon to describe the oscillations of confined gaseous plasmons.[21]

1.3 Classification of plasmonics

1.3.1 Propagating surface plasmons

Propagating surface plasmon resonance (PSPR) transpires when light interacts with a metallic surface under particular conditions, resulting in the oscillation of free electrons on the surface. These oscillations, termed surface plasmons polaritons, propagate across the surface of the metal in horizontal orientations (x- and y-axes).[22] For this resonance to occur, the incident light must strike the metal at a specific angle, enabling the light's energy to pair with the surface plasmons. At this resonance angle, the intensity of reflected light diminishes significantly, leading to a minimum in reflection, which is an effect that is acutely responsive to variations in the refractive index of the substance encasing the metal. Moreover, when the refractive index varies, such as when a different medium is introduced adjacent to the metal (e.g., from air to water), the resonance condition is modified, resulting in a change in the angle at which minimum reflection occurs. The alteration in the plasmon peak is also observable in the reflection spectra.[23] Thus, any alteration in the refractive index results in a displacement of the plasmon peak minimum evident in the reflection spectra, see Figures (1-4 a and b).

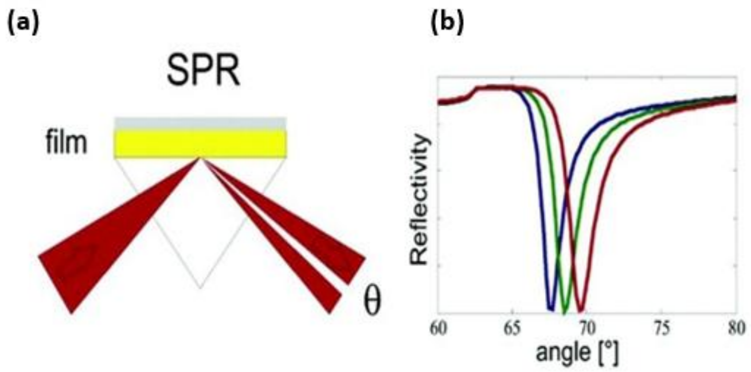

Figure 1-4: The PSPR sensing principle shows the reflection spectra as a function of angle changes, as a result of differences in the refractive index (RI) surrounding the layer. A molecular film with a thickness of 10 nm (the green line) and 20 nm (the red line), with a refractive index of 1.48 in water (n = 1.33), simulates the biomolecules' characteristics. [23]

Photons incident on a smooth metallic surface do not directly generate surface plasmons due to the propagation constant of the surface plasmon is greater than the wavenumber of the light wave in the dielectric. The difference in wave vectors reduces the direct excitation of surface plasmons by incident light. To address this limitation, various approaches can be utilised to improve the wave vector of the incident light, thus matching it with the propagation constant of the surface plasmons. Indeed, the excitation mechanism of surface plasmons can be described by three primary SPR coupling approaches, as illustrated in Figure 1-5.[24, 25]

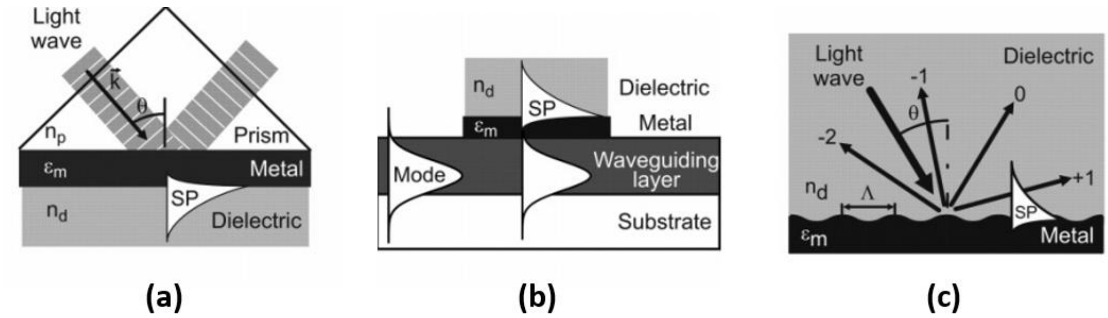

Figure 1-5: The surface plasmon (SP) excitation mechanism consists of three coupling methods (a) prism coupling, (b) waveguide coupling, and (c) grating coupling.[25]

The three coupling methods, prism coupling, waveguide coupling, and grating coupling illustrated in Figure 1-5 provide distinct approaches for the enhancement of the wavenumber of an incident wave to enable the excitation of SPR. Prism coupling is the most frequently employed method, as noted by Caucheteur *et al*.[23] The prism coupling technique can be categorised into two configurations: Kretschmann and Otto. The primary distinction between these two arrangements is the separation between the prism and the thin metal film. In the Otto configuration, a slight interstice exists between the prism and the metal film, whereas in the Kretschmann configuration, the prism is in direct contact with the metal film. The direct contact in the Kretschmann configuration obviates the necessity for precise spacing management, rendering it a more convenient and practical method than the Otto configuration.[13] Furthermore, in the Kretschmann coupling approach, the evanescent field is produced as the light beam passes through the high refractive index prism (n_p), as shown in Figure 1-5a. The evanescent waves (β) are produced when the angle of incident light (θ_0) is greater than the critical angle (θ_c) which can traverse the metal surface and travel along it with a defined propagation constant. [20, 24] Hence, by modifying the angle of the incident light, the wavenumber of the light wave can be regulated to correspond with the wavenumber of the surface plasmon resonance. Another technique for exciting surface plasmons is waveguide coupling, which involves directing light waves through an optical waveguide, as illustrated in Figure 1-5b. This method involves the interaction of the evanescent wave at the waveguide's outer boundary with the surface plasmon wave when their propagation constants are similar. Ultimately, optical excitation can be performed using a grating coupling, regarded as the original technique for exciting surface plasmons, which relies on the diffraction of light within a grating coupler, as illustrated in Figure 1-5c. This transpires when the momentum of the light wave aligned with the grating surface corresponds to the propagation vector of the surface plasmon oscillations, facilitating the efficient coupling and excitation of surface plasmons at the metal-dielectric interface by the incident light.[24, 25] Despite the significant advancements in biosensor technology achieved with this type of SPR, surface plasmon waves suffer from damping which can become a serious problem in some situations.[13]

1.3.2 Localised surface plasmons

Localised surface plasmon resonances (LSPRs) result when light is coupled resonantly to metallic structures that are smaller than the wavelength of light. The resulting optical mode is confined to a sub-wavelength region of space. Modifying the size, shape, metal type, and dielectric environment leads to changes in the properties of the LSPR. LSPR has been extensively investigated and applied in a variety of applications since it does not require a special excitation geometry.[13] LSPR is not only excited by direct exposure to conventional light but is also independent of the incidence angle.[23, 26] LSPR has been used in a wide range of applications due to its ability to adapt and potential for diverse technological applications.

When nanoparticles are exposed to light with a wavelength greater than their size, as illustrated in Figure 1-6a, resonant coupling of the plasma oscillation to the incident light enhances, the electric field surrounding the metal nanoparticles. Figure 1-6 b illustrates that changes in the refractive index (RI) of the medium close to the nanoparticle surface result in a shift in the energy of the LSPR, causing a red shift in the absorption maximum (λ max). The localised electric field associated with the plasmon mode has a decay length of roughly 20 to 40 nm, as illustrated in Figure 1-7.[22] Consequently, the electric field is highly localised within the nanoparticles, resulting in the creation of an oscillating dipole. The boosted electric field exhibits significant sensitivity to the surrounding medium. For example, the attachment of small biological molecules can induce a quantifiable change in the plasmon energy as a consequence of the change in the local refractive index. [23, 27] Hence, the shorter decay length of localised surface plasmon resonance(~20-40 nm) in comparison with propagating surface plasmon resonance (~250-1000 nm) enables LSPR to be more sensitive to change in the refractive index near the nanoparticle surface, while effectively ignoring bulk material effects. The increased sensitivity of LSPR is able to be utilised to detect biological molecule binding events, as the localised plasmon interacts with these binding contacts, resulting in quantifiable changes in plasmon energy. There is a large body of literature on the development of biosensors based on this effect.[28-30] The wider spectral width of LSPR, roughly ~80-100 nm full width at half maximum (FWHM), in contrast to the narrower PSPR spectrum of about ~50 nm FWHM for gold nanoparticles, enhances the adaptability of LSPR in many biosensor applications.[8, 9]

Several factors have been mentioned above, including electromagnetic field strength, decay length and spectral width which significantly affect LSPR properties and thus its selectivity and sensitivity in the application. [27]

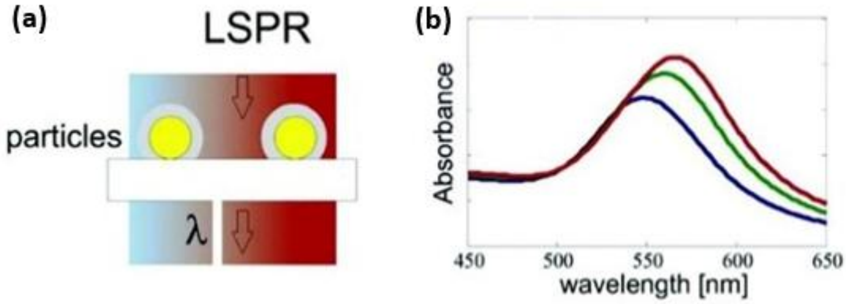

Figure 1-6: The LSPR sensing mechanism includes (a) a metallic nanoparticle that is surrounded by an electric field, the arrow on top represents the light incident on the particles, while the arrow on bottom represents the light absorbed at a specific wavelength. T shape represents light inside particles, and magnetic fields distribute resonances from high (red) to low (blue) areas around particles. and (b) a change in the peak maximum responding to alterations in the refractive index (RI) of the surrounding layer. This can be viewed through the molecular film with thickness levels of 10 nm (green line) and 20 nm (red line), with a refractive index of 1.48 in water (n = 1.33) that replicates the characteristics of biomolecules.[23]

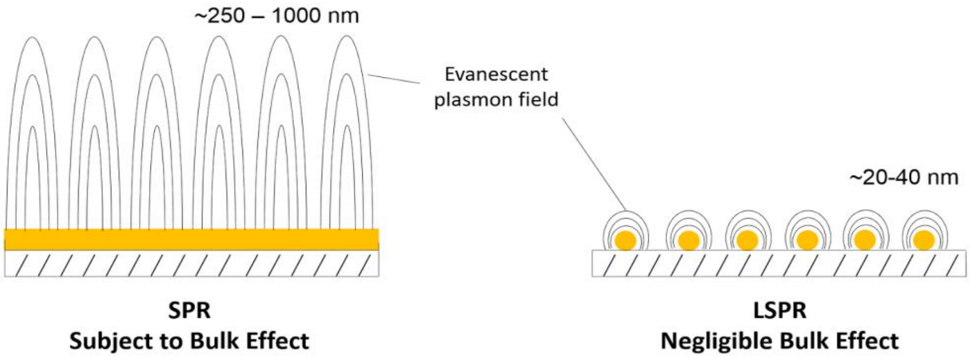

Figure 1-7: The decay length of two types of plasmon PSPR and LSPR.[22]

1.4 Plasmonic metals and their properties

The phenomenon of localised surface plasmon resonance has been extensively utilised across numerous scientific and technical areas. Silver and gold are the most often utilised metallic nanoparticles due to their unique absorption bands and distinct optical characteristics in the visible light spectrum. Gold nanoparticles are employed in sensing applications more commonly than silver, especially due to silver's greater chemical reactivity, which can restrict its practical applications. [27, 31, 32] Nanoparticles have different extinction spectra influenced by their size, shape, and surrounding environment. Figure 1-8, illustrates the extinction spectra of silver nanoparticles of differing sizes and shapes, yielding absorption maximum (λmax) between 426 nm and 782 nm. For silver nanoparticles with triangular shapes, with heights decreasing from 59 nm to 55 nm to 50 nm, the decrease in height is accompanied by a gradual redshift of the maximum wavelength, shifting from 720 nm to 747 nm to 782 nm. The control of nanoparticle form and size is enabled by various chemical production methods that enable LSPR responses to be tuned to any wavelength within the visible and near-infrared ranges.[27, 31]

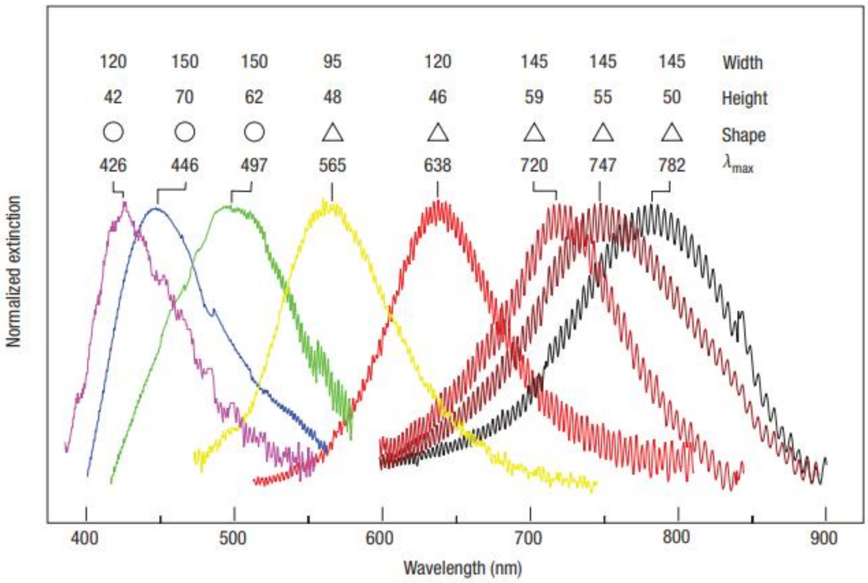

Figure 1-8: The silver nanoparticle (Ag NP) extinction spectra were measured on mica substrates of different sizes and shapes. [33]

AuNPs can be synthesised with various particle sizes including cubes, spheres, rods, branches, stars, urchins, and bipyramids. The refractive index and absorption spectra of AuNPs have been found to be strongly influenced by the shape and size of the particles.[10, 34,35] The precise location of the plasmon band might change considerably based on the shapes and sizes of the AuNPs. Figure 1-9 displays some of the diverse shapes and sizes of AuNPs, including spherical nanoparticles, cubic nanoparticles, nanobranches, and nanorods, with their individual absorption spectra (see Figures 1-9 a, b, c, and d).[34] The absorbance spectra are significantly influenced by the size of the AuNPs, as illustrated in Figures 1-9 d and e**,** where differences in the size of the nanorods' shape result in changes in peak position. This suggests that, even for AuNPs with similar shapes, the peak position can shift with size.[34]

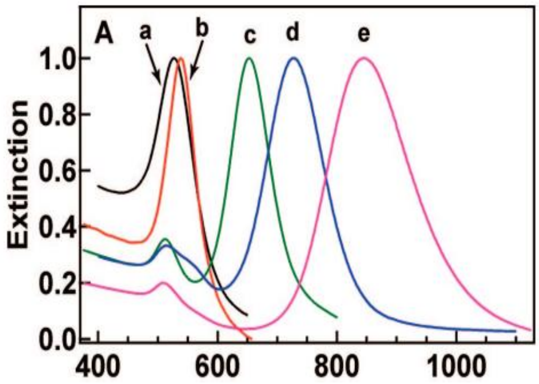

B

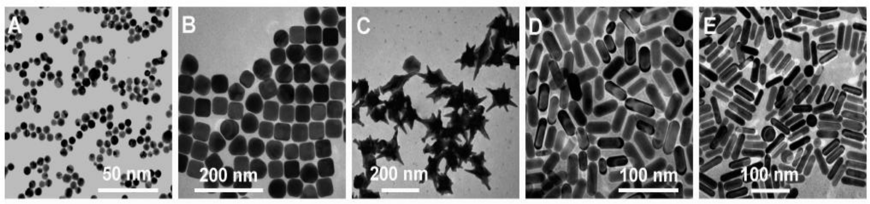

Figure 1-9: The extinction spectra of AuNPs of various shapes and sizes, (a) spherical nanoparticles,(b) cubic nanoparticles,(c) nanobranches, and (d,e) nanorods with different sizes (d)17 nm and (e)16 nm. B the TEM images of AuNPs for each of them respectively.[34]

The local refractive index near the surfaces of plasmonic nanoparticles can significantly influence the optical characteristics. A change in the refractive index of the medium close to the nanoparticle surface results in a shift in plasmon energy. The nanoparticle absorption spectrum transitions toward wavelengths that are longer as there is an increase in the refractive index near the nanoparticle surface, which is known as a "red shift". This indicates that the absorption peak of the nanoparticle will shift to shorter wavelengths (blue shift) when the refractive index decreases.[36] The AuNPs display a (LSPR) absorption peak in the visible spectrum, with the peak wavelength varying in response to changes in the dielectric constant of the surrounding medium. Accordingly, Figure 1.10 below shows an increase in the dielectric constant of the solution results in a higher refractive index, leading to a redshift in the LSPR peak wavelength from solution a to solution c.[37]

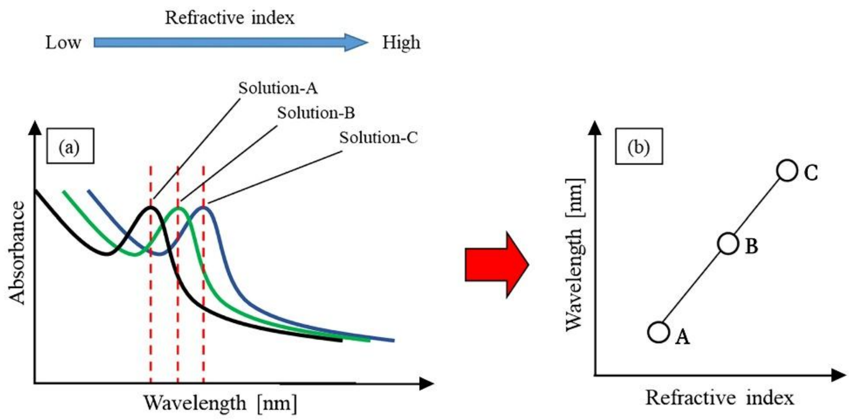

Figure 1-10: (a) Schematic representation of the difference in peak absorption wavelength according to changes in the refractive index of the surrounding medium for three different solutions, (b) measure of the refractive index sensitivity based on the change in wavelength of the absorption spectrum for three different solutions, A, B and C.[37]

AuNPs can be selectively charged either negatively or positively by using a suitable stabiliser. As an illustration, AuNPs coated with cetyltrimethylammonium bromide (CTAB) have a positive charge, whereas AuNPs coated with citrate have a negative charge.[34]

When suspended in liquid, nanoparticles have a tendency to aggregate. The reduction of gold nanoparticle aggregation is crucial for maintaining their optical properties and stability. The aggregation of AuNPs can be reduced by using organic ligands as capping agents. In addition, polymers and dendrimers containing mercapto groups and disulfides have also been used for the same purpose.[38] Polymers serve as an alternate category of surfactants utilised as direct, reducing, and stabilising agents in the seed-mediated synthesis of AuNPs. For instance, PDMA has been utilised as a reducing and shape-directing agent to synthesise AuNPs. The amine groups of PDMA offer crucial active sites for ligands in the synthesis of AuNPs with regulated sizes.[39] The terms "aggregation" and "agglomeration" are frequently employed to describe collections of particles present in liquid suspensions or a dry fine condition. These processes may occur during filtration, drying, milling, crystallisation, or storage due to sintering, combining, or interparticle bonding. A mass is referred to as an (agglomerate) when its resultant shape can be distinctly characterised or delineated. Conversely, irregular shapes frequently result from the aggregation or clustering processes experienced by the particles.[40] As previously mentioned the nanoparticles generally tend to cluster via agglomeration or aggregation processes. Agglomeration denotes the creation of loosely bonded clusters of nanoparticles, in which the individual particles remain recognisable, and the process is reversible. In contrast, aggregation involves the irreversible binding of nanoparticles into a densely packed cluster. This occurs when the attractive interactions among the particles exceed the stabilising forces, resulting in the creation of larger, permanently bound structures.[41] These clustering behaviours can significantly affect the optical and other physical properties of nanoparticles. In solutions with salts or other ions, gold nanoparticles protected by citrate demonstrate lower stability compared to protein-functionalised AuNPs, which demonstrate enhanced stability even at 4 °C.[38] In regards to this, XPS has been effectively utilised to examine nanoparticle aggregation; however, it requires complex analysis.[41]

Single particles may have different optical properties from groups of particles due to strong plasmonic interactions caused by the close distance of the particles This interaction might result in a variation in the plasmon resonance frequencies.[22] Figure 1-11 illustrates the optical properties of single particles in comparison to a group of particles. A single gold nanoparticle, for example, exhibits the normal plasmon resonance. Nevertheless, the short distance between the two adjacent plasmonic particles can result in an interaction of their nearfields, which can cause the plasmon modes of metal nanoparticles to couple when they are positioned close to each other. This coupling is based on the polarisation of the light and displays in absorption spectra as changes in wavelength.[42, 43] The redshift increases as the distance between interparticles starts to reduce.[22]

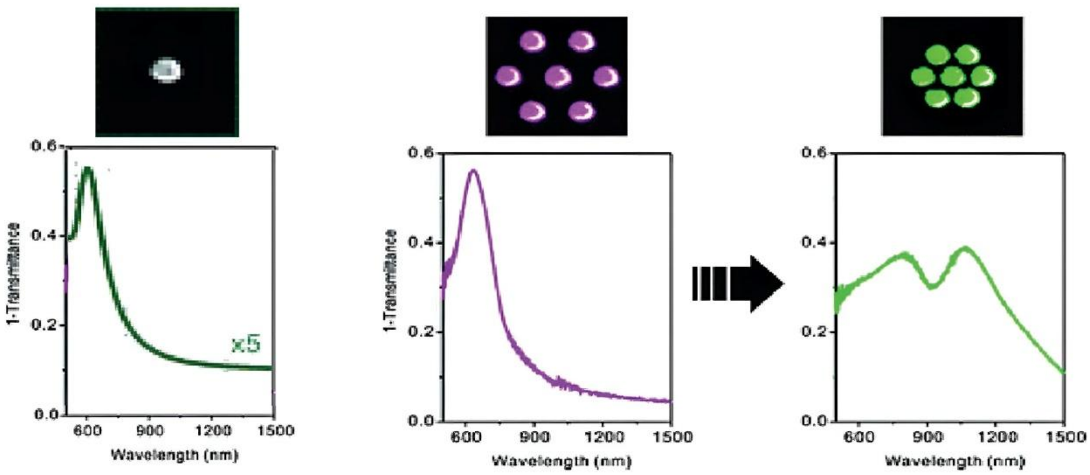

Figure 1-11: The optical properties of single particles in comparison to a group of particles.[22]

Nanoparticle coupling strengths are significantly affected by factors such as the quantity, spatial configuration, and distance between the NPs. Therefore, achieving optimal utilisation of NPs requires the uniformity of NPs clusters and careful regulation of the arrangement.[44] Plasmonic nanoparticles have also been used in a wide range of applications, including drug delivery,[45] solar cells,[46] biosensors,[47] surface-enhanced Raman spectroscopy,[48] and cancer therapy.[49]

As plasmonic nanostructures can be coupled to various emitters, such as dye molecules, quantum dots and J-aggregates. Their exchange of energy with each other thus results in plasmonic nanostructures exchanging energy with other emitters.[11] The distinctive characteristics of nanoparticles have enabled diverse applications in areas including photochemical,[50] sensing [51]and energy harvesting.[44] Gold nanoparticles have been utilised as photoprotectors for the chlorophyll a molecule. AuNPs bind to the nitrogen sites of Chl *a*, providing protection when mixed in the dark before illumination. Chl *a* becomes photoexcited during light exposure and can transfer energy to molecular oxygen, generating reactive oxygen species such as singlet oxygen. This binding of AuNPs to Chl *a* prevents the interaction of chlorophyll with reactive oxygen species, which would otherwise lead to the degradation of Chl *a*. The capacity of AuNPs to protect chlorophyll against oxidative degradation has significant implications for the conservation of photosynthetic pigments in diverse biological and technological contexts.[52]

1.5 Interaction between plasmons and materials

There are several ways that plasmonic structures can interact with molecules. The simplest kind of interaction is that the adsorption of molecules causes a change in the local refractive index, yielding a shift in the plasmon energy. [53] Optically active molecules may also have specific transitions that are close in energy to the plasmon mode. Absorption of light causes the promotion of an electron from the valence band to the conduction band, as illustrated in Figure 1-12. The promoted electron leaves behind a vacancy (a hole) and together with the promoted electron, this forms an exciton (an electron-hole pair). There are two main categories of excitons: Wannier excitons and Frenkel excitons. Wanner excitons are found in semiconductor materials, which have weak Coulomb interactions and the relative motion of electron and hole in the crystal covers many unit cells. Comparatively, Frenkel excitons can be found in insulating materials, where electrons and holes are bound by strong Coulomb interactions so that the exciton is localized on a single molecule.[53, 54]

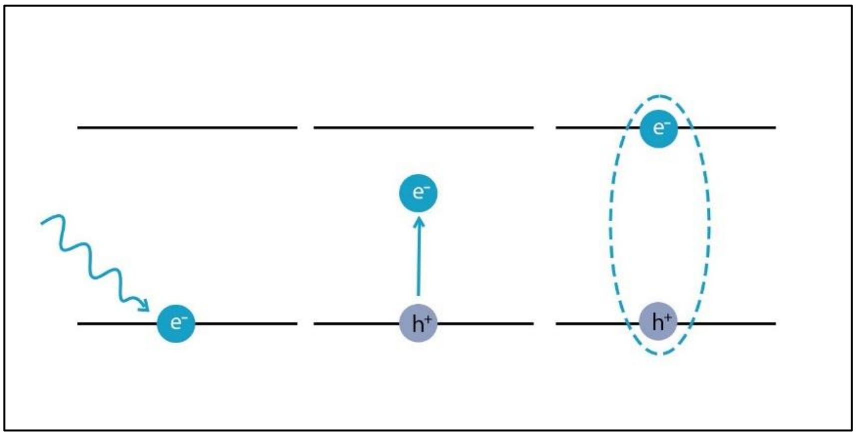

Figure 1-12: Absorption of a photon leads to promotion of an electron from the valence band to the conduction band, leading to the formation of an exciton (an electron-hole pair).

1.5.1 Strong plasmon-exciton coupling

Excitonic and plasmonic materials exchange energy.[55] There are two types of coupling between localised surface plasmons (LSPs) and excitons: strong coupling and weak coupling. An important factor affecting their interactions is the exchange of energy between LSPs and excitons. In weak coupling, the interactions between plasmons and excitons (or dipoles) do not change their energies, but the coupling may lead to the enhancement of optical activity for example fluorescence.[53] However, when the rate of exchange between the plasmon mode and the exciton exceeds their average dissipation rate, a linear combination of the plasmon and exciton states can result, leading to the formation of a new hybrid with distinct properties that neither particle possessed previously.[56] As a result of these new states, that are above and below the energy of the plasmon mode, the extinction spectrum splits, a phenomenon known as Rabi splitting. [53] The strong coupling regime is shown in Figure 1-13.

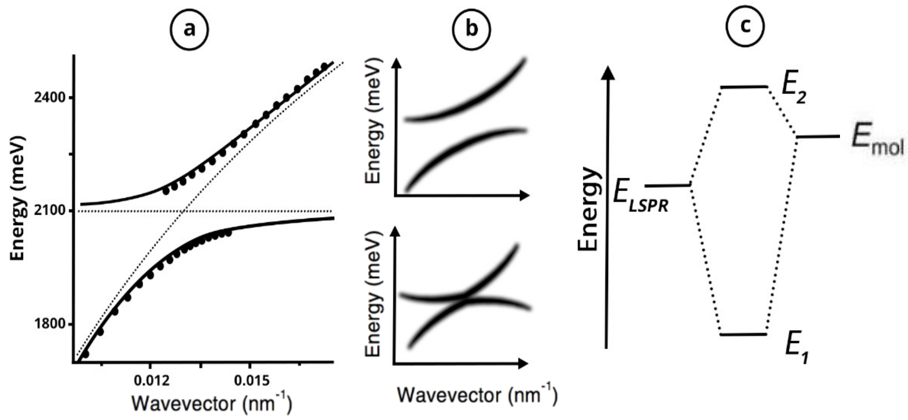

Figure 1-13: The strong coupling regime between the localised surface plasmon resonance (LSPR) mode and excitons is illustrated as follows: (a) represents the LSPR mode (dotted line) and the excitonic mode (dashed lines); (b) the top diagram reveals the splitting, whereas the bottom diagram hides the splitting underneath the linewidths; (c) demonstrates the linear combination in strong coupling between LSPR and exciton states, resulting in two new energy levels, E_1 and E_2.[57]

Figure 1-13 above displays the dispersion of modes in a coupled system. In an uncoupled system, the horizontal line corresponds to the exciton energy, and the diagonal line corresponds to the plasmon energy. The two lines should cross at the resonance when E_{LSPR} (plasmon energy) = E_{mol} (molecular energy). However, strong coupling results in an avoided crossing; the exciton modes are given by the solid curved lines, and the difference between the two modes is equal to Rabi energy.[57] These hybrid states, created by the strong interaction between plasmons and excitons, are referred to as “plexcitons”.[57] Three main theoretical frameworks are employed to explain this strong coupling phenomenon: classical, semi-classical and quantum mechanical descriptions. In specific conditions, when a broad plasmon mode interacts with a restricted exciton mode, a classical model of coupled oscillations can produce conclusions that are analytically comparable to those derived from a comprehensive quantum mechanical analysis of the system.[53]

There are three key parameters to determine strong coupling: (g) which is the rate of energy transfer between matter and light, with (k) as the rate at which the light is emitted, and (γ) is the rate at which the loss of polarisation of matter. When the rate of g, is notably higher than the other two rates, ($g \gg k, \gamma$) a strong coupling can be achieved between matter and light. In contrast, when ($g \ll k, \gamma$), weak coupling occurs as the trapped matter and light interact no more strongly than with the light or matter outside the resonator. [58]

In particular, many types of systems have been reported to exhibit strong coupling, such as dye molecules,[59-61] quantum dots,[62] and J-aggregates.[63-65] According to Torma *et al*.[57] an extensive literature review of strong plasmon-exciton coupling was conducted, including studies of J-aggregates-based strong coupling and dye molecules-based plexcitonic systems between 2004 and 2014. In 2016, Tsargorodska *et al*.[66] reported strong coupling between LSPRs and light-harvesting proteins, with the study using light-harvesting complexes 1 and 2 (LH1 and LH2) from purple bacteria, where the plasmon-excitation system was well-modelled using coupled harmonic oscillators. As a result of the strong coupling between the plasmon mode and the excitons in the proteins, this splitting can be attributed to the plasmon mode. Subsequently, through this coupling, new states above and below LSPR can be created. It was also found that the strength of this coupling is dependent on the electronic states in the LH complexes and the biomolecular coverage,[66] see Figure 1-14.

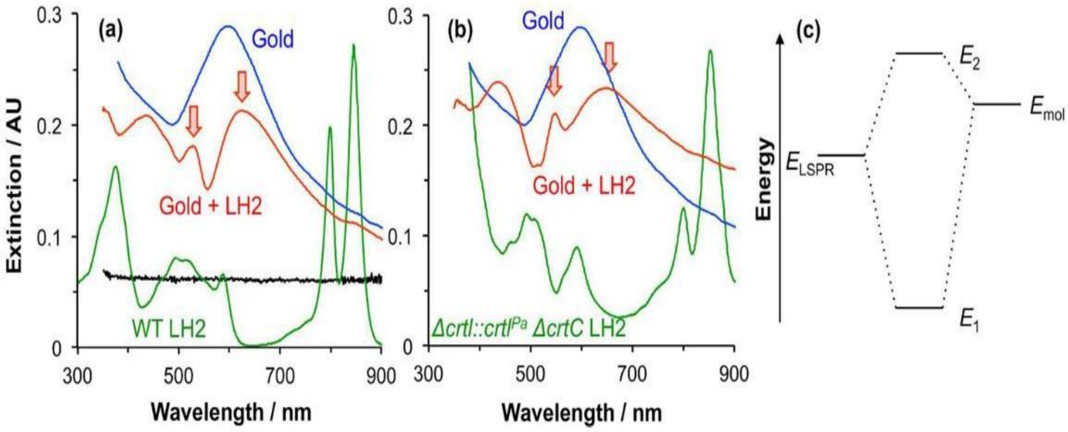

Figure 1-14: Spectra of the extinction of LH2 (green) and AuNPs before (blue) and after the attachment of LH2 (red). (b) the LH2 mutant, the black line denotes a monolayer of wild-type LH2 on glass. (c) Illustration of the energy graph of the hybridisation of the localised surface plasmon resonance (LSPR) and exciton states, resulting in the formation of two new peaks with energies E_1 and E_2.[66]

Furthermore, it was shown that synthetic light-harvesting model proteins have high coupling to plasmon modes, which may be modulated by modifying the protein's structure. For example, maquettes with a single chlorin exhibit an exciton energy of 2.06 eV, which is near the Qy transition and comparable to those observed in chlorophyll a and bacterial light-harvesting complexes. In a model with two chlorins, the exciton energy is 2.20 ± 0.01 eV, derived from the intersection between the Qx and Qy transition energies. The absorption spectrum of these model proteins, corresponding to the exciton energies, is shown in Figure 1-15 below.[11]

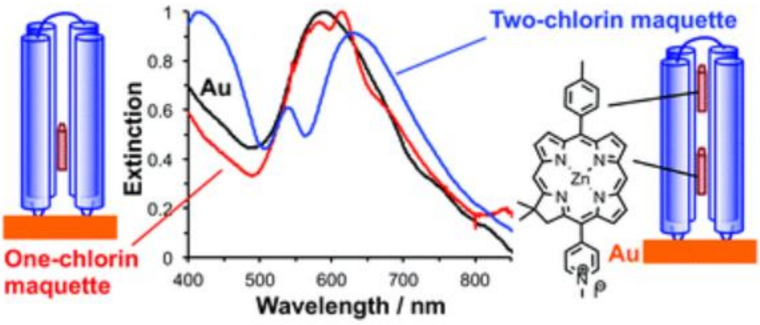

Figure 1-15: The absorption spectrum for comparison of one-chlorine Marquette and two-chlorine Marquette, with the latter showing a greater coupling strength.[11]

The pigment molecules (chromophores and carotenoids) are arranged in these pigment-protein complexes by peptide units, with the networks of energy transfer steps controlled with remarkable precision by these units. Due to their intrinsic susceptibility to become damaged during processing and high cost, proteins are unsuitable for photonic materials applications. In accordance, a pigment-polymer antenna complex was designed by Lishchuk *et al.*[67] by replacing the peptide scaffolds found in biological light-harvesting complexes with surface-grafted polymers. These polymer scaffolds were attached to chlorophyll, and the chlorophyll density was controlled by the grafting density and polymerisation time. In particular, poly(cysteine methacrylate) (PCysMA) was used in this study. Additionally, stimuli-responsive swelling of the polymer scaffold allows active control of strong plasmon–exciton coupling, resulting in programmable biomimetic excitation transfer networks (see, Figure 1-16). Lishchuk et al report strong coupling to Chl *a* covalently attached to poly(cysteine methacrylate) scaffolds. Figure 1-17 from their paper is reproduced below. In (b), the extinction spectrum of a clean gold nanostructure array is shown in green. After the growth of a fully dense polymer scaffold, the plasmon band is red-shifted (blue spectrum) because the local refractive index in the vicinity of the metal surface has changed from $n = 1$ to $n \sim 1.5$. After the covalent attachment of chlorophyll, the plasmon band displays a small splitting (red curve). Modelling of these data using a coupled oscillator model yielded a coupling energy of 0.1 eV, below the strong coupling threshold (~0.2 eV). However, when Chl *a* was attached to a reduced density surface-grafted film (e.g. Figure 1-17 f and g), a pronounced splitting of the plasmon band was observed, consistent with strong coupling, and modelling of the data yielded a coupling energy of ~0.4 eV, significantly greater than the threshold for strong coupling.[67]

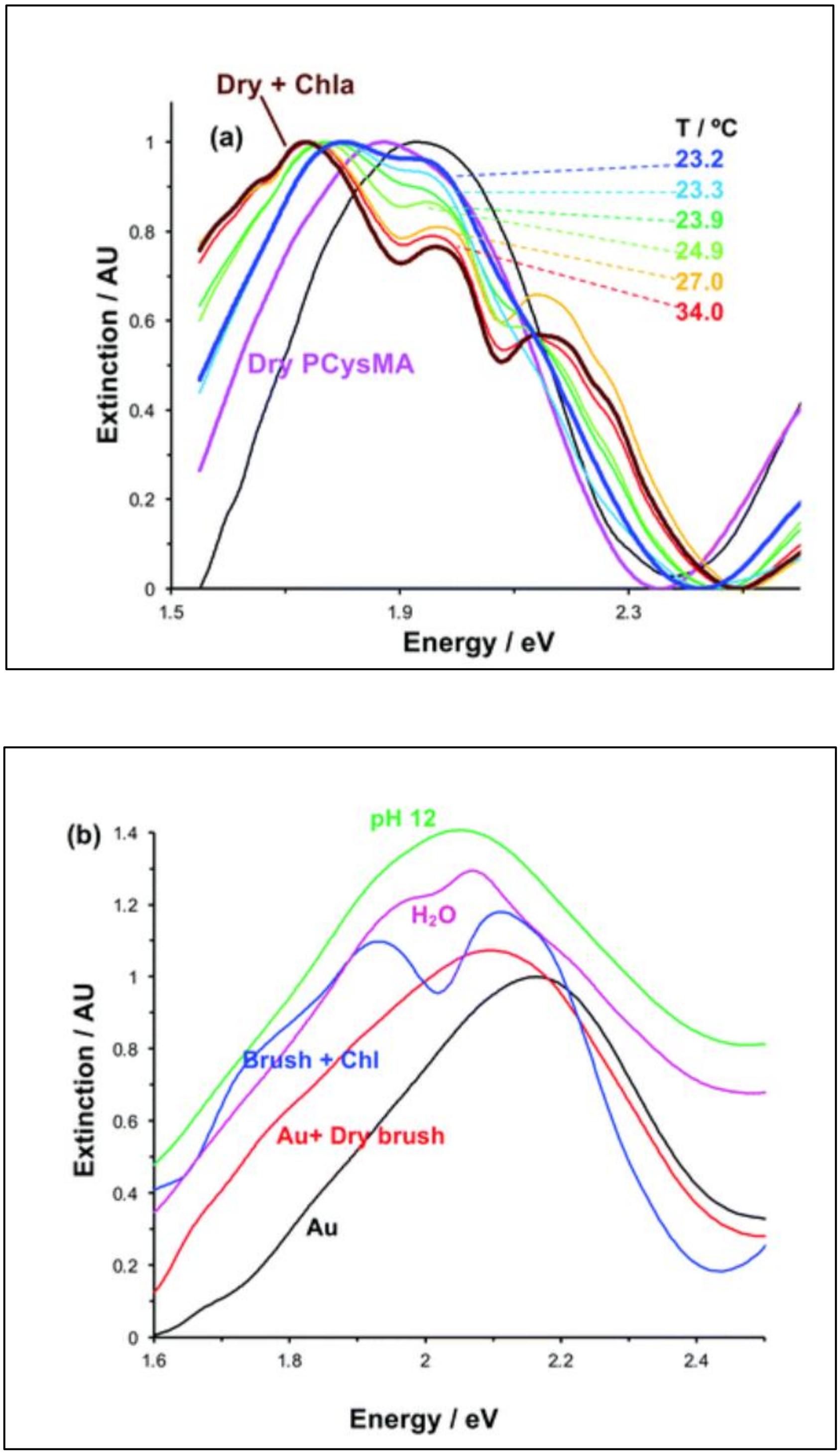

Figure 1-16: Gold-PCysMA-Chla complexes display extinction spectra at different temperatures (a) and (b) gold-PCysMA-Chla complexes in various media, air, water and pH 12.[67]

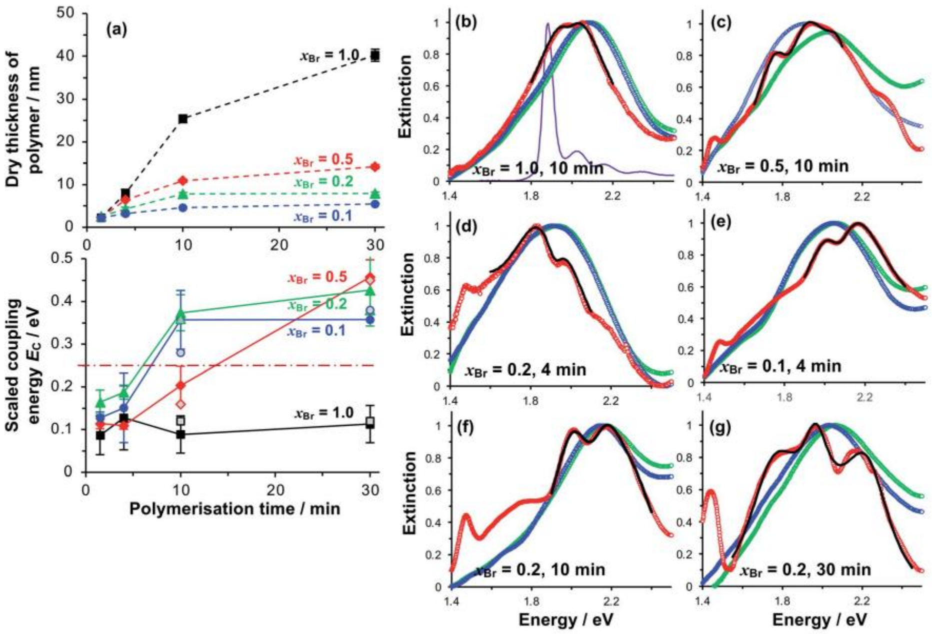

Figure 1-17: (a) Polymer dry thickness variation and scaled coupling energy EC for initiator compositions χBr = 1.0 (squares), 0.5 (diamonds), 0.2 (triangles), and 0.1 (circles). In the lower graph, the dashed horizontal line indicates a plasmon–exciton coupling threshold of 0.25 eV. Based on analysis of the relationship between coupling energies and detuning, there are open symbols for *t* = 10 and 30 min.[67]

1.5.2 Modelling of strong plasmon-exciton coupling

Strong coupling happens when light and matter exchange energy at a rate that surpasses their rates of decay, resulting in quick, coherent energy transfer. This merges the plasmon mode and exciton to create two novel "plexitonic" states. The gap that exists between these states' absorption peaks is directly correlated with the strength of the coupling; with the states displaying energy levels that differ from those of the original oscillators. The scaled coupling energy of the system (E_c) can be approximated using the subsequent formula:[67]

$$E_c \approx \sqrt{\frac{\mu^2 E_{mol}^2}{\varepsilon_0 \varepsilon_b E_{LSPR}} \frac{N}{V_{LSPR}}} \qquad \text{(Eq. 1.1)}$$

In this equation, E_{LSPR} and E_{mol} represent the energy of the uncoupled $LSPR$ and the energy of the exciton, respectively. ε_0 and ε_b are the free space permittivity and the medium's relative permittivity, respectively. N is the number of excitons in the volume of the $LSPR$ field (V_{LSPR}), and μ denotes the transition dipole moment for the exciton.[57, 67]

The expression demonstrates that the plasmon mode interacts with a number of excitons within its volume while the chromophore density in the plasmon mode impacts the system's coupling energy. A greater quantity of excitons within the mode volume can result in increased coupling energies, resulting in enhanced coupling strength. Therefore, the coupling strength increases through an augmented concentration of excitons inside the plasmonic field. Further, Todisco *et al*. demonstrated a correlation between cyanine dye molecules and silver nanoparticle arrays, as they achieved a weak, strong, or ultrastrong coupling regime by controlling the quantity of dipole molecules on the surface.[68]

Jaynes-Cummings model is effective in developing for understanding of coupled systems. The model describes the detuning (Θ) between the exciton state and LSPR state, which is the energy difference between them, defining it as follows:

$$\Theta = \omega_p - \omega_0 \qquad \text{(Eq. 2.2)}$$

Where ω_0 and ω_p are the frequencies of the exciton and plasmon modes, respectively. By applying (Ω) as the coupling strength that characterises the coupling between these states, their frequencies can be determined using the following formula:[33]

$$\omega_{\pm} = (\omega_p - \omega_0)/2 \pm \sqrt{\Omega^2 + (\omega_p - \omega_0)^2} \qquad \text{(Eq. 3.3)}$$

An analysis of the energy differences of these coupled modes, in regard to the detuning of the system, provides insights into coupled system behaviour. In the energy level diagram for the Jaynes-Cummings model, avoided crossings can be observed, which occur when coupled modes' energies, which commonly intersect with similar energy levels, do not cross as a result of strong interactions between the plasmon and exciton states, (see Figure1-18).

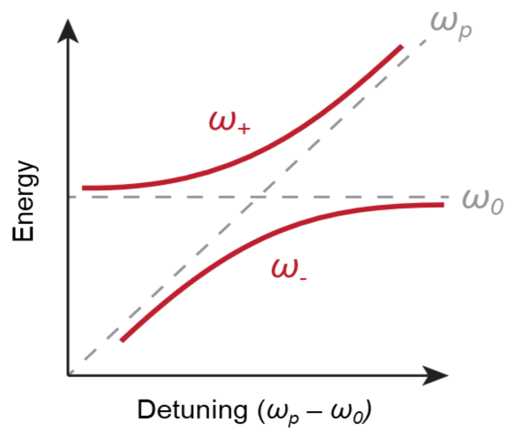

Figure 1-18: The diagram shows the avoided crossing effect with the system's detuning. It shows the energy levels of the lower (ω-) and upper (ω+) energy coupled states. The dashed lines show the energy levels for the exciton (ω_0) and plasmon states (ω_p) of the uncoupled energy.[67]

The avoided crossing is contingent upon the strength of the coupling. At the point of avoided crossing, the energy states of the interconnected system become hybridised, which reflects a combination of the exciton states and plasmon states. Therefore, by analysing the energy levels of the coupled states in relation to the detuning, it is possible to determine whether the system demonstrates strong coupling. Indeed, the strong coupling between the plasmon mode and the excitons facilitates the rapid exchange of energy, allowing for energy transfer between excitons that are not directly next to each other.[69] This phenomenon has the potential to be utilised for the long-distance transportation of energy at high speeds in light-harvesting devices. The energy of sunlight can be effectively directed on a surface to prevent undesired decoherence and charge-recombination processes commonly observed in solar energy devices.

1.6 Metals of plasmonic

1.6.1 Gold

Gold possesses a high conductivity and remarkable inertness, resulting in its significant value at (4.11×10^7 S/m).[70] In certain applications, gold is preferred due to its surface chemistry and biocompatibility. Gold exhibits an inter-band transition in the visible area of the spectrum, specifically at roughly 470 nm, and even more prominently in the UV range, at 325 nm, as shown by its colour.[71] This transition can be predicted based on the colour of gold. As a result, there is a higher level of damping at these wavelengths compared to silver, leading to an increase in the imaginary part of the dielectric function. Gold is utilised for plasmonic resonances with wavelengths greater than 600 nm due to its interband transitions. In this particular area, the level of damping is reduced, causing gold to exhibit characteristics that closely resemble those of an ideal metal.[72]

1.6.2 Silver

Silver is the most obvious plasmonic material due to its accurate representation by the Drude model. Silver exhibits the highest electrical conductivity among all metals, and it does not have any significant inter-band transitions in the visible electron spectrum at (6.30×10^7 S/m).[71] Consequently, silver exhibits the least amount of damping when used for plasmonic applications. One drawback of silver, though, is its tendency to oxidise, resulting in a steady deterioration in resonance quality and restricting its use in ambient conditions.[72]

1.6.3 Aluminium

Aluminium is a highly attractive plasmonic material as it is more cost-effective and readily accessible in comparison to gold and silver. Aluminium plasmonic devices are commonly employed in complementary metal-oxide semiconductor (CMOS) technology to enhance integration, resulting in improved efficiency. Aluminium exhibits a broad range of frequencies at which it can sustain surface plasmons, in contrast to gold and silver, which are constrained by their inter-band transition energies.[73] Aluminium exhibits inter-band transition within a range of 750 nm to 850 nm, enabling it to sustain localised surface plasmon resonances (LSPRs) throughout the majority of the visible spectrum and, significantly, in the UV regions. In the visible spectrum, however, aluminium experiences higher optical losses compared to noble metals. This is because of the increased scattering of free electrons in the material, which restricts its range of applications. The conductivity of aluminium is measured at (3.77×10^7 S/m).[74, 75]

1.6.4 Copper

Copper exhibits plasmonic characteristics that closely resemble those of gold. Additionally, its colour suggests the presence of inter-band transitions that occur towards the blue region of the visible spectrum. Copper has higher electrical conductivity than gold at (5.96×10^7 S/m) and is more cost-effective than both gold and silver.[71] Nevertheless, copper experiences quick oxidation upon exposure to oxygen, restricting its efficacy in plasmonic applications. However, the oxidation of the material can be prevented by applying a graphene coating, which preserves its plasmonic capabilities.[76, 77]

1.7 Methods for synthesising nanoparticles

1.7.1 Gold nanoparticles synthesis

The two key approaches used for the synthesis of NPs are the “top-down” and “bottom-up” methods. The top-down strategy is to start with bulk material and employ various techniques to break it down into nanoparticles for synthesis, this method includes photolithography and electron beam lithography. In contrast, a bottom-up strategy involves synthesizing the material from atomic or molecular species through chemical reactions, while both approaches successfully produce NPs in the desired shapes and sizes.

1.7.1.1 Turkevich method

The Turkevich bottom-up synthesis approach was initially described in 1951 and is one of the most frequently used methods to prepare spherical Au NPs with sizes in the range of 10 and 100 nm. [78] In this method, gold ions (Au^{3+}) are reduced to gold atoms (Au^0) through agents such as amino acids, ascorbic acid, or citrate. A stabilising agent is generally needed to overcome the tendency to flocculation of the nanoparticles, due to the attractive van der Waals forces in solution which tend to dominate the inter-particle interactions. A variety of capping/stabilising agents can be utilised to stabilise. In the widely-used Turkevich method, gold particles are synthesised from tetra chloroauric acid ($HAuCl_4$) as a source of the gold using sodium citrate as the standard reducing agent. In this case, citrate functions as a surfactant, stabilising the nanoparticles against aggregation, as well as a reducing agent.[79] Initially, it was thought that the range of particle sizes that was accessible using the Turkevich approach was limited. However, several improvements to the original technique have allowed researchers to expand the size range of particles that might be produced through the use of this technique. Frens discovered in 1973 that it is possible to produce AuNPs with sizes, ranging from 16 nm to 147 nm, by changing the ratio of reduction to stabilising agents.[80] Since reducing agents play a significant role in determining the size of resultant nanoparticles, the citrate concentration in the solution can be used to control particle size. Higher citrate concentrations generate smaller particles.[81] The synthesis process has also been demonstrated to be significantly influenced by the following additional key parameters: pH, a static temperature, solvent, and constantly homogeneous solution (vigorous stirring).[82]

1.7.1.2 Seeded growth method

The previous approach is limited to the fabrication of AuNPs with a spherical shape. However, it is possible to create AuNPs in several other shapes, such as cubes,[83] rods,[84] and tubes [85] and others. In particular, seed-mediated growth is a highly popular technique for producing AuNPs in various forms. The primary principle behind this approach is the creation of seed particles through the reduction of gold salts, which are initially reduced through a strong reducing agent, such as $NaBH_4$. The seed particles are subsequently added to the metal salt solution, together with a mild reducing agent, e.g. ascorbic acid which is beneficial in preventing further nucleation, alongside promoting the creation of rod-shaped AuNPs. Therefore, the size of AuNPs can be manipulated by altering the concentration of the initial particles, the agents used to reduce them, and the agents that guide their structure.[86]

1.7.1.3 Brust method

The Brust method, originally described by Brust in 1994,[87] is an alternative approach for synthesising AuNPs, which is based on a two-phase reaction with organic solvents that help to synthesise AuNPs with diameters of 1.5 nm and 5.2 nm. The gold salt is transferred from an aqueous phase to an organic solvent, e.g. toluene via the use of a phase transfer agent, tetraoctylammonium bromide (TOAB). As a result of the reduction of gold with sodium borohydride ($NaBH_4$) with an alkanethiol, the colour of the AuNPs changes from orange to dark brown.[88]

1.7.2 Silver nanoparticle synthesis

Chemical reduction using inorganic and organic reducing chemicals is the most commonly employed method for synthesising silver nanoparticles (AgNPs). Various reducing agents, including sodium citrate, hydroxylamine hydrochloride, sodium borohydride ($NaBH_4$), elemental hydrogen, and ascorbate, are utilised for reducing silver ions (Ag^+) in aqueous and non-aqueous solutions.[89] An AgNP synthesis technique based on citrate reduction and stabilisation was first described in 1982. [90] However, citrate-based approaches typically exhibit inadequate control over size and shape.[91] Therefore, as a reducing agent, hydroxylamine hydrochloride was used in the current study to produce monodispersed AgNPs. Silver ions (Ag^+) reduction in an aqueous solution commonly results in the formation of colloidal silver particles with sizes that span a few nanometres. Initially, the reduction of complexes that include (Ag^+) ions creates silver atoms (Ag^0) that subsequently aggregate to produce oligomeric clusters through agglomeration. These clusters eventually lead to the formation of colloidal Ag particles.[92] Previous research indicates that employing a strong reducing agent as borohydride led to the formation of small particles that were moderately monodispersed in size. Controlling the production of larger particles, though, proved to be challenging through the use of borohydride. In comparison, using a weak reducing agent such as citrate led to a low rate of reduction and production of the larger size of AgNPs.[93]

1.7.3 Hollow gold nanoprisms (HGN)

Hollow gold nanoparticles exhibit unique optical characteristics. Specifically, as the thickness of the shell is increased while maintaining a fixed outer diameter of the nanoparticle, it produces a shift towards shorter wavelengths in the LSPR peak. Nevertheless, even though the shell maintains a consistent thickness and the nanoparticles' outer diameter increases, a shift towards longer wavelengths in the LSPR peak is detected. From this, it is feasible to create spherical gold nanoparticles that demonstrate localised surface plasmon resonance throughout a broad spectrum of wavelengths. Additionally, this enables the potential to acquire nanoparticles with an LSPR peak of around 800 nm. Consequently, it is possible to create gold nanoparticles that possess plasmon energy comparable to the required excitonic energy.[94] The HGN was synthesised using the method described by Senapati *et al*.[95] The synthesis includes two sequential steps. The initial step involves the creation of tiny spherical silver nanoparticles with a diameter ranging from 3 to 6 nm, commonly referred to as silver nanoseeds. The production of hollow gold nanoprisms (HGN) occurs in the second step using the sacrificial galvanic replacement approach. The synthesis was conducted at the standard room temperature of 18-20 ˚C. In general, a variety of HNG types can be produced by modifying the quantity of Ag nanoseed at the growth step.

1.8 Polymer brushes

Polymer brushes are films of surface-bound polymers formed either by surface-initiated polymerisation, involving the growth of the polymer from surface-bound initiators or by the binding of pre-formed polymers to a surface.[96] The aim of this thesis is to examine whether polymer brushes can be used to arrange dye molecules within light fields associated with metal.

nanoparticles. Indeed, polymer brushes have shown notable potential for modifying the surface properties of materials in recent years for controlling the surface characteristics of materials. There has been interest in using polymer brushes for applications in many fields, including drug delivery[97], imaging,[98] sensing[99] and catalysis.[100] The characteristics of polymer brushes such as their mechanical stability and the capacity that they provide for controlling friction properties, adhesion and wettability, antifouling, biocompatibility, and corrosion resistance have attracted widespread interest.[101] The grafting density of the surface-grafted polymer chains plays an important role in controlling their conformations. At low grafting densities, there is a large distance between each polymer chain. Therefore, they will be separated by a greater distance than their radius of gyration in a good solvent. As a result, the polymer chains collapse and conform to the “pancake” or “mushroom” regime. When the grafting density is high enough, the polymer chains swell away from the surface due to the steric repulsion between neighbouring chains to form a “polymer brush” regime.[102, 103] Polymer brush can exhibit three distinct chain conformations as shown in Figure 1-19.

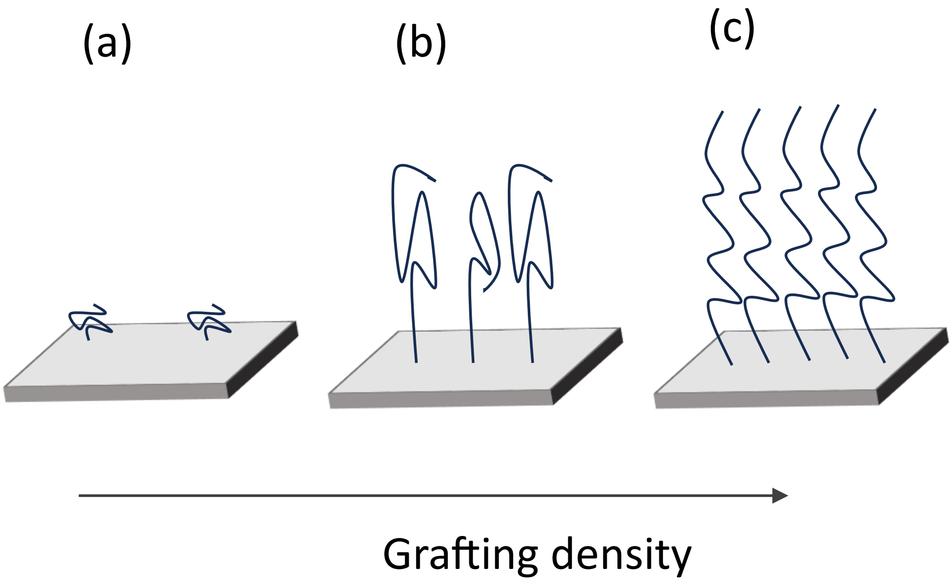

Figure 1-19: Three typical surface-attached polymer configurations with increasing grafting densities: (a) pancake regime, (b) mushroom regime, (c) brush regime.

1.8.1Grafting-to

There are two major strategies: “grafting-to” and “grafting-from”, see Figure 1-20. The process of “grafting-to” involves embedding pre-synthesised polymer molecules into a substrate, whereas “grafting-from”, is a process of growing polymer molecules from immobilised initiator molecules.[101]

The “grafting-to” approach was used by Mansky *et al.*[114] to attach the end-functionalised polymers to reactive groups on a substrate. The polymer is anchored to the surface either physically or chemically.[102] Physisorption is one of the processes used for implementing the "grafting-to" method, by dispersing polymer chains into selective solvents and resulting in selective solvation of the polymers. Polymer films are created when one block of the diblock copolymer interacts strongly with the surface, leading to the formation of an anchor layer. In this procedure, thermodynamic equilibrium controls the thickness and grafting density of polymer brushes.[104] This process is not easy to fabricate the polymer due to its requirement for the preparation of a suitable diblock copolymer before adsorption. In addition, due to the weak interaction between the block copolymer and the surface, the resulting polymer has poor thermal and solvent stability. The polymer brushes produced by using the chemisorption process though, are not highly dense because the chemisorption of the initial chain fraction forms a macromolecular barrier that hinders subsequent chain diffusion to the surface.[105]

Furthermore, there is still a limited range of substrate types that can be used, a terminal functional polymer chain end requirement, and in general, grafting efficiency decreases with increasing molecular weight. The "grafting-from" approach can be used to overcome this limitation by allowing the formation of a polymer with high grafting densities.[102, 106]

1.8.2 Grafting-from

The process of the "grafting-from" method enables the growth of films with high grafting densities. This process involves two steps: firstly, the specific initiator monolayers are covalently attached to solid surfaces; and secondly, the polymer chain grows from the initiator functionalised surface, through a process called surface-initiated polymerisation.[107] During polymer formation, propagation is only limited by the diffusion of monomers through the reaction mixture to the growing chain ends.[102] The polymer brushes formed by using this method are high-density due to the grafted chains being swollen by the monomer solution that feeds the growing layers. A wide range of polymer molecules can be used in this approach as well as almost all polymerisation methods, including nitroxide-mediated polymerisation (NMP), reversible addition-fragmentation chain-transfer (RAFT) polymerisation and atom transfer radical polymerization (ATRP).[108] Accordingly, the polymer brushes prepared with a higher grafting density by this strategy have been employed in different polymer applications such as protein separation, control of biofouling, tissue engineering, drug delivery and sensors.[108, 109]

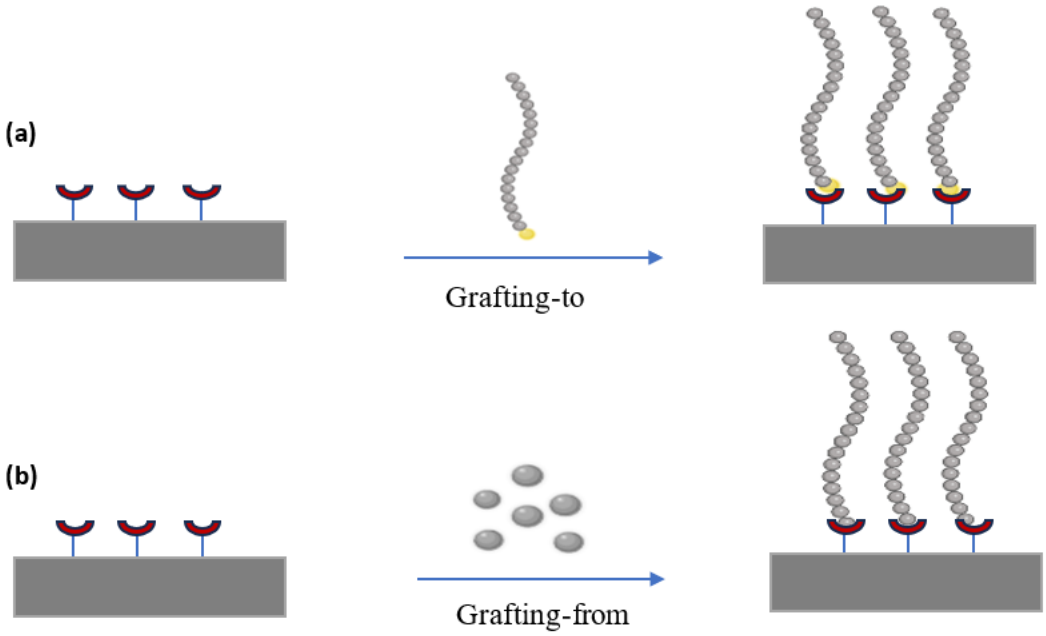

Figure 1-20: Schematic display of the two polymer synthesis methods (a) grafting to and (b) grafting from.

The properties of the solvent environment greatly influence the conformations of polymer brushes. When the solvent exhibits high compatibility with the polymer (good solvent). This, in turn, causes the brush to swell away from the surface. In such instances, it is anticipated that the polymer will experience complete wetting by the favourable solvent. Contrastingly, if the solvent is not suitable for the polymer (poor solvent), the polymer brushes will collapse in order to minimize contact with the solvent and decrease unfavourable interactions between the polymer and the solvent.[110]

1.8.3 The relationship between the densities of grafted polymers on a surface and their resulting properties

An approach that has been proven to reduce surface-bound polymers' density levels involves lowering the density of initiation sites for the polymerisation reaction through the process of co-adsorbing the initiator molecule with an inert compound. This was applied by Bao *et al.*[111] to create poly(2-hydroxyethyl methacrylate) (pHEMA) brushes that included different film densities, demonstrating a distinct correlation between lower initiator density and the thickness of the resulting polymer films.[111] This result is predicted because the polymer chains with more spatial freedom can adopt a more relaxed conformation to collapse onto themselves (i.e. "mushroom regime"). Indeed, an isolated polymer chain on a surface has a natural inclination to collapse, resulting in the formation of a random coil with the size of this coil determined by the radius of gyration. When polymer chains are grafted sufficiently close together, they undergo steric repulsion, which causes them to expand away from the surface, resulting in what is known as the “brush regime”. The degree of swelling increases as the density of surface-grafted chains increases.

The density at which the polymers are grafted onto a surface affects the reactivity of the chains. When employing small reagents in post-polymerisation modification, the brushes can display attachment rates that are almost complete. However, the introduction of larger derivatives poses challenges: steric repulsion is expected to reduce the rate of diffusion of reagents through the surface-grafted layer. Therefore, control of grafting density is especially attractive in the facilitation of further functionalisation after synthesis.[112, 113]

Zapotoczny *et al.*[114] formed mixed of self-assembled monolayers (SAMs) by coadsorbing p-tolytrimethoxysilane with p-(chloromethyl) phenyltrimethoxysilane onto silica. The latter adsorbate has a halogen initiator, but the former does not. This allowed them to control the density at which 3-(trimethylsilyl-2-propynyl) methacrylate brushes were attached.[114] In a subsequent study, researchers used an inert silane to form SAMs on silicon substrates to control the grafting density of hydroxy-terminated oligo(ethylene glycol) methacrylate (OEGMA) and methoxy-ended OEGMA films. As a result of the subsequent attachment of azobenzene units, the films with reduced density polymers exhibited a reaction yield of 50%, whereas brushes with higher density yielded only 10%.[115] The attachment of even larger structures to brushes becomes possible at high concentrations and sufficiently low grafting densities. For example, gold nanoparticles with a size of 13 nm were added to poly (N, N-(dimethylamino ethyl) methacrylate) brushes with the initiator density was controlled by employing a mixture of 2-bromo-2-methyl-N-(3 (triethoxysilyl)propyl) propenamide initiator and an inert silane. At a high polymer chain density of 0.5 nm ^{2}, the nanoparticles largely stuck to the top layer of the brush, leading to relatively low concentrations of particles. However, when the grafting density was decreased to around 0.26 nm^2, the particle concentration doubled.[116] Mixed SAMs containing initiators at variable concentrations have been used in recent studies to control PCysMA grafting density. Upon attaching chlorophyll to both a fully dense brush (χBr (Au) = 1.0) and a reduced density layer (χBr (Au) = 0.39), a change in the N1s spectrum was detected in the XPS spectra. Further, decreasing the grafting density of PCysMA reduced steric congestion, leading to a greater amount of Chl *a* (see Figure 1-21). In Figure 1-21a, the N1s spectrum of the fully dense brush before Chl *a* addition demonstrates peaks at 399.5 eV and

401.6 eV (-NH_3^+), which was attributed to neutral amine groups and protonated amine respectively. As a result of Chl *a* conjugation, the -NH_3^+ peak in the N1s spectrum showed a marked decrease in intensity, while the -NH_2 peak remained prominent. There is also an additional peak at 398.1 eV, corresponding to the nitrogen atoms in the nitrogen tetrapyrrole ring coordinated with the Zn^{2+} ion at its centre.[117] These data confirmed that Chl *a* was present within this PCysMA brush, (see Figure 1-21b). However, when the PCysMA grafting density was decreased to 0.39 ± 0.07, as illustrated in Figure 1-20c. The PCysMA layers were able to bind a greater amount of Chl *a* due to the decrease in steric congestion, as shown in Figure 1-21d. The use of a mixed SAM surface containing variable concentrations of Br initiator enabled controls of the density of grafting and consequently the reactivity of polymer chains.[118]

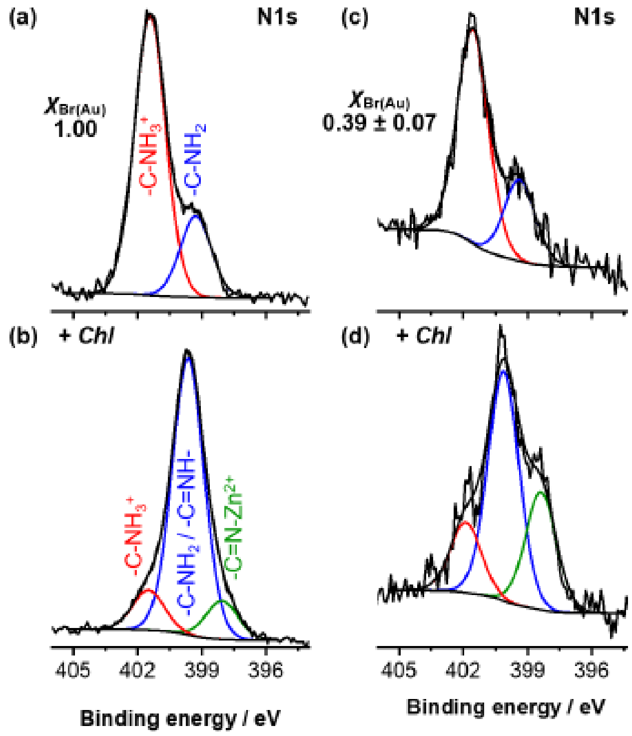

Figure 1-21: High-resolution XPS spectrum of N1s was obtained before (a) and after (b) reactions with Chl for a fully dense (χBr (Au) =1.0) PCysMA brush growing for 30 minutes. The N1s spectra are obtained for PCysMA layers with reduced density (χBr(Au) = 0.39) grown over the same time period before(c) and after (d) reaction with Chl *a*.[118]

1.8.4 Poly(2-(dimethylamino) ethyl methacrylate) (PDMA)

A Poly 2-(dimethylamino) ethyl methacrylate) (PDMA) is a water-soluble cationic polymer.[119] The chemical structure of PDMA is shown in Figure 1-22. Due to its optical transparency, conductivity, hydrophilicity, pH and temperature responsibility, and ease of fabrication, [120] PDMA is a promising candidate for a variety of potential applications, including enhanced Raman scattering (SERS),[121] drug delivery,[122] biosensors and biomedical devices. [123] In addition, PDMA is a well-known polymer that responds to a variety of environmental stimuli, such as temperature[124] and pH.[125]As pH decreases below 7, its weakly basic tertiary amine pendant groups become positively charged, whereas they remain neutral at higher pH values [126]. Thus, PDMA brushes can be quaternised by reaction with alkyl halides.

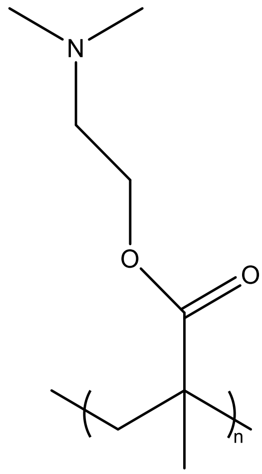

Figure 1-22: The chemical structure of PDMA

1.8.5 PDMA Quaternisation

PDMA can be quaternised by reaction with a variety of alkyl halides (q-PDMA), as shown in Figure 1-23, and the resulting material can be used in antimicrobial systems.[127] Armes and co-workers have published various investigations regarding quaternised PDMA systems, finding that PDMAEMA aqueous solutions have systematically increased in cloud points as the degree of quaternisation (DQ) of the homopolymer becomes higher. [139] Furthermore, it was determined that the cloud point of PDMAEMA aqueous solutions is strongly influenced by the degree of polymerisation.[127] In accordance, a recent study has found that q-PDMA is particularly effective at killing bacteria such as Escherichia coli, Bacillus cereus, and Staphylococcus aureus.[128] Similarly, in another study, alkyl bromides of either 1-bromododecane or 1-bromohexane were used, which found that q-PDMA was effective against E. coli and S. aureus.[129] Several alkyl halides have been successfully used in the quaternization process of PDMA such as 1-iododecane, 1-iodoheptane, and 1-iodobutane.[127] Additionally, Cheng *et al.*[129] demonstrated that the quaternisation of PDMA brushes provided useful bactericidal properties. In general, several factors can affect the degree of quantisation of PDMA polymer such as solvent polarity, the length of alkyl and the temperature of the reaction.[130]

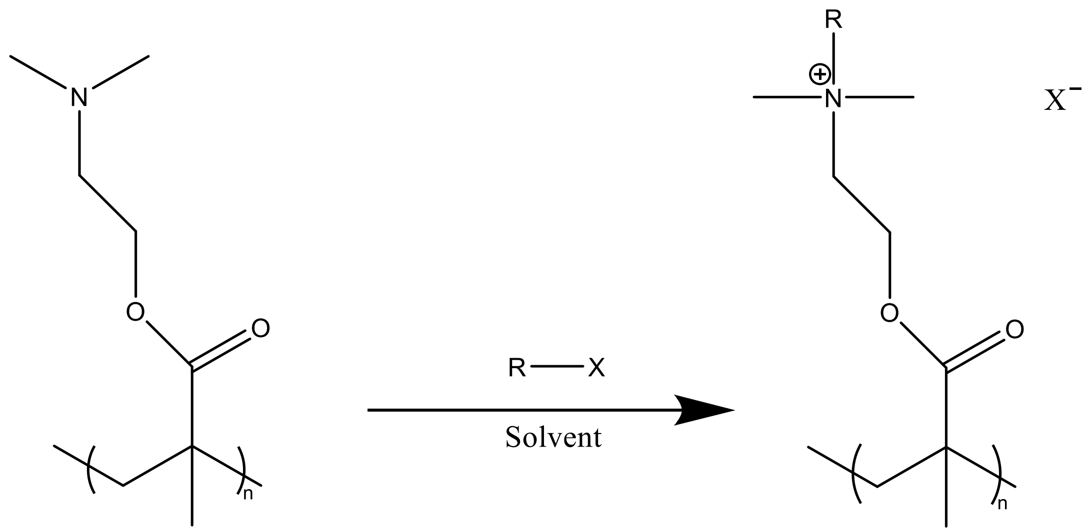

Figure 1-23: The quaternisation of PDMA with alkyl halides.

1.8.6 Dye-Functionalised Polymers

Recently, there has been significant interest in dye-functionalised polymer structures due to their important role in various applications in organic electronic devices, which include white polymer light-emitting diodes (WPLEDs) and organic light-emitting diodes (OLEDs), as well as their use as sensor molecules in environmental and biochemical applications.[131] An effective method for incorporating dyes into a polymer involves binding the dye to the pre-formed polymer, either by attaching it to the side or end chain. For example, Oregon Green was covalently coupled to PMEP polymers grafted onto gold substrates. The effect of water and KCl on the polymer conformation was studied by measuring changes in fluorescence. In water, the brushes emit a significant amount of fluorescence while being in an expanded conformation. The presence of KCl increases the screening of charges to be screened along the polymer chains, leading to a partial collapse. This is demonstrated by a significant reduction in the fluorescence intensity.[132]

Fluorescein O-methacrylate and n-butyl acrylate were also co-polymerised using ATRP to create pH-responsive dye-labelled polymer brushes. This structure exhibited fluorescence characteristics under alkaline environments, but not in neutral or acidic settings[133] Similar pH sensors were constructed using PMPC homopolymer and PMPC-co-PDPA labelled with Nile blue dye with the colour molecules in these sensors covalently bonded to pre-polymerised monomers.[133] Fluorescent nanotags were created by synthesising a bottlebrush polymer that has hundreds of DNA strands extending from it. These DNA strands have the ability to bind to hundreds of fluorescent dye molecules that are either covalently connected or non-covalently introduced through side chain attachment. The fluorescent nanotag exhibits a highly luminous signal, surpassing that of commercially available antibodies tagged with organic dyes, making it highly advantageous in the detection of protein targets.[134] An essential drawback with these structures, though, is the tendency of colour molecules to aggregate. To address this issue, Maciej *et al*.[135] proposed that the attachment of dye molecules at the terminal end of a polymer chain could potentially lead to reduced aggregation, as opposed to attaching the dye molecules within each repeating unit of the polymer chain.[135] It is also important to note that the researchers utilised alkynylated fluorescein to modify micropatterned PMMA brushes that were generated via ARGET-ATRP through the end chain which has potential uses in light harvesting.[135]

Lishchuk *et al*. designed plexcitonic compounds that were identified by coupling employing chlorophyll molecules to modify PCysMA brushes grown from gold nanostructure arrays. The brushes served as a framework to organise the pigment molecules in 3D and to facilitate strong coupling to localised surface plasmon resonances. The density of the pigment molecules associated with the system is crucial in regulating coupling strength and could be controlled by varying the polymer grafting density. Furthermore, these complexes exhibited switchable optical behaviour because the polymer scaffolds were responsive to changes in temperature and pH, enabling the activation of control over the strong coupling between plasmons and excitons.[67] Comparatively, an alternative method for introducing dye into the polymer involves initially attaching the dye molecule to the polymerisable monomer. Subsequently, polymerisation is conducted using these labelled monomers.[136] An example of this can be noted with the polymerisation of azo dye-labelled acrylic and methacrylic monomers using ATRP. The chemical reactivity of azo-labelled methacrylate polymers is greater than that of azo-labelled acrylate polymers, meanwhile, the utilisation of organic dyes functions as initiators in ATRP.[136] A derivative of Rhodamine 6G was also employed as a catalyst to commence Atom Transfer Radical Polymerisation (ATRP) for the production of homopolymers using 2-(methacryloyloxy) ethyl phosphorylcholine (MPC) monomers. Furthermore, a derivative of

Rhodamine 6G was employed to create copolymers of PMPC-co-PDPA that are responsive to changes in pH which was achieved using a sequential addition method.[137]

1.8.7 Applications of polymer brushes

Polymer brushes display a significant amount of programmability and enable simultaneous control of chemical and physical properties including stimulus-responsiveness, stiffness, self-healing, and hydrophobicity. Thus, brushes have been employed frequently in applications where the ability to control surface characteristics in a responsive fashion is required.[109] Polymer brushes provide a straightforward, adaptable, and efficient method for controlling interfacial interactions. For instance, poly2-methacryloyloxyethyl phosphoryl choline (PMAOEPC) brushes have been found to exhibit significant levels of biocompatibility and lubricity when used in water-based environments. Additionally, Poly oligoethylene glycol methacrylate (POEGMA) brushes can effectively prevent protein adsorption.[138] When compared to alternative methods of modifying surfaces, polymer brushes have been widely and successfully used to improve surface qualities such as wettability, biocompatibility, antibacterial capabilities, and resistance to corrosion.[129] Polymer brushes have been employed to create surfaces with customised chemical and biological properties to achieve the necessary interfacial qualities. Specifically, PCysMA brushes were utilised as an appropriate padding material for supported lipid bilayers (SLBs). Polymer brushes can be employed for intelligent coatings and have the ability to interact with their surrounding environment. Moreover, polymer brushes have gained increasing interest in the manufacture of sensors due to their remarkable sensitivity to factors such as pH, temperature, and ionic strength. The characteristics of the polymer used can also define the conditions under which the sensor operates. Typically, they can serve as a foundation for fluorescence sensors. Recently, the formation of complex systems has involved the incorporation of gels and nanoparticles into polymer brushes or surfactants.

1.9 Atom transfer radical polymerization (ATRP)

There is a wide variety of controlled radical polymerisation techniques such as RAFT[108], ATRP [109] and surface-nitroxide-mediated living free radical polymerization initiated nitroxide mediated polymerisation (NMP).[139] ATRP is the most frequently used radical polymerisation method for the synthesis of surface-grafted polymer brushes. ATRP has several advantages including its high tolerance toward a variety of functional groups, as well as its compatibility with both organic and aqueous media.[108] ATRP was introduced by Matyaszewski in 1995, who determined that this technique enabled to production of the well-controlled growth of surface-grafted polymer chains.[140, 141] Moreover, the ATRP process allows for the production of regular nano-structured polymers such as poly (methacrylates), polystyrene and poly (acrylates).[141, 142] The fundamental mechanism of ATRP is based on the abstraction of the halogen atom X from the alkyl halides (R-X) by the transition metal complex (Cu^{I}/L), resulting in the generation of an organic transient radical ($R^{\bullet}$), as well as a transition metal complex with a higher oxidation state ($X{-}Cu^{II}/L$) and then an alkyl radical ($R^{\bullet}$) which can react with a monomer (M). [143] Briefly, ATRP requires the initiator to have a halogen leaving group, most often alkyl halides (R-X), and the transition metal catalyst, typically (Cu^{I}/L) which is used to produce radicals at the surface ($R^{\bullet}$). A new radical is created at the chain end when the radicals are reacted with monomer (M) chains consisting of vinyl groups.[144] These ATRP components will be explained in detail in the following sections. There is an equilibrium between active and inactive that controls the activation and deactivation of radicals that propagate from the initiator or the end of the polymer chain, adding radical to monomer, and terminating by coupling or disproportionation. The general mechanism of ATRP is shown in Figure 1-24**.**[145]

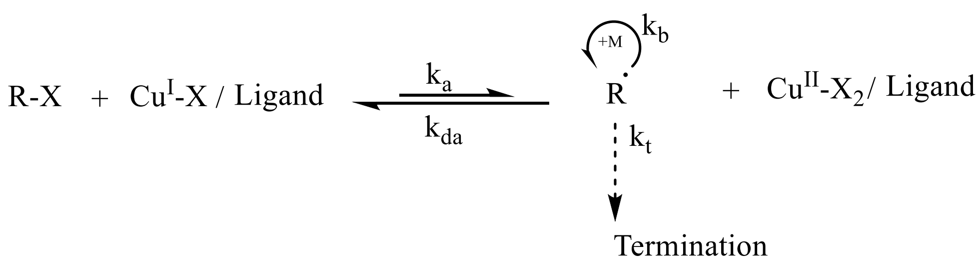

Figure 1-24: Schematic mechanism of traditional ATRP processes.[145]

The balance that is present between active and dormant chains is able to be maintained through the process of keeping propagating radicals' concentration levels low. Even though ATRP has a distinct sensitivity to oxygen, this can result in polymerisation when there are minimal amounts of oxygen. This is a result of the catalyst, which is evident in a notably higher concentration than the polymerising radicals, being capable of gathering oxygen atoms[146] Nonetheless, the oxidation of the metal complex reduces its concentration while increasing the concentration of the deactivator, thus decreasing the rate of polymerisation. The concentration of the catalyst, though, does not influence the molecular weight of the polymer. Specifically, copper halides have demonstrated the highest efficiency as catalysts for this process with ligands essential elements that frequently serve as a key component in the efficient solubilisation and stabilisation of the catalyst, which is vital for its optimal performance.[147, 148] ATRP reaction systems consist of a substrate that is modified to introduce an active initiator, a monomer, and a catalyst.

Monomers

A variety of vinyl monomers are the most frequently used monomers in ATRP to grow polymer brushes such as acrylates,[149] methacrylates,[141] and styrenes.[150] Additionally, there are other examples of monomers that are successfully polymerised with ATRP such as (meth)acrylamide and acrylonitrile. The radical propagating on these monomers can be stabilised by substituents and even when the same catalyst is used, (i.e. the atom transfer equilibrium), the constant is unique to each monomer for active and dormant species.[141]

Initiator

The initiator is responsible for the identification of the quantity of growing polymer chains. If the initiation step is rapid and the rates of chain transfer and termination are minimal, the quantity of developing polymer chains remains constant which is equivalent to the initial concentration of the initiator. As the initiator concentration increases, the average molecular weight of the resultant polymer chains correspondingly increases due to the greater number of chains developing from the increased quantity of initiator molecules available.[151] Alkyl halides are extensively used as ATRP initiators, and in regards to the use of an appropriate halide (X), well-defined polymers can be produced with narrow molecular weight distributions. The best control of the molecular weight can be achieved by using either bromine or chlorine as a halide group. This can also utilise Iodine in ATRP, especially for styrene and acrylate polymerization. Fluorine, contrastingly, is not used due to the high strength of the C-F bond, which is then unable to undergo homolytic cleavage.[141] Overall, there are several common examples of ATRP initiators including BIBB-ATMS, BIBB-APTES, and CMPTS.

Catalyst

The catalyst plays a significant role in the ATRP process as this determines where the dormant and active species exchange, (i.e. the position of the atom transfer equilibrium). The catalyst in ATRP usually consists of a transition metal and ligand.[152] The concentration of the catalyst can affect the rate of polymerisation but not the molecular weight of the polymer.[153] Additionally, an effective transition metal catalyst must display a number of characteristics. Initially, the metal needs to include more than one easily accessible oxidation state, which differs by one electron. Following this, the metal centre must present a strong affinity for halogens; while upon oxidation, the coordination sphere around the metal centre needs to expand in order for the halogen atom to be accommodated. Lastly, the metal in question should create a relatively strong complex with the ligand. Ultimately, the ATRP equilibrium position and dynamics must be suitable for the specific system.[141, 152] Among several transition metal complexes that have been investigated, the copper halide is the most efficient catalyst for ATRP.[154]

Ligands

Ligands have a key role to play in the solubilisation of the transition metal salt in the organic solvent, as well as in modifying its redox potential to enhance its dynamics and reactivity for atom transfer.[155] In ATRP, most ligands contain nitrogen atoms and are combined with Cu, such as HMTETA and PMDETA.[156]

Solvents

Solvents are sometimes required, especially when the polymer obtained is insoluble in its monomer. A wide variety of solvents have been used in ATRP, including water, alcohol, dimethyl formamide (DMF), ethyl acetate, benzene, carbon dioxide, acetone, and toluene. However, several factors need to be considered when choosing a solvent with chain transfer to the solvent as minimal as possible. Solvent-catalyst interactions should be also considered, while it is important to minimize solvent-assisted side reactions to reduce solvent poisoning, as well as side reactions caused by the solvent. A solvent poisoning occurs when a catalyst deactivates due to interactions with a solvent that block active sites or change its structure.[141]

1.9.1Advantages of atom-transfer radical polymerisation

ATRP has several advantages over the other polymerisation techniques. One of the advantages of ATRP is robust and simple and has been successfully utilised to polymerise different types of polymers including linear, star, graft, branched, and network.[157] The reaction conditions of ATRP are simple due to the lack of requirement for special equipment including Schlenk and glove boxes, enabling more scientists to synthesise polymer brushes. In this process, ATRP can be used in both organic and aqueous media with a variety of functional groups.[158] The ATRP method allows well-defined polymers to be synthesised with desired characteristics. Additionally, this enables polymers to be controlled according to their molecular weight distribution.[159] There is a wide range of monomers polymerizable by ATRP, which includes monomers from renewable sources, such as Tulipalin A, rosin acid derivatives, itaconates, and other vinyl monomers. As a result of all these advantages, ATRP polymers have become very attractive for various applications such as gene and drug delivery, bioconjugation with stimuli-responsive polymers, and tissue engineering.[160]

Simultaneously, ATRP presents certain disadvantages. One of them is the low oxygen tolerance of conventional ATRP, which makes it unsuitable for ambient use. Despite ATRP's sensitivity to oxygen, polymerisation can withstand small amounts of oxygen.[161]. A catalyst at a higher concentration than the radicals is able to counteract the effects of tiny amounts of oxygen. Nevertheless, the catalyst concentration can be reduced by the strong oxidation process, resulting in a decrease in the polymerisation rate. Peroxides may be generated in certain instances due to the presence of oxygen, which can serve as a catalyst for the process. For instance, methacrylate can undergo polymerisation with large molecular weight compounds and relatively low polydispersity when Cu (I) or Cu (II) complexes and modest quantities of oxygen are present.

Alternative techniques to ATRP, such as Activator Re-Generated by Electron Transfer (ARGET) ATRP, have been created to address the limitations of traditional ATRP. In ARGET ATRP, extra reducing chemicals are introduced to recover the active Cu (I) species from the deactivated Cu (II) species generated during radical termination reactions. This approach is an environmentally friendly technique for achieving well-regulated polymerisations and can also facilitate the grafting of various polymers onto various substrates, even in the presence of little oxygen during the process.[162]

1.10 The introduction of gold nanoparticles into polymer brushes and PDMA

Several methods have been explored for incorporating metal nanoparticles into polymer templates, including hydrophobic interactions, hydrogen bonding interactions, covalent linkage interactions, and electrostatic attraction as an external addition or in situ synthesis of nanoparticles within polymers.[163] Christau *et al.*[164] used non-ionic poly (N-isopropylacrylamide) (PNIPAM) brushes to control the spatial distribution of the hydrophobic 12-mercaptododecanoic acid (12-MDA)-coated AuNPs and hydrophilic citrate-coated AuNPs.

As AuNPs have varying hydrophobicities, various solvents were employed for incubation, resulting in distinct polymer conformations and particle distributions. Hydrogen bonds facilitated the interaction between brush and particles in this case. Bhat *et al.*[165] proposed binding negatively charged AuNPs would be attracted to positively charged poly(acrylamide) (PAAM) brushes at low pH through electrostatic attraction. The charge density of AuNPs significantly influences their dispersion within the polymer brushes. Accordingly, manipulating the pH level is the most straightforward method to regulate the charge density.[166] The distribution and quantity of AuNPs can be regulated by adjusting the pH during the incubation of poly-[2-(methacryloyloxy) ethyl] trimethylammonium chloride (PMETAC) brushes in the suspension of AuNPs. At a pH of 4, the AuNPs formed clusters because the electrostatic stabilisation was reduced. At a pH of 8, the AuNPs were electrostatically stabilised, enabling them to infiltrate the brush rather than adhering to the surface, as observed at a pH of 4. The particles and the brush interacted by electrostatic attraction, resulting in the creation of colorimetric sensors that possess unique optical characteristics.[163, 166] Polymers provide numerous advantageous characteristics, including multifunctional groups, multiformity, and well-defined structures. These traits have established them as the ideal option for creating metal nanoparticle arrays by the utilisation of patterned polymer brush models.[163] Liping Fang *et al*.[163] created a hybrid film by adding AuNPs to patterned PDMA brushes using a method based on host-guest interaction. The interaction was confirmed by employing the PDMA monomer as a competing guest. Directly utilising PDMA as a host for immobilising AuNPs is a straightforward procedure that eliminates the need for complex modifications. Moreover, the absorption band of AuNPs showed a red shift upon attachment to PDMA brushes due to the particles being brought close to each other. This proximity perturbs the dielectric constant around the nanoparticles, and the presence of PDMA further increases the surrounding dielectric constant, resulting in a redshift. Meanwhile, the surface morphology transitioned from smooth to rough with the addition of AuNPs, resulting in a significant increase in the root-mean-square (RMS) roughness from 0.45 to 2.49 nm.[163]

1.11 Photosynthesis: natural light-harvesting

Natural light-harvesting systems rely on exceptionally efficient energy transfer mechanisms. Biological light-harvesting complexes provide characteristics that make them an outstanding model for enhancing artificial technologies that depend on similar processes. Hence, it is crucial to initially comprehend the fundamental principles underlying efficient biological light-harvesting mechanisms, such as photosynthesis.[167] This is a biochemical process that involves the conversion of solar energy to chemical energy, which occurs in certain organisms, including plants and photosynthetic bacteria. Throughout evolution, nature has perfected its methods of capturing light, which in turn supplies the necessary energy to support Earth's ecosystem and sustain life. Typically, a photosynthetic organism utilises sunlight energy to synthesise oxygen and glucose molecules from carbon dioxide and water. The process of capturing solar energy is performed by pigment-protein complexes, also referred to as light-harvesting complexes (LHCs) or antenna complexes. Excitons are generated when pigments within the light-harvesting complexes absorb photons. Through this mechanism, the excitation energy is directed along an energy gradient by transferring the excitation from molecules with greater HOMO-LUMO energy difference to those with lower energy. Ultimately, the energy reaches a reaction center where photo-induced charge separation occurs. A series of electron transport processes occur within the chloroplast as a result of this charge separation, which pumps protons (H^+) from one side of the membrane to the other, creating an electrochemical proton gradient. This gradient represents stored potential energy. As the proton gradient flows back through these protein complexes, special protein enzymes (ATP synthase) drive the conformational changes required to produce adenosine triphosphate (ATP) from ADP and phosphate.[167] Photosynthetic membranes contain a variety of "components" whose function is to maximise the efficiency of transfer of excitation to a reaction centre, where charge separation occurs to begin the process of photosynthesis. In purple bacteria, light-harvesting complex 2 (LH2) captures sunlight, and transfers excitation via a series of hoping steps to light-harvesting complex 1 (LH1), which funnels the excitation into the reaction centre (RC). The ratio of LH2 to LH1-RC is selected to optimise the rate of charge separation. Growing purple bacteria in conditions of different light intensity leads to changes in the LH2:LH1-RC ratio to adapt to changing light levels, with the ratio increasing as the light level decreases. LHCs whether found in bacteria or plants, often employ comparable mechanisms to undertake the operations of light harvesting and energy transfer. Crucially, every photosynthetic unit consists of a significant amount of pigment molecules that play essential roles in photosynthesis. Pigment molecules involved in photosynthesis are usually chlorophylls or bacteriochlorophylls. A chlorophyll molecule absorbs light primarily in the visible spectrum (400-700 nm) and contains magnesium in a porphyrin ring with phytol tails in plants and algae. The bacteriochlorophylls of photosynthetic bacteria are modified porphyrin molecules with reduced pyrrole rings, which shift their absorption to near-infrared wavelengths (700-1000 nm), enabling them to harvest light energy in a variety of environments.[167]

Furthermore, carotenoids and other cofactors such as quinones or iron sulphur centres can also play a role in photosynthesis. While carotenoids capture additional light wavelengths and protect photosystems from oxidative damage, quinones function as mobile electron carriers that shuttle electrons between photosynthetic complexes. Iron-sulfur centers alternate between reduced and oxidized states during electron transfer within protein complexes, facilitating electron flow. The pigments are attached to photosynthetic proteins, with the quantity and diversity of pigment molecules ensuring the effective capture of light across the appropriate spectrum. These pigments and protein systems are known as light-harvesting complexes, with the most important stage in light-harvesting stemming from the conversion of electronic excitation into charge-separated states through the cellular membrane, which is conducted at the reaction centre (RC)–a pigment−protein form, see Figure 1.25**.**

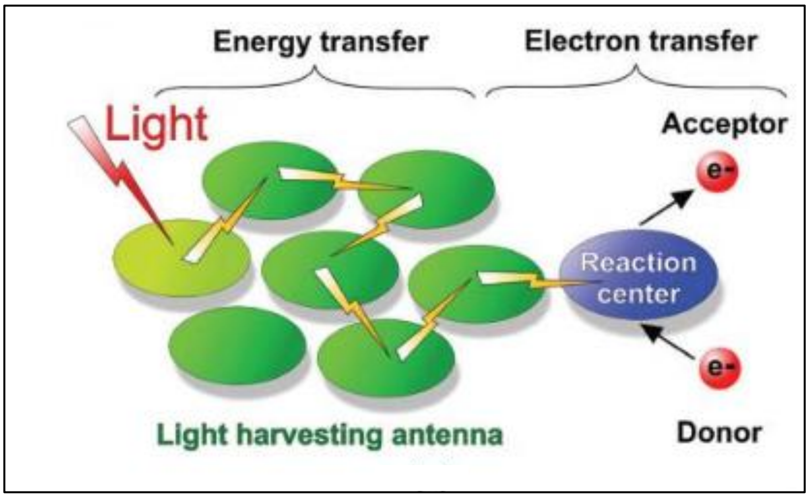

Figure 1-25: A schematic illustrates the notion of antennas in photosynthetic organisms. In this process, pigments absorb light, whether they are a kind of chlorophyll or another pigment. Energy transfer occurs as the excited state passes through the antenna system and is ultimately transmitted to the reaction centre, where electron transfer occurs, resulting in the oxidation of the electron donor and the reduction of the electron acceptor.[167]

1.11.1 Plexcitons in light-harvesting systems

There has been interest in exploring the strong coupling of plasmon modes to LHCs, driven by the hope that it might be possible to design novel materials based on a combination of strong coupling with biological or biologically-inspired materials. In photosynthetic plants and bacteria, multiple components are required to enable the capture of sunlight (antenna complexes) and its use to drive charge separation in the reaction centre (LH1-RC complexes in purple bacteria). In a synthetic biologically-inspired photovoltaic device, the aim would be to use captured sunlight to drive charge separation at electrical contacts. Thus, in place of the antenna unit and RC, a donor-acceptor pair would be required. Nevertheless, the first step would be capture of solar energy, and studies of plasmon-exciton coupling for films of synthetic light-harvesting complexes would enable the elucidation of basic principles that govern this key step. Subsequent work, outside the scope of this thesis, would then need to adapt these methods to incorporate donor and acceptor elements that would be required to drive the flow of current in a photovoltaic device. There are several significant similarities between LSPR in metal nanostructures and exciton formation in light-harvesting complexes. Metal nanostructures and protein-bound chlorophylls both generate collective oscillations of charged particles in response to electromagnetic radiation. LSPR and LHC systems can be tuned by modifying their structural properties: nanoparticle size and shape and protein scaffold arrangement. Both exhibit enhanced near-field effects, with LSPR creating strong local electromagnetic fields whereas LHCs transfer energy efficiently between chromophores. Chl *a* binds specifically to the tertiary amine on the PDMA pendant group. It is not known whether the nanoparticles bind specifically to the amine; if the brush is protonated (as is the case at pH < 7) then the nanoparticles would be expected to bind to the polymer via electrostatic interactions. However, where the pendant groups are uncharged, the principal effect of nanoparticle binding to the brush would be steric: the nanoparticle diameter is comparable to the PDMA film thickness and binding of the Chl *a* to the brush would be sterically hindered if nanoparticles are bound to the polymer before Chl *a*. In contrast, if the Chl *a* binds first to the polymer, then the resulting materials would be cationic if the Chl is bound via a dative bond to the metal ion in the centre of the chlorin structure. Therefore, while the presence of high concentrations of Chl *a* in the film would create steric hinderance to penetration of the film by nanoparticles this effect would be balanced by strong electrostatic interactions between the polycationic brush and the anionic nanoparticles. To reach the strong coupling limit, it is necessary to achieve a high enough concentration of excitons within the plasmon mode volume, estimated to be ~10^{25} m^{-3}. [66] For LSPRs associated with metal nanostructures, the plasmon mode volume extends ~10 nm from the surface; thus, a minimum concentration of excitons of ~ 10^{17} m^{-2} is required to reach the strong coupling limit, a condition that is satisfied by plant and bacterial LHCs. Large coupling energies (~0.25 eV were demonstrated for both plant and bacterial LHCs and the energies of the hybrid plexcitonic states could be programmed by using synthetic biology to change the pigment complement of the LHCs.[66]

While strong coupling has been demonstrated to monolayers of LHCs, pigment-protein complexes are not well suited to applications in technology. Not only is it slow and expensive to produce proteins, but they are also susceptible to damage during processing. Thus, a different approach is required if these exciting results are to be translated into applications. A large literature exists on the use of chlorophyll in optoelectronic devices. A popular method in this process involves spin-coating the molecules onto the substrate. For instance, Chl *a* molecules were spin-coated onto nanostructured gold in plasmon-sensitised solar cells, resulting in power conversion efficiency (PCE) because of the formation of plexcitonic states from strong plasmon-exciton interactions.[168] An electrode composed of TiO_2 and nanostructured gold in a similar experiment was immersed in a chlorophyll solution for 12 hours in order to achieve coating. Moreover, charge recombination was reduced through the presence of plasmonic gold, which improved charge separation within the cell.[169] In addition, chlorophyll may be utilised in conjunction with other biological pigments, including anthocyanin and betalain. A power conversion efficiency of 3.73% was attained when the mixture was affixed to TiO_2 in dye-sensitised solar cells.[170] These previously mentioned examples illustrate the merit of integrating the principles of natural photosynthesis into artificial systems; nevertheless, it is important to highlight that in these instances, the pigments are attached to the surface through physisorption. This provides a comparatively weak adhesion to the surface and minimal control over the molecular arrangement. The chlorophylls have a strong tendency to aggregate, leading to a reduction in the excited state lifetime, a phenomenon which is absent in biological LHCs which have structures that are optimised so that they bind high concentrations of chlorophylls (~0.6 M in plant LHCs) without concentration-quenching. Moreover, it is posited that physiosorbed chlorophylls are orientated parallel to the surface plane, leading to weak contact among neighbouring pigments and possible concentration quenching effects resulting from aggregation. Alignment parallel to the gold surface would prevent plasmon-exciton coupling because the electric field associated with the LSPR is oriented perpendicular to the metal surface. When chlorophylls are attached via a self-assembled monolayer (SAM), it facilitates efficient π-π stacking of the chlorin rings, with the molecules orientated nearly perpendicular to the surface. This results in enhanced contacts among pigment molecules, facilitating more efficient exciton coupling.[171]

1.11.3 Chlorophyll a

Photosynthetic membranes in plants and bacteria contain light-harvesting complexes that organize pigment molecules (chlorophyll and carotenoids) with exquisite precision.[67] Photosynthesis occurs when oxygen and water molecules are transformed into various products under solar light, generating chemical and biological energy.[172] Chl *a* is the most common pigment in photosynthetic organisms. As the pigment is responsible for the photosynthesis process, the effects of AuNPs on the interaction between photosynthetic pigments and light may change the photophysical behaviour of chlorophyll.[173] The name chlorophyll is derived from the Greek, chloros´, which means green and phyllon which means leaf.[174] Chl *a* received a lot of attention as a simple model for photosynthetic donor-acceptor systems and as a result of chlorophyll's conjugated double bonds within its porphyrin structure, which allows electrons to be easily excited through electromagnetic wave absorption, chlorophyll has great potential for light-emitting diode (LED) and solar cell applications.[175] Specifically, the chlorophyll structure consists of a tetrapyrrole structure known as a chlorin which serves as the foundational component of chlorophyll. In particular, chlorins are tetrapyrrole macrocycles where one of the pyrrole rings is reduced, differentiating them from porphyrins and enabling their distinctive light absorption properties. The nitrogen atoms in the macrocycle's centre are coordinated to a metal cation, most frequently a Mg^{2+} ion, however, Zn^{2+} has been observed in some bacteria that live in extremely acidic environments. The second pyrrole ring in chlorophyll a is one of four rings that contain nitrogen coordinating with the central magnesium ion and contributes significantly to the molecule's light-harvesting capability. At one of the tetrapyrrole system's corners, a further 5-membered ring is created, shattering the symmetry shared by most porphyrins. Several unsymmetrical side groups are also present; most of which are alkane or alkene substituents, although some also include carbonyls such as aldehydes or ketones. There is also a long hydrocarbon chain, the tail, which is connected to the chlorophyll by an ester linkage. Within the photosynthetic apparatus, this tail primarily serves to stabilize different protein subunits rather than directly anchor chlorophyll to the protein superstructure.[167] Their function in light-harvesting complexes as pigment molecules relates to an excited state created when sunlight-absorbed energy transfers an electron from the highest-occupied molecular orbital (HOMO) to the lowest-unoccupied molecular orbital (LUMO). These are HOMO-LUMO transitions in chlorins, with the energy of the transition dependent on the electronic structure of the pigment.[167] The two important types of chlorophyll in plants are chlorophyll a (Chl *a*) and chlorophyll b (Chl *b*).[176] These two pigments are different from one another due to their distinct absorption tendency and unique side-chain compositions, [177] as shown in Figure 1-26. In chlorophyll a, the second ring contains a methyl group (-CH_3), whereas in chlorophyll b, an aldehydic group (-CHO) is present. [178] In the visible spectrum, Chl *a* absorbs light at a wavelength between 660 and 665 nm (Q band) while chlorophyll b a absorbs light at a wavelength between 642 and 652 nm (Q band). [177] The absorbance spectrum of Chl *a* and b are shown in Figure 1-27. The position of the peak in both pigments is strongly dependent on the solvent composition around the pigment. [172]

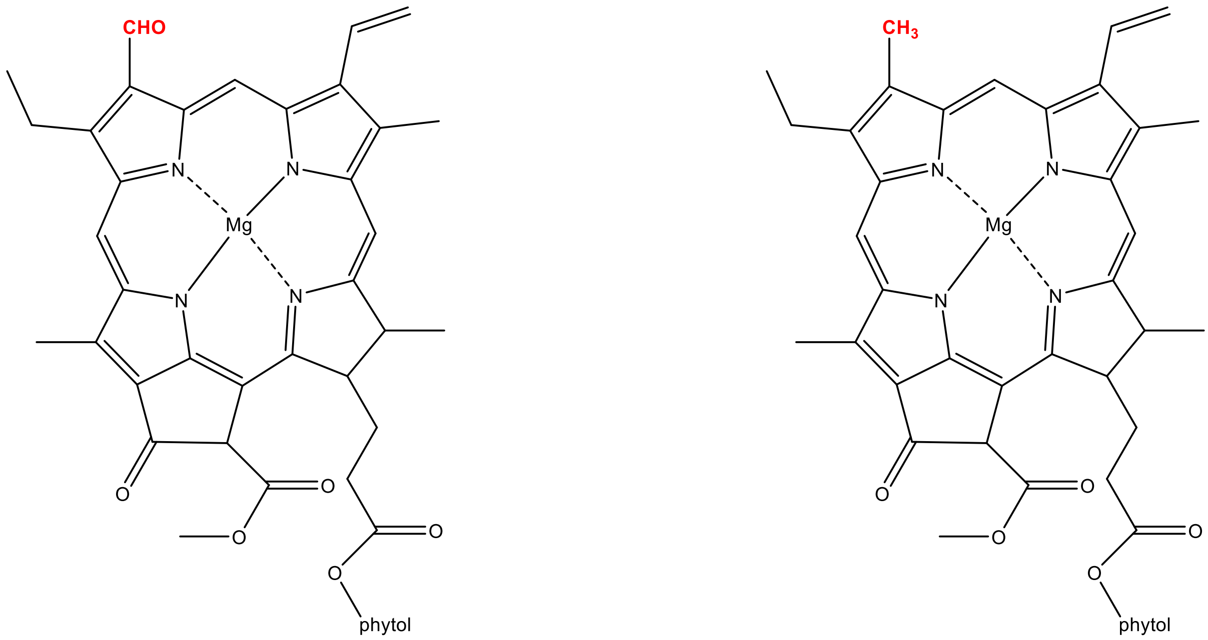

Figure 1-26: Chemical structure of chlorophyll a (right) and chlorophyll b (left).[172]

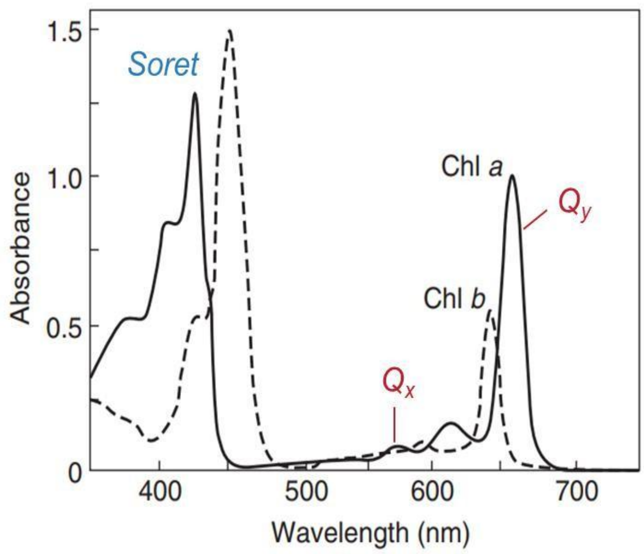

Figure 1-27: The absorbance spectrum of chlorophyll a (represented by a solid line) and chlorophyll b (represented by a dashed line).[179]

Chlorophylls can be considered the best photoreceptors in nature and are used in organic electronic devices such as organic light-emitting diodes (OLEDs) or organic photovoltaics (OPVs). Accordingly, a rapidly developing field of research is artificial photosynthesis which mimics the natural photosynthesis processes that occur in plants or bacteria. In artificial photosynthesis systems, surface plasmon technology can significantly enhance energy transfer efficiency.[180] In order to mimic natural light-harvesting complex, polymers have been successfully used to incorporate Chl *a* into artificial photosynthesis systems. However, chlorophylls have some limitations in these applications due to their high photodegradation. [52] OLEDs have recently been successfully fabricated by Ohtani *et al*.[181] with chlorophylls that were rich in carotenoids extracted from spinach due to the fact that carotenoids have improved the photostability of Chl *a* to some extent.[181]

1.11.4 Extraction of chlorophyll and purification

In 1818, Pelletier and Caventou discovered chlorophylls that can be extracted and purified using several methods.[182] Chl *a* has been extracted from natural sources using a variety of methods, including organic solvent extraction [183] and supercritical fluid extraction.[184]Typically, organic solvent extraction is used for dissolving lipids and lipoproteins. The most important step in the solvent extraction method is selecting the suitable solvents.[177] Various organic solvents can be used in chlorophyll extraction methods from plants such as ethanol, methanol, dimethylformamide, and acetone. Even though the previous solvents were more effective than acetone, it is preferred in this process.[177] Due to the semi-polar nature of acetone (CH_3COCH_3) and the non-polar nature of chlorophyll, acetone is an appropriate solvent for chlorophyll extraction. [185] The first successful isolation of chlorophyll was achieved by Tswett which led to the development of modern chromatographic technique.[174, 186] Several techniques have been reported in the literature of the pure chlorophyll a extracted from the leaves that is unstable as it lacks other leaf pigments such as carotenoids that stabilize them. It is possible to enhance the photostability of pure chlorophyll a by replacing Mg^{2+} with Zn^{2+} to form Zn-pheophytin. [187] The zinc atom was selected because the Zn chlorophyll complex is also contained in nature such as Acidophilic organisms (Rhodophyte galdieria sulphuria (Cyanidium caldarium) and purple bacteria (Acidiphilium sp.).[188] The chromatography method can be used to purify chlorophyll, which is a technique that provides many advantages including simplicity, high separation efficiency, and rapidity.[189] Particularly, column chromatography successfully separated chlorophylls a and b, although it required a high degree of technical skill, consuming a lot of solvents and time.[182]

1.11.5 chlorophyll derivatives

The primary factor limiting the use of chlorophyll is its susceptibility to degrade when exposed to moisture, light, or harsh environmental conditions.[190] The degradation of this compound also occurs when it is isolated from its natural source. This degradation can be caused by heat, light, oxygen, acids, or enzymes. As a result of this degradation process, derivatives such as chlorophyllide, pheophytin and pheophorbide, are formed.[191] Overall, there are many low-cost, accurate, and easy methods for analysing chlorophyll. Nevertheless, traditional techniques have certain constraints when it comes to accurately detect a combination of many colours due to the interference caused by the absorption spectra of the individual components in the mixture. Preferably, the components should be disassembled before the analysis. When High-Performance Liquid Chromatography (HPLC) is employed for the purpose of separating the constituents of the mixture, it becomes feasible to readily break down chlorophyll molecules into chlorophyllide and phytol chains. Due to the resemblance in absorption spectra between chlorophyll and chlorophyllide, the separation of chlorophyllide becomes challenging, resulting in imprecise analysis. Therefore, it is necessary to extract chlorophyll using a process that reduces the conversion of chlorophyll to chlorophyllide.[192] Correspondingly, chlorophyllide is produced from chlorophyll through the action of either the extraction solvent or chlorophyllase, which is a hydrolase enzyme. Chl *a* can be transformed into a pheophytin a derivative by employing MCS or mild acid to remove the core magnesium atoms from the molecules, a process known as de-metalation. The process of hydrolysis breaks down pheophytin and results in the separation of the phytol chain, forming pheophorbide a.[192] Figure 1-28 shows schematically a summary of the most prevalent transformations of Chl *a* into its derivatives.

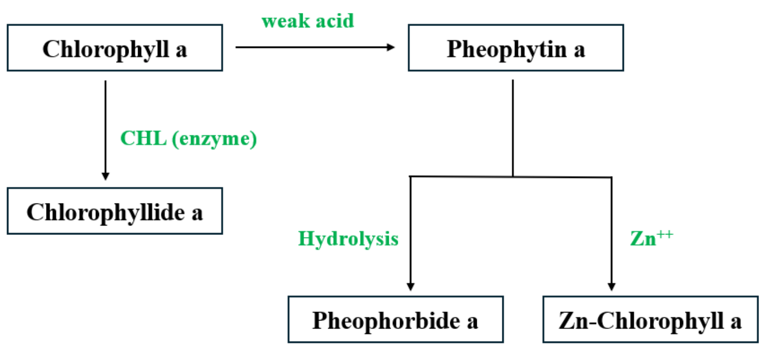

Figure 1-28: Schematic representation of Chl *a* and its most common derivatives: pheophytin a, chlorophyllide a, pheophorbide a and the ZnChla derivative.

1.11.6 Substitution of the central metal with Zn^{2+}

Chlorophyll is very reactive and can be rapidly affected by being exposed to light, high temperature, oxygen, and basic or acidic environments.[193] Research has revealed that the metalo-chlorophyll derivatives exhibit greater stability compared to natural chlorophyll. Zinc (Zn) and copper (Cu) ions were used to replace the magnesium (Mg) ions in the central ring of chlorophyll in order to address this particular issue, in comparison to natural chlorophyll. In this process, Zn chlorophyll derivatives are more commonly used due to the toxicity associated with copper ions, even though forming copper complexes is relatively straightforward.[191] Zn-chlorophyll a derivative (ZnChla) is a chemically stable version of chlorophyll a that has exceptional resistance to degradation. Additionally, ZnChla has the ability to efficiently capture red light at approximately 670 nm, unlike other forms of chlorophyll. The features of ZnChla have the potential to be useful in the development of synthetic materials that respond to light.[194] For instance, research has shown that ZnChla can serve as a photosensitiser for the production of biohydrogen from sucrose. Nevertheless, it has been shown that Mg-Chl *a* absorbs light at around 660 nm.[195]

Chapter 2: Aim and thesis structures

This study aims to design synthetic, biomimetic light-absorbing structures that replicate the essential characteristics of natural photosynthetic light-harvesting complexes using synthetic polymer systems. In particular, poly (2-dimethylamino ethyl methacrylate) (PDMA) has been selected as a scaffold to replace the peptide scaffolds that are used in photosynthetic LHCs. In nature, LHCs such as those present in bacteria and plants, exhibit exceptional efficiency in regulating the transport of excitons across significant distances. To mimic these natural systems, the aim of this thesis is to use PDMA as a scaffolding material to organise chlorophyll within plasmon modes to create plexcitonic antenna complexes. PDMA will be synthesised via ATRP from brominated solid substrates under cost-effective, environmentally friendly conditions. Chlorophyll will be isolated from spinach leaves and stabilised by replacing the magnesium (Mg) ions with zinc (Zn) ions.

The study will examine whether the tertiary amine groups in PDMA are able to form stable bonds with the metal ions in chlorophyll, enabling chlorophyll to maintain its excitonic properties. The binding of chlorophyll to these surface-grafted polymer scaffolds will be investigated using spectroscopic techniques. A central question will concern whether high enough concentrations of chlorophyll can be achieved without aggregation to enable strong plasmon-exciton coupling.

Because lithographic techniques add significant cost to manufacturing processes, an additional aim of the project will be to examine whether solution-phase processes can be used to incorporate plasmonic nanostructures into pre-formed polymer brush layers. Such processes could, if successful, provide a means to produce strongly coupled materials at low cost, that would offer efficient long-range excitation transfer.

Success in producing these systems could result in substantial progress in the design of novel molecular photonic materials, with potential uses in fields like solar energy conversion and optoelectronic devices.

Chapter 1 introduces the historical background and fundamental principles of plasmonics, focusing on plasmon-exciton coupling, especially in the context of strong plasmonic interactions. Furthermore, the chapter explores polymer brushes and their synthesis via ATRP. This chapter also provides an overview of natural light-harvesting complexes and their critical role in photosynthetic energy transfer. The review subsequently discusses state-of-the-art research on previous work of synthetic light-harvesting systems, with a particular focus on the use of polymer-based scaffolds.

Chapter 2 outlines the general aim of the current study and the specific objectives of each chapter, as well as the strategies employed to achieve these goals.

Chapter 3 provides a comprehensive description of the materials and methodologies used throughout the study. A variety of characterisation techniques, including X-ray photoelectron spectroscopy (XPS), ellipsometry, atomic force microscopy (AFM), and UV-visible spectroscopy (UV-vis), are introduced, as these methods are essential for surface analysis and in the confirmation of the surface structure.

Chapter 4 describes the synthesis of biomimetic organic light-harvesting networks similar to those found on photosynthetic light-harvesting complexes. Pigment-polymer complexes are created by synthesising poly (2-dimethylamino ethyl methacrylate) (PDMA) scaffolds surface-initiated polymerisation and binding plant-derived chlorophyll to these. The amount of chlorophyll attached to the polymer is controlled by adjusting the concentration of chlorophyll and partially converting the amine group into quaternary amides via quaternisation with alkyl halides to regulate the number of binding sites. The binding of chlorophyll to PDMA scaffolds was investigated using XPS and UV-vis spectroscopy.

Chapter 5 examines the growth of PDMA brushes on planar gold surfaces and how the grafting density of the polymer affects chlorophyll-binding. PDMA was grown from gold surfaces using disulfide-based initiators, and polymerisation was investigated by XPS, AFM, and ellipsometry. It is hypothesised that a reduction in the polymer grafting density may enhance chlorophyll binding capacity, which can be achieved through the use of mixed self-assembled monolayers.

Chapter 6 investigates the incorporation of plasmonic materials via solution-phase processes. Gold and silver nanoparticles are introduced to pre-formed PDMA brushes rather than growing their pigment-polymer complexes from surface-bound nanostructures. Proven colloidal AuNP synthesis techniques are used to create nanoparticles in solutions with specific shapes and sizes, enabling large-area surface modifications. The impact of nanoparticle size and shape on the plasmon-exciton coupling phenomenon is also explored.

Chapter 7 summarises the key findings of the thesis, and discusses challenges associated with plasmonic coupling.

Chapter 8 suggests the directions for future research and new research avenues are outlined and key areas that require deeper exploration are highlighted.

Chapter 3: Experimental Methods

3.1 Materials and methods

Glass coverslips (22 x 64 mm and thickness = 1.5 mm) were obtained from Menzel-Gläser. Silicon wafers (reclaimed, p-type, <100>) were supplied by Compart Technology (Tamworth, UK). A Carousel 12 Reaction Station (Radleys, UK) was used to prepare polymer brush samples under nitrogen. Hydrogen peroxide (30%), sulfuric acid (95%), dichloromethane, (≥ 99.8%), dimethylformamide (> 99%), magnesium sulfate, anhydrous, (≥ 62, 70%), isopropanol-2-ol (99.5 %) HPLC grade), acetone (99.8%, HPLC grade) and tetrahydrofuran (99.7%, HPLC grade) were purchased from Fisher Scientific (Loughborough, UK). Ethanol, absolute, (≥ 99.8%) and silica gel, 40-63 μm particle size were obtained from VWR international (Lutterworth, UK). Chromium chips (99%), gold wire (99%), (3-aminopropyl) triethoxysilane (APTES) (≥99%), α-bromoisobutyryl bromide (BIBB) (98%), triethylamine (≥99%), copper (I) bromide (≥99%), 2 (-dimethylamino) ethyl methacrylate (DMA) (98%), 1,1,4,7,10,10 hexamethyl triethylenetetramine (HMTETA) (97%), bis[2-(2-bromoisobutyryloxy) undecyl] disulfide, (DTBU), (97%), 11-mercapto-1-undecanol (97%) and 1-iodooctadecane (95%), gold (III) chloride hydrate, trisodium citrate dehydrate, acetic acid, (≥ 99.7%), sodium hydrogen carbonate, (≥ 99%), petroleum ether 40-60 °C, methanol, (99.99%), zinc acetate dihydrate, (99.999%), cetyltrimethylammonium bromide (CTAB), silver nitrate ($AgNO_3$), sodium borohydride ($NaBH_4$), L-ascorbic acid and sand low iron were purchased from Sigma-Aldrich UK (Gillingham, UK). All materials were used as received from the manufacturers, and all chemicals produced were of analytical grade. Additionally, spinach leaves were purchased from a local supermarket; with deionised water obtained using an Elga Pure Nanopore system with a conductivity rating of 15 MΩcm. Probes for AFM tapping (OTESPA-R3 model, with 300 kHz resonance frequency and tip radius of about 7 nm) were purchased from Bruker (Germany). Copper bromide was stored in a vacuum environment. DMA was kept at 4 °C following the elimination of the inhibitor via filtration through a short column of basic aluminium oxide. The chloroauric acid was stored in a dark place between 3 °C and 8 °C.

3.2 Cleaning glassware and substrates

Piranha solution was used to thoroughly clean all glassware and substrates prior to use to eliminate all contaminants, especially organic residues. Piranha solution is a mixture of hydrogen peroxide and concentrated sulphuric acid in a ratio of 3:7. **Caution:** piranha solution is a strong oxidising agent that can detonate spontaneously in contact with organic liquid. Indeed, extreme caution must be used when handling piranha solution. Cleaning is carried out in a face shield, and a fume cupboard, very thick rubber gloves and safety goggles are used as personal protection equipment. After piranha cleaning, the glassware was thoroughly washed with copious amounts of deionized water until testing with litmus paper indicated neutral pH, then oven-dried overnight. Lab equipment, such as tweezers and suba-seals, was washed down with acetone and then rinsed with deionized water, before being immersed in isopropanol, sonicated for 30 min, rinsed again with deionized water, and dried under a nitrogen gas stream.

3.3 Sample handling

The piranha-cleaned glass slides were carefully cut into smaller pieces (roughly 1 cm x 2 cm) using a diamond-tipped scribe and metal ruler on a glass plate that had been thoroughly cleaned with ethanol. The slides were handled with great care and only using tweezers cleaned with ethanol. Once cut, they were dried in a stream of nitrogen gas to remove any dust generated during the cutting process.

3.4 Synthesis

3.4.1 Surface self-assembled layer (SAM) preparation of the BIBB-APTES initiator

The piranha-cleaned glass substrates were functionalised with silane films by immersing the glass or silicon wafers in a 2% (v/v) ethanolic solution of 3-aminopropyltrimethoxysilane (APTES) for 30 min. Subsequently, the samples were thoroughly rinsed with ethanol, dried under nitrogen, and then annealed for 30 min at 120 °C. The silane films were further functionalised with a bromo-initiator by immersion in a solution including 0.37 mL of 2-bromoisobutyryl bromide (BIBB) and 0.4 mL of triethylamine in 60 mL of dichloromethane for 60 min. Finally, the samples were rinsed with ethanol and dichloromethane and then dried under N_2. The functionalised BIBB APTES initiator glass slides were also cut down into small pieces to enable the characterisation of the samples with different surface analysis techniques, including SE, XPS, AFM, and WCA.

3.4.2 ATRP synthesis of PDMA brushes

The monomer 2 (-dimethylamino) ethyl methacrylate (DMA) (47.1 g, 50.5 mL) was dissolved in 50 mL DMF, in a round bottom 100 mL flask. The molar ratio of (DMA/DMF) was 1:1. The reaction mixture was stirred and deoxygenated for 20 min by filling with nitrogen gas to remove any oxygen dissolved in the solution. The HMTETA ligand (0.30 mL, 0.15 mmol) was then injected into the mixture, which was then deoxygenated for 10 min before 0.14 g (0.10 mmol) of the copper catalyst Cu (I) Br was added and the mixture deoxygenated for a further 10 min. BIBB-APTES (initiator-coated wafers) were then sealed tightly in carousel tubes and deoxygenated through three repeated cycles of vacuum evacuation followed by re-filling with nitrogen. The ATRP synthesis was carried out at 90 °C within a nitrogen environment. The monomer/catalyst solution (5.0 mL) was injected into each carousel tube. As soon as polymerisation was complete, the wafer was removed from the carousel tube and washed repeatedly with IPA and ethanol to eliminate any excess monomer or catalyst. The kinetics of dry PDMA brush growth at 90 °C in DMF were studied for the desired durations (from 10 min to 2 h). The thicknesses of the different samples were characterised by SE, and the chemical compositions of the PDMA brushes were analysed through XPS.

3.4.3 ATRP growth of PDMA brushes from gold nanostructures

PDMA brushes were grown following the procedure described above, using Au-coated glass slides. For gold surfaces, the bis-disulfide compound DTBU was used as the initiator to adsorb onto the gold surface (instead of BIBB-APTES). This was done to take advantage of the strong gold-sulfur bonding of DTBU to the gold surface. However, the temperature was reduced from the normal 90 °C to 50 °C because the thermal stability of the DTBU initiator is reduced at higher temperatures, which could have led to decomposition or desorption of the initiator layer.

3.4.4 Quarterisation of PDMA brushes using alkyl halides

A 100 μM solution of 1-iodooctadecane in tetrahydrofuran (THF) was prepared, and the PDMA-coated slides were immersed in the solution for 18 h at room temperature. The quaternised PDMA samples were then taken out of the 1-iodooctadecane solution, rinsed with ethanol, and sonicated in THF for 10 min, before being dried under nitrogen gas. To determine the ideal conditions for maximum quaternisation, the same procedure was performed with various concentrations of alkyl halide.

3.4.5 Extraction of chlorophyll a from spinach

Baby spinach leaves (500 g) were removed from their stems and mid-veins. The leaves were cleaned with deionized water, dried with a paper towel, and placed in the freezer for 12 h. The frozen leaves were blended with 250 mL of acetone and the dark green pigment was separated by standard vacuum filtration, before being placed in a rotary evaporator under reduced pressure to remove the acetone and water. The residual green solids were extracted with 150 mL of 40-60 °C petroleum ether and the organic layer was washed with 60 % methanol. The dark green chlorophyll a pigment was obtained from the extract by drying with anhydrous $MgSO_4$, followed by filtration. The solvent was then removed by a rotary evaporator under reduced pressure.

3.4.5.1 Separation of pheophytin a and conversion into Zn-chlorophyll a (ZnChla)

The green chlorophyll a pigment was dissolved in 25 mL of acetic acid and stirred for three h at room temperature. The pH of the solution was then carefully adjusted to 7 by adding a saturated aqueous sodium hydrogen carbonate solution. This solution was extracted with 150 mL of DCM, washed with 90 mL of water, and the organic layer dried with $MgSO_4$. The solvent was then removed using a rotary evaporator to leave a brown solid containing pheophytin a. The pheophytin a was then purified through column chromatography using a solvent mixture of petroleum ether, diethyl ether, and acetone in the ratio 6:3:2. The formation of pheophytin a was confirmed with MS and NMR.

The pheophytin a was dissolved in 35 mL dichloromethane and a saturated solution of 0.25 g zinc acetate dihydrate dissolved in 4 mL methanol, then added. The solution was refluxed at 35°C under argon for 2 h, during which time a dark blue-green could be observed to precipitate from the dark brown solution. The organic layer was extracted with 40 mL diethyl ether, washed with water three times, dried with $MgSO_4$, filtered, and the solvent removed, as described previously. The resulting ZnChla was characterised by UV-VIS spectroscopy, NMR, and MS.

3.4.6 Synthesis of gold nanoparticles (AuNP)

All glassware used in the procedures was first cleaned in piranha solution. In a conical flask, 50 mL of 0.25 mM $HAuCl_4$ was heated to boiling on a magnetic stirrer hotplate, while 0.5 mL of 1% trisodium citrate was very slowly added dropwise while stirring continuously. After 25 s the colour changed from colourless to yellow, and finally to a deep red/purple colour, indicating the successful formation of gold nanoparticles. The solution was left at boiling temperature for a further 15 min before being removed to cool and kept refrigerated in a clean brown glass container at 8 °C until required. Nanoparticles with varying sizes can be obtained using this method, by controlling the concentration of sodium citrate (the most common reducing agent used in the synthesis of Au NPs). Nanoparticles of different sizes were prepared in this way and characterised by UV-Vis spectroscopy and AFM.

3.4.7 Synthesis of hollow gold nanoprisms (HGN)

The synthesis of hollow gold nanoprisms (HGNs) requires two steps. The first is the production of 3-6 nm diameter silver nanoparticles that act as silver "nano-seeds", and the second is the production of HGNs using sacrificial galvanic replacement.

Silver nano seeds were prepared by adding 0.5 mL of 0.01 M $AgNO_3$ dropwise to 20 mL of Milli-Q (18 M-cm) water under continuous stirring, and with the gradual addition of a 0.025 M solution of trisodium citrate (TSC). After the TSC had been added, 60 µL of 0.1 M ice-cold $NaBH_4$ stock was added dropwise at a rate that took exactly 10 s to complete, and while continuing to stir. The solution gradually turns yellow as the silver nano-seeds begin to form. This seed solution was then kept undisturbed in the dark for 2–3 h to allow the growth process to continue. For the second step, 2 mL of 0.01 M $AgNO_3$ solution was added dropwise to 0.49 g of cetyltrimethylammonium bromide (CTAB) dissolved in 45 mL of water, under continuous stirring. A 0.01 M solution of $HAuCl_4$ was then added dropwise to 300 µL of water, resulting in the solution turning brown, after which 320 µL of 0.1 M ascorbic acid was added dropwise, returning the solution to colourless. $HAuCl_4$ followed by ascorbic acid (AA) was then added to the colourless solution in quick succession. Immediately afterward, different quantities of seed solution were added to the growth solutions.

3.4.7.1 Modification of HGN surfaces with polystyrene sodium sulphonate (PSS)

A 5 mL solution of hollow gold nanoparticles was centrifuged at 8000 rpm for 15 minutes to remove excess cetyltrimethylammonium bromide surfactant. The resultant material was subsequently rinsed in 2.5 mL of water. While gently stirring, 2.5 mL of a polystyrene sulfonate stock solution and 25 µL of a 10 mM sodium chloride solution were incorporated into the centrifuged HGN solution. The combination was allowed to react overnight and subsequently recentrifuged to remove any extra of PSS. The resultant residue was subsequently dispersed in water for further analysis and characterisation.

3.4.8 Synthesis of silver nanoparticles

Silver nanoparticles (AgNPs) were synthesised by adding a mixture of 25 mL of 0.06 M sodium hydroxide and 25 mL of 0.0288 M hydroxylamine hydrochloride to a clean, covered conical flask containing 450 mL of 0.001 M Ag. The resulting reaction, which took approximately 15 minutes to complete, produced a milky tan-colored colloidal solution. To prevent light degradation of the colloidal solution, the conical flask was covered with foil and stored in the fridge for 24 hours before use.

3.5 Surface fabrication

3.5.1 Formation of polycrystalline gold film

After piranha cleaning, the glass slides were carefully washed with deionized water and subsequently dried in an oven overnight at 80 °C for 24 h. Metal films were evaporated onto clean glass slides mounted on an Edwards Auto 306 thermal evaporator (Edwards, Crawley, UK), see Figure 3-1**.** The coating systems were filled with two metal sources, chromium (Cr) and gold Au, in separate tungsten source boats. There was an evacuation of the system to a pressure of less than 3 x 10^{-6} mbar and as close as possible to 8 x 10^{-7} mbar. A current was then supplied to the boats to achieve a deposition rate of 0.1 nm/s. At this deposition rate, Cr usually deposits to a thickness of 3-5 nm and Au to 20-40 nm. The layer thicknesses and deposition rate were measured with a quartz crystal microbalance (QCM) thickness monitor, and the current gradually lowered once the required thicknesses had been reached. Following deposition, the samples were allowed to cool for at least 30 min, and nitrogen was admitted into the system. The Au and Cr thicknesses for this experiment, were typically 3 nm and 40 nm, respectively. The samples were cut into smaller pieces (~ 2 cm x 2 cm) using a diamond-tipped scribe and then immersed for 18 h in a solution of DTBU initiator dissolved in ethanol. Following immersion in DTBU, the gold-coated slides were carefully removed from the solution using tweezers to avoid contamination, rinsed with ethanol, and dried under nitrogen. They were then stored in degassed ethanol in glass tubes and kept refrigerated until needed. SE was used to determine the thicknesses of the Au, Cr layers, and the DTBU initiator.

Figure 3-1: The Edwards auto 306 vacuum coating system for depositing thin films and coatings onto substrates under controlled vacuum conditions.

3.6 Surface modification

3.6.1 The incorporation of Au NPs into APTES films

APTES-functionalised glass slides were immersed into the AuNPs suspension for the desired immobilisation time and in the dark at room temperature. Two different concentrations of gold nanoparticles were used in this experiment, saturated (as prepared) and diluted 1:1). After immersion, the samples were washed with deionized water and dried with N_2. Sample characterisation was performed using UV-Vis spectroscopy and AFM.

3.6.2 Attachment of ZnChla to PDMA brushes and q-PDMA

Different concentrations of ZnChla in a 1:3 DMF: H_2O mixture from 1 to 60 μM were used to functionalise the PDMA brushes. The brushes were immersed overnight in ZnChla solutions in a dark environment at room temperature. They were then washed with deionized water and dried in a nitrogen stream. The ZnChla-functionalised PDMA was characterised by XPS, UV-Vis spectroscopy, SE and AFM.

3.6.3 Attachment of ZnChla to AuNP-functionalised PDMA brushes

ZnChla was attached to the AuNP-functionalised PDMA brushes by immersion in ZnChla solutions for the desired immobilisation time, in the dark at room temperature. They were then rinsed in deionized water and dried in a nitrogen stream. XPS, AFM, SE and UV-Vis spectroscopy were used to characterise ZnChla-functionalised systems.

3.6.4 DTBU-functionalised polycrystalline gold films

The Cr/Au-coated glass substrate was immersed in DTBU-degassed ethanol in a 2 mM solution. To form a bromine-terminated initiator monolayer, the reaction was conducted in the refrigerator at 4 °C for 18 h. Following removal from the solution, the slides were rinsed with ethanol and dried with nitrogen. The same procedure was employed to functionalise Au nanoarray samples with DTBU.

3.6.5 The formation of mixed monolayers through self-assembly

The Cr/Au-coated silicon substrates were cut washed with ethanol and subsequently dried under a stream of nitrogen. After degassing the ethanol with nitrogen for 1 hour, ethanolic solutions were prepared with various molar ratios of bis[2-(2-bromoisobutyryloxy) undecyl] disulfide (DTBU) and 11-mercapto-1-undecanol (MUL) to obtain a total concentration of 2 mM. A similar procedure was used to fabricate single-component monolayers, with an adsorbate at a concentration of 2 mM. The slides were then immersed in the solution for 24 hours at a temperature of 4 °C. Finally, the slides were subsequently washed with ethanol and dried using a nitrogen stream.

3.7 Surface characterisation

3.7.1 Water Contact Angle Measurements

Water contact angle (WCA) measurements provide a qualitative tool for investigating various surface properties, including wettability, liquid surface tension, surface heterogeneity, and solid surface energy.[196] In particular, when a drop of liquid is placed on a flat solid surface, it spreads until it reaches equilibrium. The contact angle (θ), which can range from zero to 180°, depends on the characteristics of both the liquid and the solid surface.[197] The contact angle is defined as the angle between the surface and the tangent to the liquid surface at the three-phase boundary, as shown in Figure 3-2, In 1805, Thomas Young *et al.*[198] began studying the wettability and contact angle of surfaces. The relationship between the contact angle and the interfacial tension (surface energy) can be described by "Young's equation":

$$\gamma_{SV} = \gamma_{SL} + \gamma_{LV} \cos\theta \qquad \text{(Eq. 3.1)}$$

where (θ) is Young's contact angle, γ_{LV}, γ_{SL}, and γ_{SV} are the surface free energies of the liquid-vapor, solid-liquid and solid-vapor interfaces, respectively. This equation, known as Young's equation, applies to surfaces that are smooth, rigid, chemically homogeneous, and inert.[199] A solid surface is referred to as "hydrophilic" when the contact angle of the water droplet is less than 90 degrees, suggesting that the surface has a high surface energy and is easily wetted by water. In contrast, a surface is referred to as "hydrophobic" when the contact angle is greater than 90 degrees,[200] suggesting that the surface has a low surface energy and is difficult to wet with water, as shown in Figure 3-3.

Ultra-hydrophobic surfaces have minimal contact between a droplet and the surface and exhibit contact angles greater than 150 °.[201] The surface tension of the liquid controls the shape of the droplet. [202] For example, using the same glass substrate with three different liquid drops, such as water, mercury, and silicone oil, exhibit three different contact angle values due to their different surface tensions.[197]

Experimental procedure: Contact angles were measured using a Rame-Hart model 100-00 goniometer (Netcong, NJ, USA). The contact angle goniometer contains a sample stage for placing the substrate, a syringe for applying the liquid, and a light source for illuminating the droplet, which is examined using a magnifying microscope. Drops of liquid (2 µL) were placed on the sample surface by using a microlitre syringe containing deionized water (18.2 Ω). The syringe was carefully positioned above the sample surface, allowing an extruded droplet of water to make contact, and then retracted to leave a droplet on the surface. The contact angle was measured using a telescope equipped with a goniometer and measured from the right and the left sides, after setting the baseline parallel to and consistent with the drop line's contact with the surface. The contact angle was taken as the mean of at least three different measurements on the same sample.

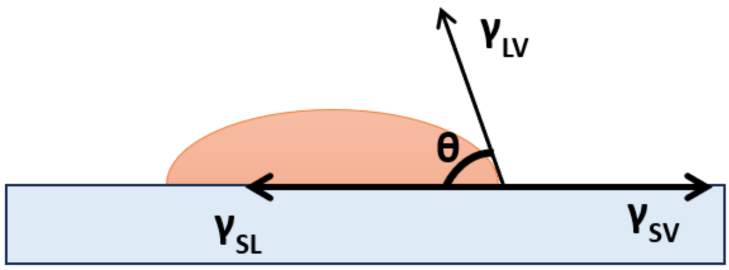

Figure 3-2: Schematic illustration of the definition of contact angle on the liquid/solid interface, with surface free energies of the liquid-vapor γ_{LV} ,solid-liquid γ_{SL} and solid-vapor γ_{SV}.

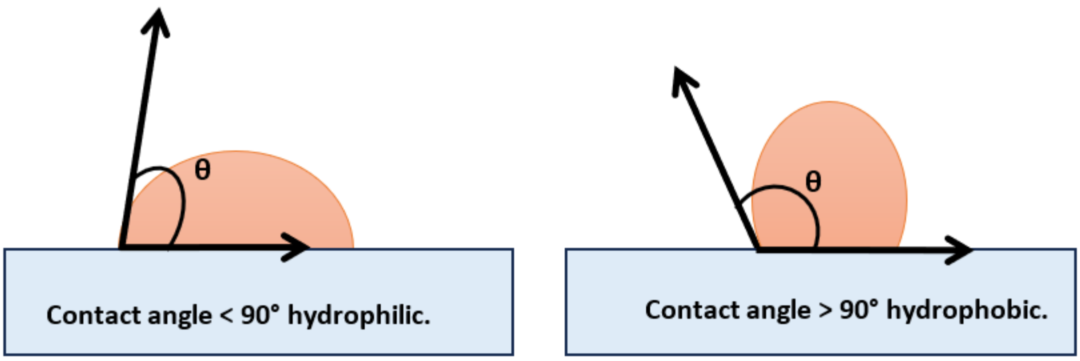

Figure 3-3: Schematic description of the hydrophilic surface (left) and the hydrophobic surface (right).

3.7.2 Ultraviolet-Visible Spectroscopy

UV-Vis spectroscopy (UV-Vis) is a powerful quantitative method for determining the absorbance of a substance as a function of wavelength.[203] This technique applies to absorption or reflectance spectroscopy within the 200-800 nm range of the electromagnetic spectrum and is commonly used for analysing the optical and electrical structure of metal nanoparticles. Molecules with π-electrons or non-bonding electrons exhibit electronic transitions when exposed to light within this range, causing an electron to transfer from the ground state to an excited state. For metals exhibiting a plasmon-resonance band, such as gold, silver, and copper, the intensity and position of the band during the formation of the solution can serve as an analytical instrument for determining metal particle size.[204, 205] This analytical method depends on the four main components of a spectrophotometer: the light source, monochromator, sample holder, and detection system, as shown in Figure 3-4. Commonly used light sources include tungsten and deuterium which can cover the UV and visible spectrum from 190 to 900 nm.[206]

Plasmon resonance occurs from the oscillation of free conduction electrons generated by interactions with electromagnetic radiation. The SPR band is observed in the 400-600 nm range, depending on the metal, with larger particle sizes resulting in a red shift and greater particle distribution leading to band broadening. Particle size is not the only factor that impacts plasmon resonance; additional parameters such as solvent and surface functionalisation also influence the precise frequency and strength of the band.[207] The operation of a UV-Vis spectrophotometer is straightforward. The light beam from the source passes through the monochromator which contains a prism and a wavelength limiter to select a specific wavelength. This wavelength can be precisely tuned and scanned across the desired range. The light that passes through the sample is then collected by the detector. Most spectrophotometers are used to examine the transmittance spectra and absorption of substances and typically cover a spectral range from 190 to 1100 nm. Within the UV-visible spectral region, three sub-regions are designated: the visible region (400 to 700 nm), the near-infrared (NIR) region (700 to 1100 nm), and the near UV region (185 to 400 nm).[208] When light passes through a thin film or a translucent liquid sample, some of the light is absorbed.[209] The Beer-Lambert law is used to determine the absorbance A at a particular wavelength, according to the following equation:

$$A = \varepsilon l c \qquad \text{(Eq. 3.2)}$$

where A is absorbance (unitless, absorbance unit AU), ε is the molar absorptivity (also termed the molar extinction coefficient) with the unit, (L $mol^{-1}cm^{-1}$), c is the molar concentration of the sample in solution in the unit (mol L^{-1}), and l is the path length of the sample in cm.[208] To determine the molar extinction coefficient, the route length must remain constant while the analyte concentration is changed. The graph of absorbance versus concentration will then produce a slope equivalent to the molar absorptivity (ε).

The transmittance (T) is the ratio of the transmitted light intensity (I) to the incident light intensity (I_0) at a specific wavelength. The percentage transmittance (T %) is defined as

$$T\% = I/I_0 \times 100 \qquad \text{(Eq. 3.3)}$$

The absorbance (A) of a sample is equal to the negative logarithm of the transmittance, while the term extinction refers to the total reduction of intensity, which includes losses from both scattering and absorption.[210]

Experimental procedure: The UV-visible absorption spectra were measured using the Cary 50 UV-visible spectrophotometer (Agilent Technologies, USA) at a scan range from 350 to 800 nm. For liquid and solid measurements, a reference sample was measured to establish a baseline before the samples themselves were placed in the cuvette and measured. Solid samples, such as the gold nanoparticles or dyes deposited in glass substrates, were measured using a homemade PTFE sample holder to ensure measurements were taken from the same area of the surface during all experiments (see Figure 3-5). Furthermore, the location of the gold nanoparticles' LSPR peak and strong coupling behavior had both already been investigated using a UV-visible spectrophotometer.

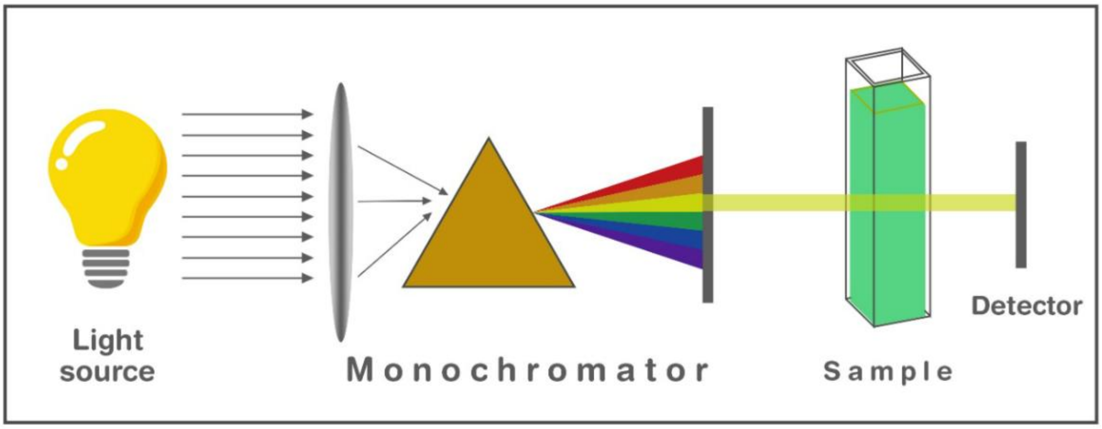

Figure 3-4: The basic components of UV-Vis spectroscopy, which include a light source, monochromator, sample and detector.

Figure 3-5: A home-made PTFE sample holder with chlorophyll a embedded into the PDMA sample.

3.7.3 Spectroscopic Ellipsometry

Spectroscopic ellipsometry (SE) can be considered a contactless and non-destructive optical technique used for measuring the thickness of thin films. In 1945, Rothen coined the term "ellipsometry" to describe an optical instrument that uses reflected light to measure thin films on solid surfaces.[211] This technique involves illuminating the sample with elliptically polarised light, making it possible to measure film thicknesses ranging from less than a nanometre to several micrometres.[212] SE can determine surface roughness and other material properties of thin films, as well as their thickness. Through the use of polarised light, this technique analyses transmission, refraction, and reflection from a surface and compares the results with previously modelled data.[211, 213] Measuring changes in light polarisation, specifically the amplitude (Ψ) and phase difference (Δ), enables the technique to be used to measure material properties such as the complex refractive index and the thickness of thin film materials. The technique is only suitable for reflective samples.[214] The setup for ellipsometry includes five fundamental elements: a light source, a rotary analyser, a polariser, a photodetector and a quarter-wave compensator.[215, 216,226] The polarised light passes through a compensator before hitting the sample at a specific angle (Φ). After interacting with the sample, the light then passes through a second compensator and a rotary analyser before reaching the photodetector. The setup of spectroscopic ellipsometry is illustrated in Figure 3-6.

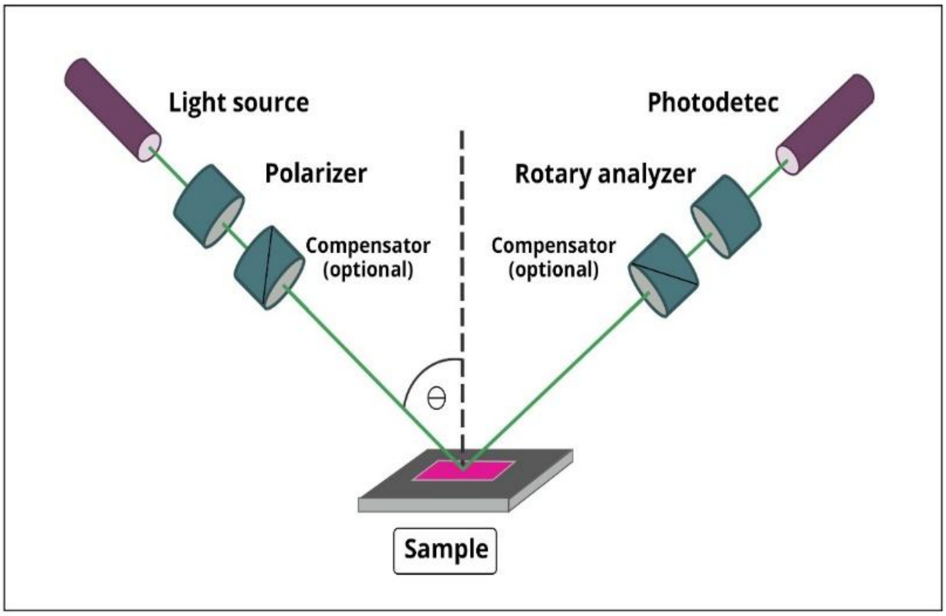

Figure 3-6: Schematic illustration of the setup for spectroscopic ellipsometry contains a light source, analyser, polariser, photodetector, and quarter-wave compensator, which assess reflected light, polarisation, intensity, and phase shift.

The two parameters—the reflective coefficients ψ and Δ—determined by an ellipsometer are dependent on the complex refractive index of the material. To derive sample properties such as film thickness from the acquired SE data, an optical model must be constructed to be consistent with the data. The Complete EASE program offers a graphical user interface for model design, data display, and model fitting for SE data. A theoretical model frequently employed to analyse ellipsometric data for semiconductors and dielectrics is the Cauchy model, which facilitates the determination of optical properties, such as the complex refractive index and the thickness of specific layers within a specified structure. A crucial aspect of a substance forming thin layers is that its optical characteristics differ from those of the same substance in its bulk material state. To accurately characterise thin films requires, therefore, the sophisticated modeling of SE data.[214] By measuring how the polarisation of light changes after reflecting off a sample, SE provides detailed information about the sample's optical properties and thickness, making it a valuable tool in materials science and engineering for characterising thin films.

Experimental procedure: SE measurements were conducted using either BIBB-APTES self-assembled monolayers (SAMs) on glass or silicon substrates, or DTBU SAMs on thin gold films. For the ellipsometry experiments, all measurements were performed with an Alpha-SE ellipsometer (J. A. Woollam Co., Lincoln, NE, USA). A He-Ne laser with a wavelength of 633 nm was used as the light source, and the angle of incidence was set at 70°.[212] Ellipsometric data fitting was done using WVASE software (J. A. Woollam Co., USA), and the root mean square error (RMSE) was calculated over all measured wavelengths to assess the quality of the fit between the measured and modelled ellipsometric constants. The glass substrate was modelled with a single layer of PK7, while the silicon substrate was modelled as SiO_2 on top of a silicon layer. The Cauchy model was applied to the PDMA layer and the BIBB-APTES films, with values determined by fitting data collected for a 30 nm dry thickness of the PDMA brush. Modeling of the SE data for chlorophyll-a (Chl *a*) incorporated into PDMA brushes was performed using the Complete Ease software (J. A. Woollam Co.) to extract the optical properties and thickness of the PDMA brush. For the PDMA and Chla-functionalized PDMA brushes, the ellipsometry data were analysed using a layer stack model, including the brush/dye-functionalised brush layer (of unknown permittivity), as well as the Si substrate and its native SiO_2 layer, and the Cr and Au layers, whose dielectric functions are either well-known or have been previously established. These dielectric functions were fixed during the modeling process. Measurements were conducted at three different angles of incidence at 55°, 60°, and 65° within the wavelength range of 250 nm to 800 nm. Three different spots on each sample were measured, and the results presented are the average of the three measurements. The following requirements should be considered during the SE measurements: First, data should be collected at inclined incidence angles. Second, the sample should have a small degree of surface roughness.[212]

3.7.3.1 Variable angle spectroscopic ellipsometry

Variable angle spectroscopic ellipsometry (VASE) is a powerful and versatile analytical technique for the research of new materials and processes. Ellipsometry, in general, is a highly accurate and repeatable technique, that stands out from most other analytical techniques by not requiring a reference material against which to compare a sample's properties, because it measures the ratio of two values. Ellipsometry is extremely sensitive to the presence of coatings, even those as thin as a few microns, as it detects both phase changes and amplitude ratios. Additionally, ellipsometry measures multiple parameters of the film at the wavelength of interest. VASE enhances the spectroscopic capability by varying the incident angles, which allows different optical paths to be traversed and provides valuable additional information. The use of multiple incidence angles optimises the sensitivity to unknown parameters, thereby increasing the quantity and quality of the data obtained. VASE uses the variable incident angles to collect ellipsometric data,[217] as shown in Figure 3-7. Through VASE analysis, many material parameters can be extracted, including surface and interfacial roughness, optical constants, and layer thickness. The technique is particularly useful for studying novel materials and processes. Data collected from VASE is both accurate and sufficiently rich to enable interpretation with sophisticated instruments and software, making it suitable for advanced research. Despite its advanced capabilities, VASE is also straightforward enough for standard measurements and applications.[217]

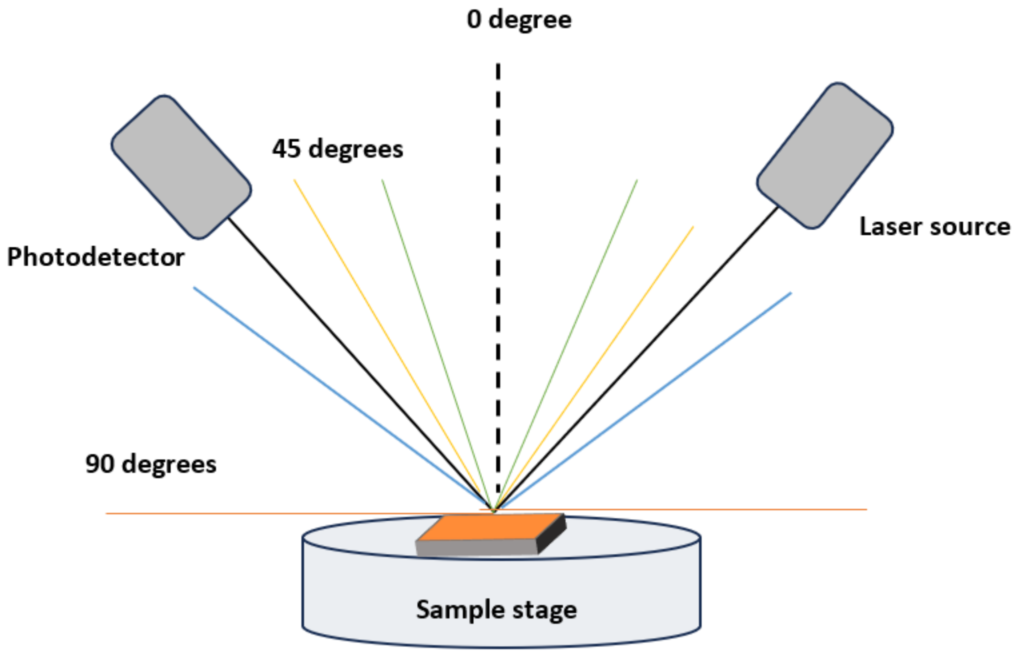

Figure 3-7: Schematic illustration of Variable angle spectroscopic ellipsometry.

3.7.4 X-ray photoelectron spectroscopy

One of the most widely used surface analysis techniques is X-ray photoelectron spectroscopy (XPS), also known as electron spectroscopy for chemical analysis (ESCA). It was invented by Kai Siegbahn in the 1960s.[218] XPS utilizes the photoelectric effect to determine the chemical composition of a material's surface, both qualitatively and quantitatively. As illustrated in Figure 3-8, an XPS system consists of an X-ray source, an electron energy analyser that quantifies electron energy distributions, a detector (usually a channel electron multiplier), and a vacuum system. The photoelectrons are often collected by a concentric hemispherical analyser (CHA), which employs electrostatic lenses to allow photoelectrons of different energies to reach the detector. The system operates under ultra-high vacuum (UHV) conditions, typically at around 10^{-10} mbar to prevent electron scattering and the absorption of residual gas molecules by the sample.[219] X-rays are generated by an electron beam pointed at an anode, producing a concentrated beam of X-rays with specific energy determined by the source material, (commonly Mg Kα (1253.6 eV) or Al Kα (1486.6 eV)).[220] X-rays with adequate energy can exceed the binding energy of electrons in atoms, resulting in the ejection of photoelectrons from the core shells of the sample atoms. The electrons emitted from the sample's surface are then collected by an electron energy analyser and an electron detector. These photoelectrons are collected and analysed based on their kinetic energies (KE), established by the X-ray energy and the binding energy (BE) of the orbital from which they are emitted. The (BE) of the electron can be determined by using the following equation:

$$\mathrm{E} = h\upsilon - \mathrm{KE} - \varphi \qquad \text{(Eq. 3.4)}$$

where φ is the spectrometer work function and hυ is the X-ray photon energy.[221] The binding energies of electrons ejected from various atomic orbitals, such as s, p, d, etc., have distinct binding energies, which are influenced by the chemical bonding and the local environment around the atom. This means that the BE of an electron depends on several factors: the type of atom from which it is ejected, the specific orbital (s, p, d, etc.) the electron comes from, the atom's chemical environment, and its oxidation state. The diagram of energy levels is displayed in Figure 3-9. XPS is particularly advantageous for determining the chemical environment of atoms within a sample. The chemical environment affects photoelectron peaks, including the influence of neighboring atoms and the oxidation state of elements.[222, 223] For instance, the binding energy of C 1s electrons is highly dependent on the electronegativity of adjacent atoms. As the electronegativity of a neighboring atom increases, so does the binding energy of the C 1s electron. This trend allows XPS to distinguish between chemical states such as C-C, C=O, and C-O (see Table 1-3 for common C 1s binding energy states).[219] In XPS, all chemicals on the surface of a sample can be detected except hydrogen and helium, since they share electrons very rarely with other elements and have very small photoelectron cross-sections.[224]

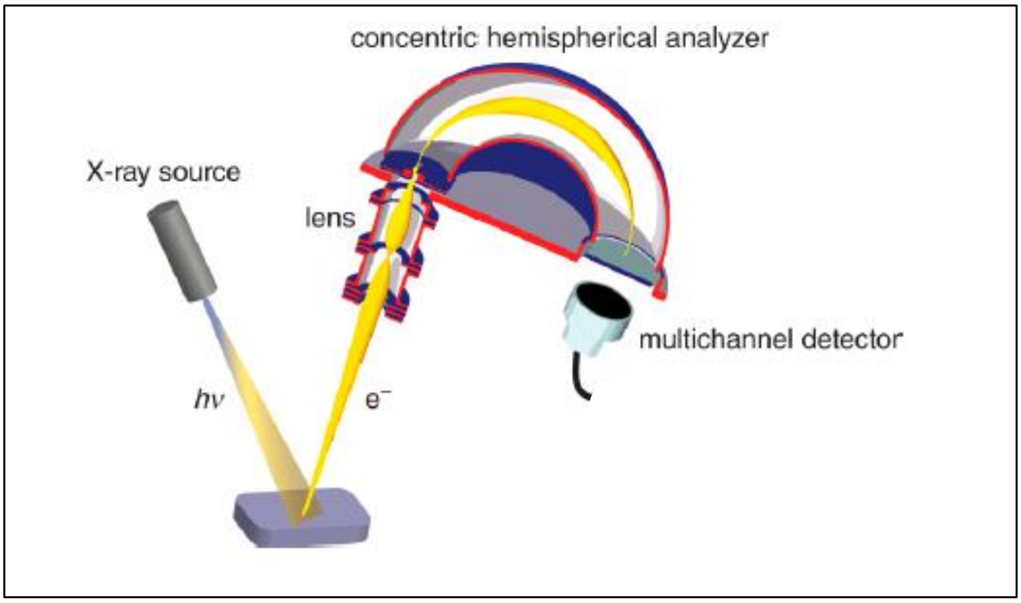

Figure 3-8: Schematic illustrates the setup of X-ray photoelectron spectroscopy including an X-ray source, photoelectrons, a concentric hemispherical analyser, and a detector.[223]

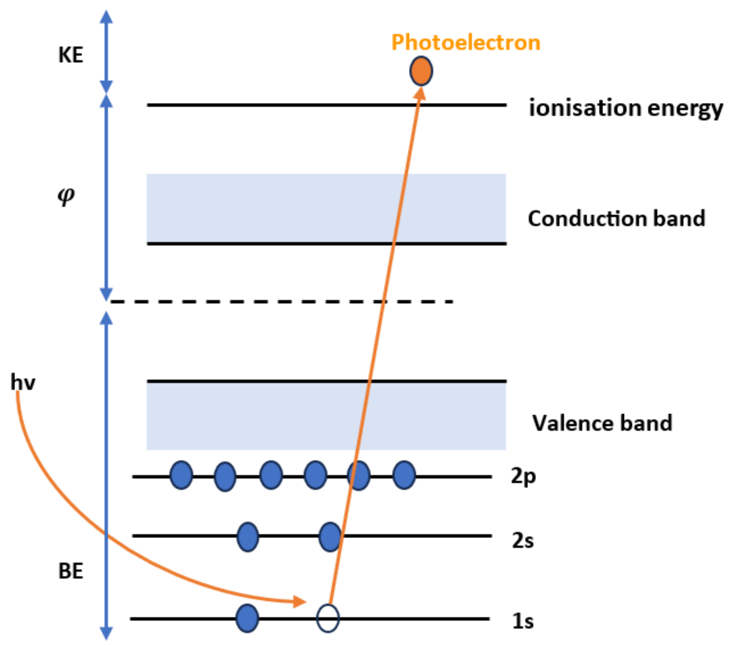

Figure 3-9: Schematic of the energy level explanation of the photoemission effect caused by an incident X-ray. The arrows show the emission of a photoelectron from the 1s orbital of an atom, KE, BE, and Φ refers to the kinetic energy, binding energy, and work function, respectively.

Table 3-1: Common C 1s binding energies (BE) of organic materials.[219]

Function Group	Structure	BE (eV)
Hydrocarbon	C—C	285.0
Ether	C—O	286.5
Carbonyl	C=O	288.0
Carboxylic Acid	COOH	289.2

The XPS spectrum is generally presented as a graph showing the binding energy of electrons against the intensity of photoelectrons. A particular set of binding energies is specific to an element. XPS is valuable for analysing sample composition by examining peak regions and photoemission cross-sections. The binding energy includes chemical information about the oxidation state, as the energy levels of core electrons are significantly affected by the atom's chemical condition. There is generally a direct correlation between the heights of peaks in an XPS spectrum and the number of photon-emitting atoms near the sample surface; however, the binding energy of specific peaks is strongly affected by atoms' local environments and chemical oxidation state.[225]

Experimental procedure: A Kratos Axis Supra spectrometer (Kratos Analytical, Manchester, UK) was employed for the experiments using X-ray photoelectron spectroscopy. This apparatus features a monochromatized Al Kα X-ray source operating at 150 W with an emission current of 8 mA, with a pressure measurement in the analysis chamber ranging from 10^{-8} to 10^{-10} mbar. Furthermore, electron energy analyser pass energies were employed to acquire high-resolution spectra (20 eV) and wide scans (160 eV). This scanning method provides overall information about composition, while a focused scan can reveal data regarding the molecular bonding environment at the surface level. The samples, measuring approximately 5×5 mm², were subsequently washed in ethanol and dried with dry nitrogen before XPS examination. The CasaXPS software (Casa, http://www.casaxps.com, U.K.) was employed to analyse all the peaks. The binding energies of all components were calibrated at 285.0 eV to the binding energy of primary hydrocarbon C1s. The elemental compositions of the samples were determined by analysing the photoelectron peaks in the corresponding regions and removing a background signal using a Shirley-type method.

3.7.5 Atomic Force Microscopy

AFM was invented in 1986 by Binnig, Quate, and Gerber based on the development of scanning tunneling microscopes (STM), which were primarily used for evaluating conducting materials. [226] Unlike STM, AFM can measure both conducting and non-conducting samples, which makes it a powerful tool across different fields such as chemistry, physics and biology. AFM operates by detecting the forces experienced by a probe's tip as it approaches the sample surface. These forces arise from several interactions, such as magnetic, electrostatic and van der Waals forces.[227] As the cantilever moves closer to the sample, changes in these forces cause the cantilever to deflect. This deflection is measured by an optical system. It is assumed that the cantilever behaviour as Hooke Spring. Thus, the force is related to deflection by Hooke's law which is used to demonstrate how force is measured between the tip and surface. [228]

$$F = -k \times x \qquad \text{(Eq. 3.5)}$$

where F is the force applied to the cantilever, k is the cantilever's spring constant and x is the deflection of the cantilever from its equilibrium point. A lower spring constant results in a greater deflection for a given force, allowing AFM to detect even very small forces. As the cantilever deflection depends on the spring constant. AFM systems consist of four key components: a cantilever with a sharp tip for probing the surface, a piezoelectric scanner to control sample movement, a photodetector to measure deflections, and a laser beam that reflects off the cantilever. The deflection of the cantilever is tracked by the photodetector.[229, 230] Additionally, a feedback system to maintain a consistent force between the tip and the surface. Figure 3-10 displays a schematic representation of an atomic force microscope setup, where the laser beam is directed at the rear of the cantilever. As the probe scans the surface, the interaction between the tip and the sample alters the laser's deflection, which is then captured by the photodetector. A feedback system adjusts the probe's position to maintain a constant interaction force between the tip and the sample surface. The tip of a scanning probe moves across the surface of a sample to analyse local properties such as magnetic properties, topography, friction, and electrical conductivity.[230, 231]

AFM tips are commonly made from either silicon or silicon nitride, each offering specific features and benefits for different applications. Silicon tips have a relatively soft surface and can be fabricated in various shapes and sizes, making them suitable for multiple AFM imaging techniques. Their versatility allows for use in a wide range of experiments, as they are compatible with diverse sample surfaces. However, due to their low mechanical strength, silicon tips may quickly wear out or break during use. In contrast, silicon nitride tips are stronger and more durable, providing better resistance to wear and breakage. This makes them ideal for high-resolution imaging of hard materials like ceramics or metals, particularly in contact and tapping mode. Despite their advantages, silicon nitride tips may be less suitable for fragile or soft samples, as they can cause more damage compared to silicon tips.[232] The movement of the AFM probe is controlled by a piezoelectric scanner, which allows motion in the X, Y, and Z axes, enabling a full scan of the sample surface. The scanner typically consists of a piezoelectric material, such as lead zirconate titanate (PZT), placed between two electrodes. When voltage is applied to the electrodes, the piezoelectric material deforms in a controlled manner, moving the scanning probe. To measure the cantilever's deflection, a laser beam is directed at its backside, and the reflected beam is detected by a position-sensitive photodiode (PSD). The position of the reflected beam on the PSD corresponds to the deflection of the cantilever, and this positional data is used to reconstruct the surface topography. Additionally, a feedback system, which includes control electronics, uses the PSD data to adjust the scanner's position, ensuring continuous contact between the tip and the sample while maintaining a constant force. During the scan, the data collected by the AFM is processed by software, which controls the instrument. This software generates high-resolution images of the sample surface, measures surface height and morphology, and provides additional sample information.[232]

The AFM produces a three-dimensional surface profile. As the shape of the probe influences the lateral dimensions, height measurements provide a precise and accurate measurement of nanoparticle height. Assuming spherical particles, the height measurement corresponds to their diameter or size.[233] Moreover, the height image can also be used to determine the roughness, patterns, and morphology of a material's surface. There are three main modes of AFM imaging: tapping, contact, and non-contact. In non-contact mode, the probe oscillates near the surface without touching it, typically at or near its resonance frequency. In contact mode, the tip remains in direct contact with the surface as it scans. However, contact mode can potentially damage soft surfaces. Tapping mode provides a compromise, where the tip intermittently contacts the surface, reducing lateral drag forces that can cause damage in contact mode. The tapping mode is considered a more efficient imaging technique in air, especially for soft samples. It provides a resolution comparable to contact mode but applies lower forces to the samples, resulting in a less damaging process. Nevertheless, the tapping mode presents two drawbacks in comparison to the contact mode: a slightly reduced scanning speed and a more intricate operation of AFM. The technique enables images of the surface topography to be computed using a feedback loop that corrects amplitude deviations.[234 235] By increasing the oscillation, the deflection signal becomes sufficient to serve as input to a control circuit, resulting in better levels of control over the topographical feedback.[232 236]

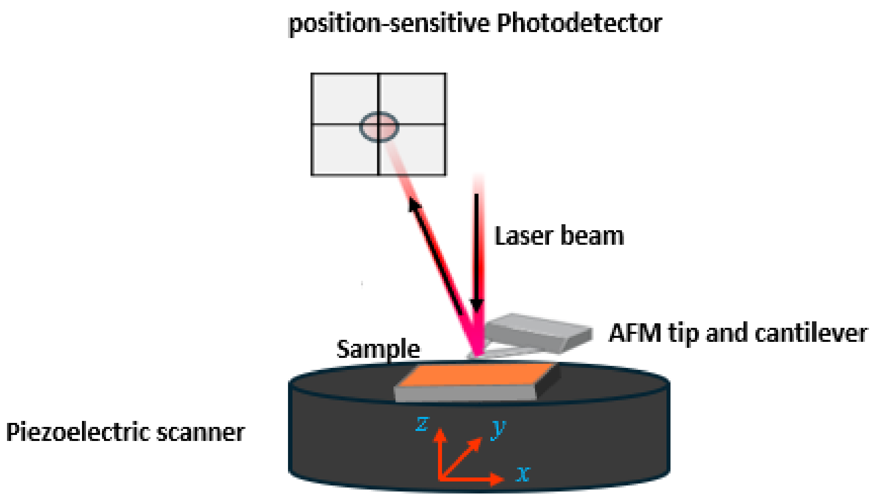

Figure 3-10: Schematic illustration of the setup for AFM, showing a probe tip on the cantilever near the sample surface.

Experimental procedure: AFM measurements were conducted using an Ambient AFM/MFM (Nanomagnetics Instruments, Ankara) at room temperature with a rectangular silicon cantilever (length 225 µm, force constant 48 N/m). The cantilever oscillated at approximately 300 kHz, with a spring constant of 17.5 N/m. Images were acquired at a resolution of 512 lines per image and a scanning frequency of 0.996 Hz in tapping mode. Before analysis, samples were rinsed with ethanol and dried using nitrogen. Carbon tape was used to attach the samples to a magnetic disc, which was positioned on the head of the scanner. An optical video stream from the microscope was utilised to ascertain the precise location of the sample, and a cantilever was aligned above it. Consequently, the laser was placed at the end of the cantilever. The horizontal and vertical positions of the reflected laser point on the photodiode were adjusted to the designated values (0, 0 for tapping mode). Utilising this tapping method, pictures of phase and height were acquired. The data was evaluated using NanoScope Analysis tools, with the images potentially revealing information on pattern and non-pattern structures, surface roughness, and polymer thickness.

3.7.6 Transmission electron microscopy

Transmission electron microscopy (TEM) is a powerful imaging technique for examining the morphology, chemical composition, and structure of many types of material, and enables samples to be viewed with sub-Angstrom resolution.[237] TEM is used to image the ultrastructure of a wide range of inorganic and biological samples, including metal nanoparticles, crystals, and large molecules. It can be considered a quantitative method for determining the shape and size of particles and their distribution. Louis de Broglie discovered that electrons behave like waves as well as particles, which led to the development of electron microscopes - the term first used by Knoll and Ruska.[238] Transmission electron microscopes have five basic components: an electron source, a sample holder, a condenser system, projector lenses, an objective lens, and lastly an imaging system for detecting the transmitted electrons, as shown in Figure 3-11.[239] The detector is placed directly below the sample from where it detects the electrons transmitted by the sample. The transition electron microscope incorporates a filament (or electron gun) that emits electrons, typically with energies of around 200 keV, from inside a vacuum column (at 10^{-5} mbar), which are then focused onto the specimen by a series of electromagnetic lenses (condenser lenses). The vacuum allows the beam to pass through without obstruction/ or interference from air molecules.[240]

How the beam of electrons interacts with the sample varies according to the thickness and atomic number of the elements present, resulting in some electrons being absorbed or dispersed. After sample engagement, the projection lenses distribute the beam onto a fluorescent screen. The specimen is displayed on this screen enabling it to be aligned manually and the beam to be focused. The microscope is equipped with a charged coupled device (CCD) camera that transforms electron intensity into a digital image. TEM employs two different methods to form the sample image – a bright field and a dark field. In bright field imaging mode, which was the predominant method used in the current study, the image is formed from the electrons that pass straight through the sample without interacting, to produce images after processing in which darker areas correspond to regions with greater sample thickness and/or constituent elements of greater mass, with areas devoid of any sample appearing bright. In dark field imaging mode, the image is formed from the electrons dispersed by their interaction with the sample, to produce an image that displays the sample as bright against a dark background.[240]

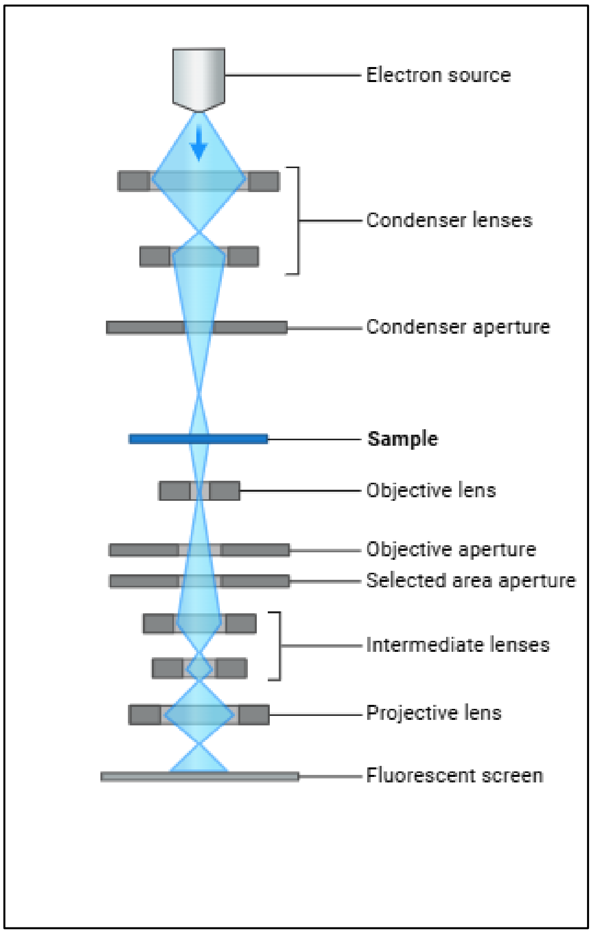

Figure 3-11: The components of a transmission electron microscope include an electron source, electromagnetic lenses, sample holder, and imaging system, which generate and accelerate electrons, focus and direct the beam, and convert signals into visible images respectively.

Experimental procedure: Samples for TEM analysis was produced by dispersing the catalyst powder in high-purity ethanol through ultrasonication. Fifty microlitres of suspension were deposited onto a holey carbon film attached to a 300-mesh copper TEM grid, then allowing the solvent to evaporate. A JEOL JEM 2100 transition electron microscope operating at 200 kV was used in the sample analysis, and particle size distributions were computed using ImageJ post-processing software. For each image, the scale bar was used as a reference to convert the length of the image to pixels per nanometre. The diameter of each particle was manually measured using the line tool, and the resultant metal particle size was recorded in an output file (Origin).

3.7.7 Mass Spectrometry (MS)

The pheophytin a and ZnChla were dissolved in acetone, containing about 5 mg each, and analysed using a Waters LCT classic ToF liquid-chromatography mass spectrometer for direct EI and LC-MS measurements. Additional information and results can be found in the related results section of subsequent chapters.

Analytical data of pheophytin a:

Rf =0.33 (6:3:1 hexane: diethyl ether: acetone); LC-TOF-MS ES+, observed. m/z = 872 (17.191 min). Calculated = 871.22 [$(M^+H)^+$, M=$C_{55}H_{74}N_4O_5$].

Analytical data of Zn-Chla:

Rf =0.37 (5:4:1 hexane: diethyl ether: acetone); LC-TOF-MS ES+, observed. m/z = 932.2 g/mol. Calculated = 934.57 g/mol [$(M^+H)^+$, M= $C_{55}H_{72}N_4O_5Zn$]. The MS of Zn-Chla can be found in Appendix 1.

3.7.8 Nuclear Magnetic Resonance (NMR)

A Bruker NMR spectrometer (Avance III HD) at 400MHz was used to collect ^{1}H NMR spectra of pheophytin a and *ZnChla*. Samples were prepared by dissolving approximately 5 mg in 5mL of chloroform-d and filtered before measuring.

Analytical data of pheophytin a:

1 H NMR (400 MHz, CDCl3) δ (ppm) = 9.40 (s, 1H, ring β-H), 8.85 (s, 1H, ring α-H), 8.58 (s, 1 H, ring δ-H) 8.02 (dd, J = 11.28, J = 5.97, 1H, vinyl, trans) 6.31 (d, J = 19.21 Hz, 1H, vinyl, cis) 6.22 (s, 1H, CH-$COOCH_3$) 6.18 (d, J = 9.16, 1H, vinyl), 5.14- 5.38 (m, H, aggregation) 5.15 (m, 1H, pythyl vinyl) 4.50 (m, 3H, CH_3) 4.46 (m, 1H, HC-CH_3), 4.31 (m, 2H, pythyl CH_2) 4.23 (br d, J = 7.71 Hz, 1H) 3.90 (s, 3H, $COOCH_3$), 3.71 (br s, 2H, CH2-CH_3) 3.71 (br s, 3H, methyl), 3.42 (s, 3H, methyl) 3.26 (s, 3H, methyl), , 2.83 (br t, J = 5.39, 2H)) 2.50- 2.64 (m, 2H), 2.19-2.36 (m, 2H), 1.90 (m, 3H), 2.08 (m, 3H) 1.82 (d, J = 6.29, 3H) 0.96-1.41 (m, pythyl CH_2), (m, pythyl vinyl, 2H)), 0.69-0.97 (m, pythyl $CHCH_3$) = 0.09, 1.60 (br s, 1H, NH).

Analytical data of ZnChla

ZnChla shows a similar NMR profile as pheophytin with broader peaks and a more pronounced shift from 9.45 to 9.6 (singlet, 1H, ring α-H), and from 9.5 to 9.7 (singlet, 1H, ring β-H). The NMR of Zn-Chla can be found in Appendix 1.

Chapter 4: Plexcitonic Complexes: Synthesis and Characterisation

4.1 Introduction

Over the past two decades, one of the greatest challenges has been to discover how to achieve efficient excitation transport over long distances in molecular and photonic materials. In molecular systems, exciton diffusion lengths are typically a few tens of nanometres in size, which significantly restricts the design of different devices. [241] Photosynthetic light-harvesting complexes (LHCs) in plants and bacteria have received significant attention as a model for effective exciton transfer in molecular systems. Peptide units within these *pigment-protein complexes,* arrange pigment molecules (chlorophylls and carotenoids) in highly specific configurations. These pigment-protein complexes have inspired considerable research into the design of biomimetic materials in applications such as solar energy capture,[242-244] photonic device fabrication,[245, 246] artificial photosynthesis,[247-249] and other research areas. However, the high cost of large-scale manufacturing and proteins' natural tendency to damage during processing, make them unsuitable for use as photonic materials.[250] As the light-harvesting systems found in nature, it is the precise arrangement of pigment molecules within these structures that enables them to transport energy efficiently, and that is what biomimetic antennae aim to mimic. This can be achieved using polymer brush films in pigment-polymer complexes as a substitute for the protein scaffolds found in natural biological light-harvesting complexes. Such plexcitonic antenna complexes show great potential as models for creating new biomimetic photonic materials.

A recent study by Lishchuk *et al*. demonstrated that surface-grafted poly (amino acid methacrylate) brushes can be used to design biomimetic pigment-polymer complexes, enabling strong coupling of excitons that can confine optical modes with an efficiency exceeding that shown in natural photosynthetic pigment-protein complexes.[67]

In this work, the possibility of using surface-grafted PDMA brushes formed ATRP as scaffolds to support Chl *a* molecule was explored. It was hypothesised that tertiary amine pendant groups on the surface-grafted polymers would coordinate with the metal ion at the centre of the Chl *a* tetrapyrrole ring, as shown in Figure 4-1. This mechanism is similar to the one by which proteins bind tetrapyrroles by haem binding sites.

Chl *a* was isolated from spinach and incubated with PDMA grown to a thickness of ~30 nm from the substrate surfaces. The binding of chlorophyll to PDMA scaffolds was investigated using XPS and optical spectroscopy. To regulate the binding process for chlorophyll attachment, tertiary amine groups on the PDMA brushes were modified by quaternisation with alkyl halides in a suitable solvent. The chlorophyll density attached to the PDMA brushes was controlled by changing the chlorophyll concentrations and partially converting the amine group into quaternary amides through quaternisation with alkyl halides, thereby regulating the number of binding sites.

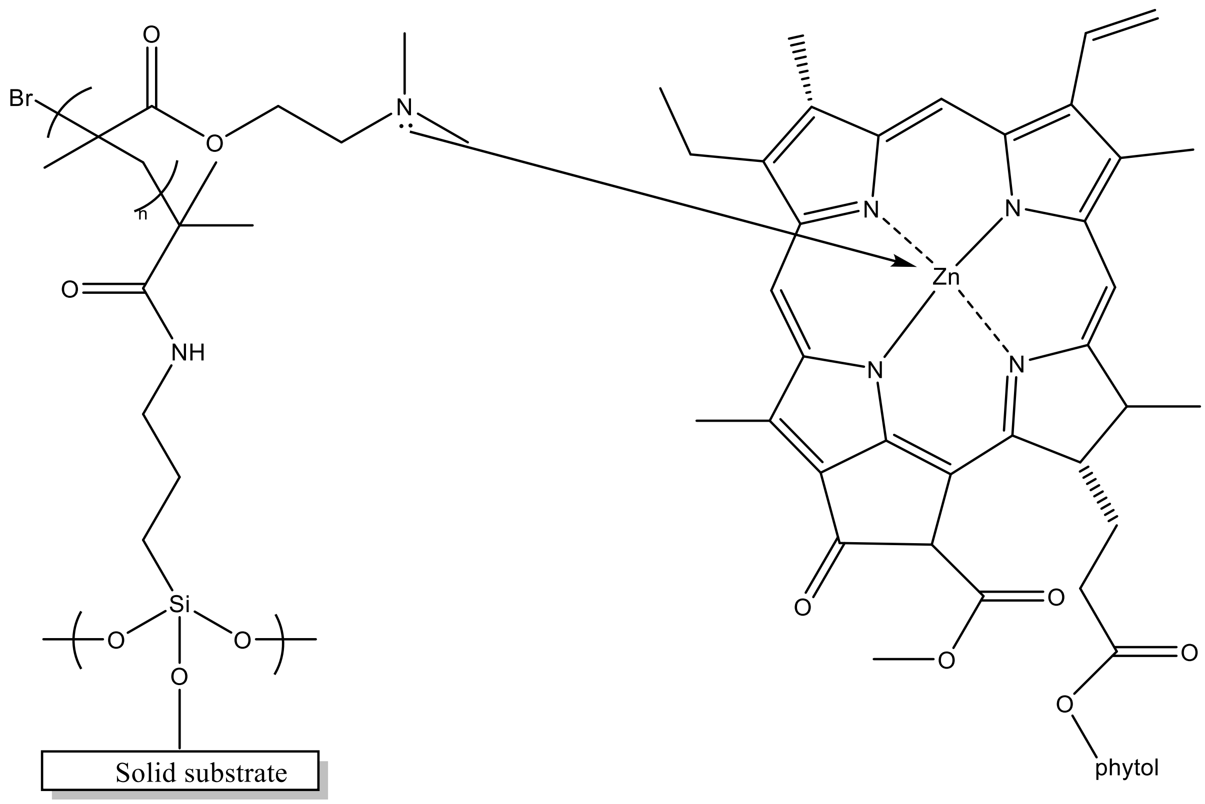

Figure 4-1: Schematic illustration of the binding of chlorophyll to the amino group in PDMA brushes.

4.2 Materials and methods

Glass coverslips (22 x 64 mm and thickness = 1.5mm) were obtained from Menzel-Gläser. Silicon wafers (reclaimed, p-type, <100>) were supplied by Compart Technology (Tamworth, UK). A Carousel 12 Reaction Station (Radleys, UK) was used to prepare polymer brush samples under nitrogen. Hydrogen peroxide (30%) and sulfuric acid (95%), dichloromethane, (≥ 99.8%) dimethylformamide (> 99%), and magnesium sulfate, anhydrous, (≥ 62, 70%) were purchased from Fisher Scientific (Loughborough, UK). Ethanol, absolute, (≥ 99.8%), silica gel and 40-63 µm particle size were obtained from VWR international (Lutterworth, UK). (3-aminopropyl) triethoxysilane (APTES) (≥99%), α-bromoisobutyryl bromide (BIBB) (98%), triethylamine (≥99%), copper (I) bromide (≥99%), 2 (-dimethylamino) ethyl methacrylate (DMA) (98%), 1,1,4,7,10,10 hexamethyl triethylenetetramine (HMTETA) (97%), tetrahydrofuran (99.7%, HPLC grade), gold (III) chloride hydrate, trisodium citrate dehydrate, acetic acid, (≥ 99.7%), sodium hydrogen carbonate, ≥ 99%, petroleum ether 40-60 ^{O}C, methanol, (99%), zinc acetate dihydrate, 1-iodooctadecane (95%), and sand low iron were purchased from Sigma Aldrich UK (Gillingham, UK). All materials were used as received from the manufacturer. Spinach leaves were purchased from a local supermarket. Deionised water was obtained using an Elga Pure Nanopore system with a conductivity rating of 15 MΩcm. Copper bromide was stored in a vacuum environment. DMA was kept at 4 °C following the elimination of the inhibitor via filtration through a short column of basic aluminium oxide.

4.2.1 Cleaning and handling of samples

Silicon wafers and glass slides were all cleaned according to the procedure that was explained previously in Chapter 3. Samples were immersed in piranha solution for 2 h, rinsed with deionized water, and dried overnight in an oven. As piranha solution is a strong oxidising agent, it should never be mixed with organic materials. The slides were cut into sizes appropriate for the particular characterisation technique being employed (~1-4 cm^2). Clean tweezers were used to handle the slides, which were then stored in sealed Eppendorf tubes until required.

4.2.2 Preparation of BIBB-APTES films

The procedure is described in detail in Chapter 3. In brief, the APTES film was prepared in 2% solution APTES in ethanol solvent for 30 min. The samples were washed with ethanol, and dried under nitrogen, before annealing on a hot plate at 120 °C for 30 min. After that, the slides were immersed in a mixture of triethylamine and 2-bromoisobutyryl bromide in dichloromethane for a further 60 min. The resulting initiator-functionalised were washed with dichloromethane, followed by ethanol, and dried under nitrogen steam. [251, 252]

4.2.3 ATRP synthesis of PDMA brushes

ATRP was used to grow polymer brushes from the BIBB-APTES initiator layer, as described in Chapter 3. The mixture of monomer DMA and DMF solvent (ratio 1:1) was placed on a round-bottom flask equipped with a magnetic stirrer. The reaction mixture was stirred and deoxygenated for 20 min at 90 °C. HMTETA and the copper catalyst Cu(I)Br were added to the solution before it was deoxygenated for an additional 10 min. Each BIBB-APTES initiator-functionalised sample then had 5 mL of monomer/catalyst solution added in Schlenk tubes. The reaction mixture was then degassed by three cycles of evacuation followed by re-filling with nitrogen, with a range of growth rates allowed for by ranging the PDMA polymerisation times from 10 min to 2 h. The polymerisation was terminated by removing the slide from the reaction mixture. Monomer and catalyst residues were removed by rinsing the slides with isopropanol and ethanol. Samples were dried after rinsing under a stream of nitrogen.

4.2.4 Quaternisation of PDMA brushes using alkyl halides

PDMA films were quaternised by immersing them in the solution of (1-iodooctadecane) in 10 ml THF for 18 h at room temperature. The quaternised PDMA (q-PDMA) samples were rinsed extensively with ethanol, then gently sonicated in THF, and dried under the N_2 stream (see Chapter 3 for more details).

4.2.5 Extraction of chlorophyll a from spinach

Chl *a* was isolated from spinach leaves using acetone, filtered, and the acetone was removed by using a rotary evaporator under reduced pressure. The green pigment was dissolved in acetic acid for three hours at room temperature for demetallation of the chlorophylls and converted to pheophytin a

Column separation was used to purify the pheophytin a by using a hexane, diethyl ether, and acetone solvent mixture in the ratio 6:3:1. MS and NMR were used to analysis the pheophytin production. The pheophytin a was then dissolved in zinc acetate dihydrate solution. The reaction involves refluxing in an argon environment at 35 °C for one hour. The resulting ZnChla was purified using column chromatography, employing the same solvent mixture of hexane, diethyl ether, and acetone in a 6:3:1 ratio.

4.2.6 Addition of ZnChla to PDMA brushes and q-PDMA

PDMA brush samples were treated with ZnChla by overnight immersion in solutions of ZnChla at concentrations ranging from 1 to 60 μM in a 1:3 DMF: H_2O mixture at room temperature. The ZnChla-functionalised PDMA brushes were then washed with deionised water and dried under N_2, before characterisation with ZnChla was characterised by UV-vis spectroscopy, XPS. SE and AFM.

4.2.7 Surface characterisation

A Rame-Hart goniometer model 100-00 (Netcong, NJ, USA) was utilised to determine water contact angles.

A Cary 50 UV-visible spectrophotometer (Agilent Technologies, USA) was used to acquire UV-visible absorption spectra over a range of wavelength from 350 to 800 nm. ZnChla solution samples were placed in standard quartz cuvettes with a 1cm optical path length. During the air measurement experiment, a homemade PTFE sample holder was used to ensure measure the same area on the surface was measured at all stages of the experiment.

The ellipsometry experiments were performed utilising an Alpha-SE ellipsometer (J. A. Woollam Co., Lincoln, NE, USA). The light source was a He-Ne laser (wavelength = 633nm) with a 70° angle of incidence. [212] Ellipsometric data were fitted using Complete EASE software (v. 6.6).

The XPS provided by Kratos Analytical, Manchester, UK, was used to collect the spectra, and the XPS data was analysed using CASAXPS (v. 2.18 software). The AFM images were produced using a Digital Instruments' Nasoscope 5 Multimode Atomic Force Microscope and the data was analysed with Nasoscope Analysis software (v.1.5)

4.3 Results and discussion

4.3.1 Preparation and characterisation of the initiator-functionalised substrates

As shown in Figure 4-2 below, initiator-functionalised surfaces were prepared by the reaction of APTES films with BIBB.

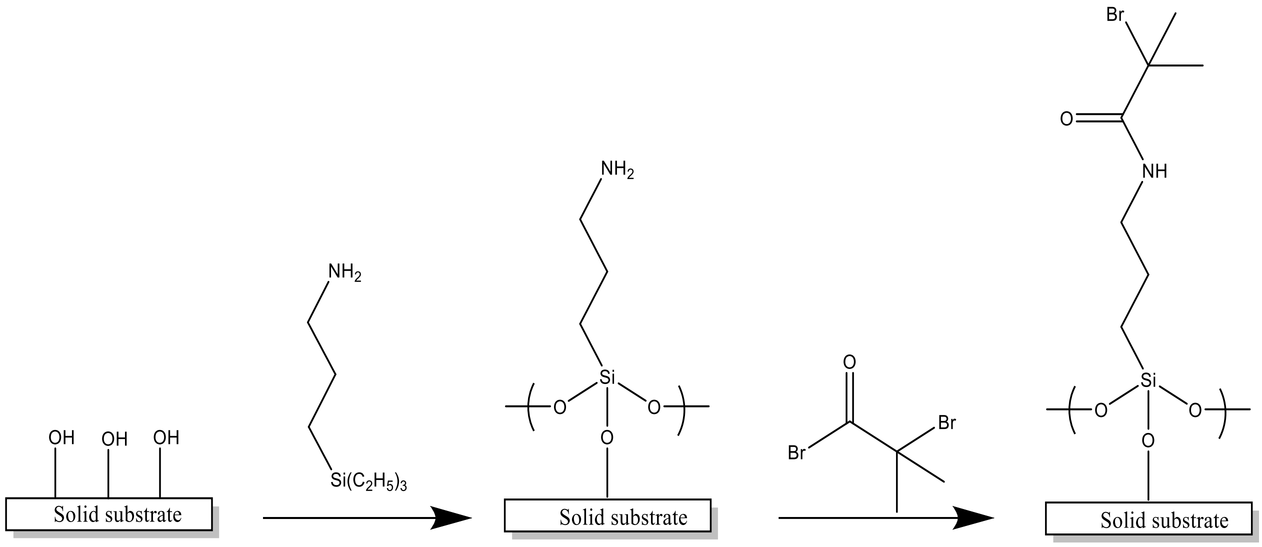

Figure 4-2: Schematic illustration of the synthesis of BIBB-APTES on a solid substrate.

The APTES and BIBB-APTES films were characterised using a wide range of surface analysis techniques, including WCA, SE, AFM, and XPS. The water contact angle was measured at three different locations on each sample piranha-cleaned silicon wafer, APTES, and BIBB-APTES films.

The contact angle for the as-received silicon wafer was 53 ± 1°. [253] After cleaning with piranha solution, the oxide surface becomes more hydrophilic with a water contact angle of 8 ± 1°.[254] The water contact angle after the deposition of APTES films was 46 ± 1° and after BIBB-APTES films 65 ± 2°, which is consistent with results reported in the literature.[138, 255, 256]

The increase in the contact angle from 46 ° to 65° is attributed to the less polar nature of the terminal bromine in the BIBB-APTES. The average thickness of the BIBB-APTES deposit on the surface was determined by SE and found to be 1.4 ± 0.4 nm for the complete layer, see (Table 4-1**).** There is a good correlation between this value and the results obtained for BIBB-APTES in the previous reports, which was 1.5 ± 0.2 nm.[257, 258]

Table 4-1: Water contact angles and film thickness for APTES & BIBB-APTES monolayers on silicon as a function of the surface chemistry changes.

Sample	Contact angle/ °	Thickness/nm
Piranha-cleaned silicon	8 ± 1	-
APTES	46 ± 1	0.8 ± 0.1
BIBB-APTES	65 ± 2	1.4 ± 0.4

The change in the contact angle was measured as a function of the time of immersion of the APTES films in a 2% solution of BIBB in DCM. The contact angle measurements confirmed that 30 min is not sufficient to produce a full-density BIBB-APTES film and that the complete reaction takes longer than 30 min to reach the limiting value. (see Figure 4-3).

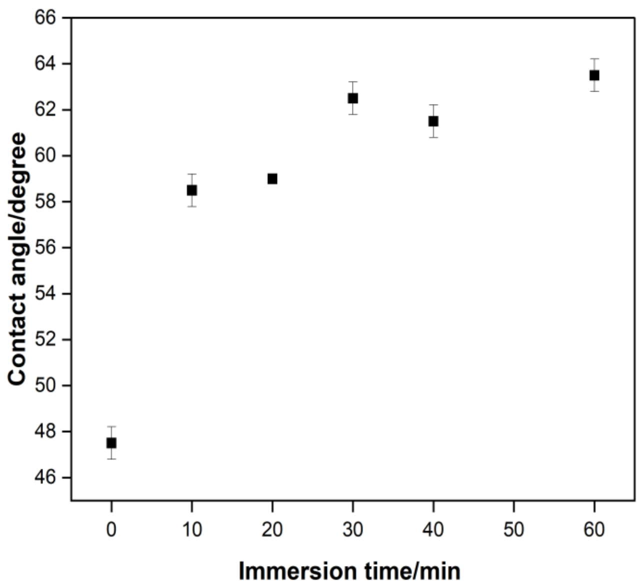

Figure 4-3: The change in water contact angle as a function of immersion time for APTES films in a BIBB solution in DCM.

The surface morphology of BIBB-APTES films was acquired using AFM tapping mode. The surface roughness was obtained from a (1 μm × 1 μm) area reaching 0.24 nm, which is indicative of smooth surfaces and therefore that high-quality films had been formed, as shown in Figure 4-4. This value is very close to the results obtained for BIBB-APTES in the previous report, which was 0.26 nm.[257]

The high-resolution XPS spectra of APTES and BIBB-APTES films are shown in Figure 4-5. For the APTES layer, the C1s spectrum displays two peaks at 285.0 eV and 286.4 eV, which are attributed to C-C-C and C-C-N, respectively. The region N1s of the APTES film shows two distinct nitrogen peaks at 399.6 eV and 401.7 eV, attributed to the amino group ($-NH_2$) and a protonated amine group ($-NH_3^+$), respectively. A protonated amine group ($-NH_3^+$) is produced during the multilayer formation of silane films, as represented in Figures 4-5a and 4-5b. For BIBB-APTES initiators, there are three components of the C1s spectra with binding energies 285.0, 286.4, and 288.4 eV, which were assigned to C-C-C, C-Br/C-NCO and O=C-N, respectively, see Figures 4-5c. The peak area ratios for the C-C-C, C-C-Br/C-NCO and O=C-N components were 5.3: 2.2: 1, which is close to the calculated ratio of 4:2:1. The N 1s spectra were fitted with two components, the first at 399.6 eV attributed to the nitrogen in ($-NH_2$) and the second at 401.9 eV attributed to a protonated amino group ($-NH_3^+$),[138, 259] (see Figure 4-5d). The Br 3d spectrum in Figure 4.5e shows two features, each of which is composed of a doublet attributed to the $Br3d_{5/2}$ and $Br3d_{3/2}$ peaks that result from spin-orbit coupling at 71.3 and 70.3 eV.[259] These results indicate the existence of bromine in two oxidation states.

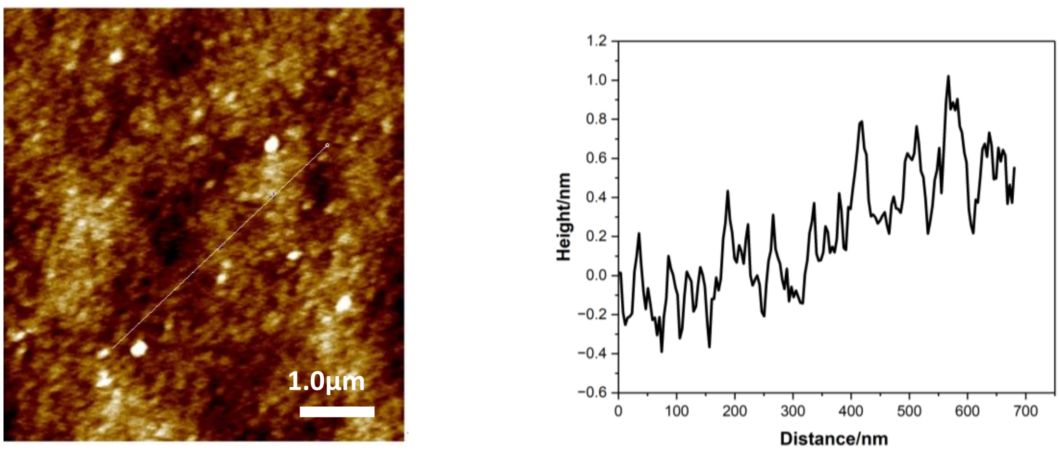

Figure 4-4: Tapping mode AFM topographical image (1μm × 1μm) for BIBB-APTES initiator on the silicon substrate and its profile section.

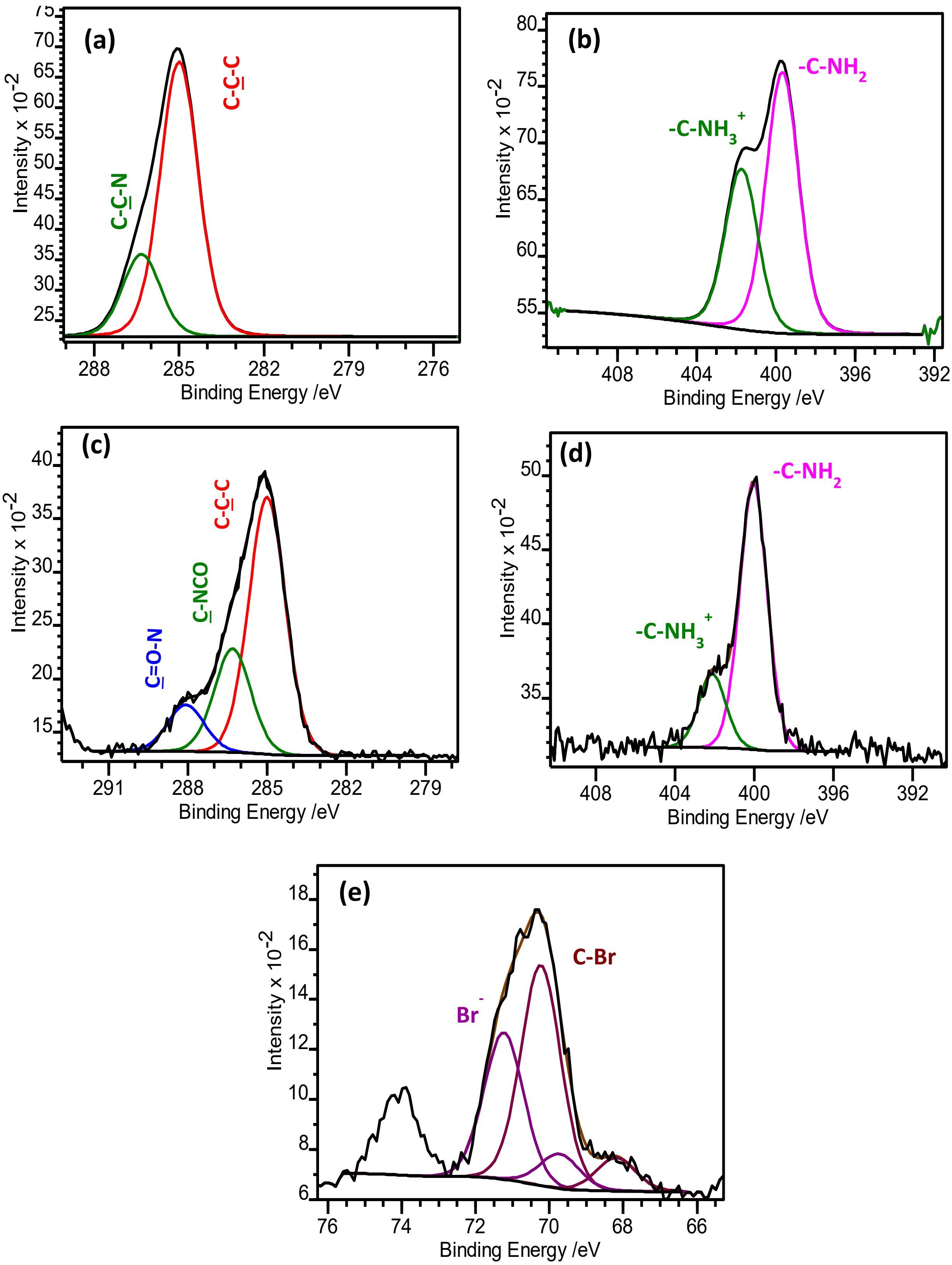

Figure 4-5: XPS high-resolution spectra of a) C1s and b) N1s spectra for APTES films on glass, (c) C1s, d) N1s, and e) Br3d spectra for BIBB-APTES films on glass.

4.3.2 Kinetics of the growth of PDMA brushes from initiator-functionalised surfaces

PDMA brushes were grown from bromine initiators following the method of Cheng *et al.* [251] The reaction is shown schematically in Figure 4-6.

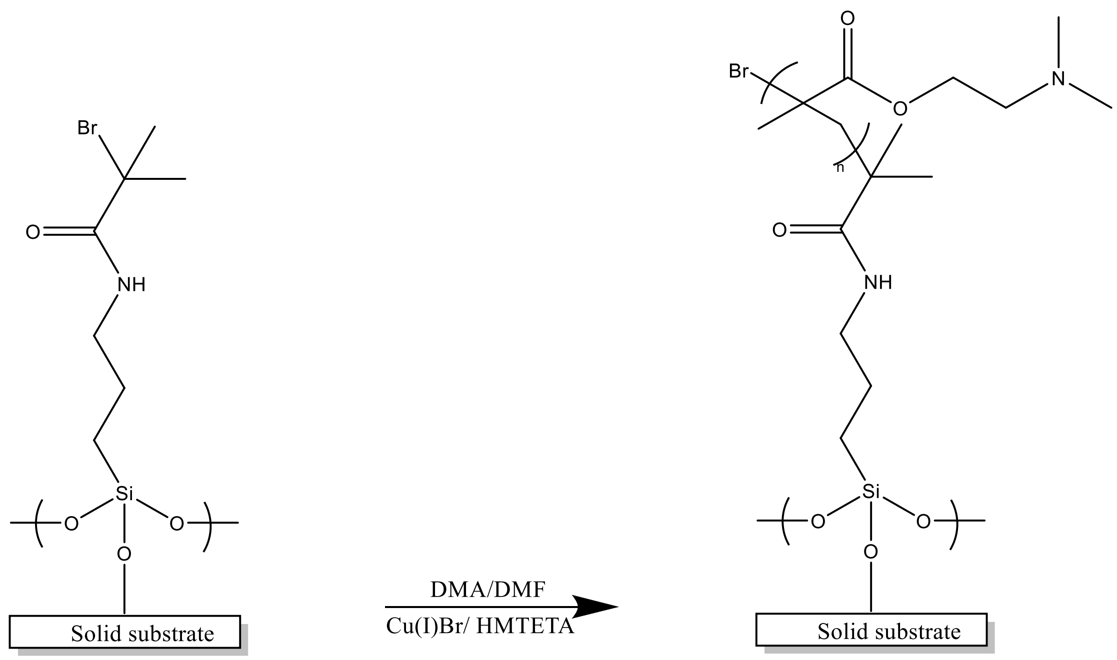

Figure 4-6: Schematic illustration of the synthesis of PDMA brushes by ATRP.

XPS, AFM, and SE were used to provide a comprehensive characterisation of the grafting of the polymer brushes, including their morphology, element composition, and thickness. Furthermore, the change in the polymer thickness as a function of polymerisation time was measured using spectroscopic ellipsometry, as illustrated in Figure 4-7**.**

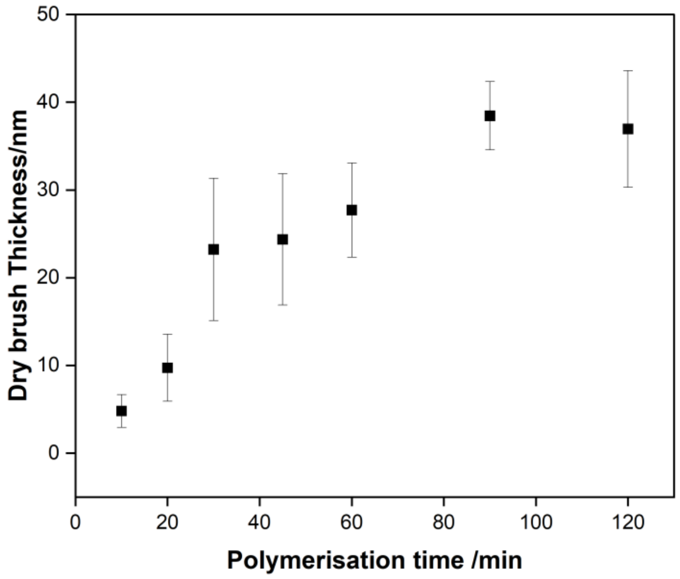

Figure 4-7: Ellipsometric dry thickness of PDMA brush as a function of polymerisation time.

Figure 4-7 shows the increase in the ellipsometric thickness of the dry surface-grafted polymer film as a function of the polymerisation time. The thickness of the surface-grafted layer increased approximately linearly up to 60 min. After 1 h, the growth rate decreased because of the increasing numbers of chain terminations and a limiting thickness of 37 ± 5 nm was reached after 90 min.

For the XPS characterisation, the PDMA brushes' high-resolution XPS spectra were obtained after a polymerisation time of 1 h (see Figure 4-8). The C1s spectrum was fitted with four components at binding energies of 285.0, 285.8, 286.8 and 288.9 eV, which are attributed to the C-<u>C</u>-C, <u>C</u>-N/ <u>C</u>-Br, C-<u>C</u>-O, and C-<u>C</u>=O, respectively (see Figure 4-8a). The experimental ratios calculated from the fitted C 1s spectrum were 3.2: 2.8: 1.1: 1, which are very close to the theoretical ratios of 3:3: 1: 1. The N1s spectrum showed a single peak at 399.6 eV, which corresponds to the amines group in PDMA consistent with the literature, [120, 260] (see Figure 4-8 b). For O1s, XPS spectra are fitted with doublet peaks, with binding energies of 532.3eV for the C=O and 533.7eV for the C-O (see Figure 4-8c).

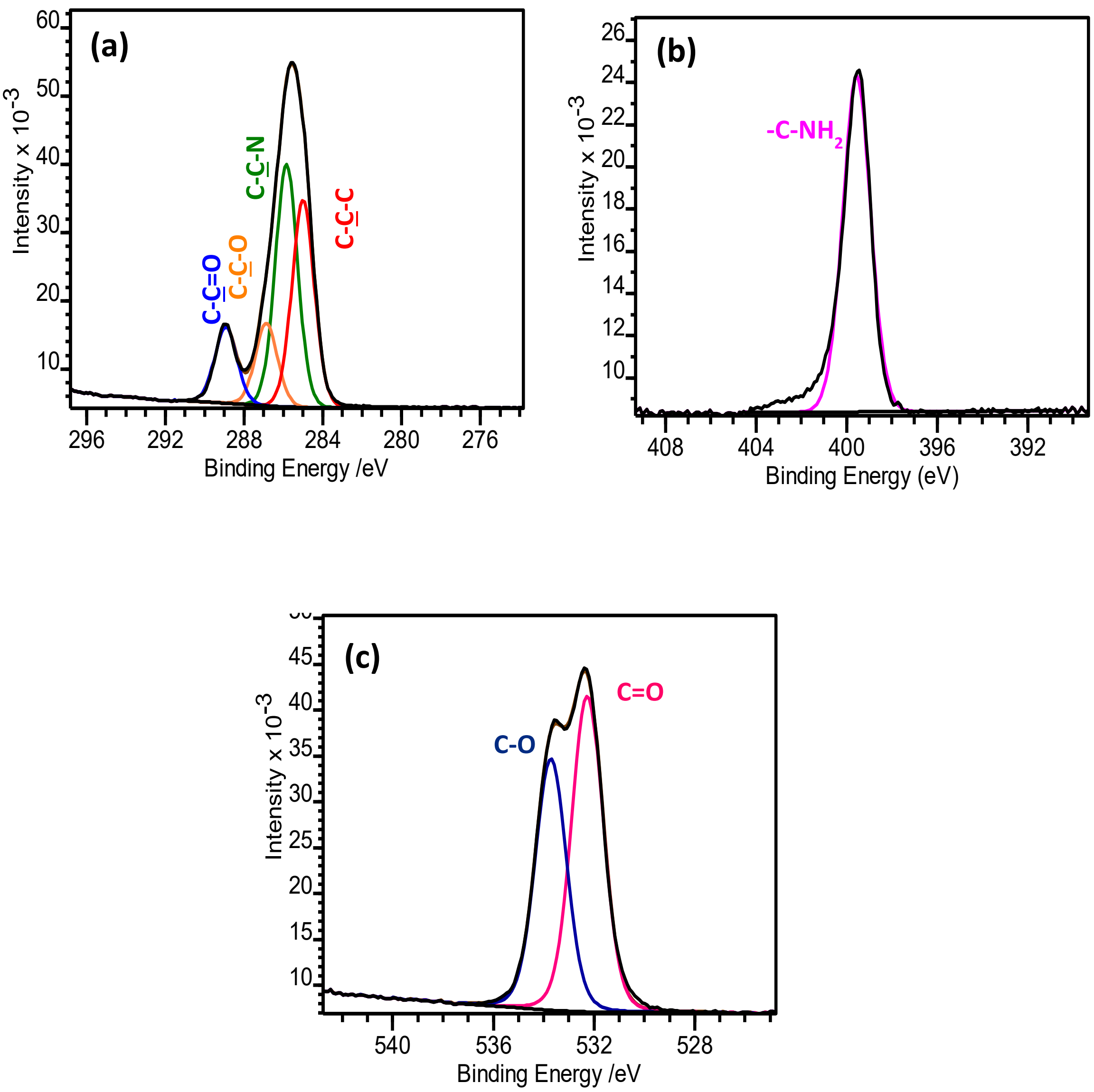

Figure 4-8: High-resolution XPS spectra of PDMA brushes: (a) C 1s spectrum. (b) N 1s spectrum, and (c) O 1s spectrum.

XPS of Si 2p high-resolution spectra for PDMA at different polymerisation times is shown in Figure 4-9. It can be seen that the area of the Si 2p peak, decreased with increasing polymerisation time. This is because the Si 2p signal becomes increasingly attenuated by the surface grafted polymer layer as its thickness increases.

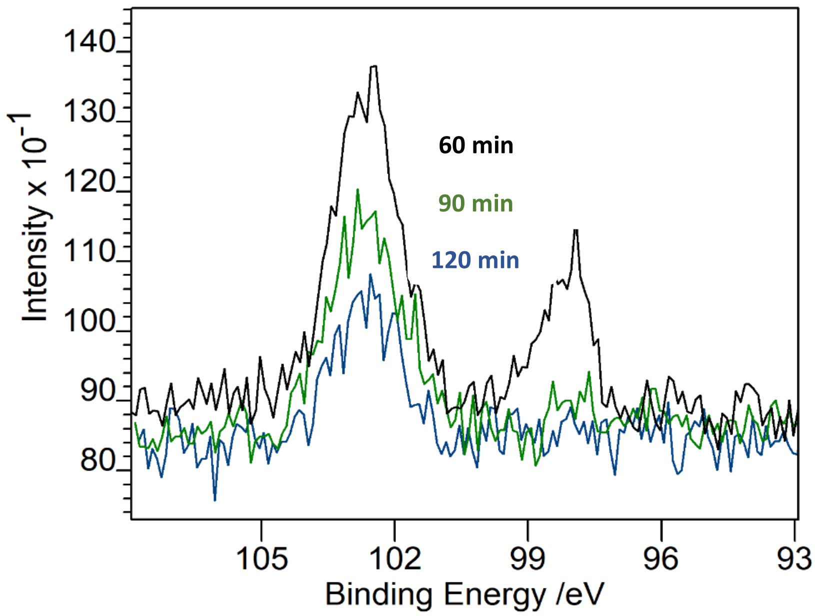

Figure 4-9: XPS Si 2p spectra of PDMA brushes after polymerisation for 60 min (black), 90 min (green), and 120 min (blue).

The RMS surface roughness of dry PDMA polymer brush was determined by AFM as a function of polymerisation time (see Figure 4-10). For all polymerisation time, the surfaces have a reasonably smooth and uniform morphology which suggests that the polymerisation reaction is occurring correspondingly uniformly across the surface. The roughness of the PDMA samples was measured in five different locations in each sample to ensure representativeness/reproducibility and accuracy. As shown in Table 4-2, the polymer's RMS roughness initially slightly increases until it reaches a steady value after approximately 30 min with a mean roughness of 0.33 ± 0.02 nm. Initially, the roughness was increased slightly due to partial polymer covering, and subsequently, the RMS value remained relatively constant over time with a roughness ≤ 0.3 nm, which is consistent with previous studies.[257] These results indicate that a smooth, uniform, and high-quality polymer film has been formed.

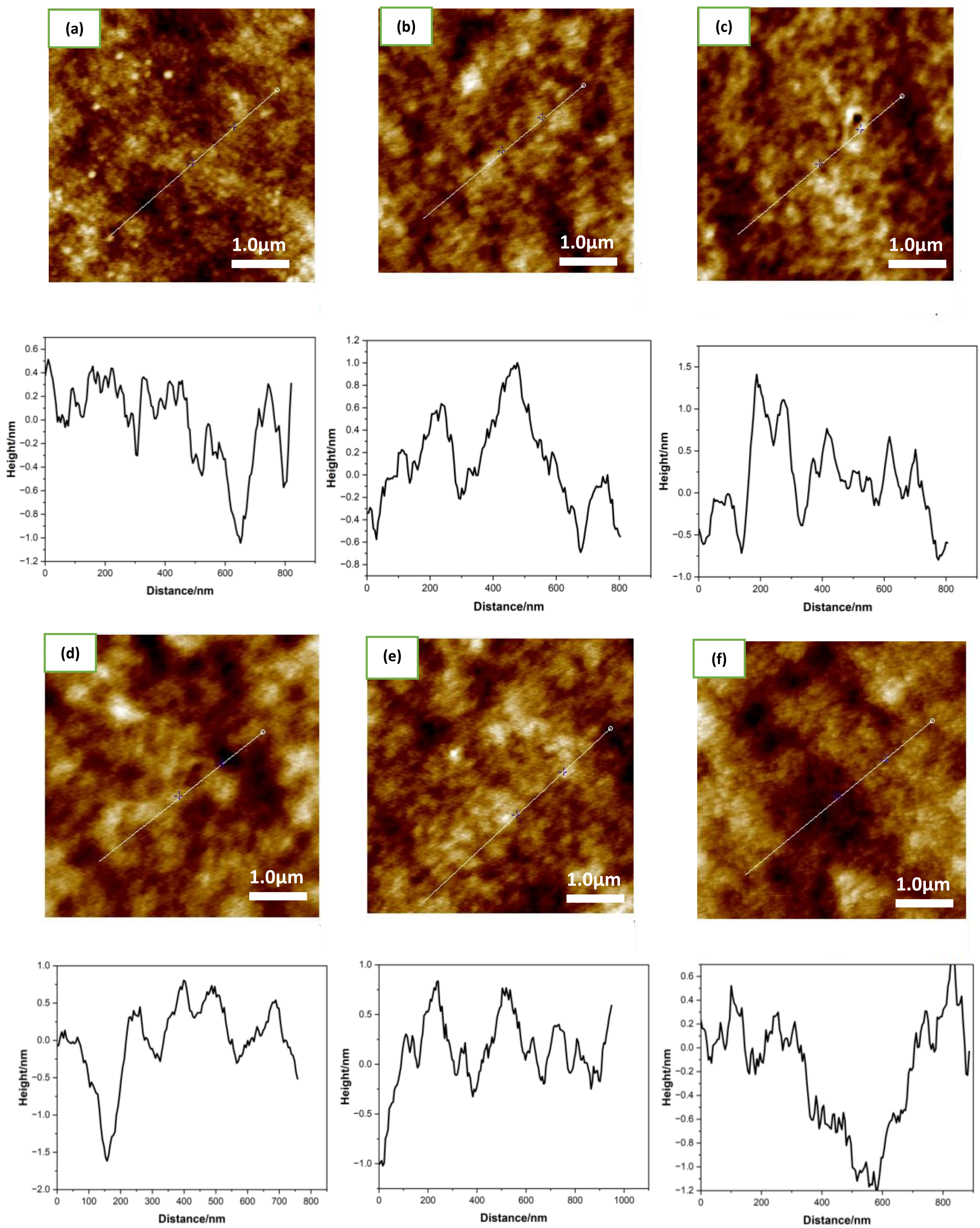

Figure 4-10: The AFM height images of the PDMA brush on a silicon substrate at different polymerisation times: (a) 10 min; (b) 20 min; (c) 30 min; (d) 45 min; (e) 60 min and (f) 120 min with their cross-sectional surface heights profiles below.

Table 4-2: Root mean square (RMS) roughness values for PDMA brush layers as a function of polymerisation time.

The time of polymerisation (min)	The mean of roughness (nm)
10	0.27 ± 0.07
20	0.29 ± 0.02
30	0.33 ± 0.02
45	0.37 ± 0.03
60	0.26 ± 0.03
120	0.35 ± 0.02

4.3.3 Addition of chlorophyll to polymer brush structures.

4.3.3.1 Chlorophyll isolation and characterisation.

Column chromatography was used to separate chlorophyll a from the other pigments present in spinach leaves. A further modification involved replacing Mg^{2+} in pheophytin a with Zn^{2+} to form Zn-pheophytin a to enhance its photostability.[52] The chlorophyll molecule is isolated using acetone, as it has a similar polarity, and can reduce side reactions. The extraction and synthetic procedure were explained in detail in Chapter 3. Chl *a* was extracted from spinach, and the central magnesium ion was replaced with Zn^{2+} to yield zinc chlorophyllide a (ZnChla) as shown schematically in Figure 4-11**.** To enable the acquisition of absorption spectra, ZnChla was dissolved in a 1:3 mixture of DMF and water. This is a necessary step because Chl *a* has limited solubility in water but more in 1:3 DMF: water mixtures, making them an ideal solvent mixture for coupling Chl *a* to PDMA. As shown in Figure 4-12, ZnChla exhibits absorption peaks at 664 nm in the red region, known as the Q band, and at 432 nm in the blue region, known as the Soret band. These results are consistent with those reported in the literature.[52] Figure 4-13 displays the ZnChla absorption intensity in solutions of the different ZnChla concentrations ranging from 1 to 30 μM. As expected, the intensity of absorption increased linearly with increasing chlorophyll concentration.

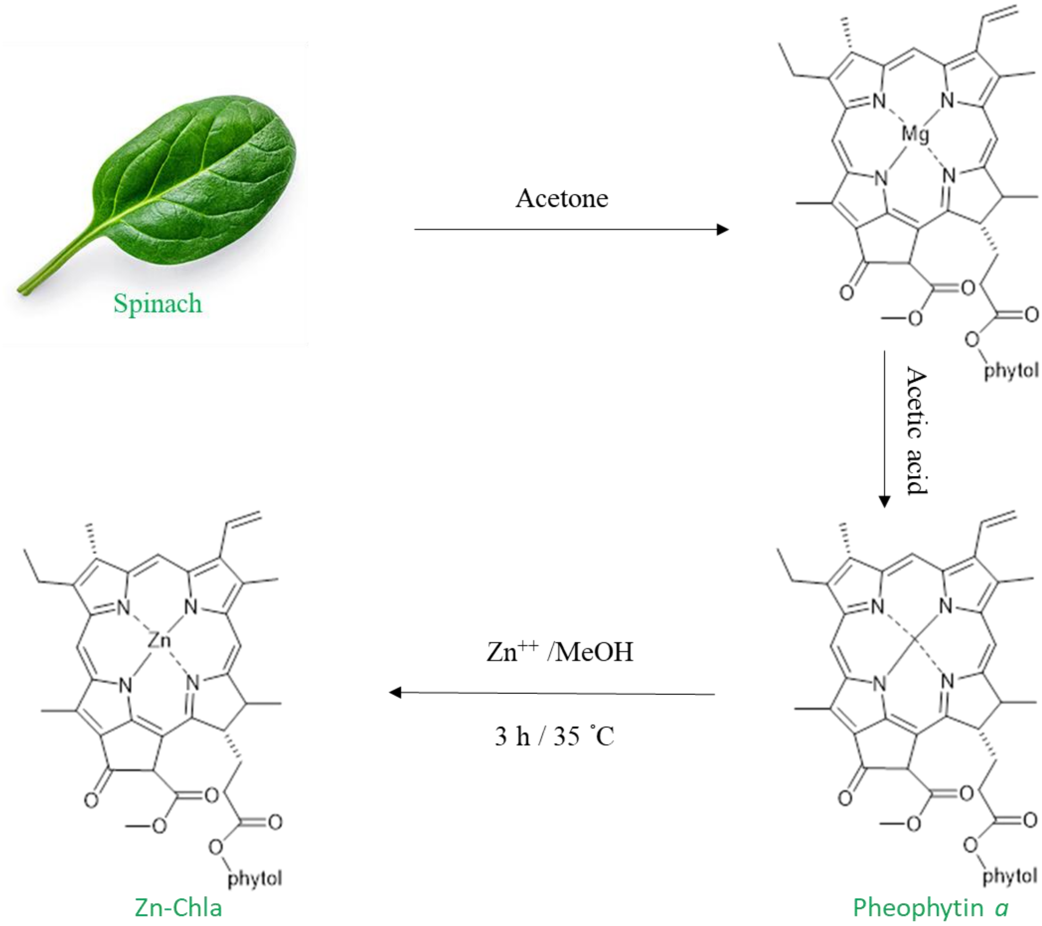

Figure 4-11: Schematic illustration of the extraction and derivatisation of Zn-Chla from spinach.

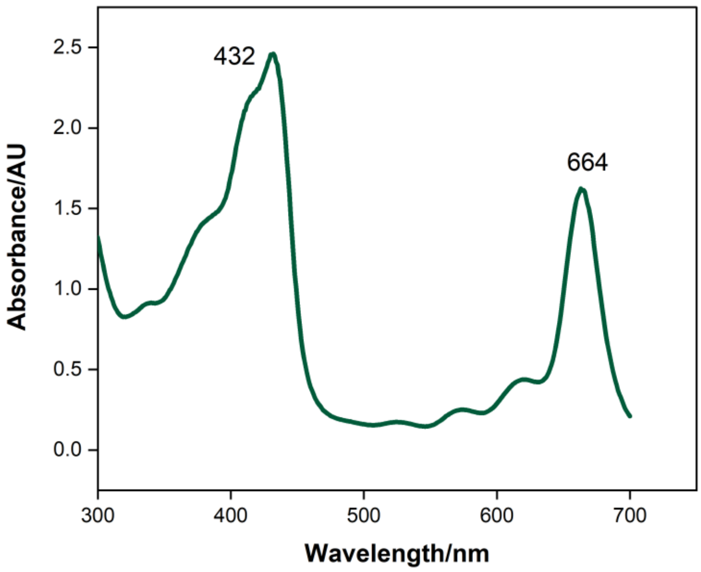

Figure 4-12: The UV-vis absorption spectrum of Zn-Chla in a 1:3 (v/v) DMF to water mixture.

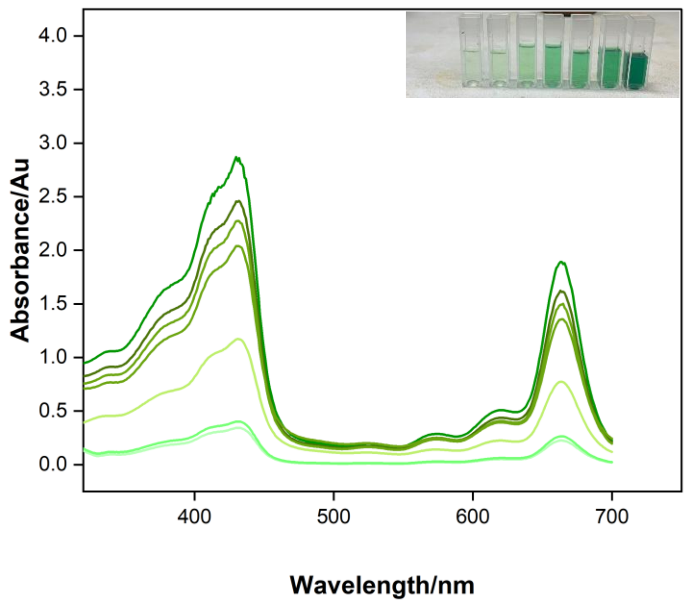

Figure 4-13: The UV-vis absorption spectra of different concentrations of Zn-Chla on DMF, water (1:3) from 1μM (lightest green) to 30 μM (darkest green).

4.3.3.2 Addition of ZnChla to PDMA brushes

In natural light-harvesting complexes, the three-dimensional arrangement of carotenoids and chlorophyll is achieved using peptide units as scaffolds. Plexcitonic antenna complexes, inspired by the structures of photosynthetic light-harvesting complexes, were designed to exhibit biomimetic structures with unique optical properties.[67] In these structures, the placement of chlorophyll pigments is coordinated by a surface-grafted polymer scaffold formed by the growth of PDMA scaffolds via atom-transfer radical polymerisation. It was hypothesised that the tertiary amine pendant groups on surface-grafted PDMA chains could coordinate to the central metal ion in the chlorophyll molecules, in a similar way that heme binding sites in proteins coordinate to tetrapyrroles. The coordination bonds are formed between the central double-charged zinc ions in the chlorophyll ring and the tertiary amine group of PDMA brushes (see Figure 4-14).

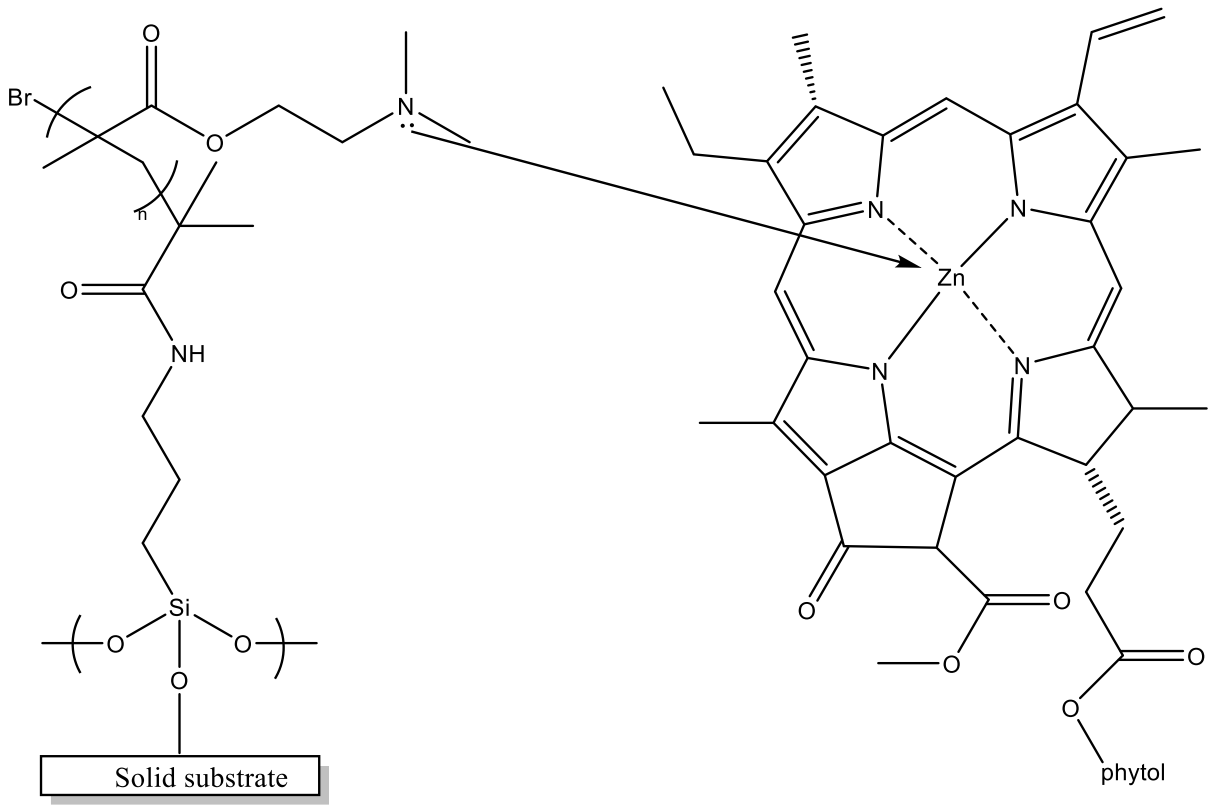

Figure 4-14: Schematic representation of the binding of chlorophyll to the amino group in PDMA brushes.

The binding of Chl *a* to PDMA scaffolds was characterised using UV-vis spectroscopy and XPS. The PDMA brush samples polymerised for 1 h were immersed in 1- 30 μM solutions of Chl *a* in a 1:3 DMF/water mixture for 24h (see Figure 4-15). In the spectrum of the ZnChla functionalised PDMA scaffold, ZnChla is bound to the polymer and while the polymer film is only 30 nm thick, the absorption bands are less intense than those in a 1cm cuvette containing dissolved ZnChla. Chl's tendency to aggregate leads to the formation of J-aggregates in which the peak positions are red shifted. A J-aggregate is a molecular aggregate that has distinct optical properties, including red shifted absorption peaks compared to individual molecules. The redshift results from electronic interactions between molecules. Lowering the energy levels shifts the absorption peak to longer wavelengths.[65] In this case, however, there is no redshift in the position of the main Qy band for chlorophyll, which indicates that Chl *a* is not aggregated in the polymer surface. These results support the current hypothesis that the tertiary amine group of the PDMA can coordinate with the metal ion at the centre of the chlorophyll molecule. Strong absorption spectra of ZnChla in solution can be seen at 432 and 664 nm, which represent the Soret and Qy transitions band, respectively (see Figure 4-16 black); there is a similar peak observed after functionalized PDMA with ZnChla with a less intense peak as expected (see Figure 4-16 red).

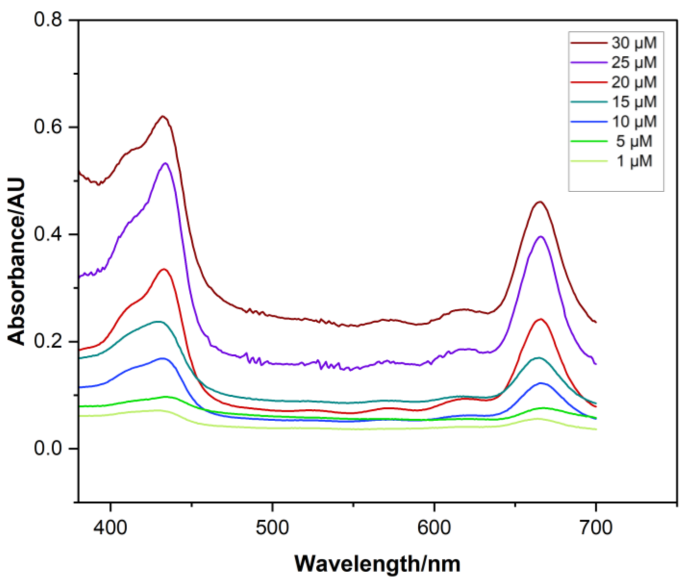

Figure 4-15: The UV-vis absorption spectrum of different concentrations of ZnChla (1-30 μM) attached to PDMA brush polymerised for 1h.

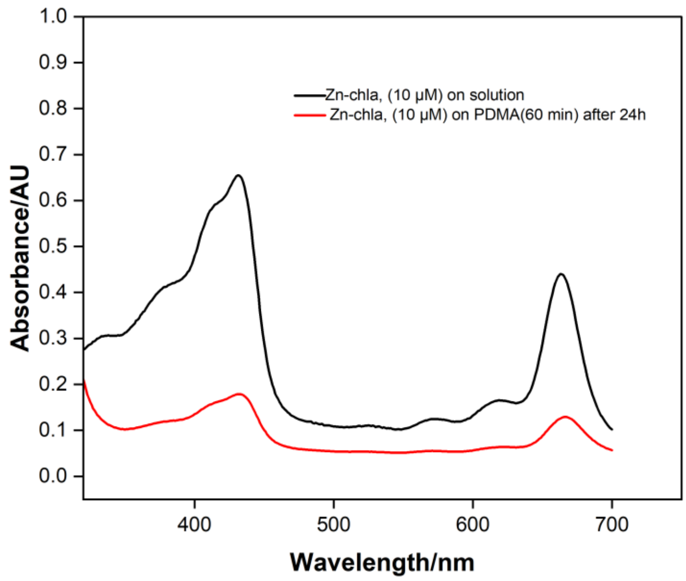

Figure 4-16: The UV-vis absorption spectrum of ZnChla 10 mM (Black) in a solution (DMF: water) mixture (1:3v/v), and after the addition of chlorophyll to PDMA for 24 h at the same concentration (Red).

Figure 4-17 shows high-resolution XPS spectra of PDMA brushes before and after binding to ZnChla**.** Zn is not observed for the as-prepared polymer (Figure 4-17a), but after the attachment to ZnChla*,* a strong peak was observed, confirming that ZnChla had bound to the PDMA (see Figures 4-17a and 4-17b). A single component with binding energy at 399.5 eV is observed in the N1s spectrum of the as-prepared polymer, which is attributed to the amino group in PDMA; following the addition of ZnChla to PDMA, two new peaks were observed. The most intense peak is at 398.5 eV, which is attributed to the nitrogen atoms in the centre of the chlorophyll ring (tetrapyrrole nitrogen atoms). A second peak is observed at 402.2 eV, which is assigned to the imine (C=N-C) bond in the chlorin ring, resulting from some demetallation of Chl *a*,[52, 261] (see Figures 4-17 c and 4-17 d). Additionally, a further increase in C1s peak intensity occurs when ZnChla molecules are added, as they contain phytol chains, as can be seen in Figures 4-17 e and 4-17 f).

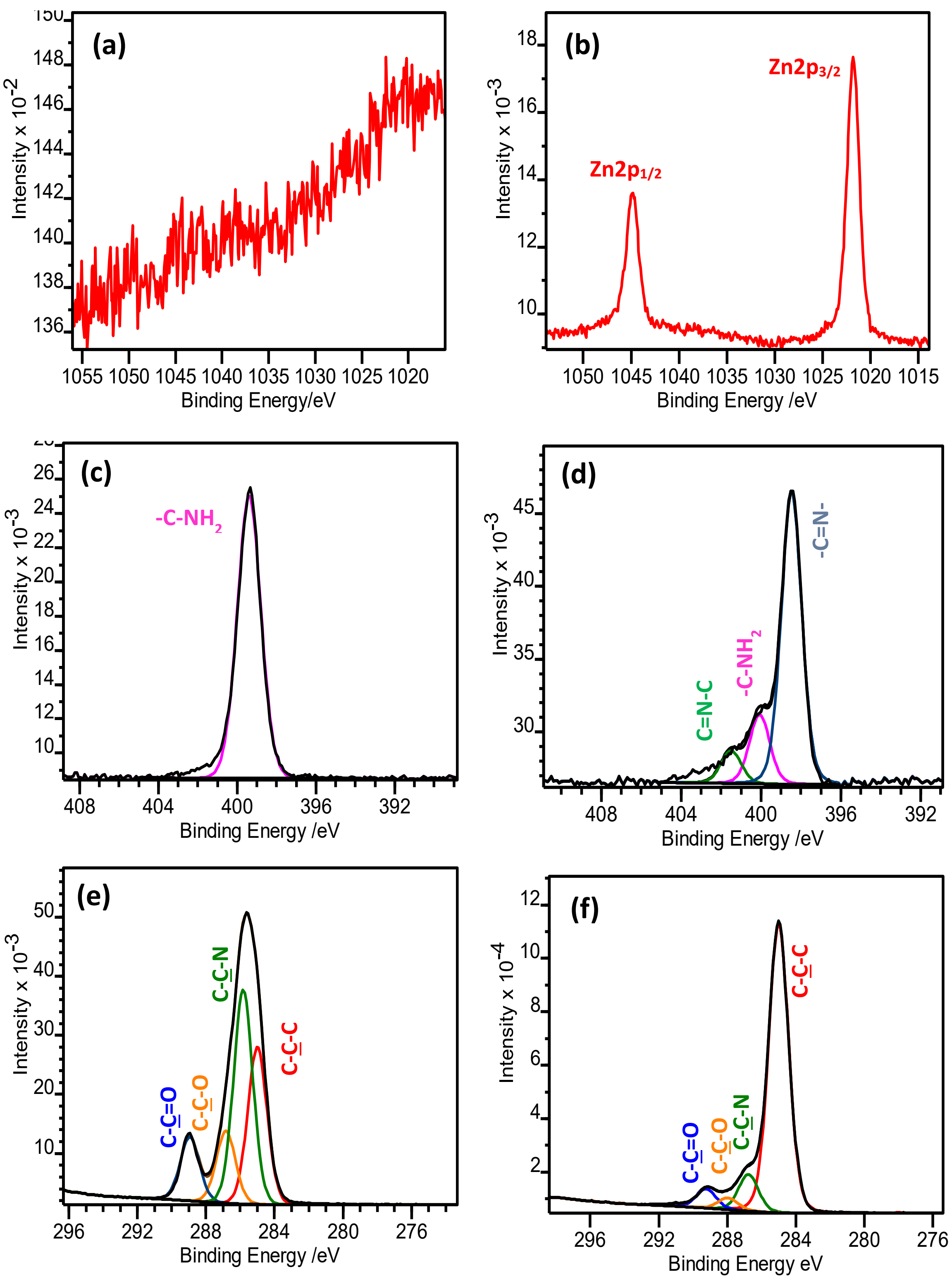

Figure 4-17: XPS spectra obtained for PDMA before chlorophyll attachment of Zn2p (a), N1s(c), and C1s (e), and after attached chlorophyll to PDMA of Zn2p (b), N1s(d), and C1s(f).

4.3.3.3 Addition of different concentrations of chlorophyll to the polymer brush

High-resolution XPS N1s spectra of PDMA brushes after immersion in a solution of Chl *a* at concentrations of 0, 10, 20, 30, and 60 µM are shown in Figure 4-18. The N 1s spectrum of the as-prepared polymer contains a single peak at 399.9 eV attributed to nitrogen in the tertiary amino pendant group ($-NH^{2+}$). After binding with Chl *a*, a new peak is observed at 398.5eV which is assigned to the nitrogen atoms in the porphyrin macrocycle of Chl *a*. As expected, the intensity of this new peak increases with higher Chl *a* concentrations, indicating that the amount of bound chlorophyll increases with the concentration of Chl *a* in the solution. In contrast, the relative intensity of the peak corresponding to the tertiary amino groups at 399.9 eV decreases as Chl *a* concentration increases.

The percentage of attachment of Chl *a* to PDMA brushes at different concentrations of Chl *a*, calculated from N 1s ratios acquired by XPS, is shown in Table 4-4**.** As evident in the table, increasing the Chl *a* concentration from 10 µM to 60 µM leads to an increase in the intensity of the 398.5 eV peak. Additionally, an increase in Chl *a* concentration results in a relative decrease in the peak at 399.9 eV corresponding to the nitrogen in the amino groups of PDMA. The process through which Chl *a* bonds requires the creation of a coordinate bond, which is in accordance with the decrease in intensity observed for the $-NH_2$ signal in comparison to the other N1s bonding environments. This reduction occurs because certain $-NH_2$ groups undergo electron-donating coordination with the metal center, making them less intense. It is hypothesised that the lone pairs of electrons in the tertiary nitrogen atoms form coordinate bonds to Zn^{2+} metal ions at the centre of the Chl *a* rings.

Table 4-3: The atomic percentage of N1s at 398.5 eV (for Chl *a*) and 399.9 eV (for amino groups in PDMA) after attachment of different concentrations of Chl *a*.

Concentration of Chl	**N1s at 398.5 eV (Chl *a*)**	**N1s (free amino group)**
10	58.145 % ± 2.31	33.33 %± 0.99
20	66.98% ± 0.49	26.16% ± 0.49
30	74.96% ± 2.84	17.13% ± 2.47
60	74.63% ± 2.40	17.76% ± 2.43

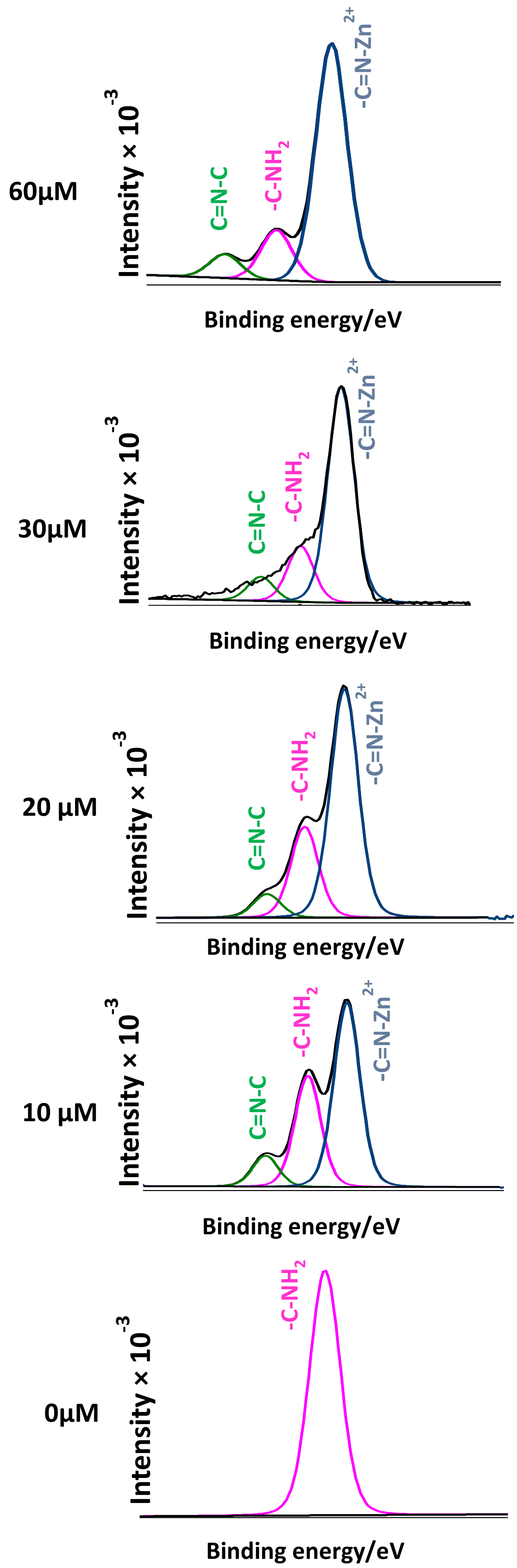

Figure 4-18: The XPS spectra of N1s at different Chl *a* concentrations (0, 10, 20, 30 and 60 µM) on PDMA polymerised for (60 min).

4.3.3.4 Binding plot for Chl on PDMA

PDMA films were immersed in ZnChla solutions with different concentrations from 1 to 60 μM at room temperature for 24 h. UV-vis spectroscopy was utilised to determine the amount of Chl *a* bonding to the PDMA brushes. The concentration of ZnChla in the solution and within the PDMA layer was determined by using the Beer-Lambert law:

$$\mathrm{A} = \varepsilon l c \qquad \text{(Eq. 3.2)}$$

Where A is the absorbance, ε is the molar extinction coefficient, l the path length and c is the concentration. The ZnChla concentration in the PDMA layer is not calculated using the path length, l, but using the thickness of the polymer brush layer on the surface, d:

$$c = \frac{\mathrm{A}}{\varepsilon \mathrm{d}} \qquad \text{(Eq. 4.1)}$$

The effective thickness of the polymer layer is determined by spectroscopic ellipsometry. It was assumed that the extinction coefficient of Chl *a* in the brush layer was the same as that of Chl *a* in the solution.

Figure 4-19 shows the dependence of the concentration of Chl *a* in the PDMA layers on the concentration of chlorophyll in the solution. The concentration of Chl *a* in the brush layer increased up to a concentration of 30 μM when it reached a limiting value of approximately 2 M. The PDMA brushes are saturated with ZnChla at this limiting value, which is three times higher than the concentration found in biological light-harvesting complexes.[67] The high concentrations of ZnChla that can be reached within the PDMA layer could be beneficial for photovoltaic applications, sensors, and bioinspired light-harvesting devices.

At a concentration of 1 M, the density of Chl *a* is ~6×10^{23} dm^{-3} ~6×10^{26} m^{3}, which exceeds the threshold to reach the strong coupling regime (~10^{25} m^{-3}). Thus, the mean Chl-Chl distance is ~ 1 nm. Calculating the distance between Chl *a* and AuNP is not so straightforward, because the extinction coefficient of the gold nanoparticles is not known accurately.

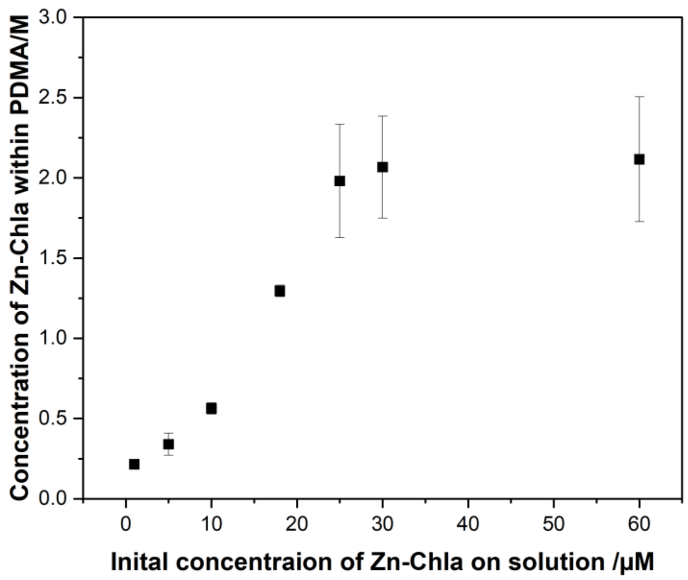

Figure 4-19: The concentration of ZnChla in PDMA brushes as a function of the initial concentration of the ZnChla solution.

4.3.3.5 Quaternisation of PDMA brushes followed by Chl *a* attachment.

The pendant groups in PDMA contain tertiary nitrogen atoms. It was hypothesised that the tertiary amine pendant groups coordinate with the central metal ion in the chlorophyll. To test this hypothesis, the tertiary nitrogen atoms were blocked by quaternising them by reaction with alkyl halides, compounds that are known to undergo quaternisation to convert tertiary amines into quaternary ammonium salts through the quaternisation reaction. Figure 4-20 shows a schematic representation of the quaternisation reaction between 1-iodooctadecane and PDMA. The degree of quaternisation (DQ) can be controlled by varying the concentration of the alkyl halide. Furthermore, the choice of solvent also has a significant impact on the efficiency of quaternisation. In poor solvents, such as n-hexane, quaternisation is restricted to the upper portion of the brush chains, whereas in better solvents, such as THF, the brushes are able to swell, thereby enabling more uniform quaternisation of the polymers, and improving attachment efficiency. This section describes the partial quaternisation of the amine groups of PDMA brushes in THF, using 1-iodooctadecane as the alkyl halide to regulate chlorophyll-binding. The effect of quaternisation on Chl *a* binding was also studied.

PDMA quaternisation was characterised by XPS analysis of the N 1s and C 1s spectra. This technique can distinguish between normal (neutral) nitrogen atoms in PDMA with a binding energy of 399.9 eV and quaternised (cationic) nitrogen with a binding energy of 402 eV. Furthermore, the degree of PDMA quaternisation can be determined from the C1s peak by calculating the ratio between the C-C-C and total carbon in PDMA before and after quaternisation, considering that 1-iodooctadecane contains 18 carbon atoms. As quaternised PDMA (q-PDMA) contains more alkyl chains from the quaternisation agent, a higher ratio indicates a greater degree of quaternisation. Figure 4-21a shows the XPS C1s spectra of un-quaternised PDMA brushes. For comparison, Figures 4-21 b, c and d, show the spectra after quaternisation, where a significant increase in the C-C-C component can be seen at 285.0 eV, as the 1-iodooctadecane concentration increases from 25 to 100 µM. This indicates the presence of the 1-octadecyl group within the PDMA brushes, and that some of the pendant amine groups have become quaternised. More specifically, the DQ increased as the 1-iodooctadecane concentration increased from 13 to 100 µM, at which point further increases up to 250 µM resulted in DQ decreases (see Figure 4-22). The drop in DQ from using 1-iodooctadecane concentrations greater than 100 µM is attributed to the hydrophobicity of 1-iodooctadecane, which hinders the reaction between the alkyl halides and the tertiary amine groups of the polymer brushes[262] A recent study has also reported that the use of 1-iodooctadecane results in partially quaternised PDMA brushes.[130]

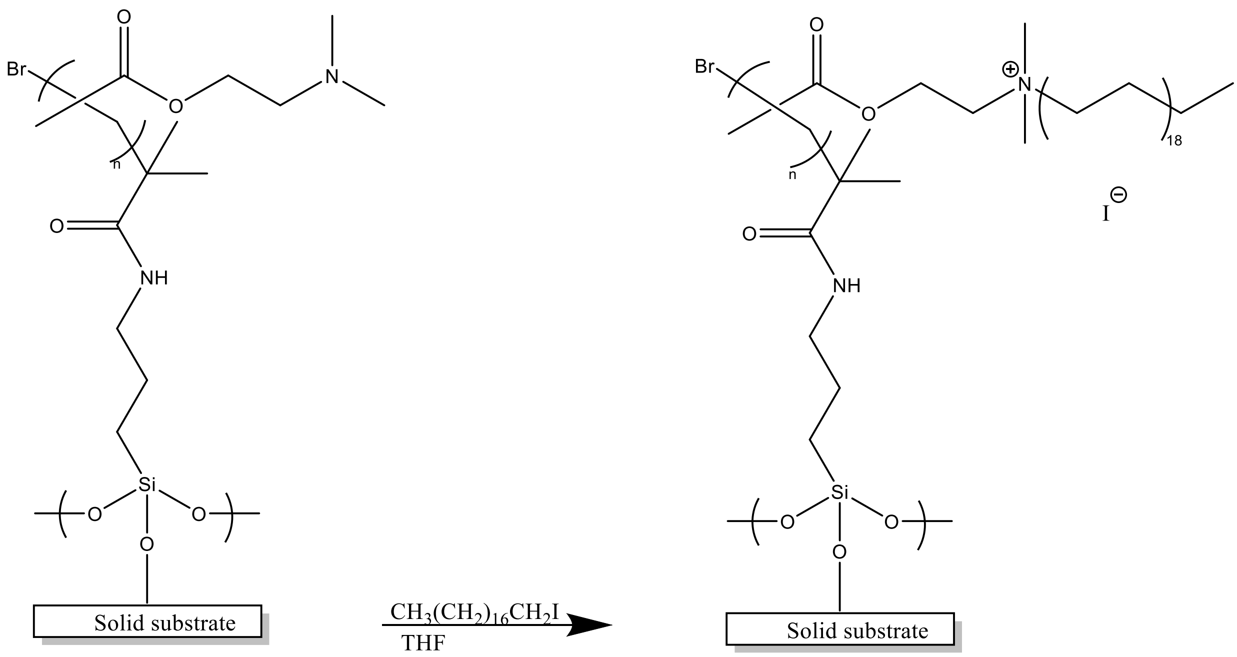

Figure 4-20: Quaternisation of PDMA brushes with 1-iodooctadecane in THF.

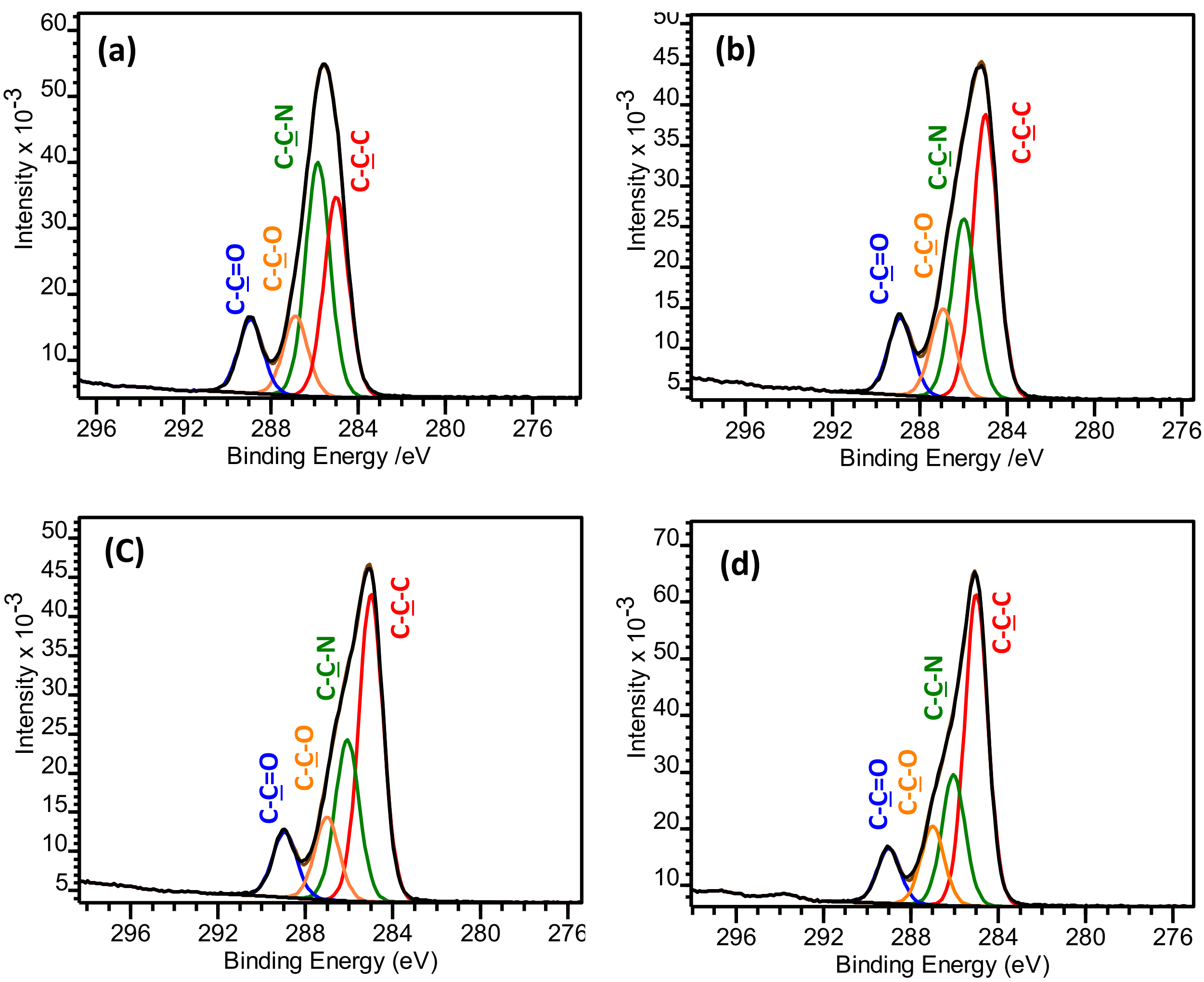

Figure 4-21: High-resolution XPS C1s spectra of (a) normal PDMA brushes, and q-PDMA brushes produced with THF containing 1-iodooctadecane in concentrations of (b) 25, (c) 50, and (d) 100µM.

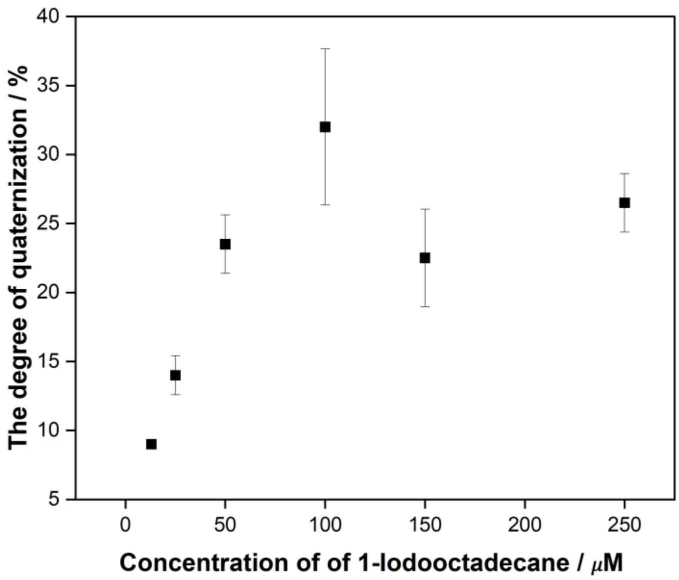

Figure 4-22: Degree of quaternisation as functions of 1-iodooctadecane concentration.

PDMA brushes quaternised to 22%, 35%, and 50%, were prepared using 1-iodooctadecane at concentrations of 25, 50 and 100 μM, respectively. Figure 4-23a shows the XPS spectrum for N1s obtained for the PDMA brushes before quaternisation, and Figures 4-23b**,** c and d the N1s spectra after quaternisation at the different 1-iodooctadecane concentrations**.** In normal PDMA, the XPS spectra for N1s show a single peak at 399.5eV, associated with the amine group on PDMA (non-quaternion). However, after quaternisation, a new peak appears in the N1s spectrum at around 403.3 eV, which is referred to as the N^{+} peak. This peak increases in intensity as the DQ increases from 22% to 35%, and then to 50%. This indicates the successful conversion of some of the amine groups into quaternary ammonium salts. These results suggest that long alkyl halide chains, such as 1-iodooctadecane, are unable to diffuse effectively within the dense hydrophilic polymer brushes, resulting in the PDMA brushes being only partially quaternised. [262]

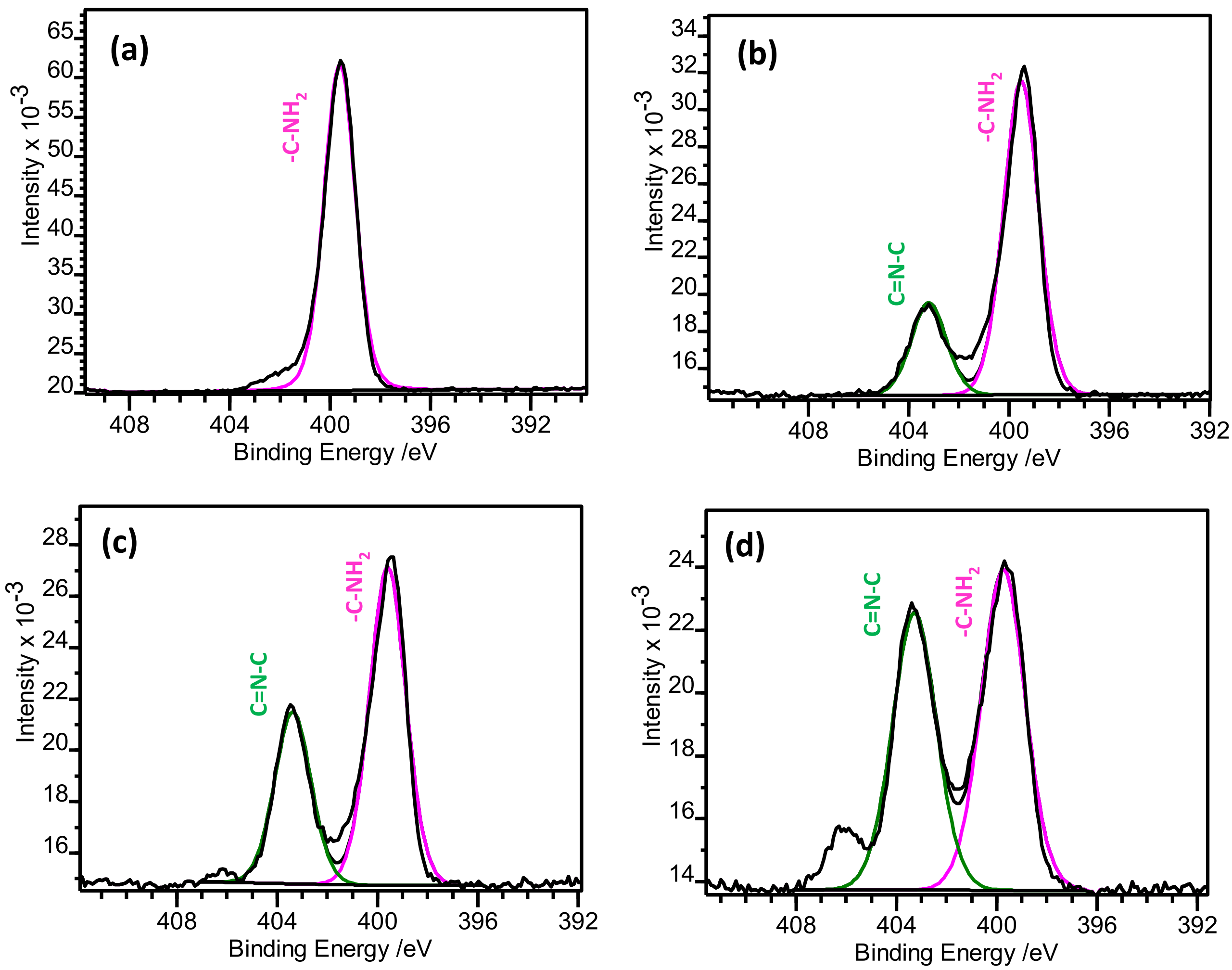

Figure 4-23: High-resolution XPS N1s spectra of (a) normal PDMA brush compared to q-PDMA brush with quaternisation degree of (b) 22 %. (c) 35 %. (d) 50 %.

4.3.3.6 Addition of chlorophyll to q- PDMA brushes

PDMA brushes with different DQs were functionalised with ZnChla. In Figure 4-24**,** the XPS N1s spectra of quaternised PDMA (q-PDMA) are shown for DQs of 28% and 50%. After ZnChla-functionalisation, the N1s peak at 398.5eV, which is attributed to nitrogen atoms in the chlorophyll ring, was more prominent for the q-PDMA with 28% DQ (Figure 4-24b) than with 50% DQ (Figure 4-24 d). This evidence from XPS spectra indicates that the N1s of q-PDMA with a higher degree of quaternisation reduce the binding of chlorophyll to the polymer. As a result, chlorophyll attachment to polymers can be controlled by changing the degree of quaternisation. Figure 4-25 shows chlorophyll UV-vis spectra attached to normal PDMA and q-PDMA at DQs of 28% and 50%. The Chl *a* absorption bands of q-PDMA were less intense than those of normal PDMA at the same concentration. In addition, there is no shift in the position of the main Qy band of chlorophyll, which indicates that Chl *a* is not aggregated in the polymer surface. This result supports the current hypothesis that the tertiary amine group of PDMA can coordinate with the metal ion at the centre of the chlorophyll.

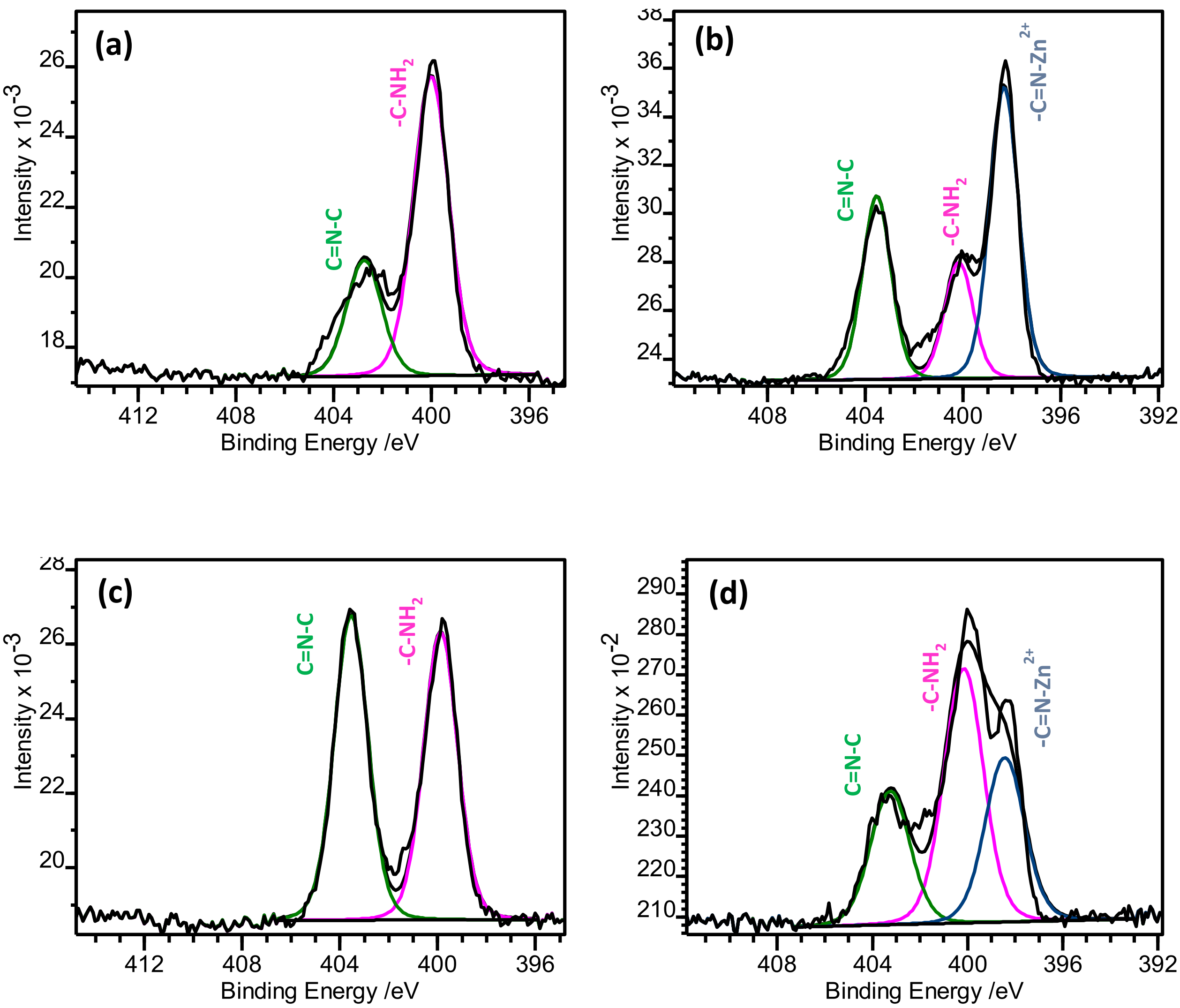

Figure 4-24: XPS spectra of N 1s before and after attachment of ZnChla to q-PDMA quaternised to 28% (a and b), as well as before and after attachment of ZnChla quaternised to 50% (c and d)

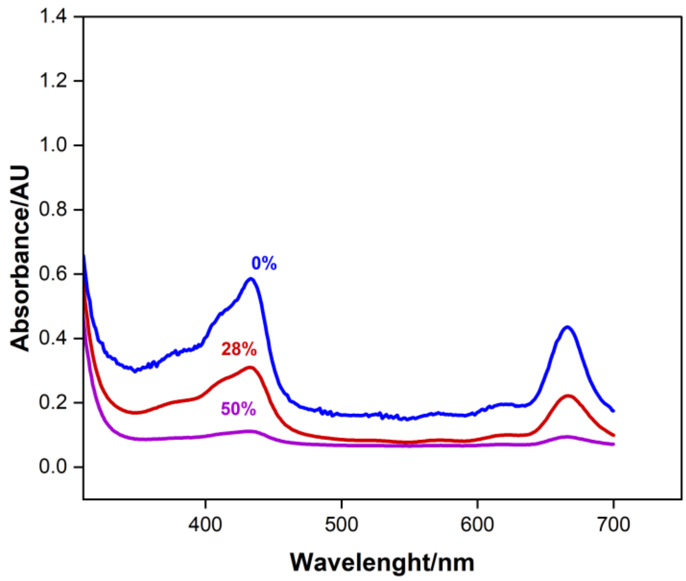

Figure 4-25: UV-vis adsorption spectra for ZnChla attached to normal PDMA and q-PDMA with the degree of quaternisation at 28% and 50%.

4.4 Conclusion

PDMA brushes were grown from bromine initiators by ATRP. XPS and SE confirmed the chemical structure and thickness of both the PDMA brushes and their BIBB APTES initiators on the surface, as well as the polymerisation kinetics of the PDMA brushes. The ellipsometric measurements showed the average initiator height to be approximately 2 nm, and that the height for the brushes reached a maximum height of 42 nm after 2 h of polymerisation. The latter result confirmed the successful growth of PDMA brushes from the initiators. AFM imaging of PDMA and their BIBB-APTES initiators confirmed the formation of high-quality films, in good agreement with ellipsometric measurements. Additionally, UV-vis spectroscopy indicated that Chl *a* was successfully attached to the PDMA brushes, and based on UV-vis data binding curves can be calculated for the attachment of Chl *a* to PDMA scaffolds. Chl *a* concentrations in the PDMA scaffolds were found to be as high as ~2 M, which is about 3 times the concentration found in biological light-harvesting complexes. The UV-vis and XPS data have demonstrated that chlorophyll density can be controlled in PDMA brushes, either by partially quaternising PDMA using 1-iodooctadecane, or by varying the chlorophyll concentration.

Chapter 5: Design of Plexcitonic Antenna Complexes

5.1 Introduction

The design of biomimetic light-harvesting systems has garnered significant attention in recent years. In the previous chapter introduced a novel approach that utilises a surface-grafted polymer scaffold to organise pigment molecules, such as chlorophyll, in three dimensions. This chapter builds upon that work to combine this new approach to the design of photonic materials with strong light-matter coupling, by integrating plasmonic elements into the materials. When molecules absorb light, it results in the transition of an electron from its ground state to a higher level of energy. Specifically, the transition usually occurs between the HOMO and the LUMO, with π-π^* electron transitions taking place within the chlorophyll ring. As the electron moves to the LUMO, a positive charge, or hole is left behind in the HOMO. The electron and hole, held together by Coulombic attraction, form an exciton.[167]

There are two types of transition. Transitions between HOMO-1 and HOMO to LUMO+1 generate intense absorption bands referred to as Soret bands. The second type involves transitions between HOMO-1 and HOMO to LUMO, resulting in weaker absorption bands, Qx and Qy. Absorption of red light leads to excitations in the Qx and Qy bands, while blue light absorption excites the Soret bands, driving the system into higher energy states (see Figure 5-1).

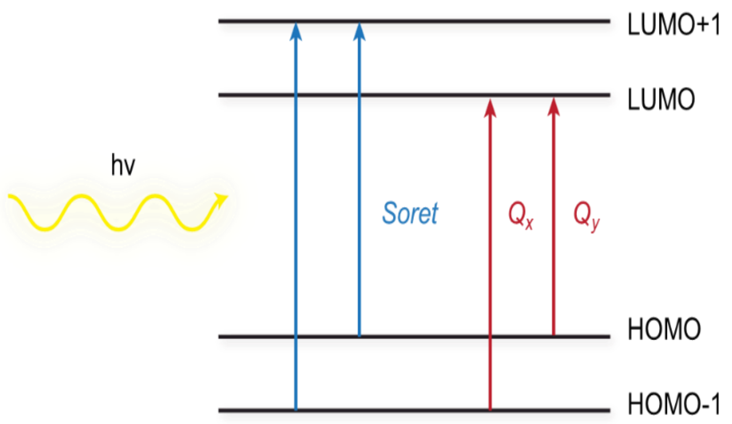

Figure 5-1: The electronic transitions Qx, Qy, and Soret of the chlorin ring are represented by the relative energies of their molecular orbitals.[167]

In molecular photonic materials, energy transfer between pigment molecules occurs through dipole-dipole interactions, specifically via Förster Resonance Energy Transfer (FRET).

However, a problem with this mechanism is that it involves incoherent excitation transfer. Thus, the rate of recombination of excitons is high and exciton diffusion lengths in polymer semiconductors are typically no larger than 10 nm.

A recent and novel approach for designing biomimetic light-harvesting systems involves the creation of pigment-polymer antenna complexes by covalently attaching chlorophyll to polymer scaffolds.[67] These scaffolds are grown from gold nanostructures using ATRP. By integrating LSPRs, plexcitonic antenna complexes are formed, where light and matter are strongly coupled. It is possible by using the plasmon mode to exchange coherent energy between pigments in the strong coupling regime.[263-265] Remarkably, plasmon-exciton coupling energies of up to 0.4 eV have been achieved, doubling the values observed in biological light-harvesting systems.[67]

The goal of this chapter is to combine the pigment-polymer complexes described in Chapter 4 with plasmonic on gold planar film. The polymer chemistry will first be characterised on planar gold surfaces, where factors such as the packing of thiols impact the packing density of pigment-polymer complexes. The packing density is crucial, as it influences the reaction rate between the pigment molecules and the scaffold. Therefore, this study will examine the polymerisation kinetics of PDMA on gold surfaces and the binding of chlorophyll before investigating the strong coupling of pigment-polymer complexes grown on gold nanostructures.

The density of chlorophyll within the polymer film is hypothesised to be controllable by adjusting the density of grafted polymers on the surface. The performance of plexcitonic antenna complexes depends on achieving the optimal grafting density, which is regulated by using a mixture of two self-assembled monolayers (SAMs), DTBU (bis[2-(2-bromoisobutyryloxy) undecyl] disulfide) and 11-mercaptoundecanol (MUL). It is possible to precisely control the grafting density of polymers by varying the ratio of DTBU to MUL. In this work, different SAM ratios were employed to control the density of PDMA brushes and, consequently, the amount of chlorophyll attached to the surface, as illustrated in Figure 5-2.

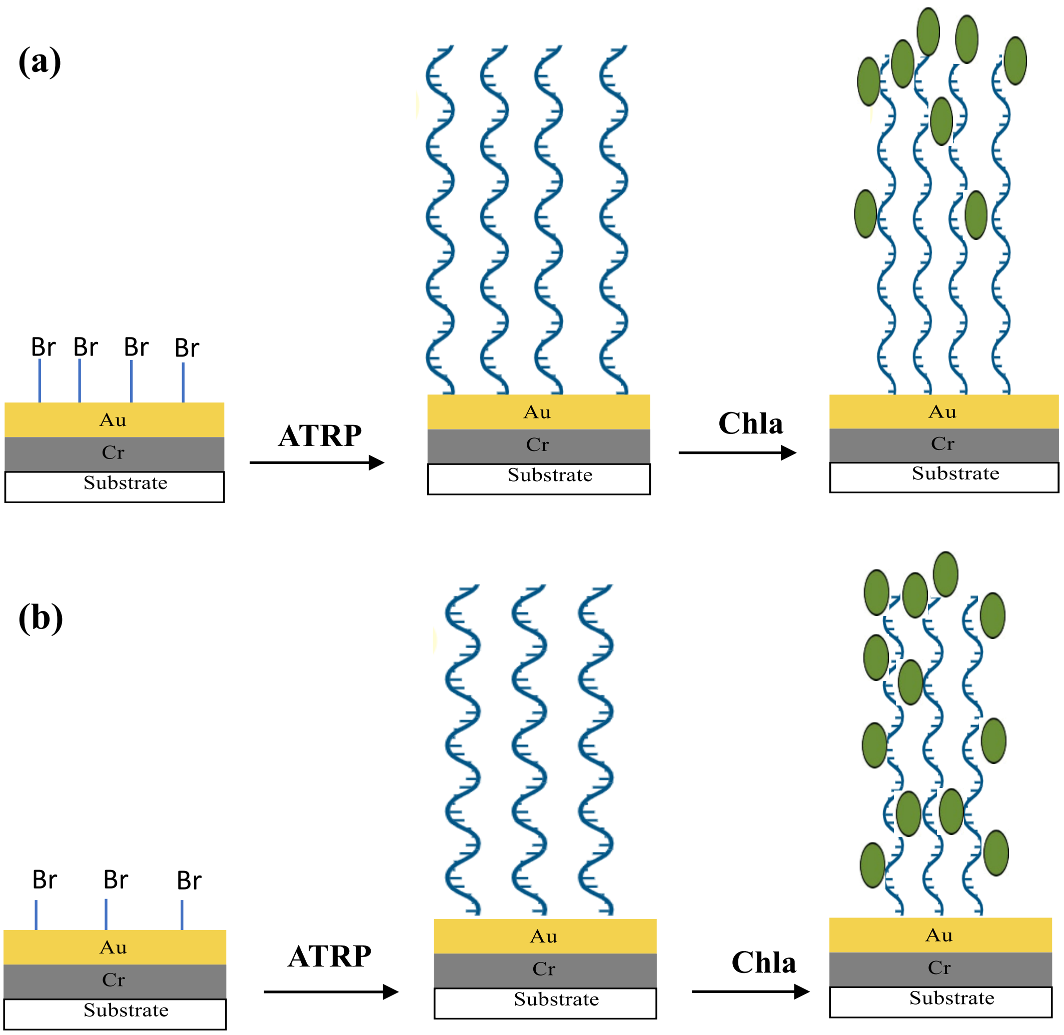

Figure 5-2: Schematic illustration of the growth of PDMA brushes at full density (a) and reduced density (b) using a mixture of DTBU and MUL, followed by ZnChla attachment.

5.2 Materials and methods

Glass coverslips (22 x 64 mm and thickness = 1.5 mm) were obtained from Menzel-Gläser. A Carousel 12 Reaction station (Radleys, UK) was used to prepare polymer brush samples under nitrogen. Hydrogen peroxide (30%) and sulfuric acid (95%), dimethylformamide (> 99%), magnesium sulfate anhydrous, (≥ 62, 70%), isopropanol-2-ol (99.5 %) HPLC grade) and acetone (99.8%, HPLC grade) were purchased from Fisher Scientific (Loughborough, UK). Ethanol, absolute, (≥ 99.8%), silica gel, 40-63 μm particle size were obtained from VWR international (Lutterworth, UK). Chromium chips (99%), gold wire (99%), copper (I) bromide (≥99%), 2 (-dimethylamino) ethyl methacrylate (DMA) (98%),1,1,4,7,10,10 hexamethyl triethylenetetramine (HMTETA) (97%), sodium hydrogen carbonate,(≥ 99%), petroleum ether 40-60 ^{O}C, methanol,(99.99%), zinc acetate dihydrate, (99.99%), bis[2-(2-bromoisobutyryloxy) undecyl] disulfide (DTBU), (97%), 11-mercapto-1-undecanol (97%) and sand low iron were purchased from Sigma-Aldrich UK (Gillingham, UK). Spinach leaves were purchased from a local supermarket. All materials were used as received from the manufacturer without further purification. Deionised water (resistance >15.0 MΩ cm) was obtained from an Elga Pure Nanopore system. Copper bromide was stored under a vacuum, and the DMA was stored at 4°C after the removal of the inhibitor by filtration through a small column of basic aluminium oxide.

5.2.1 Cleaning of glassware and substrates

Piranha solution, (a strong oxidising agent used to clean substrates and glassware), was used to remove all organic residues. It is made by mixing 30% hydrogen peroxide and 95% concentrated sulfuric acid at a ratio of 3:7. The glassware was treated with piranha solution, rinsed with deionised water until pH testing with litmus paper indicated neutral, and dried overnight at around 80 °C. The tweezers and suba-seals were cleaned using the same procedure described in Chapter 3.

5.2.2 Formation of gold substrates by thermal evaporation

The metal films were deposited onto glass substrates using the Edwards Auto 306 bell jar vacuum coating system. The deposition process began by placing clean glass slides on a stage above a current source within the vacuum chamber. The system was then evacuated to a pressure of less than 3 x 10^{-6} mbar. Optimal deposition conditions typically required a pressure of around 8 x 10^{-7} mbar. The evaporation of the metal sources, such as chromium (Cr) and gold (Au) was carried out using a high-vacuum chamber containing a filament or crucible. In this experiment, a thin layer of chromium (5-10 nm) was first deposited, followed by a thicker layer of gold (20-40 nm). As soon as the desired thickness was achieved, the current was gradually reduced, and the coated glass substrates were allowed to cool for at least 30 min before being removed from the chamber and placed in glass tubes. The detailed procedure is described further in Chapter 3.

5.2.3 Formation of self-assembled monolayers on gold surfaces

To prepare the initiator on the gold surface, the freshly coated gold slides were immersed in a solution of DTBU dissolved in ethanol. This immersion process was carried out for at least 18 hours, with the glass tubes containing the slides placed in a refrigerator at a temperature of 4°C. This procedure resulted in the formation of BIBUDT-functionalised gold surfaces. After the immersion, the gold slides were removed from the solution using tweezers, rinsed with EtOH to remove any residual DTBU, and then dried under a stream of nitrogen gas. A diamond-tipped scribe was used to carefully cut the functionalised substrates into smaller pieces, each approximately 1 cm^2 in size. Finally, the functionalised substrates were stored in the ethanol solution and placed in a refrigerator at 4 °C until they were needed for experiment use.

5.2.4 Formation of the mixture of DTBU and MUL self-assembly monolayers on gold

The DTBU initiator-functionalised adsorbate was co-adsorbed with 11-mercapto-1-undecanol (MUL) to control the grafting density of surface-grafted polymer scaffolds on gold surfaces. Three different mixtures of DTBU to MUL were used to produce the self-assembled monolayers, containing DTBU mole fractions of 0.5, 0.25, or 0.11. The molar fraction of the adsorbed initiator sites within the film was determined from the C1s peak area ratios and found to be 0.52, 0.24, and 0.11, respectively. The compositions of the resulting SAMs for the three distinct DTBU-to-MUL mixtures closely resembled the solutions from which they originated.

5.2.5 ATRP synthesis of PDMA brushes onto a gold substrate

ATRP was used to grow the polymer brush from the DTBU-functionalised gold substrate. In this experiment, DMA monomers were dissolved in DMF, using HMTETA as a ligand and Cu(I)Br as a catalyst in the ATRP reaction. Five mL of monomer/catalyst solution was added to each DTBU-functionalised gold sample in Schlenk tubes. After the desired polymerisation time had passed, the slides were removed from the solution. The functionalised slides were then washed repeatedly with IPA and ethanol to remove any excess catalyst or monomer. Dry PDMA brushes were grown kinetically at 50 °C at rates of 10 min to 1 h. Chapter 3 describes the detailed procedure in more detail.

5.2.6 Extraction of Chlorophyll from spinach

The ZnChla synthesis is described in detail in Chapter 3. Acetone was first used to extract the dark green pigment from the spinach leaves, and then the dark blue pigment was dissolved in acetic acid while stirring for three hours to obtain pheophytin a. The pheophytin was converted into ZnChla under reflux in an argon atmosphere for 1 h, using zinc acetate dehydrates dissolved in methanol.

5.2.7 Surface characterisation

The water contact angles were determined to investigate the hydrophobicity and hydrophilicity of the surface before and after the preparation of DTBU SAMs on the gold surface, using a Rame-Hart goniometer model 100-00 (Netcong, NJ, USA). A minimum of three drops of liquid were measured and averaged for each sample.

A Cary 50 UV-visible spectrophotometer (Agilent Technologies, USA) was used to measure UV-visible absorption spectra between 350 and 800 nm.

Alpha-SE ellipsometers were used for ellipsometry (J. A. Woollam Co., Lincoln, NE, USA). A He-Ne laser (λ = 633 nm) with a 70° incidence angle was used as the light source. Complete EASE software (v. 6.6) was used to fit the ellipsometric data from the thin continuous gold films after functionalization with the DTBU SAMs. They were then grafted with PDMA brushes, and the PDMA brushes were attached to Chl *a*. For each sample, three locations were measured and averaged, and the mean standard deviation was used to estimate the thickness of the thin film.

The spectra were collected using an XPS provided by Kratos Analytical, Manchester, UK. CASAXPS (v. 2.18 software) was used to analyse the XPS data.

AFM images were collected using a Digital Instruments Nasoscope 5 Multimode Atomic Force Microscope. All experiments were conducted in the open air at approximately 20°C. Nasoscope Analysis (v.1.5) was used to analyse the AFM data.

5.3 Results and discussion

5.3.1 Formation and characterisation of the initiator-functionalised substrates

As DTBU adsorbs at the gold surface, the disulphide linkage breaks so that one mole of DTBU in solution yields two moles of bromine-terminated adsorbates at the surface, as shown in Figure 5-3**.**

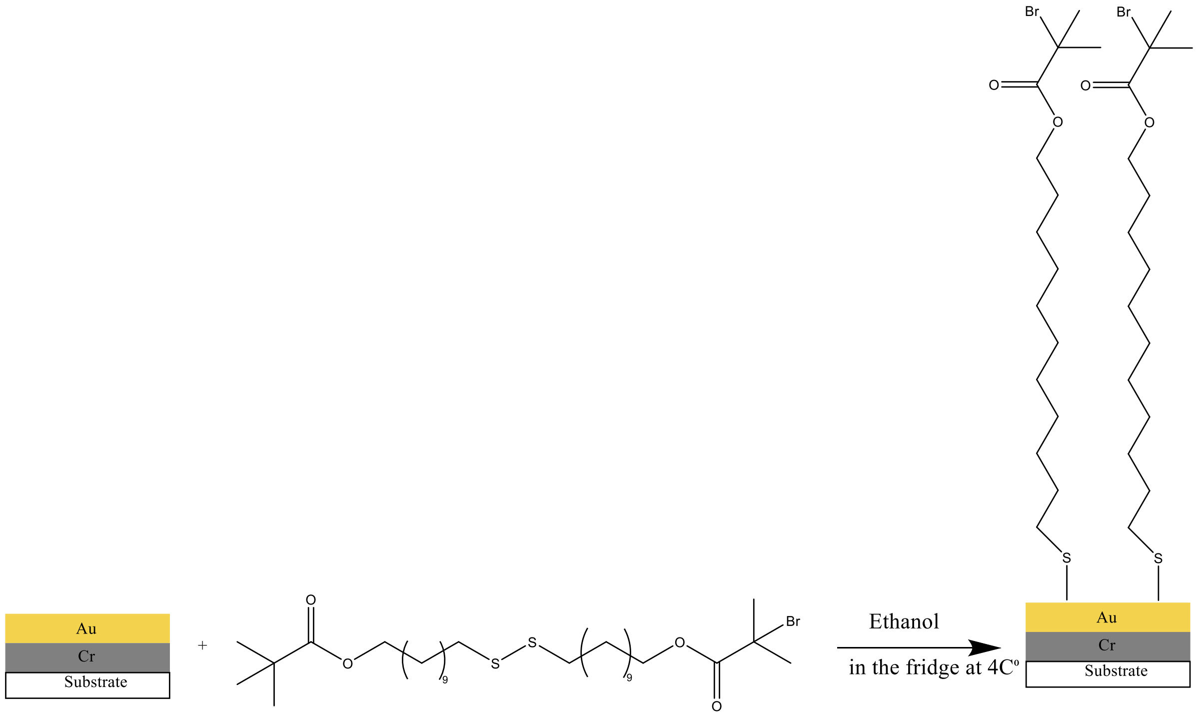

Figure 5-3: Schematic illustration of DTBU monolayer adsorption onto the gold substrate surface.

DTBU monolayers were characterized using a variety of surface analysis techniques including WCA, XPS, SE, and AFM. After cleaning with piranha solution, the WCA of the glass substrates was 7 ± 2° because the surfaces contained hydroxyl groups and a native oxide layer,[266] whereas the WCA obtained for the gold-coated surface after the adhesion of gold onto the glass was approximately 71° ±1 which is consistent with those reported in the literature. [267] The contact angle of a clean gold surface is very low because clean metal surfaces have high surface-free energies. However, gold surfaces quickly become contaminated by adsorbates from the atmosphere. This rapid contamination caused the contact angle of a clean gold surface to reach 71° ±1 in a short time.

After the adsorption of DTBU onto the gold surface in the absence of a diluent, the contact angle was found to be 74 ± 1° (see Table 5-1), consistent with the formation of a bromine-terminated SAM. There is an abundance of published work that indicates that bromine functionalised surfaces typically exhibit water contact angles in the range between 70º and 75º.[118, 268] The SE results indicated that the average thickness of the gold film was approximately 38.2 ± 1 nm, while that of the monolayers formed by the adsorption of DTBU was 0.9 ± 0.3 nm.

Table 5-1: Water contact angles and film thicknesses data of DTBU SAMs and gold clean surface, as a function of the surface chemistry changes.

Samples	Contact angle / º	Thickness/nm
Piranha -cleaned glass	7 ± 2	-
Bare gold surface	71±1	38.2 ±1
DTBU SAM	74±1	0.9 ± 0.3

Tapping mode AFM was used to characterise the gold-coated substrates. Figure 5-4 displays AFM images of the gold surface before and after functionalisation with DTBU. The surface roughness of the clean gold film was found to be approximately 0.47 ± 0.1 nm, due to the presence of large crystallites (see Figure 5-4a). Following the formation of the DTBU monolayers, the roughness was slightly reduced to 0.38 ± 0.1 nm, resulting in lower average diameters of the gold crystallites (see Figure 5-4b).

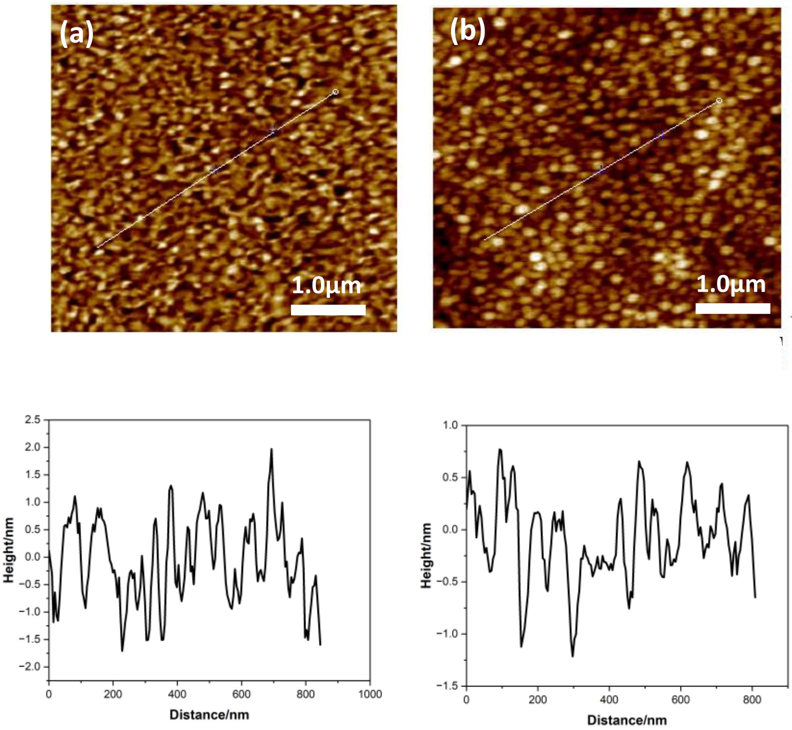

Figure 5-4: Tapping mode AFM height image (1µm × 1µm) for (a) gold-coated substrate and (b) gold-coated substrate after functionalised with DTBU with their profile section.

The high-resolution XPS C1s, S2p, O1s, Au4f, and Br3d spectra of DTBU monolayers adsorbed on a gold surface are shown in Figure 5-5**.** The Au4f spectrum of DTBU monolayers shows two peaks attributed to spin-orbit coupling (see Figure 5-5a). The $Au4f_{7/2}$ peak (84.3 eV) and the $Au4f_{5/2}$ peak (88.2 eV). The C1s spectrum displays three components with binding energies 285.0, 286.8, and 289.1 eV, which are attributed to C-C-C/C-C-S, C-C-O/ C-Br, and O-C=O, respectively, as shown in Figure 5-4 b. The S2p spectrum exhibits a doublet peak at 162.3 eV and 163.8 eV, attributable to the $S2p_{1/2}$ and $S2p_{3/2}$ peaks that result from spin-orbit coupling as shown in Figure 5-5 c. The O1s spectrum was fitted with two peaks with binding energies of 532.3 eV and 533.8 eV corresponding to C=O and C-O, respectively, (see Figure 5-4 d**)**. However, the Br3d peak of the DTBU SAMs was noisy and partially overlapped with signals from the $Au5p_{1/2}$ peak (see Figures 5-5 e**).**

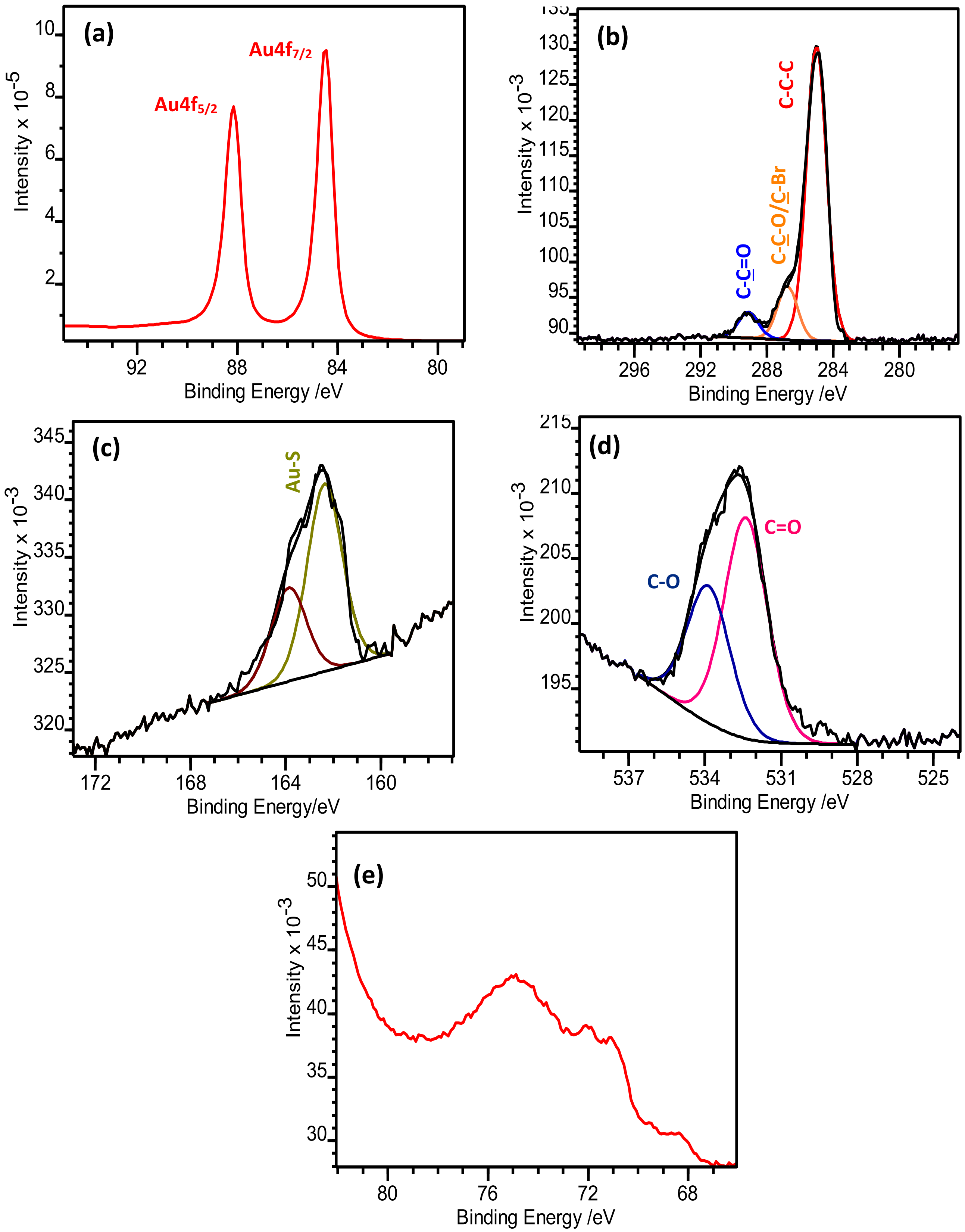

Figure 5-5: High-resolution XPS spectra of a) Au4f, b) C1s, c) S2p, d) O1s, and e) Br3d spectra of the DTBU on gold surface.

5.3.2 The kinetics of PDMA growth onto gold functionalised DTBU

ATRP procedure was used to grow PDMA brushes from DTBU-functionalised gold substrate as displayed in Figure 5-6. XPS and AFM were used to characterize the grafting of polymer brushes. The polymer thickness on the DTBU-functionalised gold substrate was measured as a function of polymerisation time, using SE as illustrated in Figure 5-7.

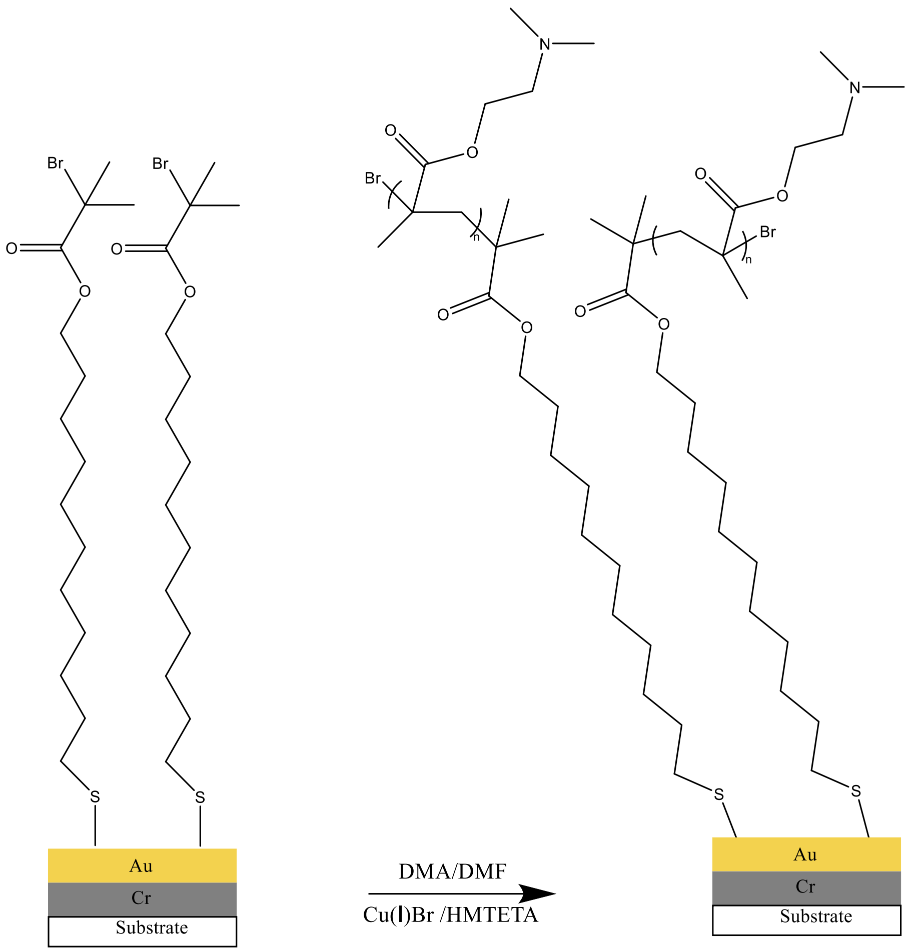

Figure 5-6: Schematic diagram showing the growth of PDMA brushes from gold surfaces by ATRP.

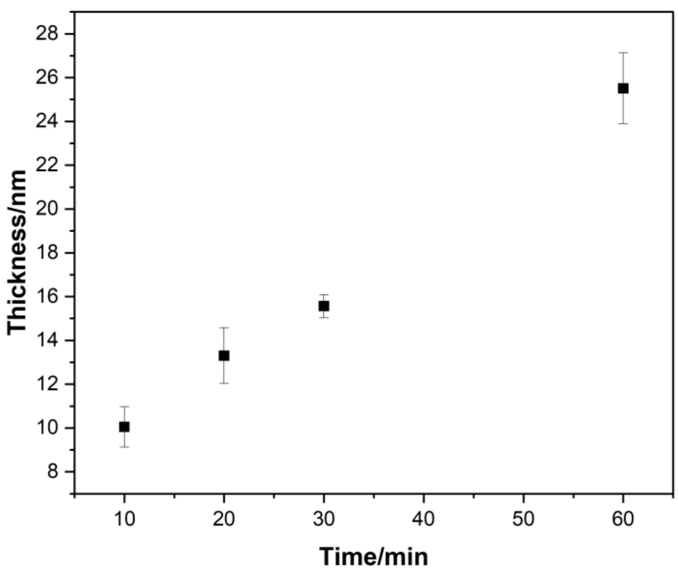

Figure 5-7: Ellipsometric dry thickness of PDMA brush as a function of polymerisation time.

PDMA brush growth was conducted at 50 °C instead of 90 °C due to poor thiol initiator layer stability. Following 1 h of polymerisation at 90°C, PDMA layers were thin with a thickness of 10 nm, while at 50 °C, stable polymer layers were formed. The thickness of PDMA on the gold-coated surface grew nearly linearly up to 30 min, reaching approximately 26 ± 2 nm after 1 h (see Figure 5-7). According to the same polymerisation time (1h), this value is lower than the 35 nm growth observed for PDMA from the BIBB-APTES film. As a result of the poor stability of the thiol initiator layer at elevated temperatures. In contrast, when the temperature was reduced to 50 °C, stable polymer layers formed, though with a slightly reduced thickness due to a slower kinetic mechanism.

After 1 h of polymerisation, the mean surface roughness of the PDMA polymer grown from DTBU on a gold-coated surface was estimated as 0.33 ± 0.04 nm (see Figure 5-8). This value is consistent with the results obtained for PDMA on the BIBB-APTES film which was found to be ≤ 0.3 nm.[257]

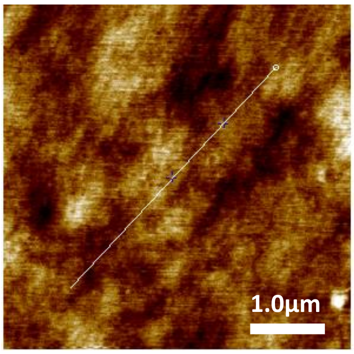

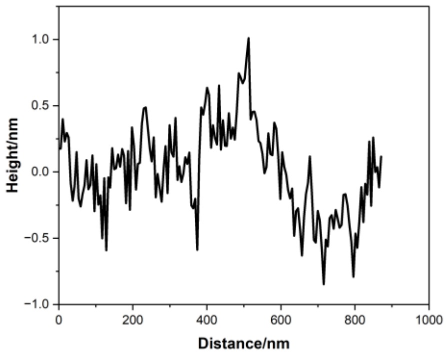

Figure 5-8: Tapping mode AFM height image (1μm × 1μm) for PDMA (1 h polymerisation time) on a gold-coated surface functionalized with DTBU, simultaneously with its profile section.

High-resolution XPS spectra of the PDMA brushes were obtained after a polymerisation time of 1 h **(**see Figure 5-9). The Au4f XPS spectrum exhibits peaks at 84.3 eV and 88.2 eV corresponding to the $Au4f_{7/2}$ and $Au4f_{5/2}$ peaks, respectively, as displayed in Figure 5-9 a. As shown in Figure 5-9 b, the C1s spectrum was fitted with four components with binding energies of 285.0, 286.0, 287.1, and 288.8 eV, corresponding to C-C-C, C-N/ C-Br, C-C-O, and C-C=O, respectively. The experimental ratios calculated from the fitted C 1s spectrum were 2.6: 2.7: 1.1: 1, which are very close to the theoretical ratios of 3 :3 : 1: 1. A single peak was observed in the N1s spectrum, corresponding to the amine group in PDMA as shown in Figure 5-9 c. A doublet peak was fitted to the XPS spectrum of O1s, with binding energies of 532.3eV for C=O and 533.7eV for C-O **(**see Figure 5-9 d**).**

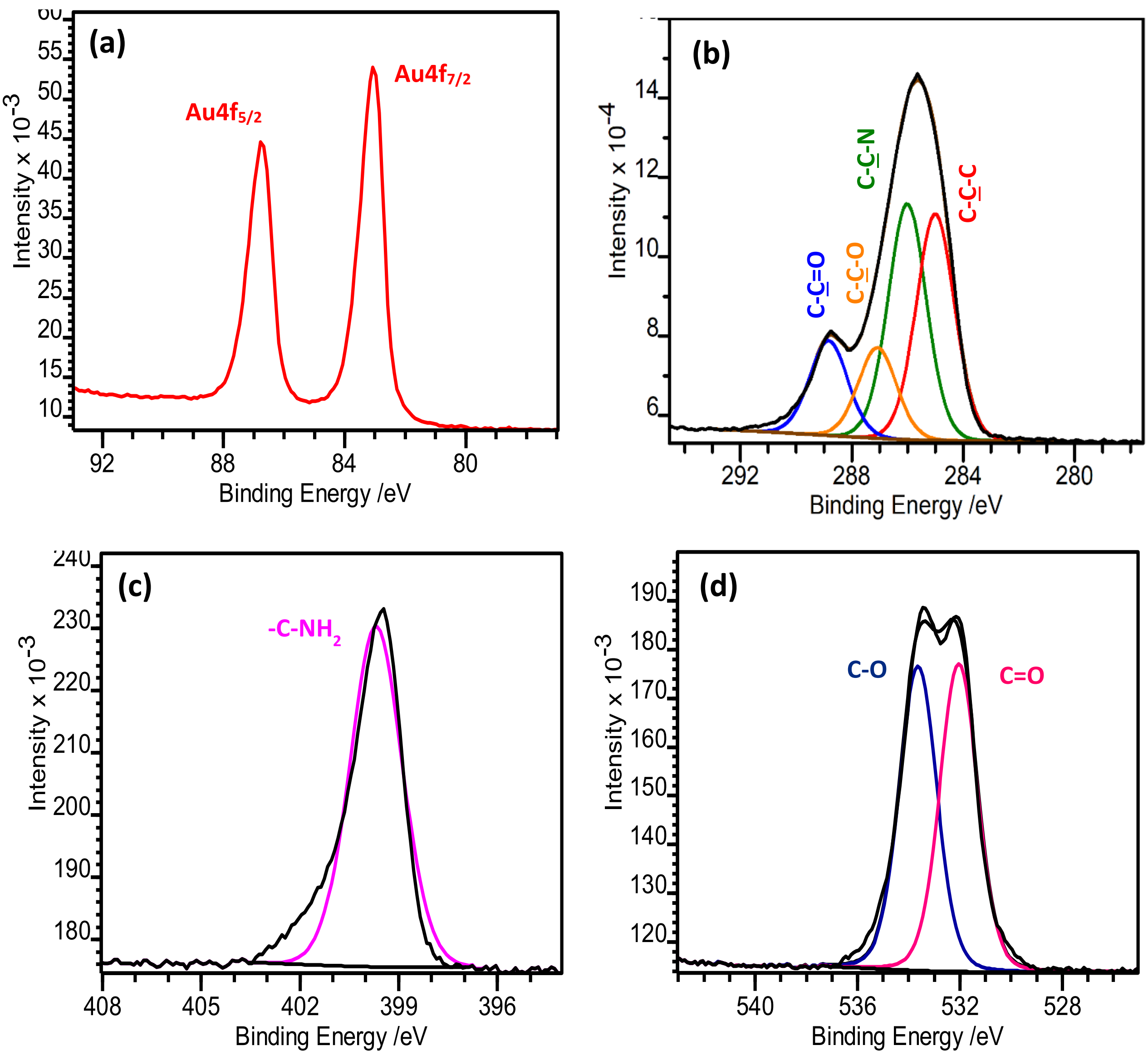

Figure 5-9: XPS high-resolution spectra of PDMA brushes (1h polymerisation) on the gold surface, (a) Au4f spectrum (b) C 1s spectrum(c) N 1s spectrum, and (d) O 1s spectrum.

5.3.3 Characterisation of mixed SAMs on gold-coated surfaces.

It was hypothesised that the Chl *a* density could be regulated by controlling the grafting density within the surface-grafted polymer films. DTBU and 11- MUL were mixed in varying proportions to form mixed SAMs on gold. When DTBU is adsorbed onto gold, it dissociates into two bromine-terminated alkyl thiolates with the MUL acting as an inert diluent. Increases in the proportion of diluent in the SAM result in reductions in chain grafting density, leading to decreases in the mean thickness of the surface grafted. Both reagents form thiolates of similar thickness after adsorption onto gold. There is evidence in the literature that when mixed SAMs are formed by adsorption from solutions containing mixtures of two different thiols, the composition at the surface is not identical to that of the solution from which the SAM is formed.[269, 270] Thus, XPS analysis was performed on the mixed SAMs to determine their compositions. The high-resolution spectra for DTBU, MUL, and mixed SAMs, are shown in Figure 5-10. The Br3d spectra for these SAMs were found to be noisy and the Br3d spectrum overlapped partially with the $Au5p_{1/2}$ peak. Consequently, the C1s spectra were used for quantitating the initiator-containing SAMs rather than the Br3d spectra. Figure 5-10 a and b display the C1s, O1s and S2p spectra for DTBU and MUL. There are three components in the C1s spectrum of DTBU SAMs with binding energies of 285.0, 286.9, and 289.2 eV, corresponding to C-<u>C</u>-C/C-<u>C</u>-S, C-<u>C</u>-O/C-Br, and O-<u>C</u>=O (see Figure 5-10 a**)**. In the C1s spectrum of 11-MUL SAM, the C-<u>C</u>-C/C-<u>C</u>-S peak appears at 285 eV, with another small peak at 286.9 eV attributable to the carbon atom adjacent to the hydroxyl group as shown in Figure 5-10 b. The XPS high-resolution spectra for mixing DTBU and MUL are 50%, 25%, and 10% as shown in Figure 5-10 c**.** Appendix 2 provides the binding energy details of the XPS-fitted peak for DTBU SAMs and MUL SAMs. It also shows the C1s component for the mixture of DTBU + MUL, with their three-mole fractions of 0.5, 0.25 and 0.11 as well as their % atomic compositions.

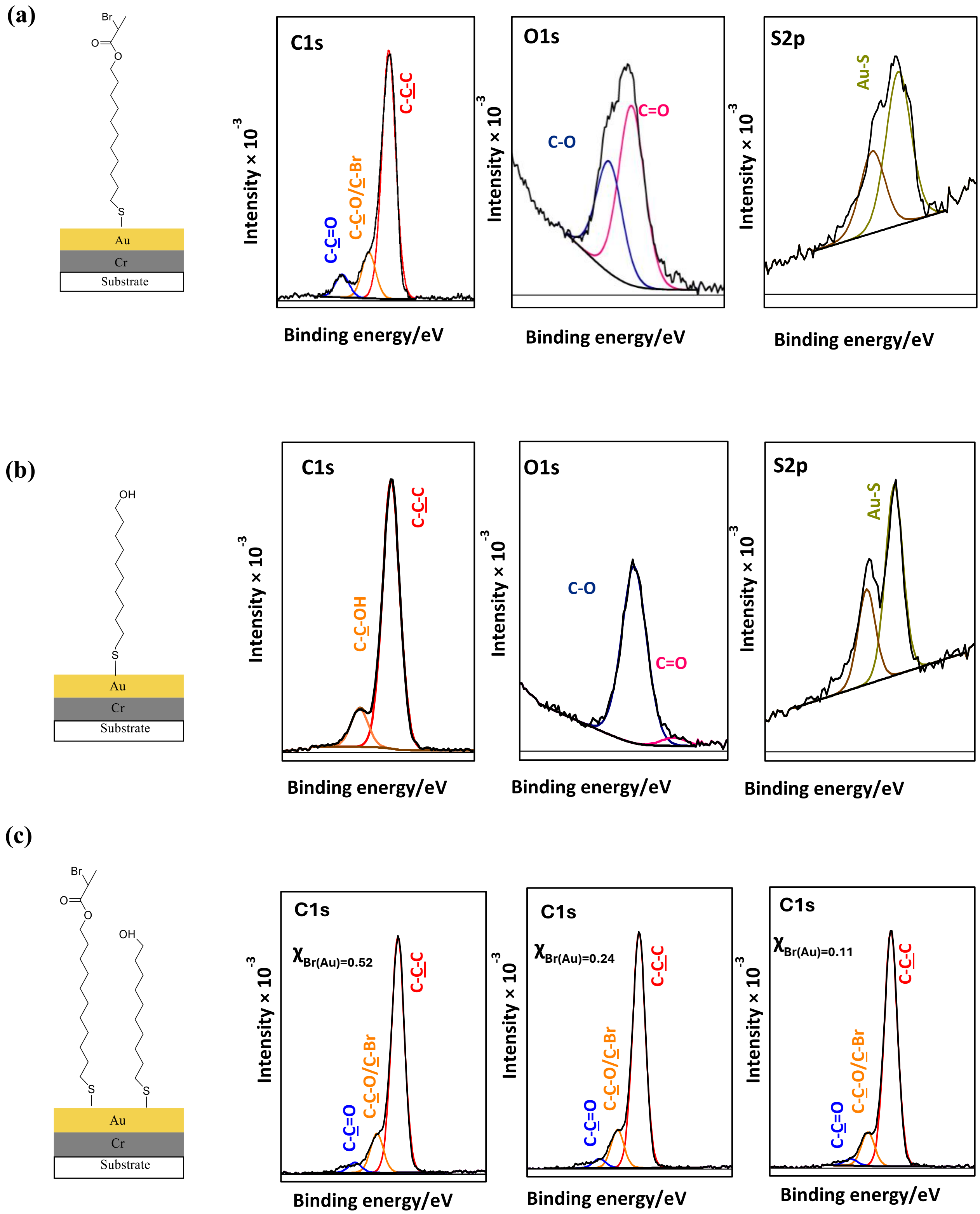

Figure 5-10: High-resolution XPS spectra of C1s, O1s, and S2p on gold surfaces, (a) DTBU, (b) MUL SAMs, and (c) the C1s spectra of a mixture of DTBU and MUL on gold, with molar fractions of the initiator of 0.52, 0.24 and 0.11 respectively.

The carbonyl functional group is exclusively found in DTBU. Therefore, the molar fraction of the adsorbed initiator site ($\chi_{\mathrm{Br(Au)}}$) within the film can be calculated through analysis of the C1s peak area ratios:

$$\chi_{\mathrm{Br(Au)}} = \frac{\chi_{Br(sol)} \times A_{exp}}{A_{calc}} \qquad \text{(Eq. 5.1)}$$

In this equation, $\chi_{Br(sol)}$ refers to the molar fraction of bromine-terminated sites in the solution, A_{exp} refers to the experimentally obtained ratio of fitted peak areas for the C1s carbonyl group compared to the C-C peak, and A_{calc} refers to the estimated ratio of the functional groups in the SAMs, based on the assumption that the surface composition is similar to that of the solution.[268]

5.3.4 Addition of Chlorophyll to Polymer Brush Structures

PDMA brushes were used to support ZnChla molecules within the plasmon mode to organise excitonic molecules of Chl *a*. Figure 5-11 displays a schematic illustration of the formation of plexcitonic antenna complexes by incubation of PDMA-grafted from continuous gold film samples in ZnChla solutions. In this process, ZnChla binds to PDMA through coordination bonds.

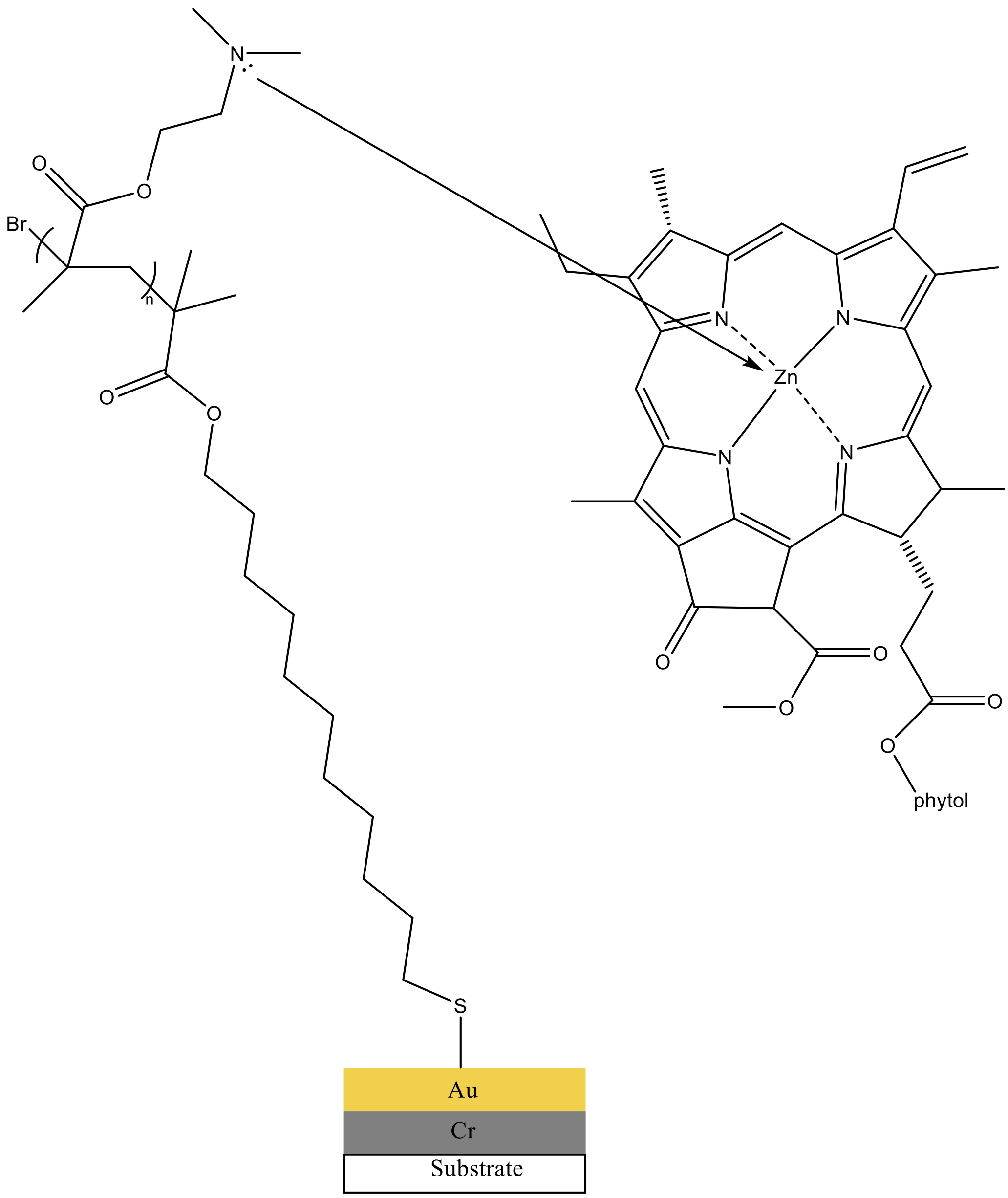

Figure 5-11: Schematic representation of chlorophyll-binding to the amino group in PDMA brushes grown from the gold-coated surfaces.

PDMA brushes grown on gold surfaces (polymerisation time of 1 h) were immersed in solutions of Chl *a* at a concentration of 20 μM. These samples were characterised using SE and XPS**.** For experimental ellipsometric measurement, Ψ (red line) and Δ (green line) data and resultant best-matched model fit (black dashed line) are shown in Figures 5-12a and b for PDMA grown on Au surfaces, (full density) before and after attachment to Chl *a*.

Modelling of the data shown in Figure 5-12a (brush only) indicated that the PDMA brush used had a thickness of a ~ 28 nm. The addition of Chl *a* introduces additional features to the spectra, arising from the characteristic absorptions of Chl *a* at ~440 nm and ~660 nm. A resulting increase in brush thickness is also observed to ~40 nm after the addition of Chl *a* to the brush which results in an extension to the polymer and the observed increase in thickness, see Figure 5-12b. The resultant calculated refractive index, n, and extinction coefficient, k, for two samples, are shown in Figure 5-12c and d for PDMA brush on Au substrate before and after attachment to Chl *a*, where n (red line) and k (green line). The n and k in Figure 5-12c show the transparent behavior dictated by the Cauchy model, whereas in Figure 5-12d, k shows the two characteristic absorption peaks at ~430 nm and ~660 nm arising from the Soret band and Q-band respectively. Overall, the results show the strong contribution of Chl *a* to the ellipsometric data and can effectively be incorporated into PDMA polymer brush systems grown on Au surfaces. Appendix 2 provides details on the models used for PDMA brushes grown on Au surfaces before and after attachment by Chl *a*.

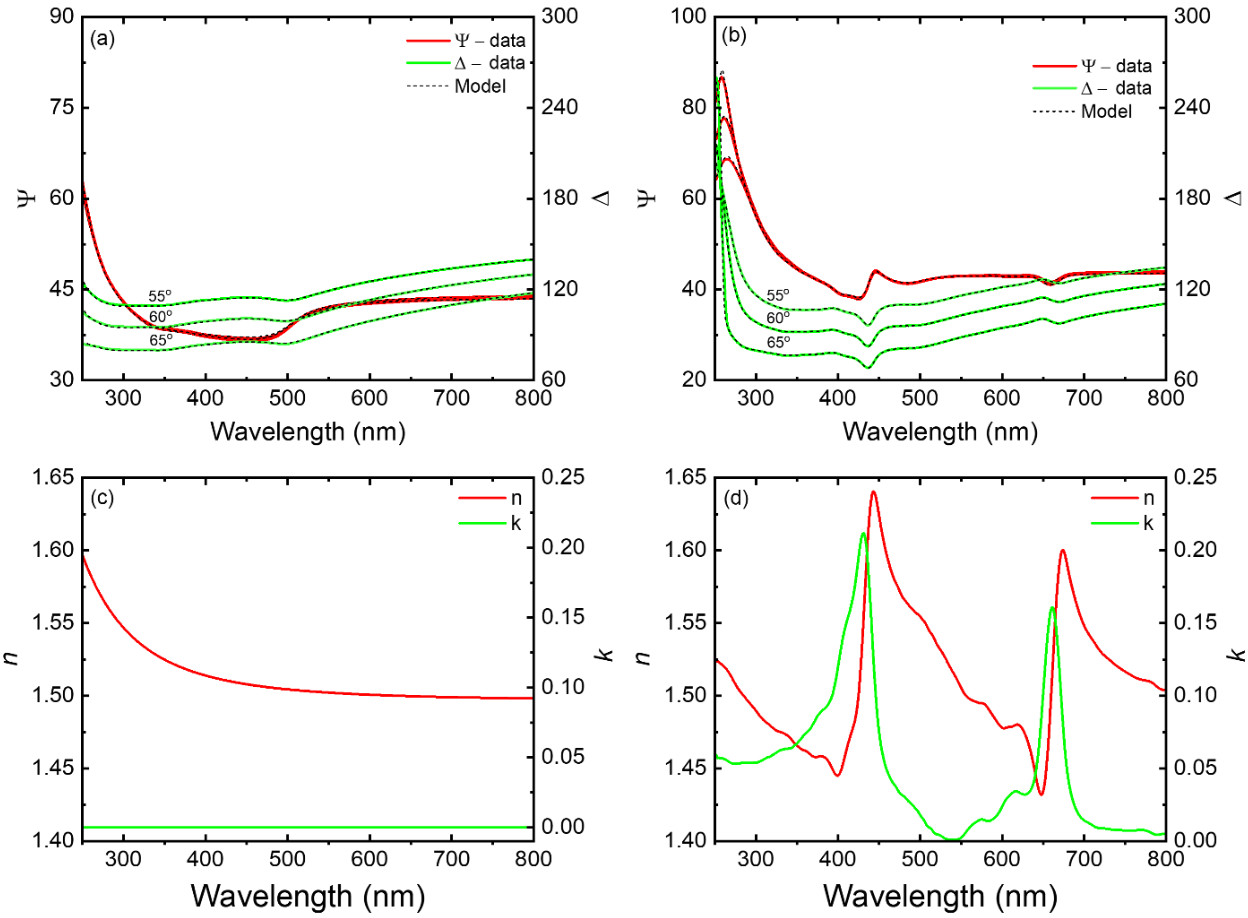

Figure 5-12: The ellipsometry data for the PDMA brush before (a) and after (b) attachment of the Chl *a*, where experimental Ψ data is shown by the red line, Δ data by the green line, and best-matched model by the black dashed lines. The resultant calculated complex refractive index for the PDMA brush before (c) and after (b) attachment of the Chl *a*, where n red line and k green line.

For XPS measurement**,** Figure 5-13 displays the XPS spectra of the Zn2p and N 1s components before and after attachment of ZnChla to a fully dense brush layer, grown from a SAM of DTBU. It is worth to menschen that during the isolation of Chl *a* from spinach, it replaced the Mg^{2+} found in the Chl *a* in the plant with Zn^{2+}. Hence, the presence of the Zn component confirms its attachment to the surface. As prepared, the polymer does not show a Zn signal (Figure 5-13 a). However, a distinct peak of Zn2p appears after ZnChla attaches to PDMA, as shown in Figures 5-13 a and b. A single component with a binding energy of 399.5 eV was observed in the N1s spectrum of the polymer, and attributable to the presence of the amino group in PDMA, as shown in Figures 5-13 c. After adding ZnChla to PDMA, the N1s spectrum of the fully dense brush showed peaks at 399.6 eV ($-NH_2$) and at 402.1 eV ($-NH^{3+}$). A minor peak is observed at 398.1 eV, (see Figure 5-13 d**)**, which can be attributed to the nitrogen atoms located at the centre of the chlorophyll ring (the tetrapyrrole nitrogen atoms). The Chl *a* peak in the N1s spectrum is small, because of the high grafting density of PDMA on gold, which may reduce the amount of chlorophyll attached.

Prior research has shown that chlorophyll-binding can be regulated by controlling the polymer's grafting density.[271] The objective of that study is to regulate the grafting density of PCysMA chains through the use of DTBU and MUL mixtures to achieve a higher concentration of chlorophyll attached to the polymer. In line with previous research, which demonstrated that decreasing the density of polymer grafting enhances the attachment of chlorophyll to the polymer surface, it will expect to obtain similar outcomes with PDMA polymer. Consequently, it is hypothesised that reducing the grafting density of PDMA will increase the quantity of chlorophyll attached to its surface.[117]

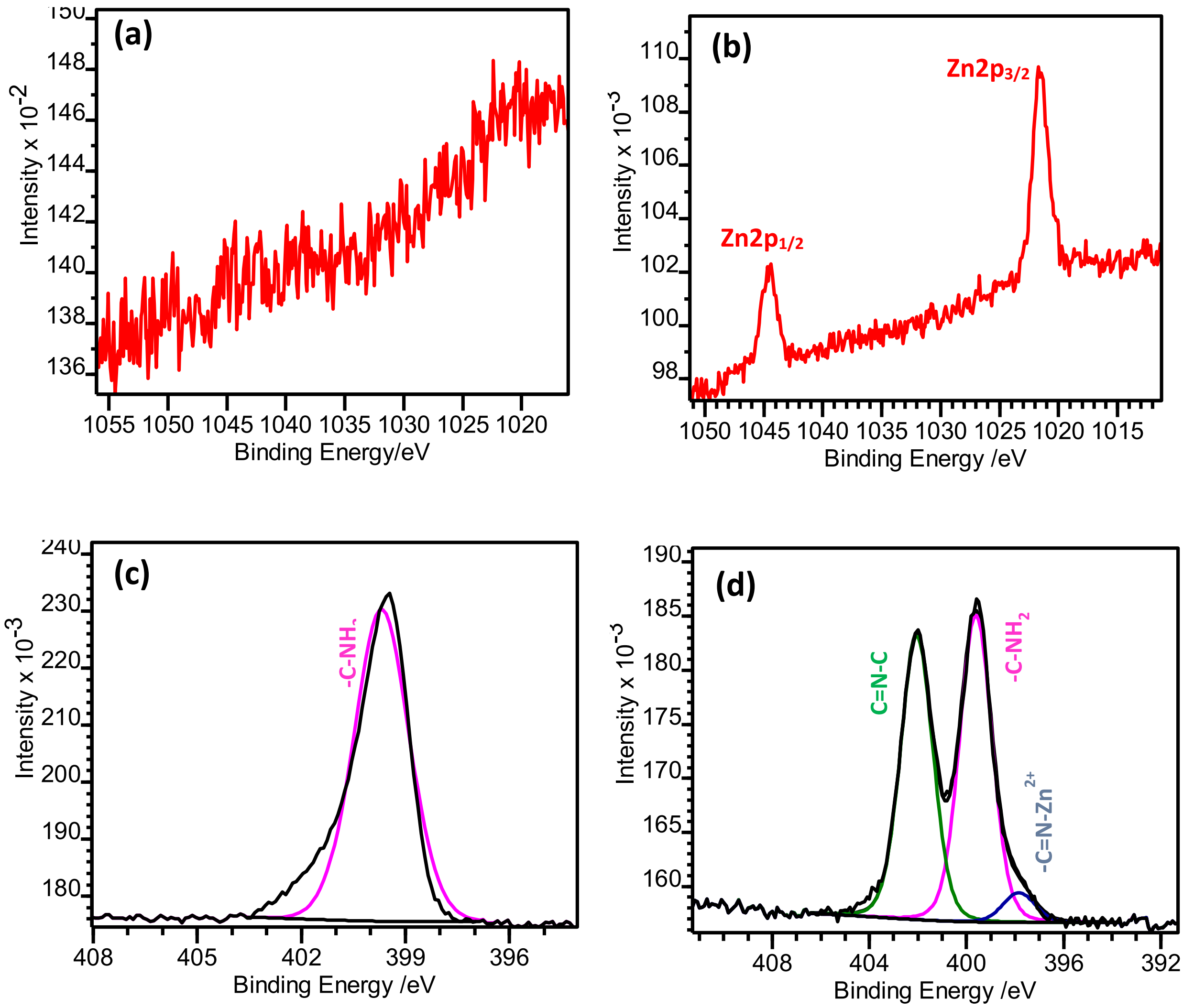

Figure 5-13: XPS spectra obtained for PDMA on the gold-coated surface of Zn2p before (a) and after (b) the attachment of chlorophyll to PDMA full density. N1s spectra before and after the attachment of chlorophyll to PDMA full density are shown in (c) and (d) respectively.

Figure 5-14 shows the introduction of chlorophyll to both a densely packed brush (χBr(Au) = 1.0) and a lower density layer (χBr(Au) = 0.24). The N1s spectrum of the fully dense brush before the addition of Chl *a* is shown in Figure 5-14 a. There is a single peak at 399.5 eV corresponding to neutral amine groups. Chl *a* conjugation results in the observation of peaks at 399.6 eV ($-NH_2$), 402.1 eV ($-NH^{3+}$), and a smaller peak at 398.1 eV, corresponding to the nitrogen atoms in the nitrogen tetrapyrrole ring which indicates coordination of the nitrogen tetrapyrrole ring with the Zn^{2+} ion at its centre, see Figure 5-14b. The recent spectral analysis confirms the existence of Chl *a* within this PDMA brush.

However, Figure 5-14c illustrates that reducing the grafting density of PDMA to 0.24 allows for more Chl *a* binding due to reduced steric hindrance. In this case, the N1s spectrum shows a decrease in the intensity of the ($-NH_2$) and ($-NH^{3+}$) peaks, while the peak for nitrogen in the tetrapyrrole ring becomes more prominent, as seen in Figure 5-14d. This suggests that when grafting densities are lower, the Chl *a* molecule has more space to attach to the PDMA layer.

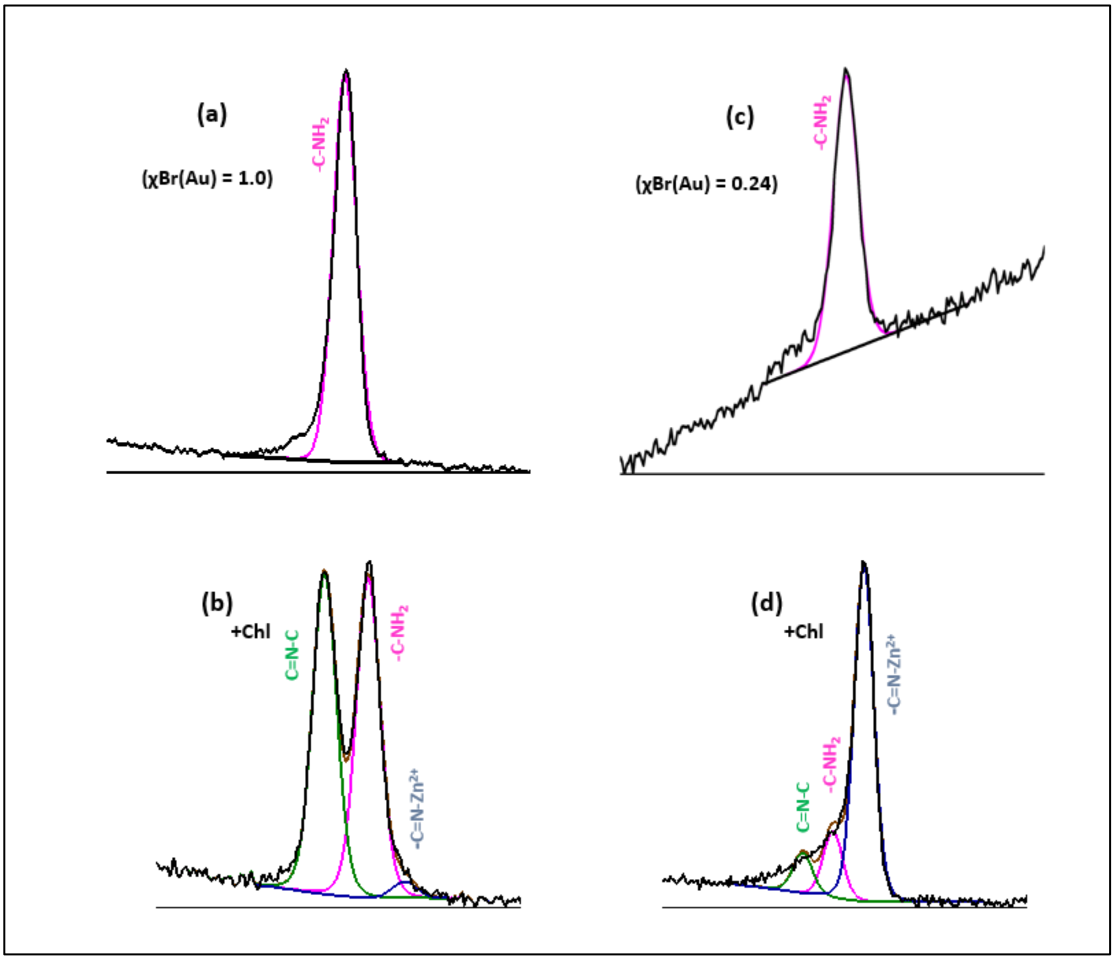

Figure 5-14: High-resolution XPS spectrum of N1s was obtained before (a) and after (b) reactions with Chl *a* for a fully dense ((χBr (Au) =1.0) PDMA brush growing for 1h. The N1s spectra are obtained for PDMA layers with reduced density (χBr (Au) = 0.24) grown over the same time period before(c) and after (d) reaction with Chl *a*.

5.4 Conclusion

PDMA was grown from a DTBU initiator on planar gold substrates and used as scaffolds to organise pigment molecules, as confirmed through XPS, AFM, and SE. After 1 hour of polymerisation, the thickness of the PDMA layer was approximately 26 ± 2 nm, which is less than what was found when PDMA was grown from BIBB-APTES. The use of mixed self-assembled monolayers offers a straightforward and efficient method for controlling the initiator concentration on gold surfaces. The XPS data indicates significantly enhanced binding of Chl to PDMA in films of reduced density (χBr (Au) = 0.24), which allows for as much as four times more Chl *a* to bind compared to the full density polymer due to the reduced steric constraints. Thus, this method can be employed to control the quantity of chlorophyll that is bound to the surface of the PDMA layer.

Chapter 6: Formation and Spectroscopic Characterisation of Solid-Supported Nanoparticle Films

6.1 Introduction

Gold and silver nanoparticles (AuNPs and AuNPs respectively) possess many intriguing physicochemical characteristics that have a wide range of existing and potential applications in fields such as drug delivery,[58] solar cells,[59] biosensors,[60] surface-enhanced Raman spectroscopy,[61] and cancer treatment. [62] Due to their optical and electronic properties, they are a valuable research platform for these types of applications.[91, 257, 272] These properties can be manipulated by exploiting the LSPR, which depends on factors such as the particles' sizes and shapes of the particles, their interactions with other particles, and the surrounding dielectric environment.[273] For some applications, it is useful if the particles can be immobilised on solid substrates rather than being dispersed as colloids within solutions.[274]

A variety of techniques have been developed for immobilising colloidal AuNPs on solid substrates including the use of electrostatic contacts, covalent interactions (using thiol or amine-terminated moieties) and weaker physical interactions such as van der Waals forces.[285] However, the nano- and microfabrication techniques that are commonly used for accurately controlling clustering and inter-particle spacing, often require specialised equipment and can be both time-consuming and expensive, with their application frequently restricted to small area modifications.[275]

In this chapter, the binding of AuNPs and AgNPs to surface-grafted polymer PDMA brushes, grown by ATRP, is examined. In this method, plasmonic nanoparticles are synthesised in solution and embedded into surface-grafted polymer brushes. An additional objective of the present work was to examine the feasibility of producing photonic films by incorporating dye molecules together with the AuNPs. In particular, Chl *a* is here bound to PDMA brush scaffolds. Previous work by Lishchuk *et al,* examined the strong coupling of LSPRs associated with arrays of gold nanostructures to Chl *a* bound to poly(cysteine methacrylate) brushes grown from the gold surface.[41] Coupling energies as large as 0.4 eV were measured (~2 times the coupling observed for biological light-harvesting complexes). However, in the work of Lishchuk *et al*, arrays of gold nanostructures were fabricated using nanolithography techniques. In this chapter, in contrast to the previously published work, the aim is to examine a solution-processing route to films that contain both plasmonic nanostructures and Chl *a*. Proven colloidal AuNP synthesis techniques are used to create nanoparticles in solutions with specific shapes and sizes, enabling large-area surface modifications.

Spherical Au nanoparticles with sizes of 10, 18, and 38 nm and hexagonal NPs and silver NPs have been compared, to test whether it was possible to observe plasmon-exciton coupling. The effect of NP diameter and shape on the coupling phenomenon is explored. Figure 6-1 shows a schematic illustration of the steps involved in the addition of ZnChla to the AuNPs-embedded PDMA brushes. The glass surface of the base layer is first given a positive charge by coating with a BIBB APTES monolayer, which induces the negatively charged citrate coated AuNPs to spontaneously arrange themselves on the surface, resulting in the reversal of the surface charge and the deposition of the nanoparticles. The stability and uniformity of the nanoparticles are ensured by surrounding them with their negatively charged citrate ligand, the electrostatic repulsion between which prevents clumping. In the final step, ZnChla is introduced into the plasmonic system. Both hexagonal gold nanoparticles and silver nanoparticles were incorporated using the same steps.

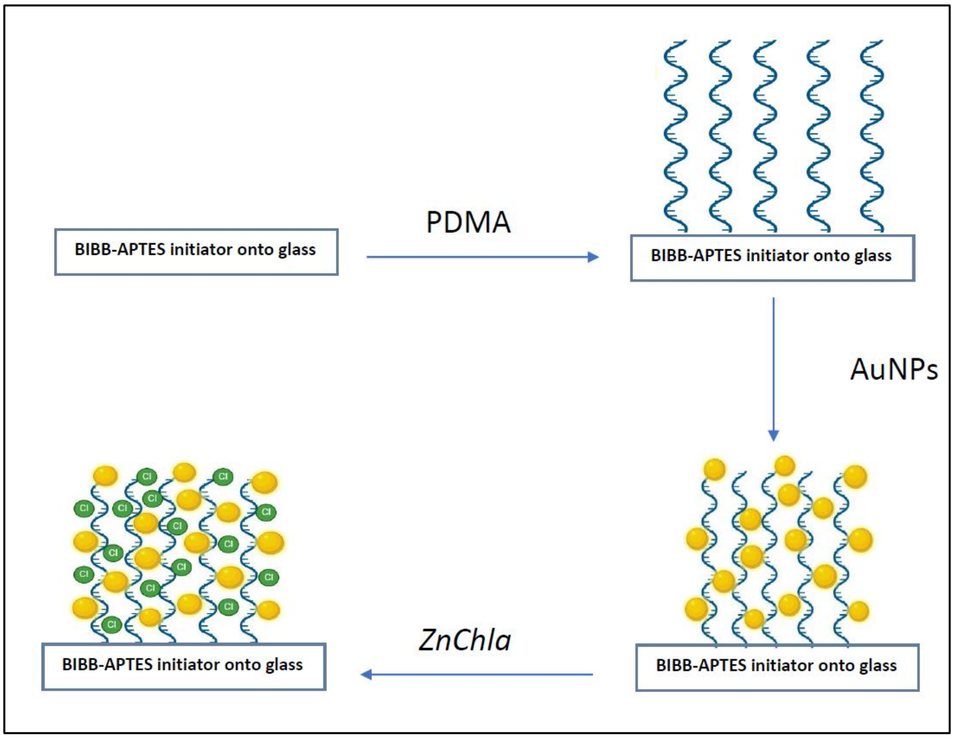

Figure 6-1: Schematic diagram showing the procedure used for the incorporation of AuNPs into PDMA brushes and the addition of ZnChla.

6.2 Materials and methods

Glass coverslips (22 x 64 mm and 1.5 mm thickness) were obtained from Menzel-Gläser. Silicon wafers (reclaimed, p-type, <100>) were supplied by Compart Technology (Tamworth, UK). Hydrogen peroxide (30%) and sulfuric acid (95%), dichloromethane, (≥ 99.8%) and dimethylformamide (> 99%), anhydrous magnesium sulfate (≥ 62, 70%) were purchased from Fisher Scientific (Loughborough, UK). Ethanol absolute, (≥ 99.8%) and silica gel (40–63 μm) were obtained from VWR international (Lutterworth, UK). (3-aminopropyl) triethoxysilane (APTES) (≥99%), α-bromoisobutyryl bromide (BIBB) (98%), triethylamine (≥99%), copper (I) bromide (≥ 99%), 2 (-dimethylamino) ethyl methacrylate (DMA) (98%), 1,1,4,7,10,10 hexamethyl triethylenetetramine (HMTETA) (97%), gold (III) chloride hydrate, trisodium citrate dehydrate, acetic acid, (≥ 99.7%), sodium hydrogen carbonate, (≥ 99%), petroleum ether 40°C–60°C, methanol, (99.99%), zinc acetate dihydrate, 99.999%, cetyltrimethylammonium bromide (CTAB), silver nitrate ($AgNO_3$), sodium borohydride ($NaBH_4$), and L-ascorbic acid were purchased from Sigma-Aldrich UK (Gillingham, UK). All procured chemicals were used as received from the manufacturer. Deionised water (resistance >15.0 MΩ cm) was obtained from an Elga Pure Nanopore system. Copper bromide was stored under a vacuum, and the DMA was stored at 4 °C after the removal of the inhibitor by filtration through a small column of basic aluminium oxide.

6.2.1 Sample cleaning and handling

The glass slides and silicon wafers were cleaned using the procedure described in Chapter 3. Substrates were immersed in piranha solution (30% H_2O_2: 98% H_2SO_4, 1:3, v/v) for 2 h, washed, and placed in an oven at 80 °C overnight to dry. The dry substrates were then cut into (1 cm x 2 cm) pieces while handling with clean tweezers.

6.2.2 Preparation of APTES-BIBB initiator

The piranha-cleaned glass substrates were functionalized by immersion for 30 min in an ethanolic solution of 2% APTES, thoroughly washed with ethanol, dried under nitrogen, and then annealed for 30 min at 120 °C. The slides were then immersed in DCM for 30 min, and the silane films functionalized with BIBB and triethylamine. Finally, the samples were rinsed in ethanol and dichloromethane, before being dried using nitrogen steam.

6.2.3 ATRP synthesis of PDMA brushes

A detailed description of the growth of PDMA brushes on BIBB-APTES-initiated glass substrates is given in Chapter 3. DMA monomers were dissolved in DMF, HMTETA was used as the ligand, and Cu(I)Br as the catalyst for the ATRP reaction. 5 mL of monomer/catalyst solution was added to BIBB-APTES initiator-functionalised samples in Schlenk tubes at 90 °C. Immediately the desired polymerisation time had elapsed the slides were removed from the solution, and the wafers were washed continuously with IPA followed by ethanol, to remove any excess monomer or catalyst.

6.2.4 Synthesis of gold nanoparticles

The gold nanoparticles were synthesised by heating $HAuCl_4$ (0.25 mM) in a conical flask placed on a hotplate until boiling, at which time trisodium citrate (1%) was added dropwise while continuously stirring. After approximately 25 s the formation of AuNPs is visibly indicated by the solution turning a deep red/purple colour. The solution was kept boiling for a further 15 min, cooled and stored in a clean brown glass container in a fridge at 8 °C. Nanoparticles of different sizes can be formed by using different concentrations of sodium citrate.

6.2.5 Synthesis of hollow gold nanoprisms

Briefly, the first step involves forming silver nano-seeds with a diameter of 3-6 nm. The second step involves using sacrificial galvanic replacement. The silver nano seed is prepared by adding $AgNO_3$ to Milli-Q water, trisodium citrate, $NaBH_4$ stock, CTAB, $HAuCl_4$, and ascorbic acid. The solution is kept undisturbed for 2-3 hours. The seed solution is added to the growth solution immediately after the second addition. More details can be found in Chapter 3.

6.2.5.1 Modification of HGN surfaces with polystyrene sodium sulphonate (PSS)

A 5mL solution of HGNs was centrifuged at 8000 rpm for 15 min to eliminate any excess CTAB, and the resulting material was resuspended in 2.5 mL of water. While gently stirring, 2.5 mL of PSS stock solution (10 mg/5 mL) and 25 µL of 10 mM NaCl solution were added to the centrifuged solution and left to react overnight, before being recentrifuged to eliminate excess PSS. The resulting residue was then dispersed in water for further analysis.

6.2.6 Synthesis of silver nanoparticles

Silver nanoparticles (AgNPs) were synthesised by using 450 mL of silver nitrate (0.001 M) in a clean, conical flask container, to which a mixture of 25 mL of sodium hydroxide (0.06 M) and 25 mL of hydroxylamine hydrochloride (0.0288 M) was added. This yields a milky tan of a liquid, with the reaction requiring around 15 min for completion. The conical flask must be covered with foil to avoid light deterioration of the colloidal solution and stored in the fridge for 24 h before use. The nanoparticles were characterised using UV-visible spectroscopy and AFM.

6.2.7 Extraction of chlorophyll from spinach

The ZnChla synthesis is described in detail in Chapter 3. In summary, chlorophyll a was extracted from spinach leaves by first extracting the dark green pigment with acetone and then dissolving the dark blue pigment in acetic acid under continuous stirring for 3 h to obtain pheophytin a. Zinc acetate dihydrate dissolved in methanol was then used to convert pheophytin into ZnChla by reflux in an argon atmosphere for 1 h.

6.2.8 Incorporation of AuNPs and AgNPs onto APTES substrate

APTES-functionalized glass slides were immersed in solutions containing gold nanoparticles or silver nanoparticles at room temperature for the desired immobilization time, washed with deionized water and dried with N_2.

6.2.9 Incorporation of AuNPs, AgNPs and HGNs into PDMA brush

The PDMA sample was immersed in the different types of nanoparticles in solution for 24 h in the dark at room temperature, to form PDMA films functionalized with these NPs.

6.2.10 Attachment of ZnChla to PDMA brush

The functionalised PDMA brush samples were then immersed in ZnChla solutions and left overnight at room temperature. The samples were then rinsed with deionized water and dried under a nitrogen stream.

6.3 Surface Analysis

Water contact angles were determined using a Rame-Hart goniometer model 100-00 (Netcong, NJ, USA). It was measured and averaged at least three drops of liquid per sample.

A Carry 50 UV-visible spectrophotometer was used (Agilent Technologies, USA) to measure UV-visible absorption spectra between 350 and 900 nm. A custom-built PTFE sample holder was used to take an air measurement experiment for at least two measurements at the same sample on the surface.

The ellipsometry experiments were conducted using Alpha-SE ellipsometers (J. A. Woollam Co., Lincoln, NE, USA). Lasers were used to provide light of 633 nm wavelength at an incidence angle of 70° and the ellipsometry data was fitted using EASE software (version 6.6). Three spots were measured and averaged for each sample and the thickness was estimated as the mean with the standard deviations used as a measure of precision.

X-ray photoelectron spectroscopy (XPS) was performed using a Kratos Axis Supra spectrometer (Kratos Analytical, Manchester, UK). Data from XPS were analysed using CASAXPS (v. 2.18) software.

The AFM images were collected with a Digital Instruments Nasoscope 5 Multimode AFM. All experiments were conducted under ambient conditions. AFM data was analysed using the Nasoscope Analysis software (v.1.5). TEM imaging was conducted by Dr. Kamalika. The solution of HGN was dropped directly onto the TEM grid and allowed to dry in the air. TEM imaging was performed on the loaded grid.

6.4 Results and Discussion

6.4.1 Synthesis and characterization of differently sized AuNPs

According to the literature, AuNPs were prepared by using trisodium citrate ($Na_3C_6H_5O$) as a reducing agent.[276] Figure 6-2 shows a simple, cost-effective, and fast method of chemically reducing the tetrachloroauric acid ($HAuCl_4$) with trisodium citrate $Na_3C_6H_5O$ to create gold nanoparticle suspensions.

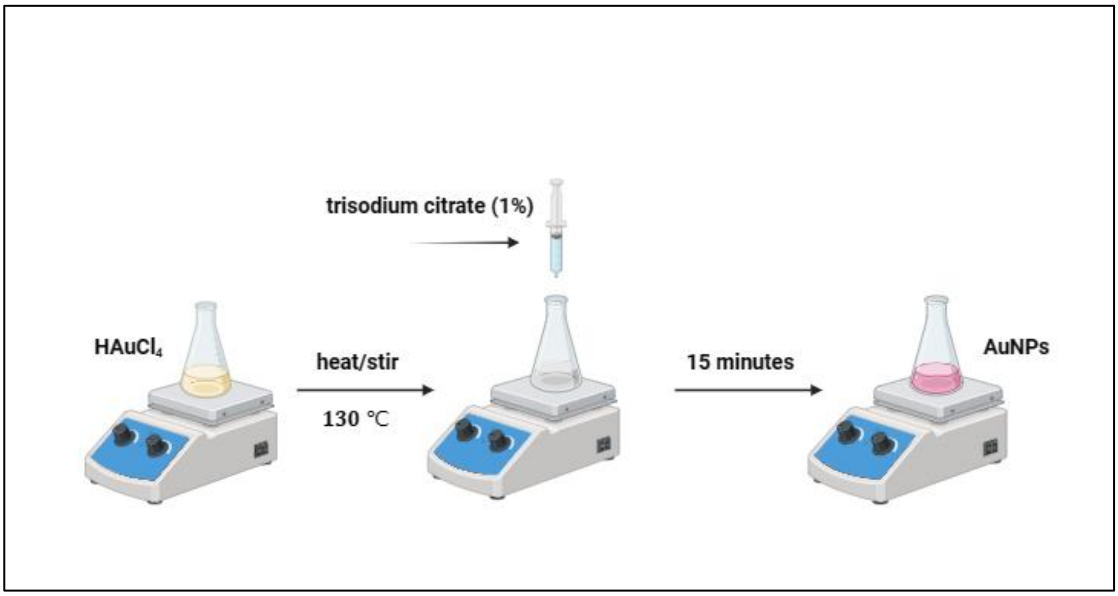

Figure 6-2: Schematic representation of the preparation of gold nanoparticles by reduction with $Na_3C_6H_5O$.

The $HAuCl_4$ solution (0.25 mM) was heated until boiling point, at which point 0.5 mL of 1% $Na_3C_6H_5O$ was added dropwise under continuous stirring**.** The colour of the $HAuCl_4$ solution changed from light yellow to colourless and eventually to dark red within a few minutes, indicating the successful production of the AuNPs (see Figure 6-2). The size of nanoparticles produced by the reduction of $HAuCl_4$ depends on the reducing agent used and its concentration and can be controlled by changing the concentration of citrate in the solution. Higher concentrations of citrate result in the production of smaller particles.[276] AuNPs were prepared with diameters of 10, 18, and 38 nm (NPI, NPII, and NPIII, respectively) and characterised using UV–vis spectra and AFM. Figure 6-3 shows the absorbance spectra of solutions containing the three sizes of AuNPs in the prepared concentrations. AuNPs of three different average sizes were synthesised using the Turkevich method described above. Three singles narrow plasmon peaks with the wavelength maximum absorbance (λ max) were found at 519, 523, and 531 nm and correspond to particles of 10, 18, and 38 nm, respectively.

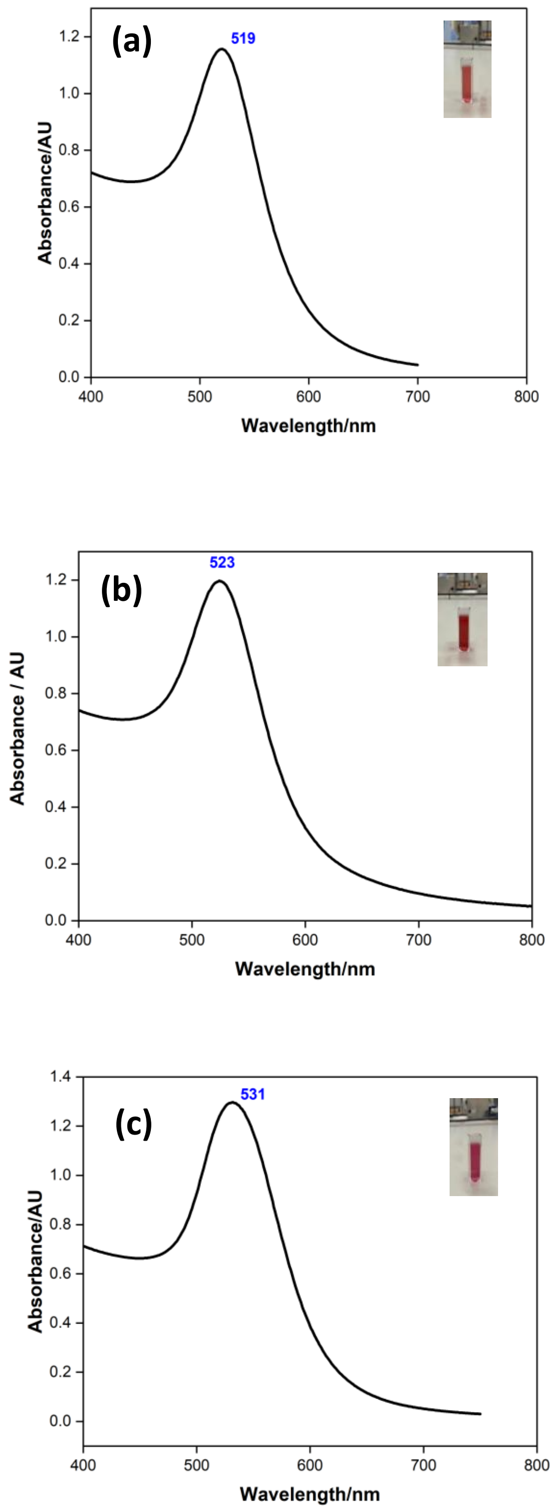

Figure 6-3: UV-vis absorbance spectra of different AuNPs in solution, (a) NPI, (b) NPII and (c) NPIII. The insets show photographs of cuvettes filled with suspensions of the AgNPs.

The size of gold nanoparticles has been determined from literature depending on the maximum wavelength of UV-vis absorbance for each type.[277] In general, the plasmon energy is expected to decrease with increasing particle size. Thus, 10 nm gold nanoparticles absorb in the blue-green region of the electromagnetic spectrum, whereas 100 nm particles absorb in the red region (plasmon energy ~ 2 eV).

Figure 6-4 shows three different AuNPs (concentrated as prepared and diluted 1-1 in water) with their corresponding surface plasmon bands**.** As expected, it can be seen that the plasmon peak for all three types of AuNPs remains in the same position after dilution, with a reduction only in intensity. However, for all three particle sizes, the optical characterisation of AuNPs in solution differs from those immobilised onto APTES substrates. APTES has three ethoxy groups that can attach to hydroxyl groups on glass surfaces, as well as an amino group for further modification. It should be noted that APTES is the best substrate for immobilising gold nanoparticles, owing to the electrostatic interactions between positive amino groups on the APTES and negatively charged AuNPs.[289] As illustrated in Figure 6-5, all three sizes show a blue shift of approximately 3 nm in their absorbance peak positions, due to the change in the refractive index of the surrounding medium from water (n = 1.33) to air (n = 1). A similar behaviour has been observed for gold nanoparticles immobilised onto glass in previous studies.[278] Figure 6-5c shows a broad shoulder peak at around 650 nm, which arises due to the aggregation of neighbouring particles, especially for concentrated samples. Therefore, diluted concentrations (1:1 in water) are most effective in preventing aggregation for surface immobilisation.

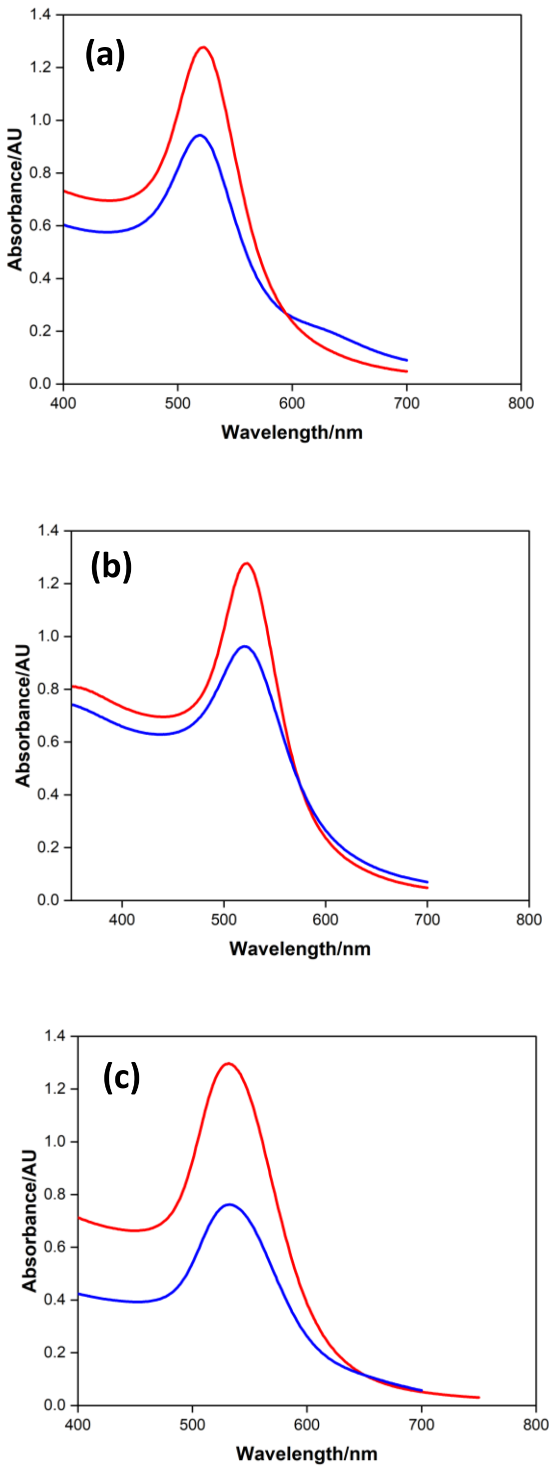

Figure 6-4: UV-vis absorbance spectra of different AuNPs in solution: (a) NPI, (b) NPII, and (c) NPIII. The red lines represent spectra of AuNps at the prepared concentration and the blue lines spectra acquired after a 1:1 dilution of the suspension in deionised water.

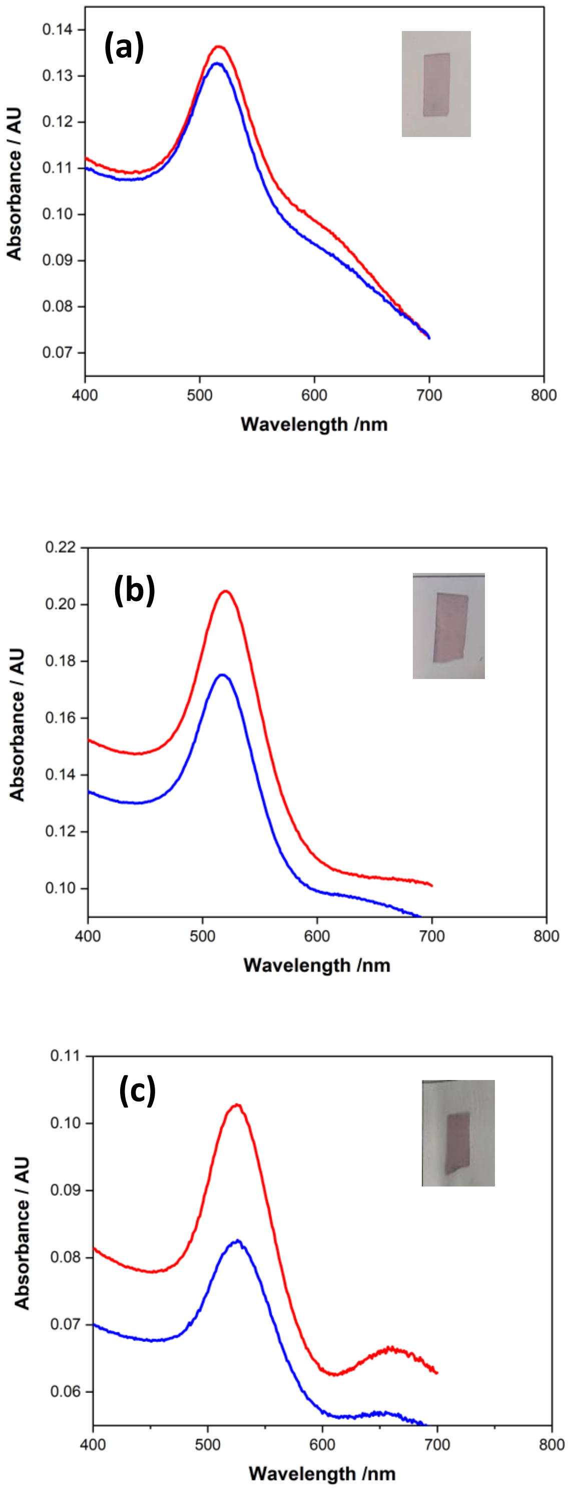

Figure 6-5: UV-vis absorbance spectra of different AuNPs onto APTES surface.: (a) NPI, (b) NPII, and (c) NPIII. The red lines represent spectra of AuNps at the prepared concentration and the blue lines spectra acquired after a 1:1 dilution in deionised water. The insets show photographs of the AuNPs after adsorbing onto the APTES surface.

The AFM height images for all three types of AuNPs are shown in Figure 6-6**.** These images illustrate the morphologies of immobilised AuNPs in APTES-functionalised glass substrates after immersion for 24 h in nanoparticle suspensions. As previously mentioned, the positive amine groups (–NH_2) in APTES bind to the negatively charged AuNPs to provide full surface coverage (the density of the particles on the surface).[279, 280] Particles are closely packed with small spaces between them, leading to the plasmonic coupling between neighbouring particles. The immobilisation of gold nanoparticles requires 24 h to achieve complete coverage. In addition, AFM could be used to determine the gold nanoparticle size (nm) and compare the results with estimates based on UV/vis spectroscopy. However, AFM is not the best method for determining nanoparticle size, because in general, for nanoparticles, the particle radius is comparable to the tip radius- thus there is the convolution of the tip and sample. Nevertheless, the results are consistent with those obtained by UV/vis measurements, as given in Table 6-1. To measure the particle size by AFM, the AuNPs were immersed in APTES film for a few minutes to avoid full coverage of the surface, taking into consideration the effect of tip-sample convolution (see Figure 6-7). From both the height and phase images, the particles are observed to be fairly evenly spaced and spherical. Comparing Figure 6-6 with Figure 6-7, it is apparent that the particles are closely packed in full coverage image (see Figure 6-6), where the AFM tip is imaging the boundaries between the particles. This is seen through the dark lines which correspond to the region where the slopes of adjoining particles are in opposite directions, resulting in an overestimation of the particle size. As expected, the particles appear larger in Figure 6-7 compared to the full-coverage images due to tip-sample convolution effects.

Table 6-1: Comparison of UV and AFM for particle size determination (nm)

Samples	UV/nm	AFM/nm
NPI	10 ± 2	11 ± 1
NPII	18 ± 2	14 ± 3
NPIII	38 ± 3	35 ± 4

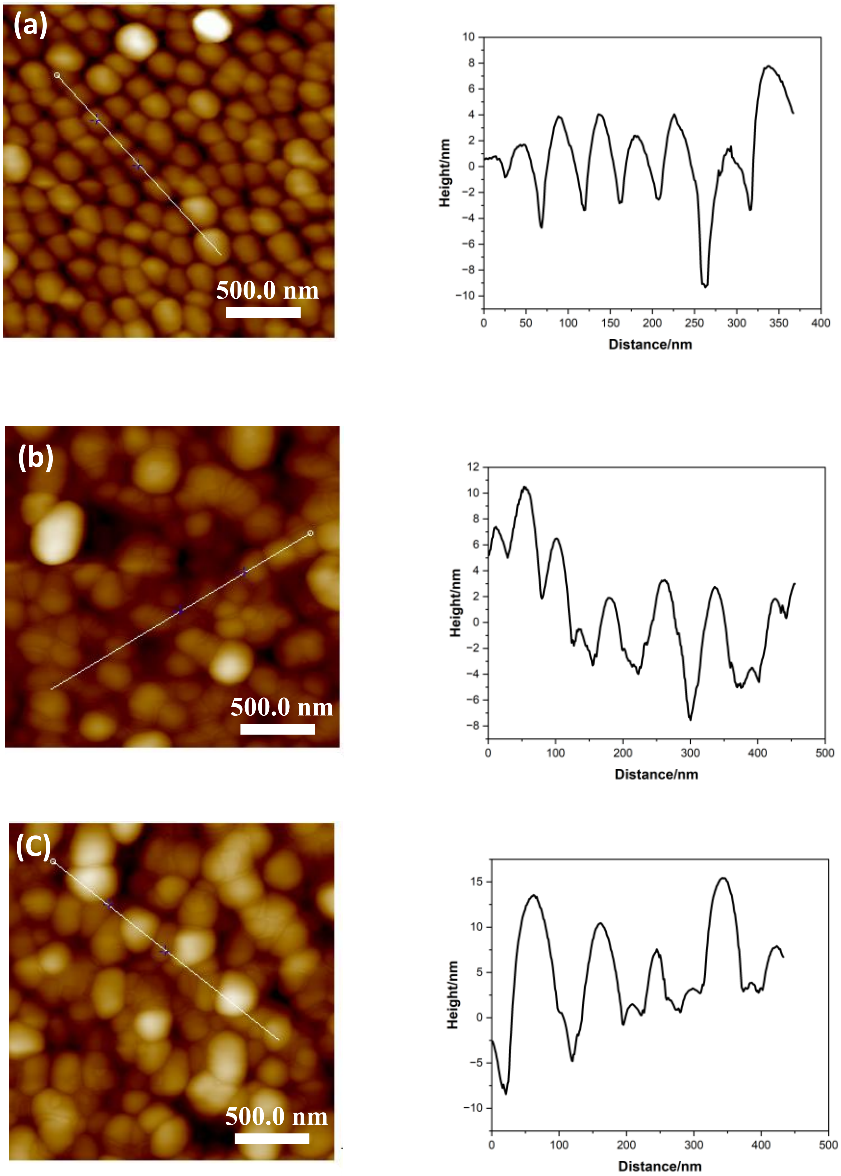

Figure 6-6: The AFM tapping mode height images of AuNPs adsorbed onto APTES film (a) NPI, (b) NPII, and (c) NPIII. The cross-section surface profiles are shown on the right of each image.

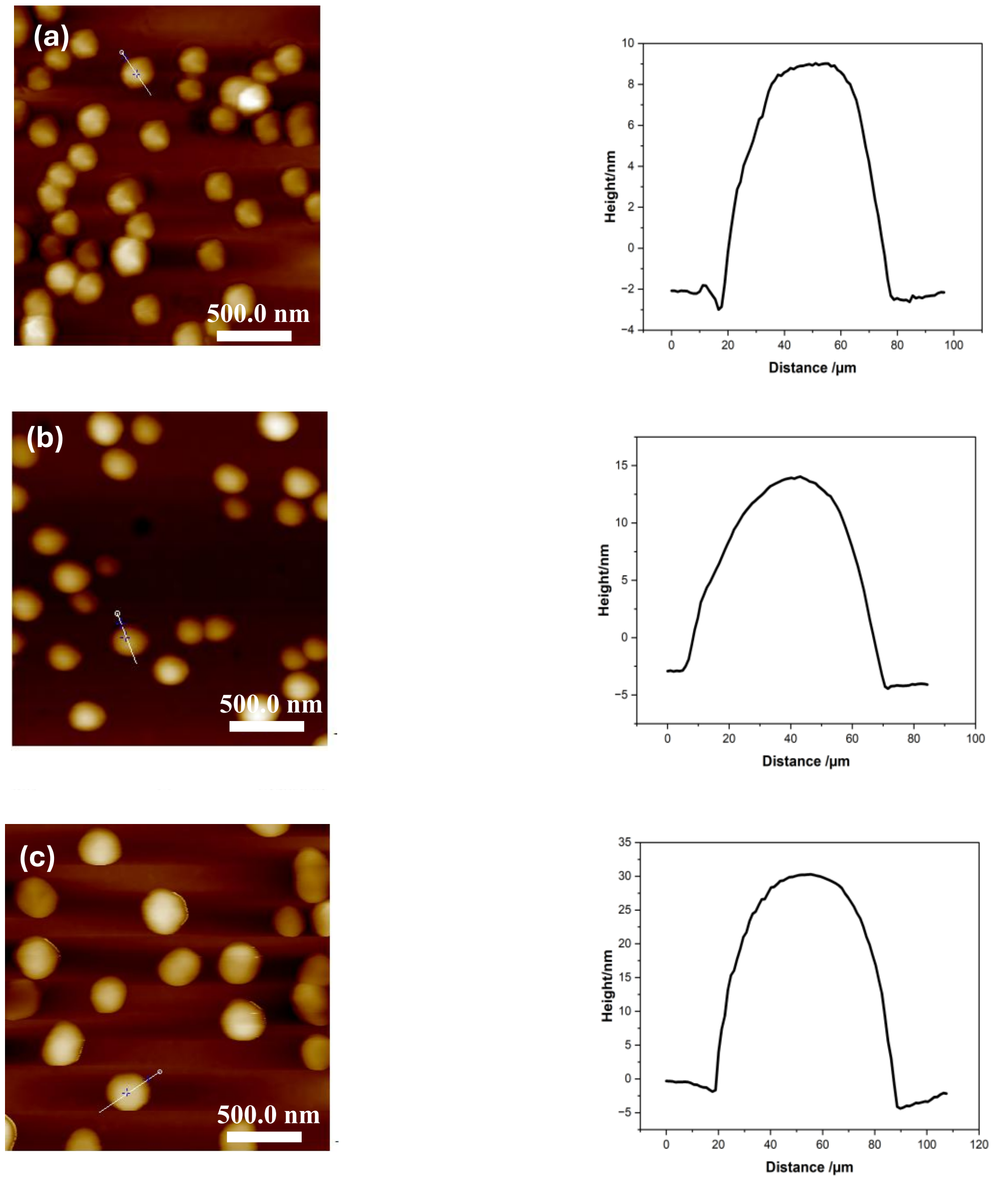

Figure 6-7:AFM height images of AuNPs (a) NPI, (b) NPII, and (c) NPIII and cross-section surface profiling (far right).

6.4.2 Incorporation of AuNPs into PDMA brushes

AuNPs were bound to 15 nm thick PDMA brush samples into which differently sized AuNPs were incorporated by immersing the samples for 24 h in AuNPs suspension in water. At neutral pH, PDMA brushes are positively charged because protons bind to the tertiary amine in the pendant group.[261] This enabled the negatively charged AuNPs because citrate ions are surrounded on them to bind to the positively charged polymer chains via electrostatic interaction, as shown in Figure 6-8**.**

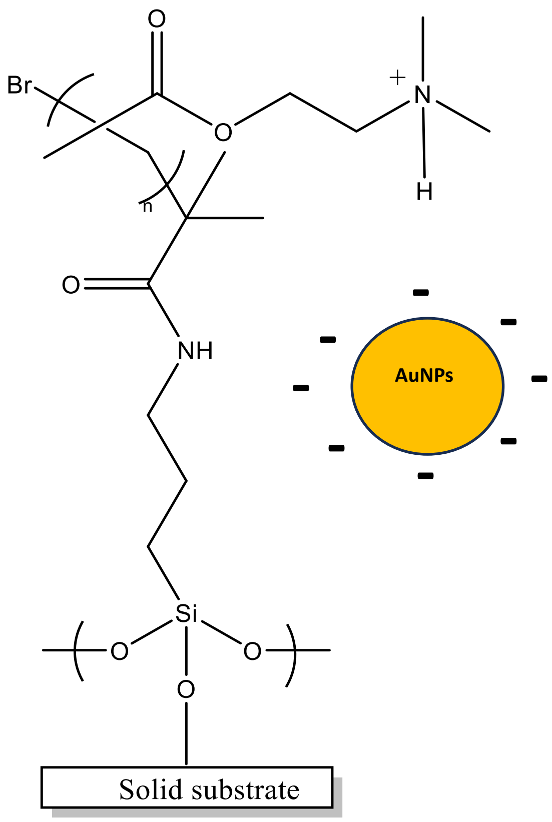

Figure 6-8: A schematic representation of the electrostatic interaction of AuNPs with PDMA chains.

The optical properties of the PDMA brush functionalised with the three differently sized AuNPs were characterised with UV-vis absorption spectroscopy, and their morphology was analysed using AFM. Figure 6-9 shows the UV-vis absorption spectra of three different sizes of AuNPs embedded in polymer brush surfaces. Both the positions and intensities of the absorbance peaks differ from those observed in the solution. After the incorporation of AuNPs into polymer brush surfaces, the position of the plasmon band shifts slightly from 519, 523, and 531 nm in solution to 514, 518, and 527 nm in polymer brush, respectively. The blue shift in the plasmon band is due to dipole-dipole interactions between particles [281], while the decrease in the peak intensity is due to the difference in sample path length. Particle aggregates were not found in the brush samples made with the NPI and NPII sizes, but a small aggregate of around 660 nm was found in those made with the NPIII size.

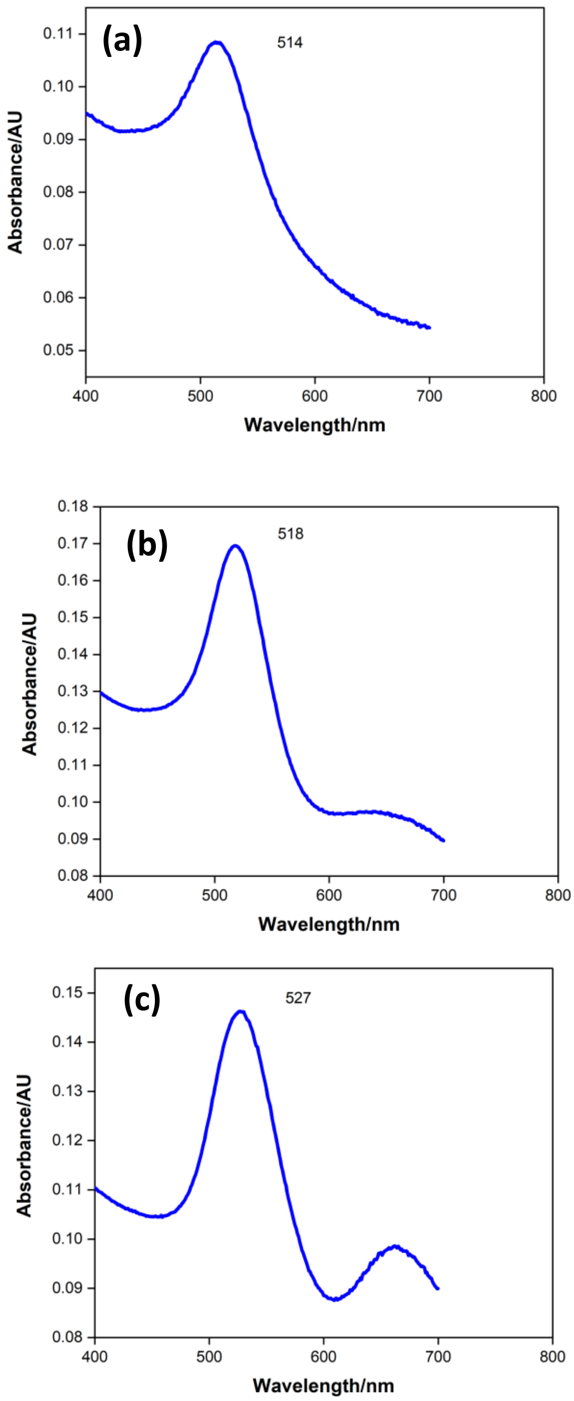

Figure 6-9: UV-vis absorbance spectra of AuNPs with different sizes, (a) NPI, (b) NPII, and (c) NPIII. All samples were diluted (1:1) in water after embedding in 15 nm thick PDMA brushes for 24 h immobilisation time.

After comparing the behavior of small particles in the previous figures with the behavior of larger particles, it was found that larger particles tend to aggregate more than small particles. This aggregation led to the study of the effect of PDMA brush thickness on the plasmon resonance for the NPIII embedded within the PDMA brush, as shown in Figure 6-10. The maximum absorption of NPIII incorporated into PDMA brushes (15 nm thickness) is 527 nm, accompanied by a broad shoulder peak at 650 nm indicative of particle aggregation (Figure 6-10, blue spectrum). However, a redshift in the plasmon band position was observed for both the thicknesses of 20 and 30 nm PDMA brushes with the maximum absorption peak shifting to 545 nm (see Figure 6-10 green and red spectrum, respectively). This broad peak at 545 nm was likely caused by the formation of another type of gold nanoparticle, with sizes overlapping and contributing to the observed redshift. Therefore, gold nanoparticles with a thickness of 15 nm will be more stable.

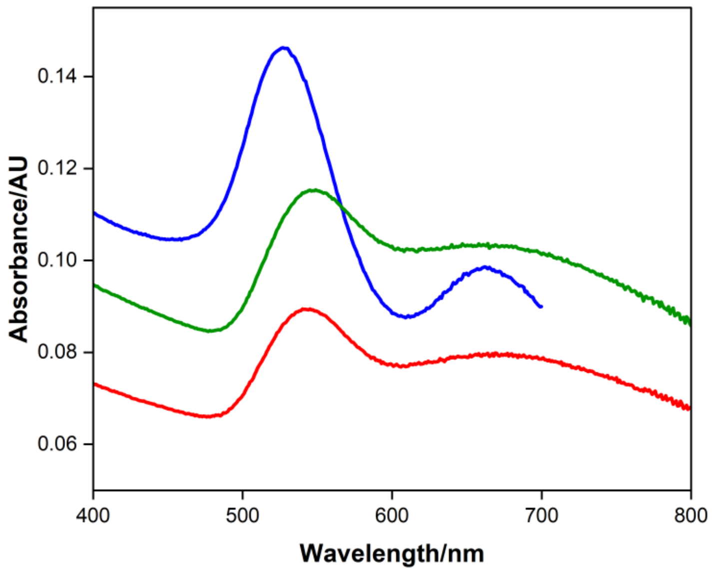

Figure 6-10: The extinction spectra of NPIII-embedded PDMA brushes as a function of brush thickness: 15 nm (blue), 20 nm (green), and 30 nm (red).

AFM tapping mode topographical images were taken to examine the distribution of AuNPs across the polymer surfaces. Figure 6-11a shows the image of the PDMA before immersion with AuNPs, where it can be seen that the polymer appears to be smooth and has completely covered the surface, which had a root mean square roughness (RMS) of approximately 0.33 ± 0.02 nm. Figures 6-11 b, c and d show the images of the PDMA brushes after incorporating the three differently sized AuNPs - NPI, NPII, and NPIII, respectively. Incorporating the AuNPs increased the roughness of the surfaces, with an RMS of 3.44 ± 0.14 nm. Due to this increased roughness, the brushes tend to collapse, causing the adsorbed AuNPs to be closer to one another, which is useful for controlling interparticle distances.[281] This finding is consistent with the results reported in the literature mentioned earlier in this thesis.[163]

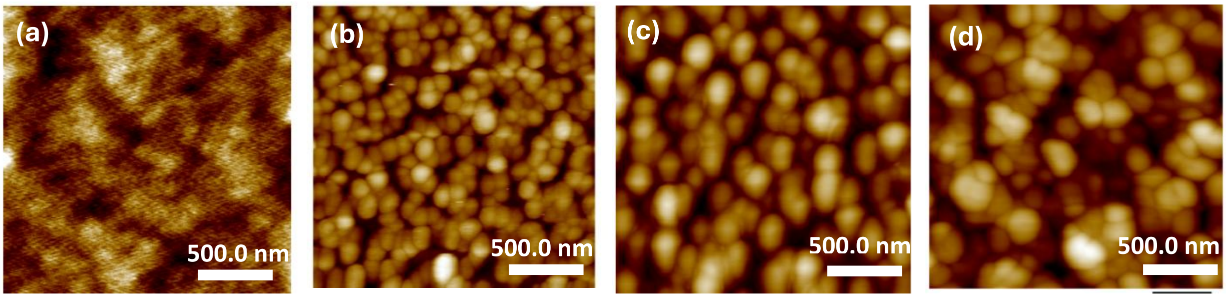

Figure 6-11: The AFM height images of the PDMA brush (15 thick), (a) before immersion with AuNPs, (b) after immersion with NPI, (c) NPII, (d) NPIII for 24h immobilisation time.

The XPS data for the three different sizes of gold nanoparticles embedded within PDMA brushes is shown in Figure 6-12**.** The XPS data exhibits a narrow and intense peak for $Au4f_{7/2}$ at a binding energy of 84.3 eV and for $Au4f_{5/2}$ at a binding energy of 88.5 eV. This indicates the successful attachment of the three different sizes of AuNPs to the PDMA brushes. The XPS spectra of Au4f for both gold nanoparticles synthesised in solution and evaporated gold films on the glass prepared in the previous chapter were similar, with a minor shift to higher binding energy for the $Au4f_{5/2}$ peak in the gold nanoparticles, likely due to surface oxidation of the nanoparticles (e.g., $Au^0 \leftrightarrow Au^{3+}$).

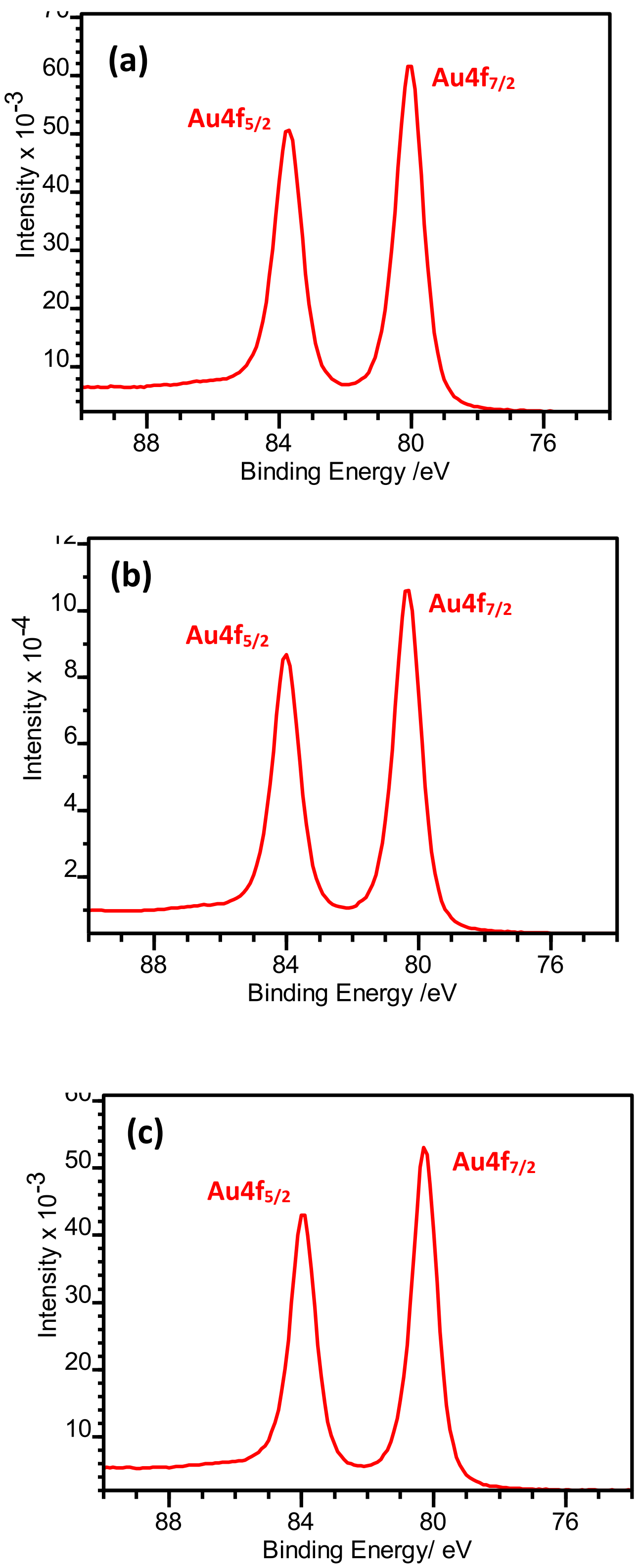

Figure 6-12: An XPS high-resolution spectrum of Au4f was collected for (a) NPI, (b) NPII, and (C) NPII on PDMA (15 nm thickness).

6.4.3 Addition of chlorophyll Chl *a* to brush structures

After the incorporation of AuNPs into PDMA brush films, the binding of Chl *a* to the films was investigated. It was hypothesised that tertiary amine groups in the polymer would coordinate with the central metal ion in Chl *a*, as illustrated in Figure 6-13.

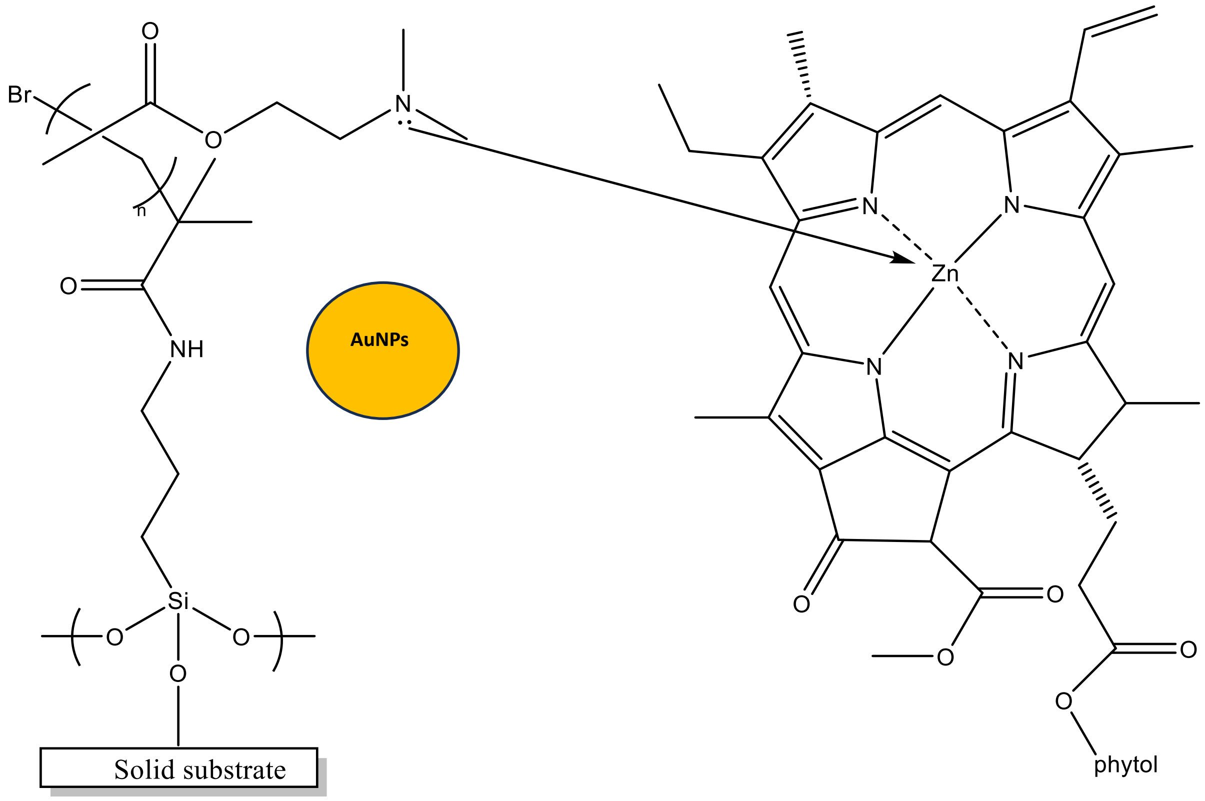

Figure 6-13: A schematic representation of the possible mechanism for plasmon-exciton coupling between AuNPs and ZnChla supported by PDMA brushes.

The optical characteristics of the differently sized AuNPs embedded in the ZnChla-functionalized PDMA brushes were analysed using UV-vis spectroscopy. Figure 6-14a-c shows the absorbance spectra of the PDMA brushes embedded with NPI, NPII, and NPII, before (red) and after (blue) the addition of chlorophyll. The plasmon band is found to be red shifted after the addition of chlorophyll for all nanoparticles, NPI, NPI and NPII, respectively. The redshift in the plasmon band is attributed to the change in the local refractive index after binding the dye molecules to the film, and the redshift is larger for the NPI and NPII nanoparticles with (12 and 15 nm respectively) than for the NPIII with (6nm). Several studies indicate that smaller gold nanoparticles with a diameter of less than 20 nm exhibit a greater redshift compared to larger nanoparticles.[282,283] For strong coupling, it is necessary to have spectral overlap between the plasmon and the exciton. For a 650 nm transition, there is negligible spectral overlap, and ultra-fast excitation transfer between the exciton and the plasmon is not possible.

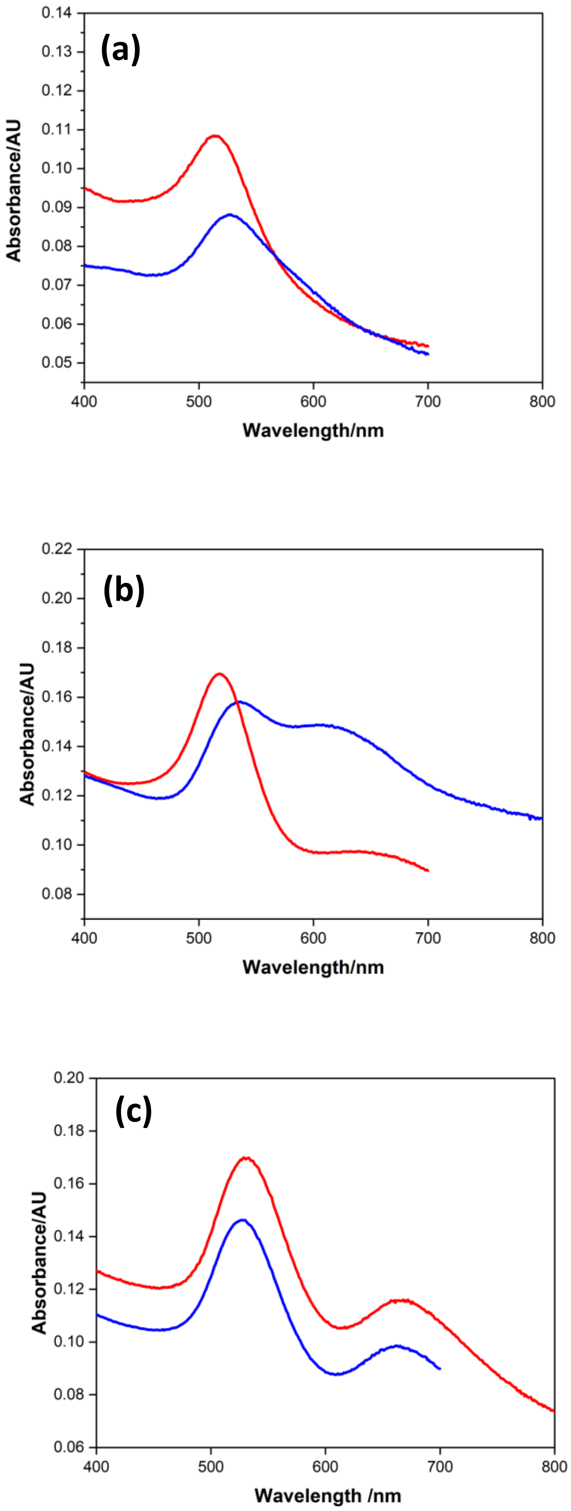

Figure 6-14: The extinction spectra of (a) NPI-, (b) NPII- and (c) NPIII-embedded PDMA brushes before the attachment of ZnChla 25 μM (red), and after the attachment of ZnChla 25 μM (blue)

Figure 6-15 shows the extinction spectra of NPIII-embedded PDMA with a high concentration of chlorophyll as a function of energy instead of wavelength. A strong plasmon-exciton interaction is not possible to be achieved because of the large separation between the maximum absorption resonance of NPIII (2.42 eV) and that of ZnChla (1.86 eV). As a result, the observed red shift was due to the changes in the refractive index near the particle surface.

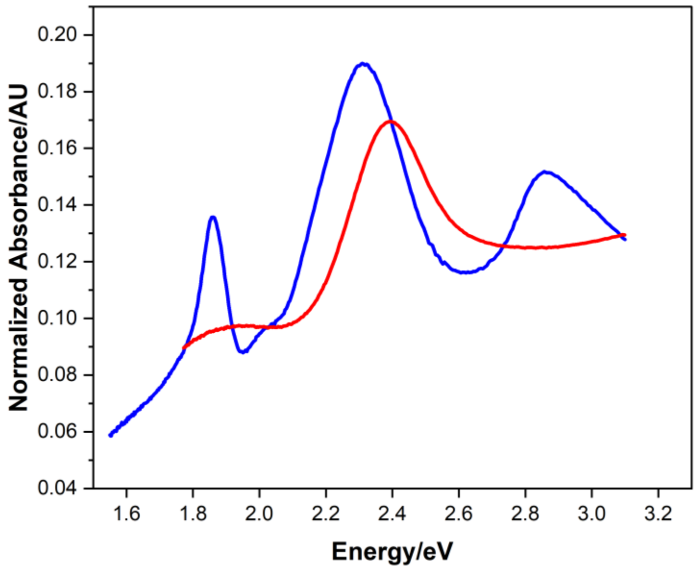

Figure 6-15: Extinction spectra of NPIII-embedded PDMA brushes before the attachment of ZnChla (red) and after the attachment of ZnChla (blue).

XPS N1s spectra were acquired to confirm chlorophyll attachment to PDMA brushes. Figure 6-16 shows the XPS high-resolution N1s spectra for the NPI, NPII, and NPIII AuNPs incorporated into PDMA brushes, after ZnChla attachment**.** All sized AuNPs exhibit three unique components in their N1s spectra, with binding energies of 398.5, 400.4, and 402.4 eV. The primary peak is observed at 398.5 eV, indicating the presence of nitrogen atoms located near the core of the chlorophyll ring. The peak was more distinct from NPII, which agrees with the findings from the UV analysis. The primary peaks indicate that the chlorophyll has effectively bonded with the AuNPs embedded within the PDMA brushes. The peaks with binding energies 400.4 eV and 402.4 eV correspond to the amino group in PDMA, and the imine (C=N-C) bond in the chlorin ring, respectively.

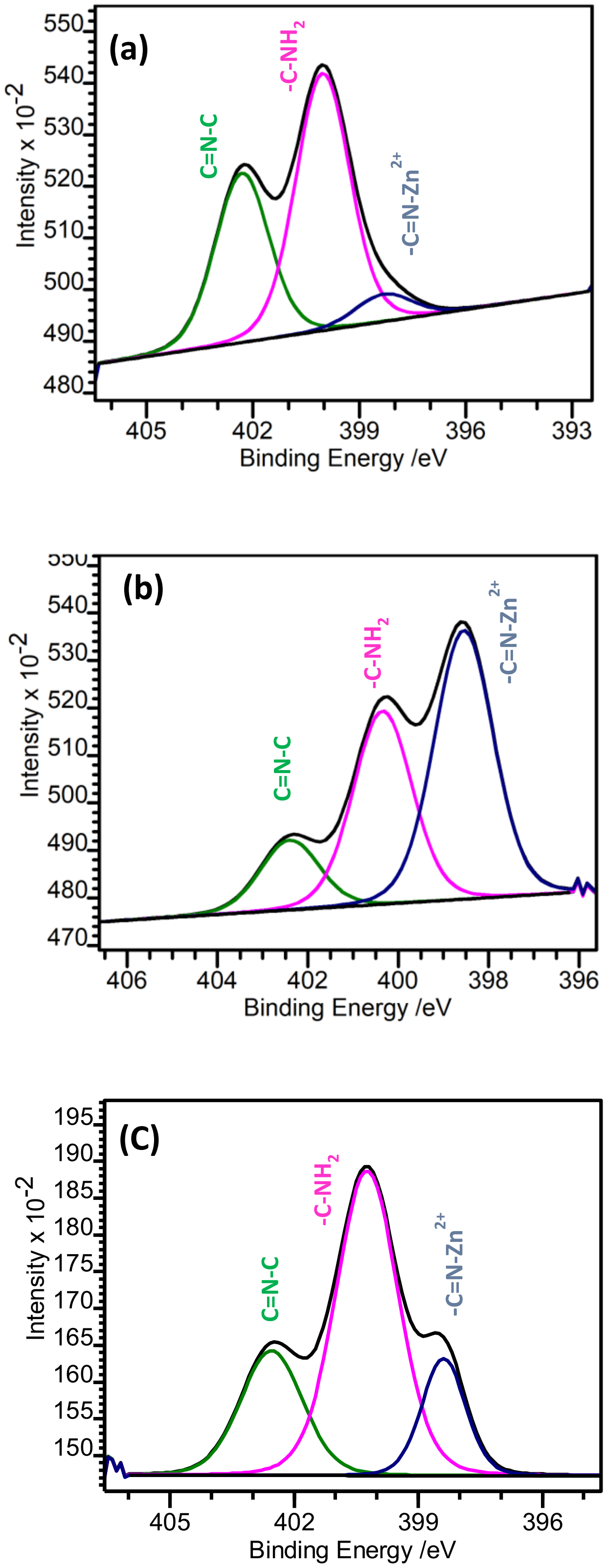

Figure 6-16: XPS high-resolution N1s spectra for PDMA brushes embedded with (a) NPI, (b) NPII, and (c) NPIII after the attachment of ZnChla 25 μM.

6.4.4 Hollow gold nanoprisms

6.4.4.1 Synthesis of hollow gold nanoprisms and modification with polystyrene sodium sulfonate (PSS)

Hollow gold nano prisms (HGN) were prepared via a two-step process, that followed the method reported in the research literature.[95] The first step involves the synthesis of small, spherical silver nanoparticles with a diameter ranging from 3 to 6 nm, referred to as silver nanoseeds. The HGNs are produced in the second step by sacrificial galvanic replacement. The synthesis was conducted at standard room temperature (18-20 ˚C).

During the second step, CTAB is employed as a surfactant that directs the shape of the substance, while L-ascorbic acid acts as a gentle reducing agent that reduces Au^{3+} and any remaining silver ions that are present in the solution. Circular hollow cavities at the centre of triangular prisms are formed by sacrificial galvanic replacement, where gold cations are chemically reduced by a metal in the absence of any external electric current.[95, 284]

The spherical silver seed acts as a sacrificial template, with the driving force for the reaction coming from the difference in the standard reduction potentials between the Ag^{+}/Ag^{0} redox pair and the $Au^{3+/}Au^{0}$ redox pair. Three Ag atoms are oxidized to Ag^{+} ions, at the same time as one Au^{3+} ion is reduced to Au^{0}, leading to the creation of a hollow interior. The equation for the reaction is the following:[284]

$$3Ag\ (s) + AuCl_4 \rightarrow Au\ (s) + 3Ag\ (aq) + 4\ Cl^{-} \qquad \text{(Eq. 6.1)}$$

6.4.4.2 Characterization of hollow gold nanoprisms

There is a close match between the surface plasmon energy of HGNs and the Chl *a*. The HGNs were characterised using UV–vis spectra and TEM, with the UV-vis being used to obtain the extinction spectra of the silver nanoseeds. The absorption spectra of HGNs using the Ag nanoseeds (150 µL) after treatment with polystyrene sodium sulphonate are shown in Figure 6-17. Maximum absorption was observed at 675 nm, which is close to the chlorophyll Q band wavelength. The TEM images shown in Figure 6-18, show that the particles have mostly hexagonal shapes without any holes, and with an average edge length of 70 ±10 nm.

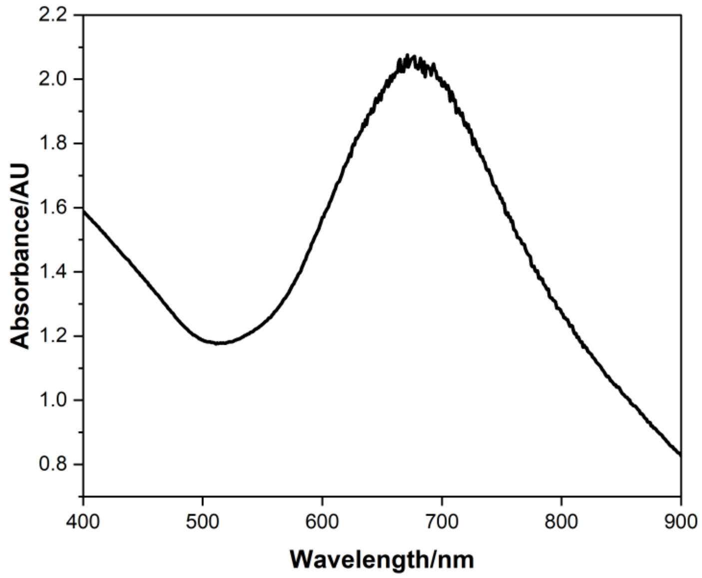

Figure 6-17: UV-vis absorbance spectra of HGN in solution after treatment with polystyrene sodium sulphonate.

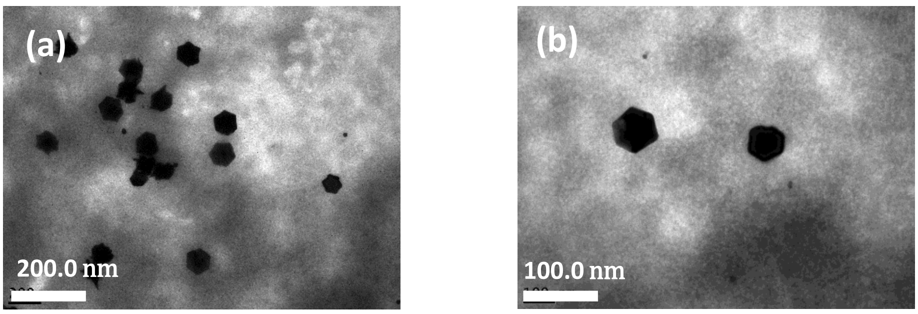

Figure 6-18: TEM images of HGN in solution after treatment with polystyrene sodium sulphonate (a) and (b).

6.4.4.3 Incorporation of HGN into PDMA brushes followed by the addition of chlorophyll (Chl *a*)

A similar mechanism could be employed when embedding HGNs into PDMA brushes. The positively charged polymer chains bind HGNs to the brush after they have been incorporated into the polymer. The addition of Chl *a* led to the formation of coordination bonds between the positively charged metal ion at the centre of the chlorophyll (Zn^{+2}) of ZnChla and the lone pair of the amino group (see Figure 6-19).

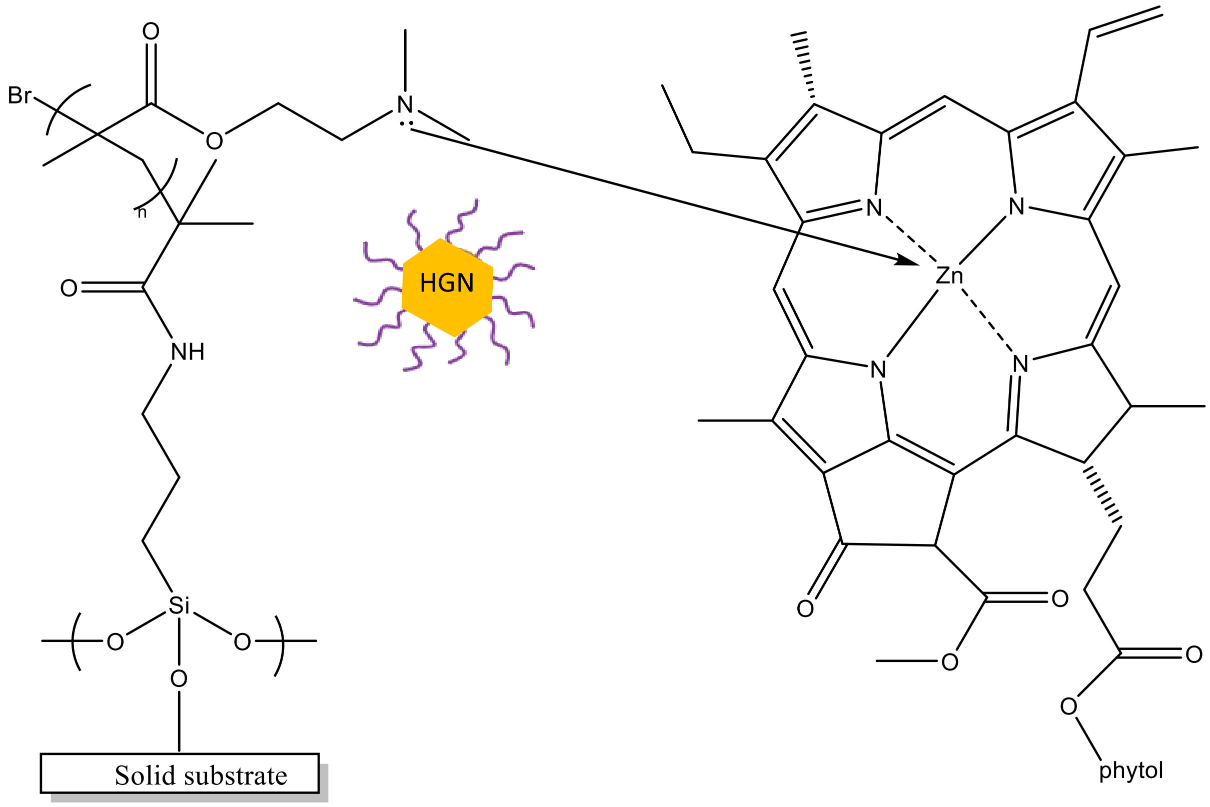

Figure 6-19: A schematic representation of the possible mechanism of plasmon-exciton coupling between HGN and ZnChla supported by PDMA brushes.

The optical characteristics of HGNs embedded in PDMA and functionalised with ZnChla were analysed using UV. Figure 6-20 displays the absorption spectrum of HGNs functionalised with polymer brushes before and after the addition of chlorophyll. Incorporating HGNs into polymer brushes resulted in a red shift caused by the change in the refractive index of the surrounding medium.

After the addition of chlorophyll at concentrations of 5 and 15 μM, the plasmon band's position was also redshifted for the same reason (see Figure 6-20). Although there were similarities in the energies of the HGNs and chlorophyll, no strong coupling was observed.

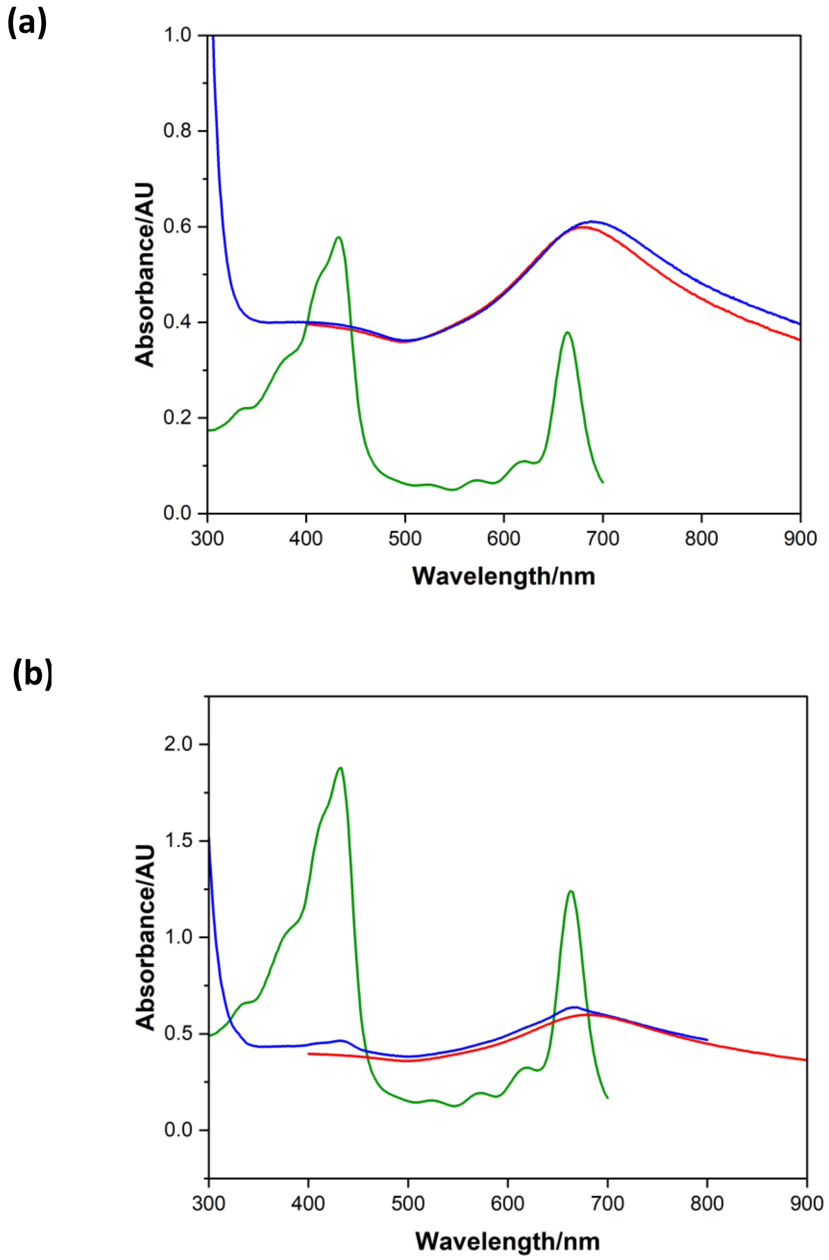

Figure 6-20: The extinction spectra of (a) HGN-embedded PDMA brushes full density (polymerisation time 1h) before (red) and after (blue) attachment of ZnChla 5 μM, compared with the extinction spectra of ZnChla 5 μM in solution (green). (b) Extinction spectra of HGN-embedded PDMA brushes before (red) and after (blue) attachment of ZnChla 15 μM, compared with the extinction spectra of ZnChla 15 μM in solution (green).

6.4.2 Sliver nanoparticles

6.4.2 .1 Synthesis and characterisation of AgNPs

Silver nanoparticles (AgNPs) were prepared according to procedures described in previous research.[285] The colloidal silver nanospheres are produced by reducing silver nitrate with hydroxylamine hydrochloride with an average size of 50 nm. The nanoparticles were characterised with UV-visible spectrometry and AFM. Figure 6-21 shows the absorbance spectra of the silver nanoparticles with a single plasmon peak at λ max 430 nm, which is consistent with the literature.[286]

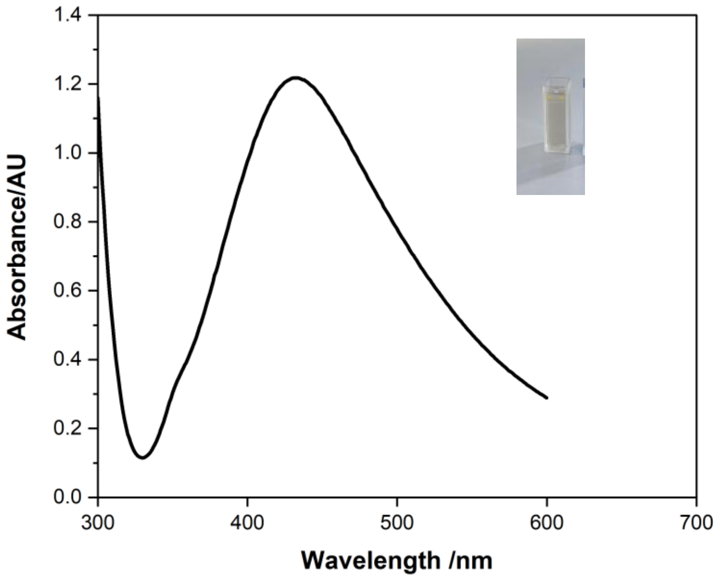

Figure 6-21: Extinction spectra of AgNPs in solution with an image showing the colour of AgNPs in a cuvette.

The AFM height image for AgNPs is shown in Figure 6-22. This image provides a detailed view of the surface morphology of the AgNPs that were immobilised on APTES-functionalised glass substrates after being immersed in the nanoparticle suspension for the desired time. The high-resolution topographical information revealed by the AFM technique allows for a comprehensive understanding of the size, shape, and distribution of the silver nanoparticles on the prepared substrate surface.

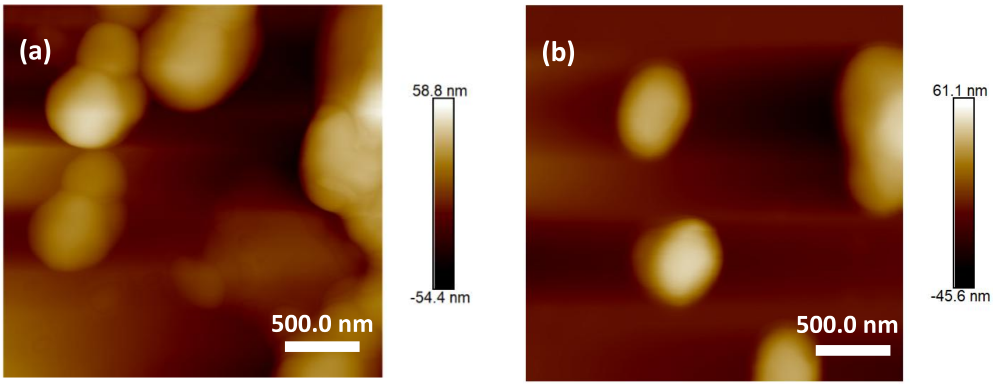

Figure 6-22: The tapping mode AFM height images (500 nm × 500 nm) of AgNPs adsorbed onto APTES (a) and (b).

6.4.2.2 The addition of chlorophyll to PDMA brushes with embedded AgNPs

As shown in Figure 6-23, AgNPs embedded into PDMA brushes also exhibited similar behaviour. The silver nanoparticles, which are coated with negatively charged nitrate ions, are bound to the positively charged polymer chains of the PDMA brushes. The addition of chlorophyll molecules results in the formation of coordination bonds between the central metal atoms in the Chl *a* and the lone pairs of electrons in the amino groups present in the PDMA polymer chains, leading to the organisation of the excitonic Chl *a* molecules within the plasmonic PDMA-AgNPs structures.

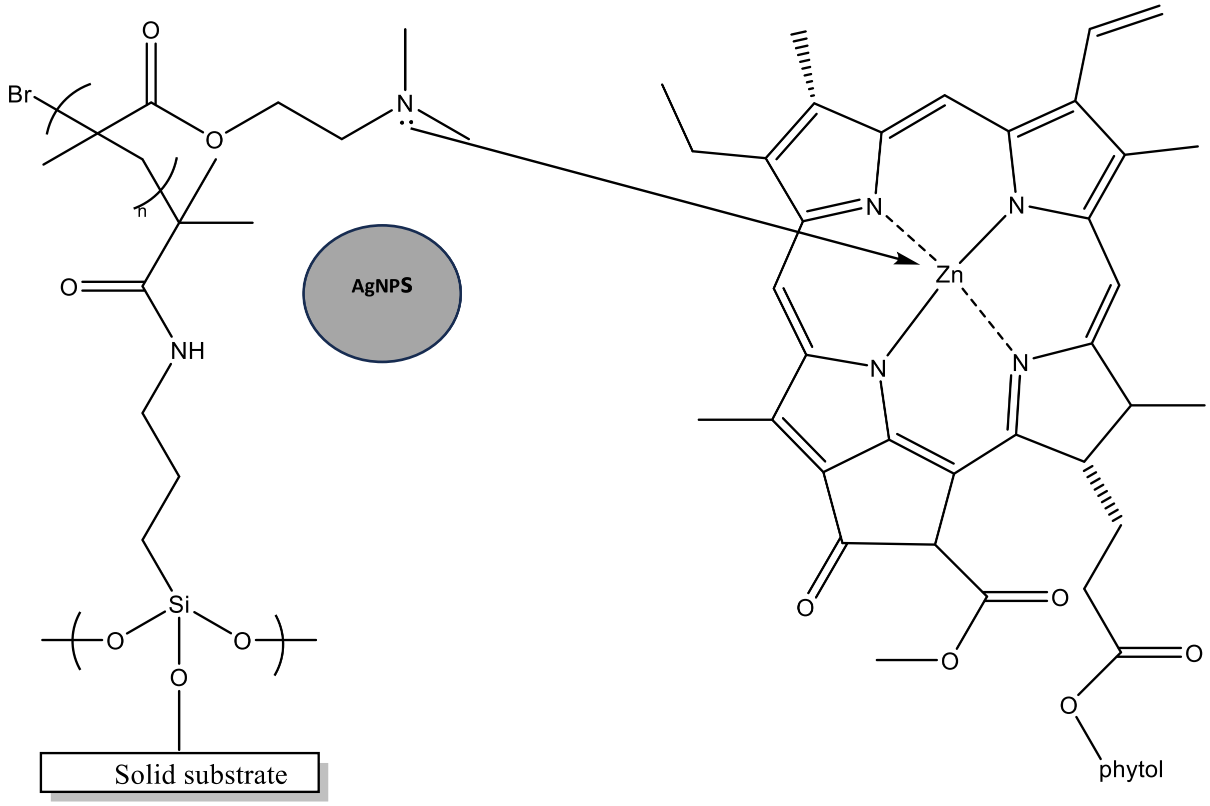

Figure 6-23: A schematic representation of the possible mechanism of plasmon-exciton coupling between AgNPs and ZnChla supported by PDMA brushes.

UV-visible absorption spectroscopy was used to analyse the optical properties of AgNPs embedded in PDMA and functionalised with ZnChla. Figure 6-24 shows the absorption spectrum of AgNPs functionalized with polymer brushes before and after the addition of chlorophyll. After incorporating AgNPs into polymer brushes, a blueshift was observed as a result of a change in the refractive index of the surrounding medium. There is a significant redshift of the AgNPs' plasmon peak from 364 nm to 404 nm. Although the energies of the gold nanoparticles and chlorophyll were similar, no strong coupling was observed.

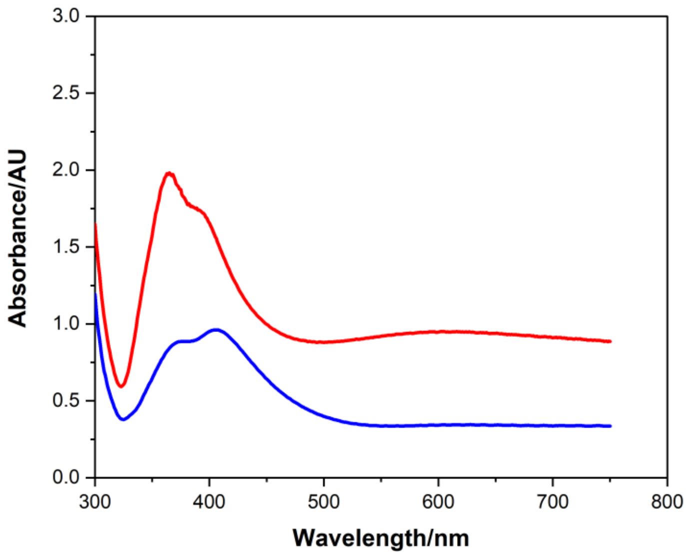

Figure 6-24: The extinction spectra of AgNPs-embedded PDMA brushes (red) before attachment of ZnChla and (blue) after attachment of ZnChla.

6.5 Conclusion

Citrate-stabilised spherical gold nanoparticles with diameters of 10, 18, and 38 nm, were prepared in a single reduction step. Nanoparticles were immobilised by binding to PDMA brushes. Subsequently, ZnChla was also bound to the surface-grafted polymers. However, there was no evidence of plasmon-exciton coupling in these materials., probably due to the large gap between the energy of the AuNP's LSPR and the energy of the ZnChla Qy transition. As a result, gold nanoparticles were synthesised with energies of 675 eV, which is close to the energy of the chlorophyll absorption, but there was again no evidence of plasmon-exciton coupling. Silver nanoparticles were synthesised with more energetic plasmons, close to the energy of the Chl *a* Soret band at 430 nm. Nevertheless. no strong coupling occurred. Thus, it is concluded that solution-phase processes in which metal nanoparticles are embedded in surface-grafted polymer brush films may not be effective at yielding strong plasmon-exciton coupling, even when high pigment loadings are achieved.

Chapter 7: Conclusion

This thesis has explored the feasibility of replicating the light-harvesting complexes found in nature, which are organised around peptide scaffolds that enable the efficient long-distance transfer of excitons. In particular, PDMA scaffolds were investigated as potential supports for excitonic Chl *a* molecules, in order to create plexcitonic antenna complexes. In Chapter 4, surface-grafted PDMA brushes were synthesised through ATRP and employed as scaffolds to support chlorophyll. The hypothesis that tertiary amine pendant groups on the PDMA would coordinate with the metal ion at the core of the Chl *a* tetrapyrrole ring, was investigated. The growth of PDMA brushes was characterised using, XPS, spectroscopic ellipsometry and AFM. A film thickness of 42 nm was achieved after a polymerisation time of 2 h. Chl *a* was extracted from spinach and incubated with PDMA grown to a thickness of ~30 nm from BiBB-APTES initiator surfaces. The binding of chlorophyll to PDMA scaffolds was confirmed using XPS and optical spectroscopy. Remarkably, Chl *a* concentrations in PDMA scaffolds reached up to ~2M, about three times the concentration found in biological light-harvesting complexes. UV-vis data indicated no shift in the main Chl *a* Qy absorption, suggesting that these high concentrations were achieved without aggregation and, hence, without concentration quenching of excited states. A PDMA brush with a partial quaternary structure can be utilised to regulate the density of chlorophyll by employing either 1-iodooctadecane or a varying concentration of chlorophyll. It can be concluded that polymer scaffolds for chlorophyll may be useful for future uses as biologically inspired energy transport systems, capable of transferring energy similarly to light-harvesting complexes coupled to plasmonic systems. The results are consistent with the hypothesis that Chl *a* binds to PDMA brushes via the coordination of the tertiary amines in the pendant groups to the Chla metal centre. This approach may be promising for the construction of pigment-polymer antennas. As long as pigment-polymer antenna complexes are successfully formed by binding ZnChla to PDMA, plexcitonic antenna complexes on gold planar surfaces can be constructed.

The growth of PDMA from DTBU on planar gold surfaces was studied using XPS, AFM, and SE. After a polymerisation time of 1 h, the thickness of PDMA was 26 ± 2 nm, which is less than the thickness observed when PDMA was polymerised from BIBB-APTES for the same time which reached 35 nm. The amount of chlorophyll that could be added to the PDMA polymer was restricted, however, which prompted the use of mixed self-assembled monolayers (DTBU and MUL). The use of the latter reduces the grafting density of the polymer, which leads to an increase in the chlorophyll's binding ability and hence the amount that could be bound. To regulate the concentration of the DTBU initiator on the gold surfaces, it was co-adsorbed with an inert thiol (11-MUL) from solutions with different ratios of the two adsorbates. XPS studies showed the 11-MUL has a small efficiency advantage over DTBU initiator disulfides, due to its smaller relative size. The XPS data revealed a greatly enhanced binding of Chl *a* to PDMA in films of reduced density (χBr (Au) = 0.24), enabling an increase of up to four times the amount of Chl *a* attached to full dance polymer due to the decreased steric hindrance.

The embedding of plasmonic materials within PDMA brushes was examined as an alternative strategy for constructing pigment-polymer antennas on gold surfaces. Initial attempts with AuNPs did not achieve strong plasmon-exciton coupling due to the energy difference between the nanoparticles' LSPR and ZnChla's transition. Further exploration with HGN and AgNPs also could not achieve the desired coupling. Even at higher pigment concentrations, solution-phase procedures using metal nanoparticles inside surface-grafted polymer brush films may not effectively facilitate plasmon-exciton coupling.

Chapter 8: Future Work

Future research may expand upon the findings of this study by investigating many promising areas. One promising area for exploration is the investigation of alternative light-harvesting molecules. The synthetic modification of chlorophyll results in low yields, which limits its scalability for practical application. Commercially available organic dyes, such as rhodamine dyes, could be investigated as alternative and potentially simpler synthetic routes for developing these polymer systems. Rhodamine dyes, for example, exhibit strong absorption at around 550 nm, and the plasmonic surfaces can be spectra-tuned to match the dye's absorption, thereby enabling strong plasmon-exciton coupling.[287] Exploring these alternative light-harvesting molecules could lead to enhanced performance and scalability for applications in areas like solar energy harvesting and optoelectronics.

Furthermore, future studies may concentrate on patterning PDMA brushes deposited on DTBU substrates utilising lithographic methods such as electron beam lithography (EBL). EBL offers precise control over the size and shape of nanostructures, facilitating more comprehensive investigations of strong coupling phenomena and potentially enhancing coupling strength. Patterned brushes may enhance plasmon-exciton interactions by generating tailored nanostructures that optimize the effects, reduce the density, and accommodate a sufficient number of excitons. Initially, extinction spectra will be acquired for PDMA layers both with and without Chl *a* binding to investigate optical alterations. This study will evaluate the impact of grafting density and chlorophyll concentration on coupling strength, as this energy is contingent upon exciton concentration. This patterning approach could lead to the development of advanced plasmonic and excitonic devices with enhanced light-matter interactions and improved performance for various applications, such as optoelectronics, photocatalysis, and energy harvesting.

A key topic for more investigation is the optimisation of the polymerisation process to enhance the attachment of Chl *a* to the polymer surface. This study found that densely packed PDMA brushes induced steric hindrance, preventing the appropriate accommodation of Chl *a* molecules and reducing the number of excitons within the plasmon system, hence reducing coupling strength. To address this, future research could focus on regulating the grafting density of the PDMA brushes by controlling the polymerisation time t of the surface-grafted polymers or by using patterned polymer brushes created through lithography techniques to reduce the density. This would help to optimise the distribution and concentration of Chl *a* within the polymer brushes. Additionally, this study can be expanded by employing depth profiling using XPS in conjunction with argon gas cluster sputtering to more thoroughly characterise the distribution of Chl *a* within the PDMA brushes, depending on the degree of polymerisation and brush grafting density. This depth-resolved analysis could provide valuable insights into how the Ch *a* is incorporated within the polymer brushes and how this impacts the plasmon-exciton coupling.

The present study was unable to achieve strong coupling between plasmonic nanoparticles, specifically AuNPs or AgNPs, and chlorophyll. In the following stage, it could be beneficial to investigate strong coupling through the use of iodinated Nile Red (INR) as the dye in combination, aiming to achieve this strong coupling by bonding INR molecules to AuNP-embedded PDMA brushes. BIBB-APTES can be used to produce polymer brushes on a glass substrate. The polymer brushes offer a stable support system that enables the controlled interaction between the INR dye and the LSPR of the embedded AuNPs. This arrangement has the potential to generate a strong plexcitonic complex, characterised by improved optical properties resulting from the intense plasmon-exciton interaction.

A second possible approach consists of incorporating AuNPs into PDMA brushes modified with a commercially available dye, such as Cyanine3 NHS ester (Cy3-NHS ester). The flexibility to adjust the overlap between the LSPR and exciton through the use of various dyes and polymer systems allows for the optimisation of conditions conducive to strong coupling and plexciton formation.

These directions offer significant opportunities to enhance our comprehension of plexcitonic complexes and investigate novel applications in nanophotonics, light harvesting, and other fields.

Chapter 9: References

1. V. G. Achanta, *Reviews in Physics*, 2020, **5**, 100041.
2. W. Shao, Z. Liang, T. Guan, J. Chen, Z. Wang, H. Wu, J. Zheng, I. Abdulhalim and L. Jiang, *Journal of Materials Chemistry A*, 2018, **6**, 8419-8429.
3. I. Vangelidis, A. Theodosi, M. J. Beliatis, K. K. Gandhi, A. Laskarakis, P. Patsalas, S. Logothetidis, S. R. P. Silva and E. Lidorikis, *Acs Photonics*, 2018, **5**, 1440-1452.
4. M. Li, U. Guler, Y. Li, A. Rea, E. K. Tanyi, Y. Kim, M. A. Noginov, Y. Song, A. Boltasseva and V. M. Shalaev, *ACS Energy Letters*, 2018, **3**, 1578-1583.
5. G. Barbillon, T. Noblet, B. Busson, A. Tadjeddine and C. Humbert, *Journal of materials science*, 2018, **53**, 4554-4562.
6. M. Dolci, J. F. Bryche, C. Leuvrey, S. Zafeiratos, S. Gree, S. Begin-Colin, G. Barbillon and B. P. Pichon, *Journal of Materials Chemistry C*, 2018, **6**, 9102-9110.
7. J. A. Huang, Y. Q. Zhao, X. J. Zhang, L. F. He, T. L. Wong, Y. S. Chui, W. J. Zhang and S. T. Lee, *Nano letters*, 2013, **13**, 5039-5045.
8. V. G. Kravets, A. V. Kabashin, W. L. Barnes and A. N. Grigorenko, *Chemical reviews*, 2018, **118**, 5912-5951.
9. S. Hayashi and T. Okamoto, *Journal of Physics D: Applied Physics*, 2012, **45**, 433001.
10. V. Amendola, R. Pilot, M. Frasconi, O. M. Maragò and M. A. Iatì, *Journal of Physics: Condensed Matter*, 2017, **29**, 203002.
11. A. Lishchuk, G. Kodali, J. A. Mancini, M. Broadbent, B. Darroch, O. A. Mass, A. Nabok, P. L. Dutton, C. N. Hunter and P. Törmä, *Nanoscale*, 2018, **10**, 13064-13073.
12. A. Rider, K. Ostrikov and S. Furman, *The European Physical Journal D*, 2012, **66**, 1-19.
13. J. Jana, M. Ganguly and T. Pal, *RSC advances*, 2016, **6**, 86174-86211.
14. D. Maystre, in *Plasmonics: from basics to advanced topics*, Springer, 2012, 39-83.
15. J. M. Garnett, *Philosophical Transactions of the Royal Society of London. Series A, Containing Papers of a Mathematical or Physical Character*, 1904, **203**, 385-420.
16. U. Fano, *Annalen der Physik*, 1938, **424**, 393-443.
17. A. Otto, *Zeitschrift für Physik A Hadrons and nuclei*, 1968, **216**, 398-410.
18. R. H. Ritchie, E. Arakawa, J. Cowan and R. Hamm, *Physical review letters*, 1968, **21**, 1530.

19. S. K. Gray, *The Journal of Physical Chemistry C*, 2013, **117**, 1983-1994.
20. F. B. Kamal Eddin and Y. W. Fen, *Molecules*, 2020, **25**, 2769.
21. A. Moores and F. Goettmann, *New Journal of Chemistry*, 2006, **30**, 1121-1132.
22. J. Liu, M. Jalali, S. Mahshid and S. Wachsmann-Hogiu, *Analyst*, 2020, **145**, 364-384.
23. J. Jatschka, A. Dathe, A. Csáki, W. Fritzsche and O. Stranik, *Sensing and bio-sensing research*, 2016, **7**, 62-70.
24. C. Caucheteur, T. Guo and J. Albert, *Analytical and bioanalytical chemistry*, 2015, **407**, 3883-3897.
25. J. Homola, *Chemical reviews*, 2008, **108**, 462-493.
26. J. Homola, *Analytical and bioanalytical chemistry*, 2003, **377**, 528-539.
27. S. Unser, I. Bruzas, J. He and L. Sagle, *Sensors*, 2015, **15**, 15684-15716.
28. J. Cuanalo Fernandez, J. Urrutia Anguiano, S. Guerra Hernandez, N. Korneev, M. De la Mora Mojica, A. Reyes–Coronado, I. Cosme Bolanos, S. Mansurova and R. Ramos Garcia, 2022,
29. P. P. A. Suthanthiraraj and A. K. Sen, *Biosensors and Bioelectronics*, 2019, **132**, 38-46.
30. A. Bonyár, *Biosensors*, 2021, **11**, 527.
31. J. N. Anker, W. P. Hall, O. Lyandres, N. C. Shah, J. Zhao and R. P. Van Duyne, *Nanoscience and Technology: A Collection of Reviews from Nature Journals*, 2010, **30**, 308-319.
32. G. Liang, Z. Luo, K. Liu, Y. Wang, J. Dai and Y. Duan, *Critical reviews in analytical chemistry*, 2016, **46**, 213-223.
33. J. N. Anker, W. P. Hall, O. Lyandres, N. C. Shah, J. Zhao and R. P. Van Duyne, *Nature materials*, 2008, **7**, 442-453.
34. H. Chen, X. Kou, Z. Yang, W. Ni and J. Wang, *Langmuir*, 2008, **24**, 5233-5237.
35. V. Amendola and M. Meneghetti, *The Journal of Physical Chemistry C*, 2009, **113**, 4277-4285.
36. G. Shakhgildyan, L. Avakyan, M. Ziyatdinova, G. Atroshchenko, N. Presnyakova, M. Vetchinnikov, A. Lipatiev, L. Bugaev and V. Sigaev, *Journal of Non-Crystalline Solids*, 2021, **566**, 120893.
37. M. Hamamoto and H. Yagyu, *Journal of Nanoparticle Research*, 2023, **25**, 158.
38. Y. You, S. Lim and S. Gunasekaran, *ACS Applied Nano Materials*, 2020, **3**, 1900-1909.

39. J. E. Ortiz-Castillo, R. C. Gallo-Villanueva, M. J. Madou and V. H. Perez-Gonzalez, *Coordination Chemistry Reviews*, 2020, **425**, 213489.
40. G. Nichols, S. Byard, M. J. Bloxham, J. Botterill, N. J. Dawson, A. Dennis, V. Diart, N. C. North and J. D. Sherwood, *Journal of pharmaceutical sciences*, 2002, **91**, 2103-2109.
41. S. V. Sokolov, K. Tschulik, C. Batchelor-McAuley, K. Jurkschat and R. G. Compton, *Analytical chemistry*, 2015, **87**, 10033-10039.
42. W. Rechberger, A. Hohenau, A. Leitner, J. Krenn, B. Lamprecht and F. Aussenegg, *Optics communications*, 2003, **220**, 137-141.
43. K. H. Su, Q. H. Wei, X. Zhang, J. Mock, D. R. Smith and S. Schultz, *Nano letters*, 2003, **3**, 1087-1090.
44. X. Lin, S. Ye, C. Kong, K. Webb, C. Yi, S. Zhang, Q. Zhang, J. T. Fourkas and Z. Nie, *Journal of the American Chemical Society*, 2020, **142**, 17282-17286.
45. B. Kang, M. M. Afifi, L. A. Austin and M. A. El-Sayed, *Acs Nano*, 2013, **7**, 7420-7427.
46. Y. A. Pritom, D. K. Sikder, S. Zaman and M. Hossain, *Nanoscale Advances*, 2023, **5**, 4986-4995.
47. L. B. Sagle, L. K. Ruvuna, J. A. Ruemmele and R. P. Van Duyne, *Nanomedicine*, 2011, **6**, 1447-1462.
48. J. Kneipp and K. Kneipp, *ACS nano*, 2024.
49. R. Taheri-Ledari, F. Ganjali, S. Zarei-Shokat, R. Dinmohammadi, F. R. Asl, A. Emami, Z. S. Mojtabapour, Z. Rashvandi, A. Kashtiaray and F. Jalali, *Nanoscale Advances*, 2023, **5**, 6768-6786.
50. J. r. Polte, T. T. Ahner, F. Delissen, S. Sokolov, F. Emmerling, A. F. Thünemann and R. Kraehnert, *Journal of the American Chemical Society*, 2010, **132**, 1296-1301.
51. P. G. Jamkhande, N. W. Ghule, A. H. Bamer and M. G. Kalaskar, *Journal of drug delivery science and technology*, 2019, **53**, 101174.
52. S. Barazzouk, L. Bekalé and S. Hotchandani, *Journal of Materials Chemistry*, 2012, **22**, 25316-25324.
53. E. Cao, W. Lin, M. Sun, W. Liang and Y. Song, *Nanophotonics*, 2018, **7**, 145-167.
54. Y. M. Lee, S.-E. Kim and J. E. Park, *Nano Convergence*, 2023, **10**, 34.
55. X. Liu, T. Galfsky, Z. Sun, F. Xia, E. c. Lin, Y. H. Lee, S. Kéna-Cohen and V. M. Menon, *Nature Photonics*, 2015, **9**, 30-34.

56. G. Zengin, G. Johansson, P. Johansson, T. J. Antosiewicz, M. Käll and T. Shegai, *Scientific reports*, 2013, **3**, 3074.
57. P. Törmä and W. L. Barnes, *Reports on Progress in Physics*, 2014, **78**, 013901.
58. J. R. Tischler, M. S. Bradley, Q. Zhang, T. Atay, A. Nurmikko and V. Bulović, *Organic Electronics*, 2007, **8**, 94-113.
59. T. Hakala, J. Toppari, A. Kuzyk, M. Pettersson, H. Tikkanen, H. Kunttu and P. Törmä, *Physical review letters*, 2009, **103**, 053602.
60. L. Shi, T. Hakala, H. Rekola, J.-P. Martikainen, R. Moerland and P. Törmä, *Physical review letters*, 2014, **112**, 153002.
61. A. Väkeväinen, R. Moerland, H. Rekola, A. P. Eskelinen, J. P. Martikainen, D.-H. Kim and P. Törmä, *Nano letters*, 2014, **14**, 1721-1727.
62. H. Groß, J. M. Hamm, T. Tufarelli, O. Hess and B. Hecht, *Science advances*, 2018, **4**, eaar4906.
63. P. Vasa, W. Wang, R. Pomraenke, M. Lammers, M. Maiuri, C. Manzoni, G. Cerullo and C. Lienau, *Nature Photonics*, 2013, **7**, 128-132.
64. G. Zengin, M. Wersäll, S. Nilsson, T. J. Antosiewicz, M. Käll and T. Shegai, *Physical review letters*, 2015, **114**, 157401.
65. A. M. Fales, S. J. Norton, B. M. Crawford, B. G. DeLacy and T. Vo-Dinh, *Physical Chemistry Chemical Physics*, 2015, **17**, 24931-24936.
66. A. Tsargorodska, M. L. Cartron, C. Vasilev, G. Kodali, O. A. Mass, J. J. Baumberg, P. L. Dutton, C. N. Hunter, P. i. Törmä and G. J. Leggett, *Nano Letters*, 2016, **16**, 6850-6856.
67. A. Lishchuk, E. Csányi, B. Darroch, C. Wilson, A. Nabok and G. J. Leggett, *Chemical Science*, 2022, **13**, 2405-2417.
68. F. Todisco, M. De Giorgi, M. Esposito, L. De Marco, A. Zizzari, M. Bianco, L. Dominici, D. Ballarini, V. Arima and G. Gigli, *Acs Photonics*, 2018, **5**, 143-150.
69. W. J. Tan, P. A. Thomas, I. J. Luxmoore and W. L. Barnes, *The Journal of Chemical Physics*, 2021, **154**.
70. W. G. Chung, E. Kim, Y. W. Kwon, J. Lee, S. Lee, I. Jeong and J. U. Park, *Advanced Functional Materials*, 2024, **34**, 307990.
71. J. C. Lin, P. Liatsis and P. Alexandridis, *Polymer Reviews*, 2023, **63**, 67-126.
72. E. Le Ru and P. Etchegoin, *Principles of Surface-Enhanced Raman Spectroscopy: and related plasmonic effects*, Elsevier, 2008.

73. R. Rajasekharan Unnithan, M. Sun, X. He, E. Balaur, A. Minovich, D. N. Neshev, E. Skafidas and A. Roberts, *Materials*, 2017, **10**, 383.

74. E. C. Ashigwuike, O. J. Ushie, R. Mackay and W. Balachandran, *Sensors and Actuators A: Physical*, 2015, **229**, 154-165.

75. P. R. West, S. Ishii, G. V. Naik, N. K. Emani, V. M. Shalaev and A. Boltasseva, *Laser & photonics reviews*, 2010, **4**, 795-808.

76. Q. Fu, M. Stein, W. Li, J. Zheng and F. E. Kruis, *Nanotechnology*, 2019, **31**, 025302.

77. A. Zareei, S. Gopalakrishnan, Z. Mutlu, Z. He, S. Peana, H. Wang and R. Rahimi, *ACS Applied Electronic Materials*, 2021, **3**, 3352-3364.

78. T. Yonezawa and T. Kunitake, *Colloids and Surfaces A: Physicochemical and Engineering Aspects*, 1999, **149**, 193-199.

79. S. J. Amina and B. Guo, *International journal of nanomedicine*, 2020, **15**, 9823.

80. M. Shah, V. Badwaik, Y. Kherde, H. K. Waghwani, T. Modi, Z. P. Aguilar, H. Rodgers, W. Hamilton, T. Marutharaj and C. Webb, *Frontiers in Bioscience-Landmark*, 2014, **19**, 1320-1344.

81. X. Ji, X. Song, J. Li, Y. Bai, W. Yang and X. Peng, *Journal of the American Chemical Society*, 2007, **129**, 13939-13948.

82. S. Yang, Y. Wang, Q. Wang, R. Zhang and B. Ding, *Colloids and Surfaces A: Physicochemical and Engineering Aspects*, 2007, **301**, 174-183.

83. Y. Chen, X. Gu, C.-G. Nie, Z.-Y. Jiang, Z.-X. Xie and C.-J. Lin, *Chemical communications*, 2005, 4181-4183.

84. A. Gole and C. J. Murphy, *Chemistry of Materials*, 2004, **16**, 3633-3640.

85. C. R. Bridges, P. M. DiCarmine, A. Fokina, D. Huesmann and D. S. Seferos, *Journal of Materials Chemistry A*, 2013, **1**, 1127-1133.

86. Z. C. Xu, C. M. Shen, C. W. Xiao, T. Z. Yang, H.-R. Zhang, J. Q. Li, H. L. Li and H. J. Gao, *Nanotechnology*, 2007, **18**, 115608.

87. M. Brust, M. Walker, D. Bethell, D. J. Schiffrin and R. Whyman, *Journal of the Chemical Society, Chemical Communications*, 1994, **7**, 801-802.

88. M. Giersig and P. Mulvaney, *Langmuir*, 1993, **9**, 3408-3413.

89. K. M. Abou El-Nour, A. a. Eftaiha, A. Al-Warthan and R. A. Ammar, *Arabian journal of chemistry*, 2010, **3**, 135-140.

90. P. Lee and D. Meisel, *The Journal of Physical Chemistry*, 1982, **86**, 3391-3395.

91. Y. Hang, A. Wang and N. Wu, *Chemical Society Reviews*, 2024,**53**,2932-2971.

92. A. Tao, P. Sinsermsuksakul and P. Yang, *Angewandte Chemie-International Edition in English*, 2006, **45**, 4597.
93. I. Begum, F. Ameen, Z. Soomro, S. Shamim, S. AlNadhari, A. Almansob, A. Al-Sabri and A. Arif, *Journal of King Saud University-Science*, 2021, **33**, 101231.
94. I. Grabowska-Jadach, D. Kalinowska, M. Drozd and M. Pietrzak, *Biomedicine & Pharmacotherapy*, 2019, **111**, 1147-1155.
95. D. Senapati, T. Senapati, P. S. Wate, R. Kanchanapally, Z. Fan, A. K. Singh and P. C. Ray, *Chemical Communications*, 2012, **48**, 6034-6036.
96. G. C. Ritsema van Eck, L. Chiappisi and S. De Beer, *ACS Applied Polymer Materials*, 2022, **4**, 3062-3087.
97. A. M. Bhayo, Y. Yang and X. He, *Progress in Materials Science*, 2022, **130**, 101000.
98. D. Li, L. Xu, J. Wang and J. E. Gautrot, *Advanced Healthcare Materials*, 2021, **10**, 2000953.
99. Q. A. Besford, H. Yong, H. Merlitz, A. J. Christofferson, J. U. Sommer, P. Uhlmann and A. Fery, *Angewandte Chemie International Edition*, 2021, **60**, 16600-16606.
100. Y. Zhang, M. Li, B. Li and W. Sheng, *Langmuir*, 2024, **40**, 5571-5589.
101. A. M. Bhayo, Y. Yang and X. He, *Progress in Materials Science*, 2022,**130**, 101000.
102. A. Bousquet, H. Awada, R. C. Hiorns, C. Dagron-Lartigau and L. Billon, *Progress in Polymer Science*, 2014, **39**, 1847-1877.
103. S. Z. Moghaddam and E. Thormann, *Current opinion in colloid & interface science*, 2020, **47**, 27-45.
104. A. Halperin, M. Tirrell and T. Lodge, *Macromolecules: Synthesis, Order and Advanced Properties*, 1992, 31-71.
105. J. O. Zoppe, N. C. Ataman, P. Mocny, J. Wang, J. Moraes and H.-A. Klok, *Chemical reviews*, 2017, **117**, 1105-1318.
106. M. Kim, S. K. Schmitt, J. W. Choi, J. D. Krutty and P. Gopalan, *Polymers*, 2015, **7**, 1346-1378.
107. S. Edmondson, V. L. Osborne and W. T. Huck, *Chemical society reviews*, 2004, **33**, 14-22.
108. S. Banerjee, T. K. Paira and T. K. Mandal, *Polymer Chemistry*, 2014, **5**, 4153-4167.
109. W. Wei, J. L. Faubel, H. Selvakumar, D. T. Kovari, J. Tsao, F. Rivas, A. T. Mohabir, M. Krecker, E. Rahbar and A. R. Hall, *Nature Communications*, 2019, **10**, 5527.
110. R. R. Bhat, M. R. Tomlinson, T. Wu and J. Genzer, *Surface-initiated polymerization* , Springer Link, 2006,**198**, 51-124.

111. Z. Bao, M. L. Bruening and G. L. Baker, *Macromolecules*, 2006, **39**, 5251-5258.
112. M. Lillethorup, K. Shimizu, N. Plumeré, S. U. Pedersen and K. Daasbjerg, *Macromolecules*, 2014, **47**, 5081-5088.
113. R. Barbey, V. Laporte, S. Alnabulsi and H.-A. Klok, *Macromolecules*, 2013, **46**, 6151-6158.
114. M. Szuwarzyński, K. Wolski, A. Pomorska, T. Uchacz, A. Gut, Ł. Łapok and S. Zapotoczny, *Chemistry–A European Journal*, 2017, **23**, 11239-11243.
115. A. Dirani, X. Laloyaux, A. E. Fernandes, B. Mathy, O. Schicke, O. Riant, B. Nysten and A. M. Jonas, *Macromolecules*, 2012, **45**, 9400-9408.
116. S. Christau, T. Möller, Z. Yenice, J. Genzer and R. von Klitzing, *Langmuir*, 2014, **30**, 13033-13041.
117. V. Spampinato, G. Ceccone and S. Giordani, *Biointerphases*, 2015, **10**,019006.
118. E. Csányi, D. B. Hammond, B. Bower, E. C. Johnson, A. Lishchuk, S. P. Armes, Z. Dong and G. J. Leggett, *Langmuir*, 2024, **40**, 14527-14539.
119. J. R. Du, F. Du, K. Yang, J. Zheng, K. Ma, C. Du and H. Yang, *Journal of Membrane Science*, 2023, **683**, 121868.
120. M. Flejszar, K. Ślusarczyk, P. Chmielarz, J. Smenda, K. Wolski, M. Wytrwal-Sarna and M. Oszajca, *Polymer*, 2022, **257**, 125268.
121. S. Gupta, M. Agrawal, M. Conrad, N. A. Hutter, P. Olk, F. Simon, L. M. Eng, M. Stamm and R. Jordan, *Advanced Functional Materials*, 2010, **20**, 1756-1761.
122. S. Lai, H. Wang, N. Qiao, H. Shang, X. Sun, Z. Wang, Q. Li, Y. Lu and X. Zhang, *Journal of Sol-Gel Science and Technology*, 2022, **103**, 139-150.
123. R. Dong, R. P. Molloy, M. Lindau and C. K. Ober, *Biomacromolecules*, 2010, **11**, 2027-2032.
124. J. Niskanen, C. Wu, M. Ostrowski, G. G. Fuller, S. Hietala and H. Tenhu, *Macromolecules*, 2013, **46**, 2331-2340.
125. M. Thomas, M. Gajda, C. Amiri Naini, S. Franzka, M. Ulbricht and N. Hartmann, *Langmuir*, 2015, **31**, 13426-13432.
126. L. A. B. Rawlinson, S. M. Ryan, G. Mantovani, J. A. Syrett, D. M. Haddleton and D. J. Brayden, *Biomacromolecules*, 2010, **11**, 443-453.
127. M. A. De Jesús-Téllez, D. M. Sánchez-Cerrillo, P. Quintana-Owen, U. S. Schubert, D. Contreras-López and C. Guerrero-Sánchez, *Macromolecular Chemistry and Physics*, 2020, **221**, 1900543.
128. V. Y. Shevtsov, T.-Y. Hsin and Y.-T. Shieh, *Polymer Chemistry*, 2022, **13**, 1429-1436.

129. Z. Cheng, X. Zhu, Z. Shi, K. Neoh and E. Kang, *Industrial & engineering chemistry research*, 2005, **44**, 7098-7104.
130. T. Manouras, E. Koufakis, S. H. Anastasiadis and M. Vamvakaki, *Soft Matter*, 2017, **13**, 3777-3782.
131. A. M. Breul, M. D. Hager and U. S. Schubert, *Chemical Society Reviews*, 2013, **42**, 5366-5407.
132. X. Dai, F. Zhou, N. Khan, W. T. Huck and C. F. Kaminski, *Langmuir*, 2008, **24**, 13182-13185.
133. A. Nese, N. V. Lebedeva, G. Sherwood, S. Averick, Y. Li, H. Gao, L. Peteanu, S. S. Sheiko and K. Matyjaszewski, *Macromolecules*, 2011, **44**, 5905-5910.
134. M. F. Fouz, K. Mukumoto, S. Averick, O. Molinar, B. M. McCartney, K. Matyjaszewski, B. A. Armitage and S. R. Das, *ACS Central Science*, 2015, **1**, 431-438.
135. M. Kopeć, S. Tas, M. Cirelli, R. van der Pol, I. de Vries, G. J. Vancso and S. de Beer, *ACS Applied Polymer Materials*, 2019, **1**, 136-140.
136. N. Li, J. Lu, X. Xia, Q. Xu and L. Wang, *Dyes and Pigments*, 2009, **80**, 73-79.
137. J. Madsen, N. J. Warren, S. P. Armes and A. L. Lewis, *Biomacromolecules*, 2011, **12**, 2225-2234.
138. S. A. Ahmad, G. J. Leggett, A. Hucknall and A. Chilkoti, *Biointerphases*, 2011, **6**, 8-15.
139. C. J. Hawker, A. W. Bosman and E. Harth, *Chemical reviews*, 2001, **101**, 3661-3688.
140. R. Barbey, L. Lavanant, D. Paripovic, N. Schuwer, C. Sugnaux, S. Tugulu and H. A. Klok, *Chemical reviews*, 2009, **109**, 5437-5527.
141. K. Matyjaszewski and J. Xia, *Chemical reviews*, 2001, **101**, 2921-2990.
142. W. A. Braunecker and K. Matyjaszewski, *Journal of Molecular Catalysis A: Chemical*, 2006, **254**, 155-164.
143. T. Pintauer and K. Matyjaszewski, *Chemical Society Reviews*, 2008, **37**, 1087-1097.
144. M. Szewczyk-Łagodzińska, A. Plichta, M. Dębowski, S. Kowalczyk, A. Iuliano and Z. Florjańczyk, *Polymers*, 2023, **15**, 1234.
145. F. Lorandi, M. Fantin and K. Matyjaszewski, *Journal of the American Chemical Society*, 2022, **144**, 15413-15430.
146. T. E. Patten and K. Matyjaszewski, *Accounts of chemical research*, 1999, **32**, 895-903.
147. J. S. Wang and K. Matyjaszewski, *Macromolecules*, 1995, **28**, 7901-7910.

148. K. Matyjaszewski, D. A. Shipp, J.-L. Wang, T. Grimaud and T. E. Patten, *Macromolecules*, 1998, **31**, 6836-6840.
149. K. A. Davis and K. Matyjaszewski, *Macromolecules*, 2000, **33**, 4039-4047.
150. Y. Kotani, M. Kamigaito and M. Sawamoto, *Macromolecules*, 2000, **33**, 6746-6751.
151. T. E. Patten and K. Matyjaszewski, *Advanced Materials*, 1998, **10**, 901-915.
152. N. V. Tsarevsky, W. A. Braunecker and K. Matyjaszewski, *Journal of organometallic chemistry*, 2007, **692**, 3212-3222.
153. K. Matyjaszewski, *Current Opinion in Solid State and Materials Science*, 1996, **1**, 769-776.
154. K. Matyjaszewski, *Solid State Mater. Sci*, 1996, **1**, 769.
155. J. Xia, X. Zhang and K. Matyjaszewski, ACS Publications, 2000.
156. L. f. Fang, N. c. Wang, M. y. Zhou, B. k. Zhu, L. p. Zhu and A. E. John, *Chinese Journal of Polymer Science*, 2015, **33**, 1491-1502.
157. K. Matyjaszewski, *Advanced Materials*, 2018, **30**, 1706441.
158. R. Kumar, A. Welle, F. Becker, I. Kopyeva and J. Lahann, *ACS applied materials & interfaces*, 2018, **10**, 31965-31976.
159. I. D. Grishin, E. I. Zueva, Y. S. Pronina and D. F. Grishin, *Catalysts*, 2023, **13**, 444.
160. K. Matyjaszewski and N. V. Tsarevsky, *Journal of the American Chemical Society*, 2014, **136**, 6513-6533.
161. G. Szczepaniak, L. Fu, H. Jafari, K. Kapil and K. Matyjaszewski, *Accounts of Chemical Research*, 2021, **54**, 1779-1790.
162. Z. Zhang, X. Wang, K. C. Tam and G. Sèbe, *Carbohydrate polymers*, 2019, **205**, 322-329.
163. L. Fang, Y. Li, Z. Chen, W. Liu, J. Zhang, S. Xiang, H. Shen, Z. Li and B. Yang, *ACS applied materials & interfaces*, 2014, **6**, 19951-19957.
164. S. Christau, T. Möller, F. Brose, J. Genzer, O. Soltwedel and R. von Klitzing, *Polymer*, 2016, **98**, 454-463.
165. R. R. Bhat, J. Genzer, B. N. Chaney, H. W. Sugg and A. Liebmann-Vinson, *Nanotechnology*, 2003, **14**, 1145.
166. D. Boyaciyan, P. Krause and R. Von Klitzing, *Soft matter*, 2018, **14**, 4029-4039.
167. R. E. Blankenship, *Molecular mechanisms of photosynthesis*, John Wiley & Sons, 2021.
168. F. Nan, S. J. Ding, L. Ma, Z. Q. Cheng, Y. T. Zhong, Y. F. Zhang, Y. H. Qiu, X. Li, L. Zhou and Q. Q. Wang, *Nanoscale*, 2016, **8**, 15071-15078.

169. S. Barazzouk and S. Hotchandani, *Journal of Applied Physics*, 2004, **96**, 7744-7746.
170. N. Patni, S. G. Pillai and P. Sharma, *International Journal of Energy Research*, 2020, **44**, 10846-10859.
171. H. Furukawa, T. Watanabe and K. Kuroda, *Chemical Communications*, 2001, 2002-2003.
172. C. Houssier and K. Sauer, *Journal of the American Chemical Society*, 1970, **92**, 779-791.
173. A. Mezacasa, A. Queiroz, D. Graciano, M. Pontes, E. Santiago, I. Oliveira, A. Lopez, G. Casagrande, M. Scherer and D. dos Reis, *Journal of Photochemistry and Photobiology A: Chemistry*, 2020, **389**, 112252.
174. C. Jubert and G. Bailey, *Journal of chromatography A*, 2007, **1140**, 95-100.
175. R. D. Sandiningtyas and V. Suendo, 2010, 859-873.
176. T. Mirkovic, E. E. Ostroumov, J. M. Anna, R. Van Grondelle, Govindjee and G. D. Scholes, *Chemical reviews*, 2017, **117**, 249-293.
177. A. Hosikian, S. Lim, R. Halim and M. K. Danquah, *International journal of chemical engineering*, 2010, **2010**, **,** 391632.
178. R. Mandal and G. Dutta, *Sensors International*, 2020, **1**, 100058.
179. H. K. Lichtenthaler and C. Buschmann, *Current protocols in food analytical chemistry*, 2001, **1**, F4. 3.1-F4. 3.8.
180. P. Samyn, V. K. Rastogi, N. S. S. Baba and J. Van Erps, *Catalysts*, 2023, **13**, 986.
181. N. Ohtani, N. Kitagawa and T. Matsuda, *Japanese Journal of Applied Physics*, 2011, **50**, 01BC08.
182. A. Khalyfa, S. Kermasha and I. Alli, *Journal of agricultural and food chemistry*, 1992, **40**, 215-220.
183. D. Simon and S. Helliwell, *Water research*, 1998, **32**, 2220-2223.
184. M. Herrero, J. A. Mendiola, A. Cifuentes and E. Ibáñez, *Journal of Chromatography a*, 2010, **1217**, 2495-2511.
185. M. Rinawati, L. Sari and K. Pursetyo, 2020, **441** 012056.
186. E. Dikio and D. Isabirye, *Bulletin of the Chemical Society of Ethiopia*, 2008, **22**, 301-304.
187. N. Nurhayati and V. Suendo, *Jurnal Matematika dan Sains*, 2011, **16**, 65-70.
188. K. Csatorday, R. MacColl and D. Berns, *Proceedings of the National Academy of Sciences*, 1981, **78**, 1700-1702.

189. H. H. Strain, B. T. Cope and W. A. Svec, in *Methods in enzymology*, Elsevier, 1971, **23**, 452-476.

190. D. Činčárová, J. Hájek, M. Dobřichovský, M. Lukeš and P. Hrouzek, *Algal research*, 2021, **56**, 102298.

191. G. Özkan and S. E. Bilek, *Food chemistry*, 2015, **176**, 152-157.

192. X. Hu, A. Tanaka and R. Tanaka, *Plant methods*, 2013, **9**, 1-13.

193. A. Hosikian, S. Lim, R. Halim and M. K. Danquah, *International journal of chemical engineering*, 2010, **2010**, 391632.

194. S. Sakai, T. Noji, M. Kondo, T. Mizuno, T. Dewa, T. Ochiai, H. Yamakawa, S. Itoh, H. Hashimoto and M. Nango, *Langmuir*, 2013, **29**, 5104-5109.

195. Y. Takeuchi and Y. Amao, *Bioconjugate chemistry*, 2003, **14**, 268-272.

196. K. G. Kabza, J. E. Gestwicki and J. L. McGrath, *Journal of Chemical Education*, 2000, **77**, 63.

197. D. O. Njobuenwu, E. O. Oboho and R. H. Gumus, *Leonardo Electronic Journal of Practices and Technologies*, 2007, **10**, 29-38.

198. R. Tadmor, *Langmuir*, 2004, **20**, 7659-7664.

199. T. S. Meiron, A. Marmur and I. S. Saguy, *Journal of colloid and interface science*, 2004, **274**, 637-644.

200. H. Mirsandi, W. J. Smit, G. Kong, M. W. Baltussen, E. Peters and J. Kuipers, *Experiments in Fluids*, 2020, **61**, 1-18.

201. L. Afferrante and G. Carbone, *Journal of Physics: Condensed Matter*, 2010, **22**, 325107.

202. E. Celia, T. Darmanin, E. T. de Givenchy, S. Amigoni and F. Guittard, *Journal of colloid and interface science*, 2013, **402**, 1-18.

203. F. S. Rocha, A. J. Gomes, C. N. Lunardi, S. Kaliaguine and G. S. Patience, *The Canadian Journal of Chemical Engineering*, 2018, **96**, 2512-2517.

204. L. Prati, A. Villa, C. E. Chan-Thaw, R. Arrigo, D. Wang and D. S. Su, *Faraday discussions*, 2011, **152**, 353-365.

205. R. A. Sheldon, I. W. Arends and A. Dijksman, *Catalysis Today*, 2000, **57**, 157-166.

206. B. L. Diffey, *Methods*, 2002, **28**, 4-13.

207. R. Sharma, D. Bisen, U. Shukla and B. Sharma, *Recent Res Sci Technol*, 2012, **4**, 77-79.

208. T. G. Mayerhöfer, S. Pahlow and J. Popp, *ChemPhysChem*, 2020, **21**, 2029-2046.

209. W. Schnabel, *Polymers and light: fundamentals and technical applications*, John Wiley & Sons, 2007.
210. W. Mäntele and E. Deniz, *Journal*, 2017, **173**, 965-968.
211. A. Rothen, *Review of Scientific Instruments*, 1945, **16**, 26-30.
212. H. Fujiwara, *Spectroscopic ellipsometry: principles and applications*, John Wiley & Sons, 2007.
213. E. Garcia-Caurel, A. De Martino, J.-P. Gaston and L. Yan, *Applied spectroscopy*, 2013, **67**, 1-21.
214. G. Jellison Jr, *Thin solid films*, 1998, **313**, 33-39.
215. P. Tengvall, I. Lundström and B. Liedberg, *Biomaterials*, 1998, **19**, 407-422.
216. R. H. Muller, 1971.
217. J. A. Woollam, B. D. Johs, C. M. Herzinger, J. N. Hilfiker, R. A. Synowicki and C. L. Bungay, 1999, **10294**, 1029402.
218. N. Alov, *Journal of Analytical Chemistry*, 2005, **60**, 297-300.
219. F. A. Stevie and C. L. Donley, *Journal of Vacuum Science & Technology A*, 2020, **38**, 063204.
220. K. Watanabe, H. Yamazui and R. *Technical Journal*, 2017, 34-40.
221. S. Kasani, K. Curtin and N. Wu, *Nanophotonics*, 2019, **8**, 2065-2089.
222. M. R. Alexander, R. Short, F. Jones, W. Michaeli and C. Blomfield, *Applied surface science*, 1999, **137**, 179-183.
223. V. Gupta, H. Ganegoda, M. H. Engelhard, J. Terry and M. R. Linford, *Journal of Chemical Education*, 2014, **91**, 232-238.
224. Q. Wei, W. Gao, D. Hou and X. Wang, *Applied Surface Science*, 2005, **245**, 16-20.
225. J. Watts, *Chapter*, 2003, **5**, 149-156.
226. S. Hembacher, F. J. Giessibl, J. Mannhart and C. F. Quate, *Physical review letters*, 2005, **94**, 056101.
227. A. Noy, D. V. Vezenov and C. M. Lieber, *Annual Review of Materials Science*, 1997, **27**, 381-421.
228. S. Guriyanova, D. S. Golovko and E. Bonaccurso, *Measurement Science and Technology*, 2009, **21**, 025502.
229. S. Cárdenas-Pérez, J. J. Chanona-Pérez, J. V. Méndez-Méndez, I. Arzate-Vázquez, J. D. Hernández-Varela and N. G. Vera, *Trends in food science & technology*, 2019, **87**, 59-72.
230. F. J. Giessibl, *Reviews of modern physics*, 2003, **75**, 949.

231. G. J. Leggett, *Analytica chimica acta*, 2003, **479**, 17-38.
232. S. Maghsoudy-Louyeh, M. Kropf and B. Tittmann, *The Open Neuroimaging Journal*, 2018, **12**.
233. J. Grobelny, F. W. Delrio, N. Pradeep, D. I. Kim, V. A. Hackley and R. F. Cook, *Gaithersburg,* Springer Link, 2009, **697**,71-82.
234. Y. F. Dufrêne and P. Hinterdorfer, *Pflügers Archiv-European Journal of Physiology*, 2008, **456**, 237-245.
235. L. Jiang, J. Weber, F. M. Puglisi, P. Pavan, L. Larcher, W. Frammelsberger, G. Benstetter and M. Lanza, *Materials*, 2019, **12**, 459.
236. A. A. Tseng, *Nano Today*, 2011, **6**, 493-509.
237. T. Paulauskas, C. Buurma, E. Colegrove, B. Stafford, Z. Guo, M. K. Chan, C. Sun, M. J. Kim, S. Sivananthan and R. F. Klie, *Acta Crystallographica Section A: Foundations and Advances*, 2014, **70**, 524-531.
238. E. Ruska, *Reviews of modern physics*, 1987, **59**, 627.
239. J. M. Howe and H. Saka, *MRS bulletin*, 2004, **29**, 951-957.
240. K. McDonald, M. Morphew, P. Verkade, T. Müller-Reichert and J. Kuo, *Electron Microscopy: Methods and Protocols*, Humana Press, 2007,143-173.
241. G. J. Hedley, A. Ruseckas and I. D. Samuel, *Chemical Reviews*, 2017, **117**, 796-837.
242. F. Odobel, Y. Pellegrin and J. Warnan, *Energy & Environmental Science*, 2013, **6**, 2041-2052.
243. J. W. Springer, P. S. Parkes-Loach, K. R. Reddy, M. Krayer, J. Jiao, G. M. Lee, D. M. Niedzwiedzki, M. A. Harris, C. Kirmaier and D. F. Bocian, *Journal of the American Chemical Society*, 2012, **134**, 4589-4599.
244. J. L. Brédas, E. H. Sargent and G. D. Scholes, *Nature materials*, 2017, **16**, 35-44.
245. S. Mubeen, J. Lee, N. Singh, S. Krämer, G. D. Stucky and M. Moskovits, *Nature nanotechnology*, 2013, **8**, 247-251.
246. J. Sun, J. Zhang, M. Zhang, M. Antonietti, X. Fu and X. Wang, *Nature Communications*, 2012, **3**, 1139.
247. T. S. Balaban, *Accounts of chemical research*, 2005, **38**, 612-623.
248. D. Gust, T. A. Moore and A. L. Moore, *Accounts of Chemical Research*, 2001, **34**, 40-48.
249. D. Gust, T. A. Moore and A. L. Moore, *Accounts of chemical research*, 2009, **42**, 1890-1898.

250. A. Lishchuk, C. Vasilev, M. P. Johnson, C. N. Hunter, P. Törmä and G. J. Leggett, *Faraday Discussions*, 2019, **216**, 57-71.
251. N. Cheng, P. Bao, S. Evans, G. Leggett and S. Armes, *Macromolecules*, 2015, **48**, 3095-3103.
252. S. Alang Ahmad, A. Hucknall, A. Chilkoti and G. J. Leggett, *Langmuir*, 2010, **26**, 9937-9942.
253. S. Han, R. Yang, C. Li and L. Yang, *Applied Sciences*, 2019, **9**, 566.
254. M. Sypabekova, A. Hagemann, D. Rho and S. Kim, *Biosensors*, 2022, **13**, 36.
255. M. F. Heinig, A. Bastos da Silva Fanta, J. B. Wagner and S. Kadkhodazadeh, *ACS Applied Nano Materials*, 2020, **3**, 4418-4427.
256. J. J. Yin, F. Wahid, Q. Zhang, Y. C. Tao, C. Zhong and L. Q. Chu, *Macromolecular Materials and Engineering*, 2017, **302**, 1700069.
257. G. Panzarasa, S. Aghion, G. Marra, A. Wagner, M. O. Liedke, M. Elsayed, R. Krause-Rehberg, R. Ferragut and G. Consolati, *Macromolecules*, 2017, **50**, 5574-5581.
258. R. Barbey and H.-A. Klok, *Langmuir*, 2010, **26**, 18219-18230.
259. R. Basu, C. Kinser, J. Tovar and M. Hersam, *Chemical physics*, 2006, **326**, 144-150.
260. A. Zengin, G. Karakose and T. Caykara, *European polymer journal*, 2013, **49**, 3350-3358.
261. A. Heidari, K. D. Safa and R. Teimuri-Mofrad, *Molecular Catalysis*, 2023, **547**, 113338.
262. E. Koufakis, T. Manouras, S. H. Anastasiadis and M. Vamvakaki, *Langmuir*, 2020, **36**, 3482-3493.
263. C. Gonzalez-Ballestero, J. Feist, E. Moreno and F. J. Garcia-Vidal, *Physical Review B*, 2015, **92**, 121402.
264. J. Galego, F. J. Garcia-Vidal and J. Feist, *Physical Review Letters*, 2017, **119**, 136001.
265. J. Feist, J. Galego and F. J. Garcia-Vidal, *ACS Photonics*, 2018, **5**, 205-216.
266. D. S. Wright, B. S. Flavel and J. S. Quinton, *2006 International Conference on Nanoscience and Nanotechnology,* IEEE, 2006, 634-636.
267. M. E. Abdelsalam, P. N. Bartlett, T. Kelf and J. Baumberg, *Langmuir*, 2005, **21**, 1753-1757.
268. E. Csanyi, D. Hammond, B. Bower, E. Johnson, A. Lishchuk, S. Armes, Z. Dong and G. Leggett, , *Langmuir*, 2024, **40**, 14527–14539.

269. K. E. Nelson, L. Gamble, L. S. Jung, M. S. Boeckl, E. Naeemi, S. L. Golledge, T. Sasaki, D. G. Castner, C. T. Campbell and P. S. Stayton, *Langmuir*, 2001, **17**, 2807-2816.

270. V. Lacour, K. Moumanis, W. M. Hassen, C. Elie-Caille, T. Leblois and J. J. Dubowski, *Langmuir*, 2017, **35**, 4415-4427.

271. E. Csányi, D. B. Hammond, B. Bower, E. C. Johnson, A. Lishchuk, S. P. Armes, Z. Dong and G. J. Leggett, *Langmuir*, 2024.

272. M. S. Verma, J. L. Rogowski, L. Jones and F. X. Gu, *Biotechnology advances*, 2015, **33**, 666-680.

273. K. A. Willets and R. P. Van Duyne, *Annu. Rev. Phys. Chem.*, 2007, **58**, 267-297.

274. A. J. Haes, W. P. Hall, L. Chang, W. L. Klein and R. P. Van Duyne, *Nano letters*, 2004, **4**, 1029-1034.

275. F. Pena-Pereira, R. M. Duarte and A. C. Duarte, *TrAC Trends in Analytical Chemistry*, 2012, **40**, 90-105.

276. S. K. Ghosh, A. Pal, S. Kundu, S. Nath and T. Pal, *Chemical physics letters*, 2004, **395**, 366-372.

277. M. Iqbal, G. Usanase, K. Oulmi, F. Aberkane, T. Bendaikha, H. Fessi, N. Zine, G. Agusti, E.-S. Errachid and A. Elaissari, *Materials Research Bulletin*, 2016, **79**, 97-104.

278. L. Shao, Q. Ruan, R. Jiang and J. Wang, *Small*, 2014, **10**, 802-811.

279. H. H. Kyaw, S. H. Al-Harthi, A. Sellai and J. Dutta, *Beilstein journal of nanotechnology*, 2015, **6**, 2345-2353.

280. A. F. Scarpettini and A. V. Bragas, *Langmuir*, 2010, **26**, 15948-15953.

281. F. Fernique and G. Weick, *Physical Review B*, 2020, **102**, 045420.

282. S. Gupta, P. Uhlmann, M. Agrawal, S. Chapuis, U. Oertel and M. Stamm, *Macromolecules*, 2008, **41**, 2874-2879.

283. F. Stete, P. Schoßau, W. Koopman and M. Bargheer, 2018, **122**, 17976–17982.

284. X. Huang and M. A. El-Sayed, *Journal of advanced research*, 2010, **1**, 13-28.

285. Y. Sun, B. T. Mayers and Y. Xia, *Nano Letters*, 2002, **2**, 481-485.

286. N. Leopold and B. Lendl, *The Journal of Physical Chemistry B*, 2003, **107**, 5723-5727.

287. V. Giannini, R. Rodríguez-Oliveros and J. A. Sánchez-Gil, *Plasmonics*, 2010, **5**, 99-104.

288. X. Li, L. Zhou, Z. Hao and Q. Q. Wang, *Advanced Optical Materials*, 2018, **6**, 1800275.

Appendix 1 - Chapter 4

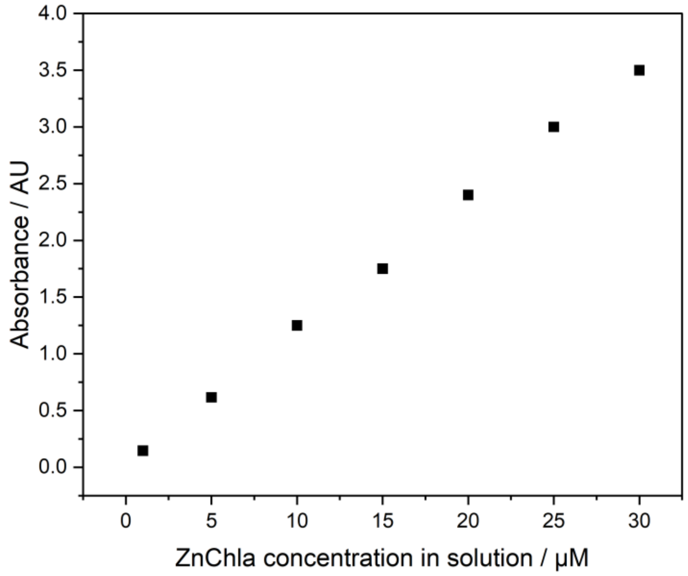

Figure A1-1: The calibration curve for Chla concentrations is a function of their absorbance.

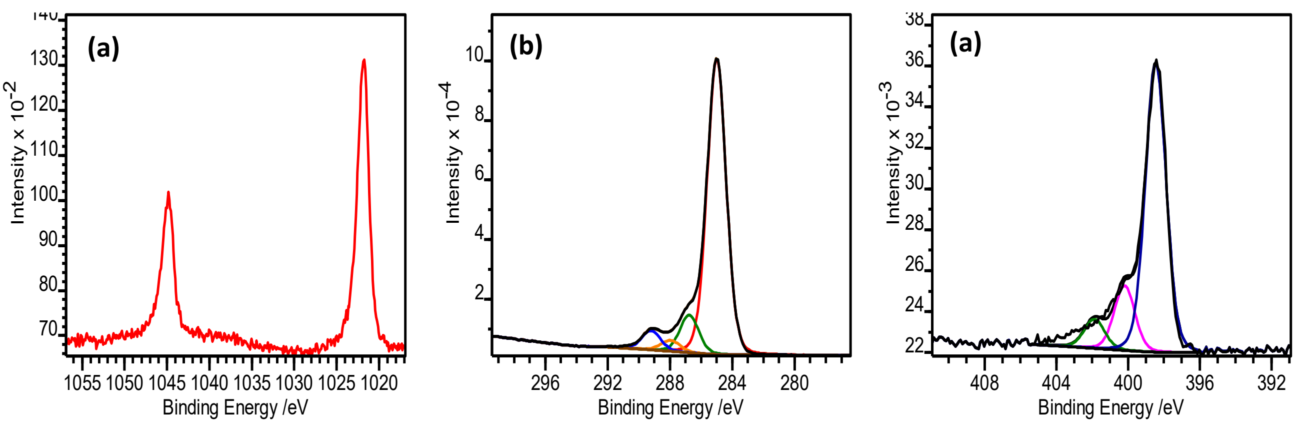

Figure A1-2: High resolution of (a) Zn2p, (b) C1s, (c) and N1s XPS spectra of drop-casted Chl on the glass substrate.

Table A1-1: XPS fitting details of a drop-cast of Chl onto glass slide of C1s, O1s, N1s, and Zn2p.

The Peak	BE of fitted peaks / eV	FWHM / eV	Composition /atomic %
C1s	285.0 286.6 287.7 289.2	1.44 1.44 1.44 1.44	80.6 9.7 5.6 4.1
O1s	532.4 533.7	1.90 1.90	59.1 41.0
N1s	398.4 400.1 401.7	1.30 1.30 1.30	78.1 13.9 8.1
Zn2p	1022	1.48	2.2

Table A1-2: The model used for fitting spectroscopic ellipsometry data for PDMA grown from BIBB-APTES.

Layer	**Material**	**Fitted parameters**	**Comments**
Layer #2	PDMA polymer	*d*	Cauchy model is used to describe the optical properties of PDMA brush film, where *d* is the thickness of the adsorbed layer in nm. The parameters A, B and C are Cauchy model fit parameters allowed to fit during the modelling
Layer #1	BIBB-APTES	*d*	Cauchy model is used to describe the optical properties of BIBB-APTES film, where *d* is the thickness of the adsorbed layer in nm. The parameters A, B and C are Cauchy model fit parameters allowed to fit during the modelling
Substrate	BK7 glass	-	*n* = 1.515

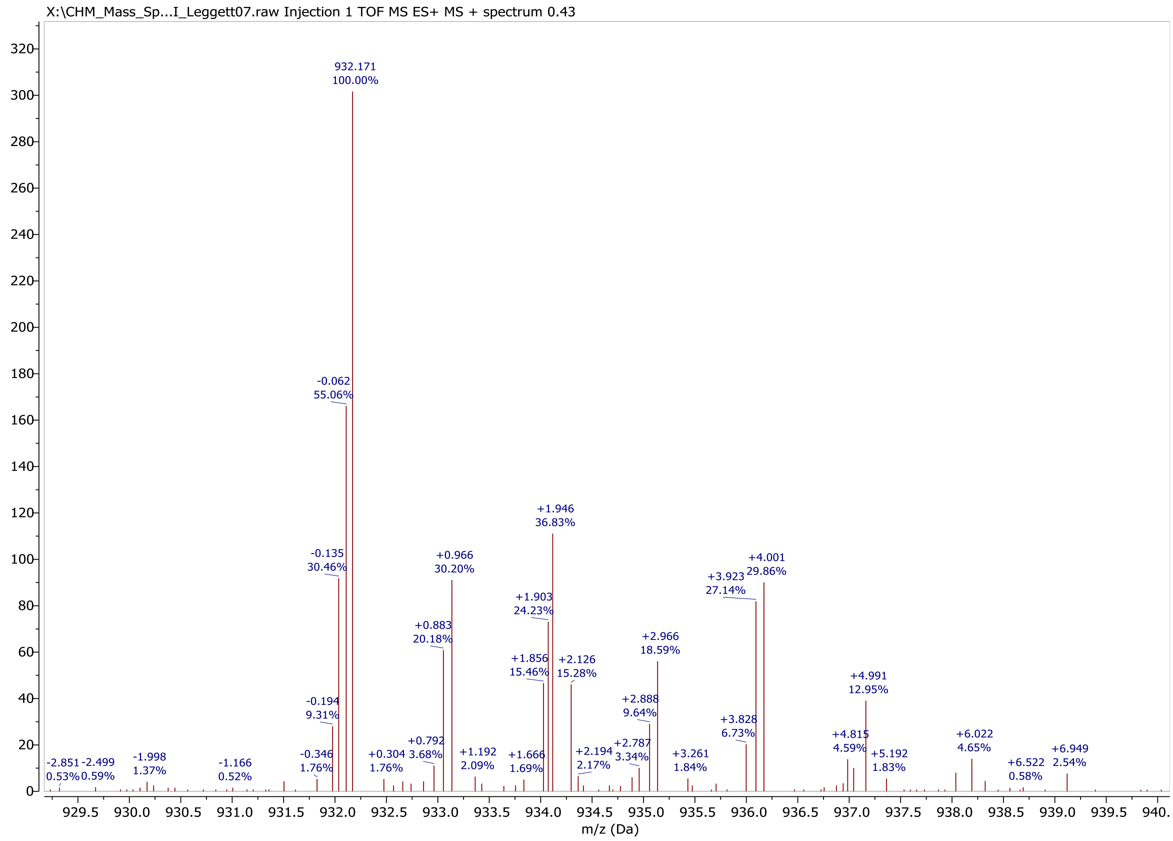

Figure A1-3: The MS of Zn-Chla**.**

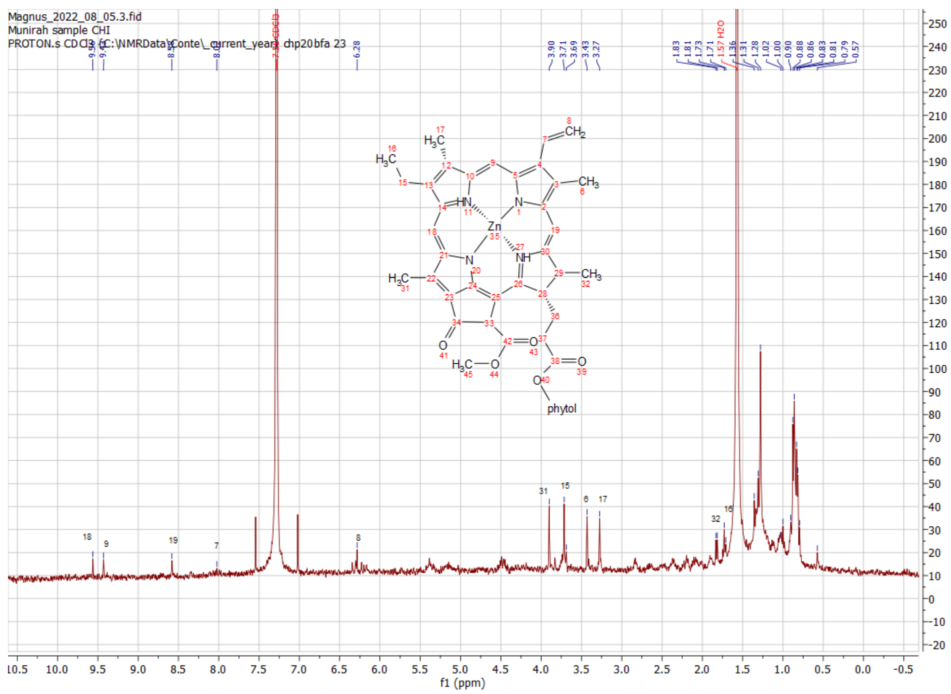

Figure A1-4: The NMR of Zn-Chla**.**

Appendix 2 - Chapter 5

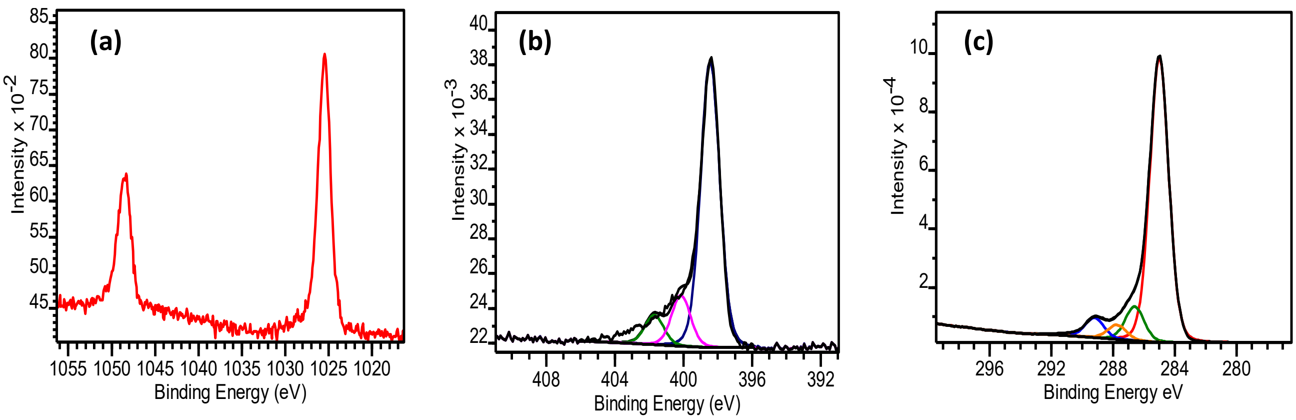

Figure A2-1: High resolution of (a) Zn2p, (b) N1s, (c) and C1s XPS spectra of drop-casted Chl on the gold substrate.

Table A2-1: XPS fitting details of a drop-cast of Chl onto the gold surface of C1s, O1s, N1s, and Zn2p.

The Peak	BE of fitted peaks / eV	FWHM / eV	Composition /atomic %
C1s	285.0 286.8 288.0 289.3	1.40 1.40 1.40 1.40	76.4 12.5 5.0 6.1
O1s	532.5 533.9	2.04 2.04	71.0 29.0
N1s	398.7 400.4 402.0	1.41 1.41 1.41	66.0 26.0 8.1
Zn2p	1022	1.48	2.4

Table A2-2: The details of XPS fitting for DTBU SAMs.

The Peak	BE of fitted peaks / eV	FWHM / eV	Composition /atomic %
C1s	285.00 286.8 289.1	1.42 1.42 1.42	8.7 14.4 6.8
O1s	532.4 533.9	2.0 2.0	61.7 38.3
S2p	162.4 163.9	1.74 1.74	66.7 33.3

Table A2-3: The details of XPS fitting for MUL SAMs.

The Peak	BE of fitted peaks / eV	FWHM / eV	Composition /atomic %
C1s	285.00 286.9	1.19 1.19	87.5 12.5
O1s	533.2 531.6	1.56 1.56	95.6 5.7
S2p	162.4 163.9	0.92 0.92	66.7 33.3

Table A2-4: The XPS fitted peak for the C1s for the mixture of DTBU + MUL, with χBr(Au) = 0.52.

The Peak	BE of fitted peaks / eV	FWHM / eV	Composition /atomic %
C1s	285.00 286.7 288.5	1.24 1.24 1.24	82.70 13.7 3.6

Table A2-5: The XPS fitted peak for the C1s for the mixture of DTBU + MUL, with χBr(Au) = 0.2.4

The Peak	BE of fitted peaks / eV	FWHM / eV	Composition /atomic %
C1s	285.00 286.8 288.3	1.22 1.22 1.22	83.23 13.5 3.3

Table A2-6: The XPS fitted peak for the C1s for the mixture of DTBU + MUL, with χBr(Au) = 0.11.

The Peak	BE of fitted peaks / eV	FWHM / eV	Composition /atomic %
C1s	285.00 286.8 288.1	1.20 1.20 1.20	85.28 12.3 2.5

Table A2-7: The model used for fitting spectroscopic ellipsometry data for PDMA film on an Au/ Cr/ Si substrate stack.

Layer	Material	Fit Parameters	Comments
Layer #3	PDMA Brush	*d*=27.63 nm ± 0.01 nm, A=1.496 ± 0.001, B=0.000597± 0.000196, C=0.000356± 0.000009	Cauchy model is used to describe the optical properties of PDMA brush film, where *d* is the thickness of the adsorbed layer in nm. The parameters A, B and C are Cauchy model fit parameters allowed to fit during the modelling
Layer #2	Gold	*d*	Au optical constants and thickness were determined before brush deposition using a B-Spline model and the thickness of the deposited gold film was determined to be ~33 nm and was fixed during the modelling of PDMA brush film
Layer #1	Chromium	*d*	Cr optical constants were determined before brush deposition by the B-Spline model and the thickness of the deposited chromium layer was determined to be ~ 9 nm which was fixed during the PDMA brush fitting.
Native Oxide	SiO_2	-	Thickness fixed 1.5 nm optical constants used from Complete Ease library
Substrate	Si	-	Optical constants used from Complete Ease library

Table A2-8: The model used for fitting spectroscopic ellipsometry data for PDMA film on an Au/ Cr/ Si substrate stack.

Layer	Material	Fitted parameters	Comments
Layer #3	Chla funcitonalised PDMA Polymer Brush	d= 38.96 ±0.57 nm	*d* is the thickness of the adsorbed layer in nm, ε_∞ is the high-frequency permittivity. Kramers-Kronig (KK) consistent B-Spline was used with a resolution of 0.02 eV to model the lineshape of the ellipsometry spectra and extract the KK consistent optical constants of the material.
Layer #2	Gold	-	Au optical constants and thickness were determined before brush deposition using a B-Spline model and the thickness of the deposited gold film was determined to be ~33 and was fixed during the modelling of Chla PDMA brush film
Layer #1	Chromium	-	Cr optical constants were determined before brush deposition by the B-Spline model and the thickness of the deposited chromium layer was determined to be ~ 9 nm which was fixed during the Chl-a brush fitting.
Native Oxide	SiO_2	-	Thickness fixed at 1.5 nm; optical constants used from Complete Ease library
Substrate	Si	-	Optical constants used from Complete Ease library

Appendix 3 - Chapter 6

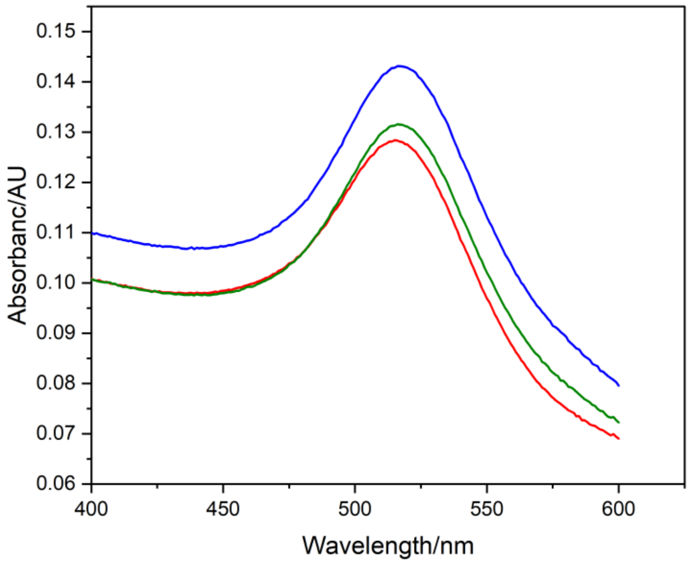

Figure A3-1: The absorbance spectra of the concentration of NPI (λ max at 519 nm) on the APTES surface after 24 hours for three different runs1, 2, and 3.

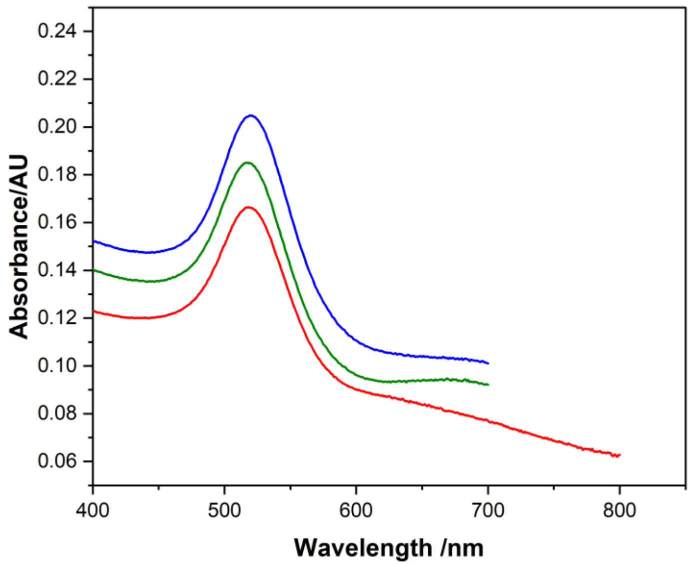

Figure A3-2: The absorbance spectra of the concentration of NPII (λ max at 523 nm) on the APTES surface after 24 hours for three different runs1, 2, and 3.

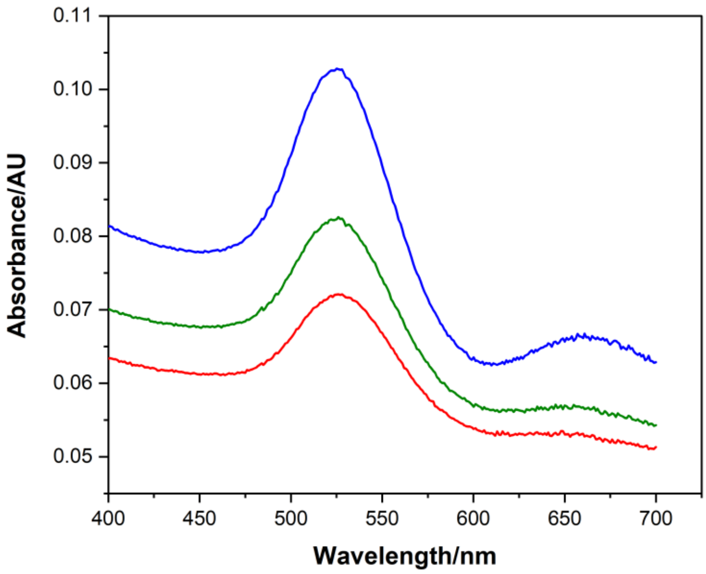

Figure A3-3: The absorbance spectra of the concentration of NPIII (λ max at 531 nm) on the APTES surface after 24 hours for three different runs1, 2, and 3.

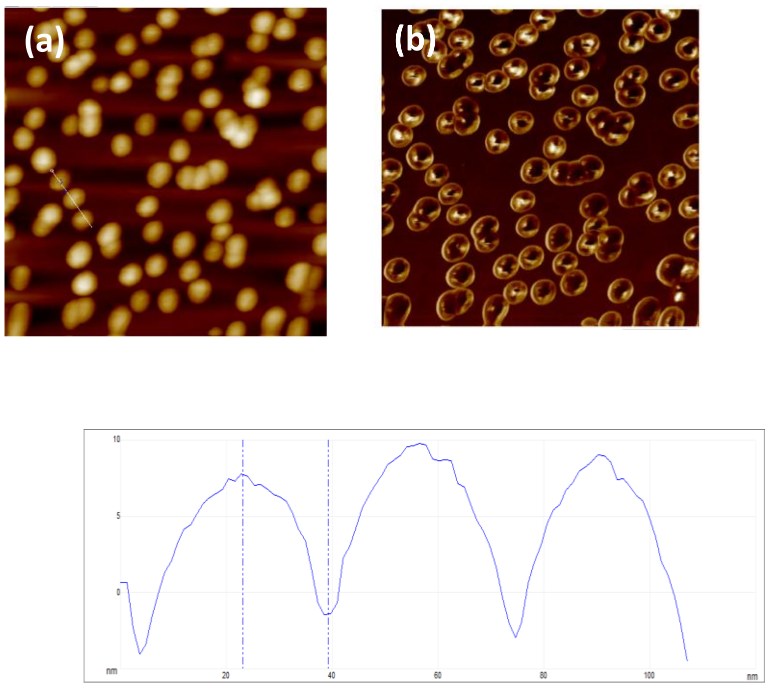

Figure A3-3: AFM height images of NPI on APTES surface (a) and phase image (b) with cross-section surface profiling (down).

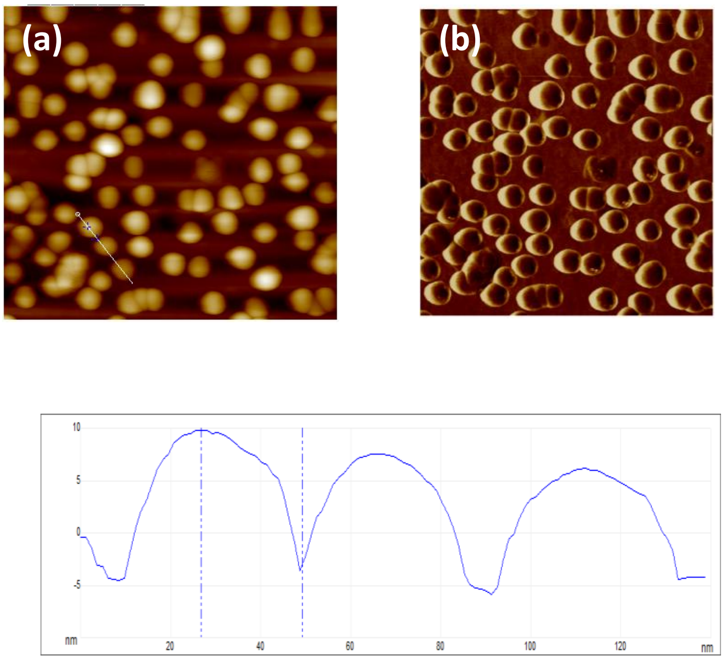

Figure A3-4: AFM height images of NPI on APTES surface (a) and phase image (b) with cross-section surface profiling (down).

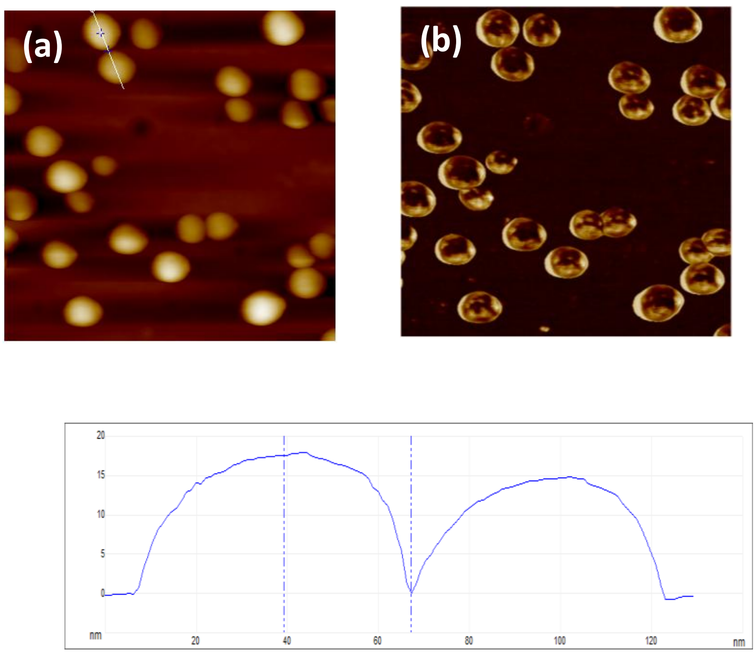

Figure A3-4: AFM height images of NPII on APTES surface (a) and phase image (b) with cross-section surface profiling (down).

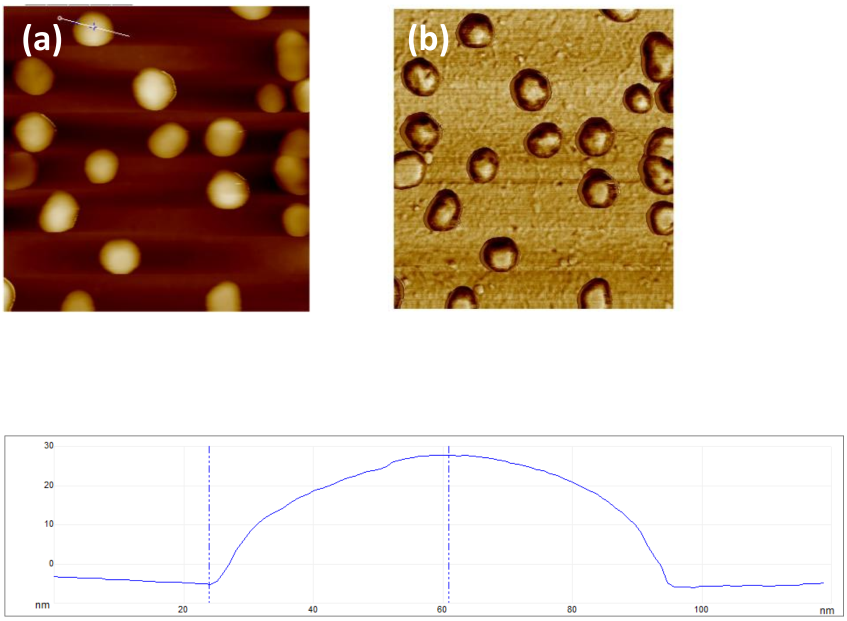

Figure A3-5: AFM height images of NPIII on APTES surface (a) and phase image (b) with cross-section surface profiling (down).